General Disclaimer

One or more of the Following Statements may affect this Document

- This document has been reproduced from the best copy furnished by the organizational source. It is being released in the interest of making available as much information as possible.

- This document may contain data, which exceeds the sheet parameters. It was furnished in this condition by the organizational source and is the best copy available.

- This document may contain tone-on-tone or color graphs, charts and/or pictures, which have been reproduced in black and white.

- This document is paginated as submitted by the original source.

- Portions of this document are not fully legible due to the historical nature of some of the material. However, it is the best reproduction available from the original submission.

EOSL

Electro-Optics Systems Laboratory
Department of Electrical and Computer Engineering

Theoretical and Experimental Analyses of the Performance of Two-Color Laser Ranging Systems

Kwaifong E. Im • C. S. Gardner

E.O.S.L. No. 85-006 • August 1985

University of Illinois at Urbana-Champaign

UILU-ENG-85-2552

THEORETICAL AND EXPERIMENTAL ANALYSES OF THE PERFORMANCE OF TWO-COLOR LASER RANGING SYSTEMS

by

K. E. Im
C. S. Gardner

EOSL No. 85-006

Technical Report
August 1985

Supported by
Contract No. NASA NSG-5049

NATIONAL AERONAUTICS & SPACE ADMINISTRATION
Goddard Space Flight Center
Greenbelt, Maryland 20771

ELECTRO-OPTIC SYSTEMS LABORATORY
DEPARTMENT OF ELECTRICAL AND COMPUTER ENGINEERING
COLLEGE OF ENGINEERING
UNIVERSITY OF ILLINOIS
URBANA, ILLINOIS 61801

ABSTRACT

In satellite laser ranging, atmospheric refraction increases the optical pathlength from the ground to an orbiting satellite. Two-color laser ranging systems can be used to determine the atmospheric delay by measuring the difference in propagation times between optical pulses transmitted at the two different wavelengths. The differential propagation time can also be used to infer surface pressure.

The statistical properties of the signals reflected from the retro-reflector equipped satellites are studied. It is found that coherence interference between pulse reflections from retro-reflectors of different ranges on the array platform is the primary cause of signal fluctuations.

The performance of a cross-correlation technique for estimating the differential propagation time is analyzed by considering both shot noise and speckle. For the retro-reflector arrays, timing performance is dominated by interference induced speckle, and the differential propagation time cannot be resolved to better than the pulse widths of the received signals.

The differential timing measurements obtained over a horizontal path are analyzed. The results are used to verify both the two-color ranging measurement technique and the cross-correlation timing algorithm.

The ocean-reflected pulse measurements obtained from the airborne two-color laser altimeter experiment are presented. The reflected pulse shapes are used to infer the sea state and the ocean wind speed. The measured differential propagation times are used to verify the pressure measurement technique.

ACKNOWLEDGEMENTS

The authors would like to acknowledge Dr. James B. Abshire of NASA-Goddard Space Flight Center for his interesting and helpful discussions pertinent to this work. In particular, we appreciate his efforts in developing a fast response two-color laser ranging system which was used to acquire measurements needed for this research.

Thanks also go to Ms. Jan F. McGarry for her work in data acquisition software, and to Mr. H. Edward Rowe and Mr. Richard S. Chabot for their assistance throughout the experiments.

This research was supported by the National Aeronautics and Space Administration under Grant NSG-5049.

TABLE OF CONTENTS

Page

1. INTRODUCTION

The feasibility of using pulsed lasers to range to earth-orbiting satellites was first demonstrated by researchers at the NASA-Goddard Space Flight Center in 1964 [Plotkin et al., 1965]. Since then, this technique has been used by numerous groups for applications in global surveying [Smith et al., 1972], geophysical research [Smith et al, 1973], and positioning [Smith et al., 1973]. In these applications, pulsed laser ranging systems are used to estimate the distances from ground-based ranging sites to retro-reflector equipped satellites by measuring the roundtrip optical propagation times. The accuracies of these systems are limited by the effects of atmospheric refraction, which increases the average optical pathlength between the ranging site and the orbiting satellite by 2.5 meters when the satellite is near zenith and by more than 13 meters when it is at 10° elevation [Abshire and Gardner, 1985]. Several formulas have been developed which can correct range errors to centimeter level for the single-color systems [Saastamoinen, 1972; Marini and Murray, 1973; Gardner, 1977; Davis et al., 1984; Treuhaft et al., 1984]. However, these formulas require accurate meteorological measurements at the ranging site during the satellite pass, which may not be feasible, particularly in certain inaccessible regions of the earth. An alternate approach is to employ two-color laser ranging systems to determine the atmospheric correction directly by measuring the propagation time difference induced by dispersion between pulses at two different optical frequencies [Prilepin, 1957; Bender and Owens, 1965]. Because the atmospheric dispersion in the optical frequency band is small, the differential propagation times must be measured with picosecond-level accuracies if cm-level ranging accuracies are desired [Bender and Owens, 1965].

More recently, the multicolor laser ranging technique has been extended to applications in remote sensing of atmospheric pressure. By using the facts that the atmosphere is dispersive, and the group refractivity is proportional to the surface pressure, Gardner [1979] proposed a remote sensing technique to globally measure atmospheric pressure using a two-color laser altimeter. Making pressure measurements over the ocean using this remote technique is highly desirable because the weather over land usually originates from oceans. Accurate measurements of ocean surface pressure would allow better seasonal climate modelling and long-range weather forecasting. In general, when the altimeter uses 1.064 - and 0.353-μm YAG laser wavelengths, picosecond timing accuracies are required for millibar-level pressure accuracies.

The differential timing accuracy, in general, is strongly dependent on the orientation and the local height distribution of the target surface profile with respect to the optical axis. Experimental results obtained using high speed detectors indicate that picosecond timing accuracy is achievable for specular targets like non-dispersive retroreflectors [Abshire and Kalshavon, 1983; Im et al., 1983; Abshire and Gardner, 1985]. However, these target geometries constitute only a small fraction of the targets which are available. In order to extend the applicability of the two-color ranging technique, targets with randomly varying local surface profiles, such as the ocean and satellites containing retroreflector arrays, must also be considered. The reflections from such targets present three major difficulties for timing estimation. First, the reflected pulses are broadened due to the range spreads of the target surface profiles. Second, the time-resolved speckle fluctuations within the received pulses will distort the pulse shapes when the range spreads of the targets are longer than the transmitted

laser pulse widths [Tsai and Gardner, 1985]. Third, the mean received pulse shapes from randomly changing target surfaces are generally not known a priori so that conventional optimal timing estimators cannot be used. The achievement of picosecond timing accuracy when ranging to targets of opportunity is, therefore, a challenging task which requires careful investigation of both the reflection process and the ranging receiver design. This dissertation is centered around these two aspects, with emphasis on the two-color ranging accuracy in the presence of major noise sources such as shot noise, speckle, and background noise.

Chapter 2 reviews the established theories behind the pulsed laser ranging technique, the two-color atmospheric correction technique, and the two-color pressure measurement technique, and their corresponding accuracies.

In the first portion of Chapter 3 the statistics of the diffuse target reflected laser signal [Gardner, 1982] is summarized. The statistics of the signals reflected from the cube-corner reflector arrays is studied, using partially developed speckle theory and Fresnel diffraction. This study has practical application in ranging to the existing retroreflector-equipped satellites such as the Laser Geodynamic Satellite (LAGEOS) and Geodetic Earth Orbiting Satellites (GEOS).

In addition to the range errors induced by the atmosphere, the performance of the laser ranging systems is also limited by the presence of noise. In Chapter 4 the performance of the Maximum-Likelihood timing estimators are investigated under the influence of the time-resolved speckle and background radiation.

When the targets of interest have temporally varying local surface profiles, it is not possible to predict the mean reflected signal a priori.

Consequently, the Maximum Likelihood estimators, which require knowledge of the mean signal, cannot be used. In Chapter 5 a two-color cross-correlation estimator is studied and its corresponding performance is analyzed. The results are applied to the pulse reflections from ground diffuse targets, earth-orbiting CCR arrays, and the ocean.

For high precision two-color laser ranging, the transmitted laser beams at the two frequencies must be aligned so that the reflected signals are highly correlated. Any misalignment will cause decorrelation of the laser pulse shape and degrade the timing performance of the cross-correlation estimator. In addition, the relative displacement between the transmitter and receiver axes can influence the amount the signal strength received by the system, which in turn affects the timing performance because the timing accuracy is directly proportional to the signal strength. In Chapter 6 we investigate the system alignment effects on the performance of the cross-correlation differential timing estimator.

In parallel with the theoretical research on the two-color cross-correlation technique, experimental research has been undertaken at NASA-Goddard Space Flight Center to verify the feasibility of this technique under actual field conditions. In Chapter 7 we report on the recent two-color range measurements made over the horizontal paths. These measured results are analyzed and compared with the predictions based upon the theory of Chapter 5.

An airborne two-color altimeter experiment was conducted in April of 1985 at NASA/Goddard-Wallops Flight Facility in which the ocean-reflected signal measurements were collected. The primary objectives of this mission were to verify the two-color pressure measurement technique and the cross-correlation technique. The processed results are analyzed and discussed in Chapter 8.

2. RANGING AND PRESSURE MEASUREMENT TECHNIQUES : REVIEW

2.1 Introduction

Both single- and two-color satellite laser ranging (SLR) systems can be used to estimate distance by measuring the round-trip propagation times of the laser pulses. However, the performance of such systems is limited by the effects of atmospheric refraction, which increases the optical pathlengths between the satellite and the ranging site, and the effects of atmospheric turbulence, which introduces random fluctuations in the refractivity along the propagation path. Atmospheric refraction increases the average round-trip optical pathlength to an orbiting satellite by 2.5 m when it is near zenith and by more than 13 m when the satellite is at 10° elevation. Strong turbulence can introduce random errors of about several cm at 10° elevation [Abshire and Gardner, 1985]. Consequently, atmospheric refraction is the most dominant source of error in satellite ranging. Normally, the error contributions due to turbulence are negligible.

2.2 Ranging Geometry

The geometry for a satellite laser ranging system and its ground target is shown in Fig. 2.1. The round-trip straight-line pathlength R_s is the parameter of interest. However, due to the atmospheric refraction effect, the round-trip optical pathlength R_o is longer than R_s. The atmospheric correction AC (that is, the range error due to atmospheric refraction) is the difference between the round-trip optical pathlength and the straight-line pathlength:

$$AC = (R_o - R_s) . \qquad (2.1)$$

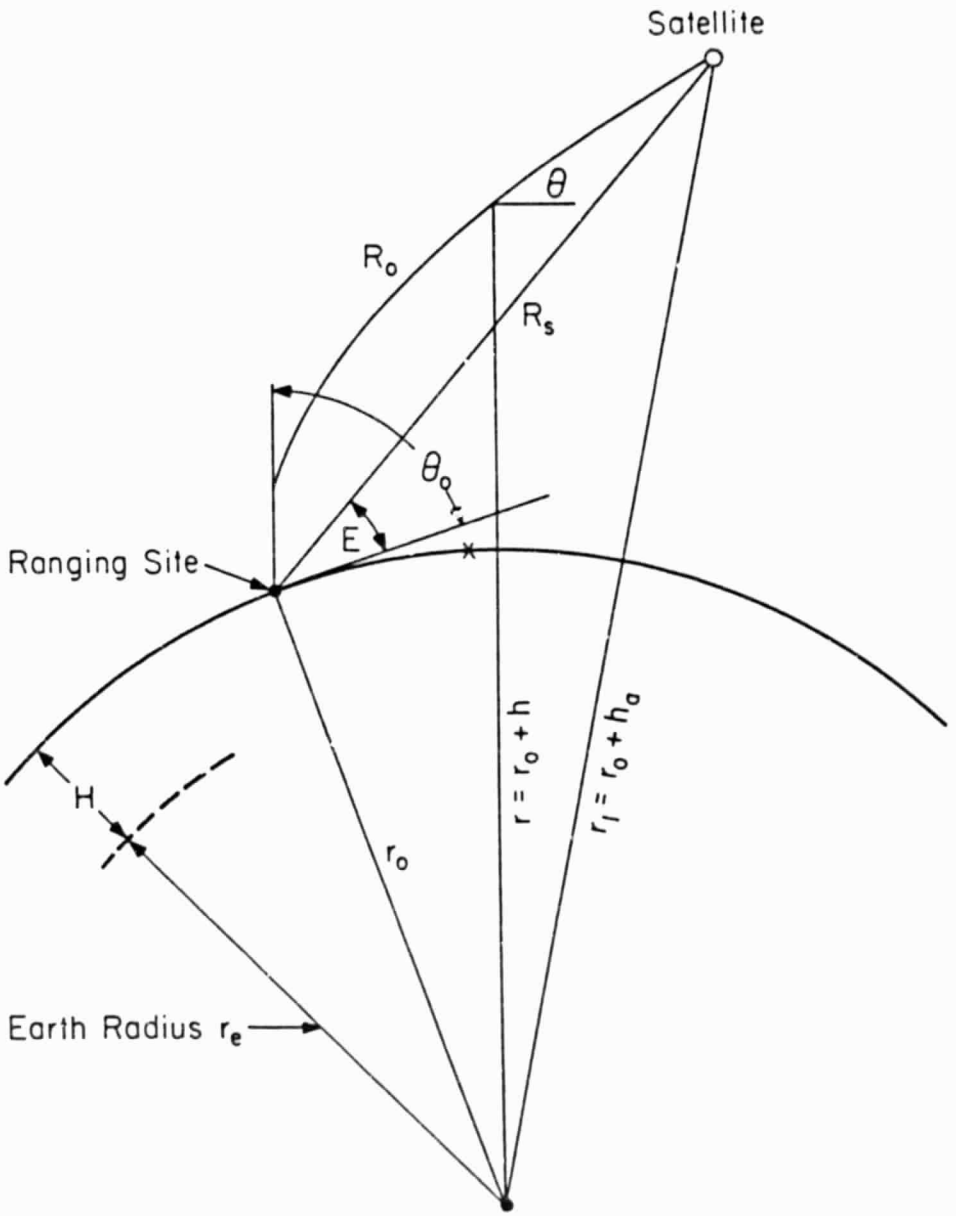

Fig. 2.1. Geometry of satellite and ground target.

The optical pathlength between the satellite and the ground target is defined as the integral of the group refractive index along the ray path:

$$R_o = 2 \int_c n_g \, dl \tag{2.2}$$

where dl is an incremental length along the ray path c, and n_g is the group refractive index. This refractive index is related to the group refractivity N_g by [Marini and Murray, 1973]

$$n_g = 1 + 10^{-6} N_g \, . \tag{2.3}$$

If the horizontal refractivity gradients are small, the ray path will lie entirely in a plane. In this case, the optical pathlength for a pulsed laser system is given by [Marini and Murray, 1973]

$$R_o = 2 \int_{r_{earth}}^{r_{sat}} \frac{(1 + 10^{-6} N_g)}{\sin \theta} \, dr \tag{2.4}$$

where r is the geocentric altitude, and θ is given by Snell's Law for a spherical stratified medium. The atmospheric correction in the spherically symmetrical atmosphere is thus

$$AC = 2 \int_{r_{earth}}^{r_{sat}} \frac{10^{-6} N_g}{\sin \theta} \, dr + \left[2 \int_{r_{earth}}^{r_{sat}} \frac{dr}{\sin \theta} - R_s \right] \, . \tag{2.5}$$

The first term in Eq. (2.5) is the velocity correction error, while the second term is the difference between the geometric length of the ray and the straight-line path.

2.3 Atmospheric Correction Model For Single-color Laser Ranging

The atmospheric correction can be evaluated by using an appropriate model for the group refractivity. For typical refractivity profile that includes the nonsymmetric behavior of the atmosphere, AC can be modeled approximately as [Gardner and Axford, 1980]

$$AC = \frac{\beta_1}{\sin E} + \frac{\beta_2}{\sin^3 E} + \frac{\beta_3 \cos \alpha}{\sin E \tan E} + \frac{\beta_4 \sin \alpha}{\sin E \tan E} \qquad (2.6)$$

where E is the elevation angle, α is the azimuth angle, and the coefficients β_1, β_2, β_3, β_4 are functions of the refractivity profile and laser wavelength. The first two terms in Eq. (2.6) are spherical correction terms corresponding to a spherically symmetric atmosphere, while the last two terms include the effects of horizontal refractivity gradients. Marini and Murray [1973] have developed accurate formulas for calculating β_1 and β_2 in terms of the surface pressure, temperature and water vapor pressure at the ranging site during the satellite pass. More recently, Gardner [1977] has derived expressions for β_3 and β_4 in terms of the horizontal pressure and temperature gradients at the ranging site. Both formulas have been checked extensively by comparing them with the ray tracing data. The results indicate that the error in approximating the atmospheric correction with a formula of the form given by Eq. (2.6) is less than a few centimeters for elevation angles above 20°.

If ranging accuracies of a few centimeters or less are desired, an extensive weather station network may be required to obtain sufficiently accurate measurements of the meteorological parameters during the satellite pass [Gardner et al., 1978]. This requirement may limit the applicability of the single-color laser ranging systems.

2.4 Two-color Laser Ranging Technique

Two-color laser ranging provides an attractive alternative to models for determining the atmospheric correction because requirements on surface meteorological data can be eliminated. The technique is based upon the fact that the dispersion in the atmosphere is frequency dependent. This causes the optical pathlength at the two different frequencies to be proportional to the path-integrated atmospheric density. Therefore, the difference in optical pathlengths at two laser frequencies is a measure of the refractive conditions existing over the propagation path at the instant the measurements are taken and can be used to estimate the atmospheric correction [Bender and Owens, 1965].

Let R_{o_1} and R_{o_2} denote the round-trip optical pathlengths at wavelengths λ_1 and λ_2 respectively. Then the atmospheric correction at wavelength λ_1 is approximately

$$AC_1 = \gamma (R_{o_2} - R_{o_1}) = \gamma \Delta R \tag{2.7}$$

where

$$\gamma = (n_{g_1} - 1) / (n_{g_2} - n_{g_1}) \tag{2.8}$$

and n_{g_1} and n_{g_2} are the group refractive indices of the atmosphere measured at wavelengths λ_1 and λ_2, respectively. Equation (2.7) is accurate at optical frequencies. If we ignore the small water vapor effects at optical frequencies, γ can be written as

$$\gamma = f(\lambda_1) / (f(\lambda_2) - f(\lambda_1)) \tag{2.9}$$

where

$$f(\lambda_i) = 0.965 + 0.0164\ \lambda_i^{-2} + 0.000228\ \lambda_i^{-4}\ , \quad i=1,2, \tag{2.10}$$

and λ_i is expressed in units of micrometers. The function $f(\lambda_i)$ accounts for the atmospheric disperion which is responsible for the difference in path-lengths at the two frequencies. It is derived by curve fitting the actual experimental measurements of the dispersion. In Table 2.1 γ is listed for all pairwise combinations of the fundamental (1.064-μm), doubled (0.532-μm) and tripled (0.355-μm) YAG laser wavelengths.

The RMS error in atmospheric correction (σ_{AC_1}) is related to the RMS error in differential pathlength ($\sigma_{\Delta R}$) through

$$\sigma_{AC_1} = \gamma\ \sigma_{\Delta R}\ . \tag{2.11}$$

Because γ is on the order of ten for all wavelength pairs, it is necessary to determine the differential pathlength with an accuracy which is approximately ten times greater than the desired accuracy for the atmospheric correction. Therefore, in order to achieve cm-level accuracy in atmospheric correction, which is typical by using a single-color system, the differential pathlength must be measured to an accuracy of a few millimeters, or equivalently, the differential propagation time of the optical pulses at the two frequencies must be measured to an accuracy of a few picoseconds.

This accuracy requirement can be eased considerably if the results of many measurements during the satellite pass are averaged. However, the satellite position must be taken into account when measurements are averaged because both AC_1 and ΔR are functions of the satellite azimuth and elevation angles. In general, regression models are used to fit the calculated values of the atmospheric correction to Eq. (2.6) before averaging [Gardner and Axford, 1980].

TABLE 2.1.

ATMOSPHERIC CORRECTION TO DIFFERENTIAL PATHLENGTH RATIO

$\lambda_1(\mu m)$	$\lambda_2(\mu m)$	γ
1.064	0.532	21.1
1.064	0.355	7.45
0.532	1.064	-22.1
0.532	0.355	12.1
0.355	1.064	- 8.45
0.355	0.532	-13.1

2.5 Surface Pressure Measurement Technique

Although the atmospheric correction depends on the atmospheric pressure, temperature, and humidity along the propagation path, theoretical results show that it is most sensitive to pressure [Gardner, 1979]. In fact, when the laser is pointed at nadir, AC is approximately proportional to the atmospheric pressure at the earth's surface. Therefore, surface pressure can be computed from measurements of AC.

If the straight-line pathlength (R_s) between the satellite and the laser footprint on the earth's surface is known, AC can be calculated by using the single-color timing measurements and Eq. (2.4). Because R_s must be known to within a few centimeters for the approach to be effective, it is probably not practical. An alternate approach is to use a two-color laser ranging system to determine AC by calculating the differential pathlength measured at the two frequencies:

$$\Delta R = AC_1 - AC_2. \tag{2.12}$$

In general, Eq. (2.6) must be used to determine ΔR. However, for pressure measurement applications we are only interested in situations where the nadir angles are small. In this case, the gradient correction terms given by Eq. (2.6) contribute less than 1 cm as compared with 2- to 5-meter contribution from spherical connection terms. Consequently, the more simplified model given by Eq. (2.5) can be used for pressure measurement applications without loss of accuracy. If Eqs. (2.5) and (2.12) are evaluated and then solved for the atmospheric pressure at the ranging site, we obtain [Gardner, 1979]

$$P = \frac{-b + (b^2 - 4ad)^{1/2}}{2a} \quad , \tag{2.13}$$

$$a = 4.73 \times 10^{-8} \; \frac{f(\lambda_1) - f(\lambda_2)}{T \sin^2 E} \; \frac{2}{3 - K^{-1}} \quad , \tag{2.14}$$

$$d = \frac{F(\theta_c, H) \; \Delta R \sin E}{2[f(\lambda_1) - f(\lambda_2)]} - 2.24 \times 10^{-4} e \quad , \tag{2.15}$$

$$b = -2.357 \times 10^{-3} + \frac{1.084 \times 10^{-8} \; TK}{\tan^2 E} - \frac{1.5 \times 10^{-13} \; T^2}{\sin^4 E} \frac{K^2}{2-K} \quad , \tag{2.16}$$

$$F(\theta_c, H) = 1 + 0.0026 \cos (2\theta_c) - 0.0003 (H) \quad . \tag{2.17}$$

$$K = 1.163 + 0.00968 \cos (2\theta_c) - 0.00104 \; T + 0.00001435 \; P \quad , \tag{2.18}$$

where

e = water vapor pressure at the laser footprint (mbar),

P = atmospheric pressure at the laser footprint (mbar),

T = temperature at the laser footprint (°K),

θ_c = co-latitude of the laser footprint,

H = altitude of the laser footprint above sea level (km),

and the remaining parameters were described in earlier sections of this chapter.

2.6 Pressure Measurement Error

In a realistic system it will not be possible to determine the parameters ΔR, E, e, and T exactly. Therefore, it is important to assess the effect of errors in these parameters on the accuracy of the recovered pressure. An approximate expression for the RMS pressure error is [Gardner, 1979]

$$\sigma_P = \left[\left(\frac{\partial P}{\partial_{\Delta R}}\ \sigma_{\Delta R}\right)^2 + \left(\frac{\partial P}{\partial E}\ \sigma_E\right)^2 + \left(\frac{\partial P}{\partial e}\ \sigma_e\right)^2 + \left(\frac{\partial P}{\partial T}\ \sigma_T\right)^2\right]^{1/2} \tag{2.19}$$

where $\sigma_{\Delta R}$, σ_E, σ_e, σ_T are the RMS errors in ΔR, E, e, and T, respectively. The partial derivatives can be calculated by taking the derivatives of Eq. (2.13). The results are

$$\frac{\partial P}{\partial \Delta R} \approx \frac{0.212 \sin E}{f(\lambda_1) - f(\lambda_2)} \text{ (mbar/mm)} \quad , \tag{2.20}$$

$$\frac{\partial P}{\partial E} \approx \frac{10^{-3} P}{\tan E} \text{ (mbar/mrad)} \quad , \tag{2.21}$$

$$\frac{\partial P}{\partial e} \approx 0.095 \text{ (mbar/mbar)} \quad , \tag{2.22}$$

$$\frac{\partial P}{\partial T} \approx -\frac{2.55 \times 10^{-6} P}{\tan^2 E} + \frac{3.4 \times 10^{-5} P^2}{T^2 \sin^2 E} + \frac{4.2 \times 10^{-11} PT}{\sin^4 E} \text{ (mbar/°c)} \quad . \tag{2.23}$$

Although the pressure sensitivity to temperature error is greatest at the lower elevation angles, its value above 20° is quite small. At 20° elevation, a temperature error of 50°C would contribute less than 1 mbar to the pressure error. Thus, only a crude estimate of the surface temperature is required. An accuracy of 20-30°C is easy to obtain and should be adequate.

The pressure sensitivity to errors in water vapor pressure is constant with respect to elevation angle. A 10-mbar error in water vapor pressure will contribute approximately 1 mbar to the surface pressure error. Since water

vapor pressure can approach 40 mbar when the surface temperature and relative humidity are high, its effects cannot be ignored. Fortunately, with the development of the microwave radiometry, sufficiently accurate information on water vapor pressure is accessible. Current radiometers can measure this parameter to a 90% accuracy [Prabhakara et al., 1982]. For an extremely humid condition of 40 mbar, a 10% error in water vapor pressure measurement corresponds to about 0.4 mbar error in surface pressure. Consequently, by using information collected by radiometers, the error due to water vapor pressure can be reduced to an insignificant amount.

The pressure sensitivity in elevation angle is only significant at the lower elevation angles. At 40° or above, however, a 1-mrad error in elevation angle contributes less than 1 mbar error in surface pressure. Since pointing accuracies of 100 μrad or less are easily obtained with current technology [Fitzmaurice, 1975], the resulting pressure errors should be less than a few tenths of a millibar.

The dominant error source of this technique is the differential path-length measurement. The sensitivity depends both on the choice of wavelengths and on the elevation angle. At low elevation angles the laser pulses travel through more of the atmosphere so the pressure effects are more significant. In addition, ΔR is greater for larger wavelength differences because of greater differences in group refractivity. $\partial P/\partial \Delta R$ is plotted vs. elevation angle in Fig. 2.2 for three possible wavelength combinations of fundamental, doubled, and tripled ND:YAG laser frequencies. When ranging at nadir using the 0.355- and 1.064-μm wavelengths, the required differential pathlength accuracy is 0.6 mm/mbar, which requires a timing accuracy of 2 psec/mbar.

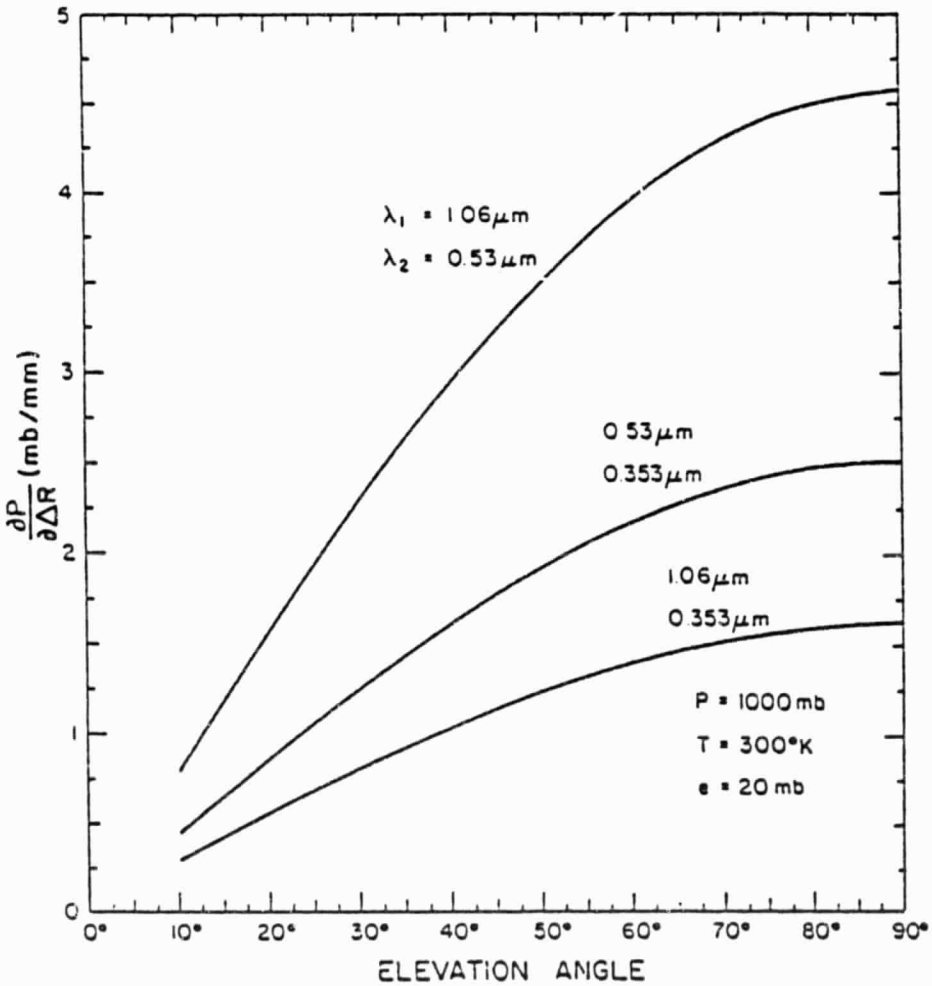

Fig. 2.2. Pressure measurement sensitivity to differential pathlength errors as a function of the satellite elevation angle.

Although the pressure sensitivity to errors in ΔR decreases as the elevation angle is decreased, other error factors become more significant. Consequently, the best performance will be obtained with the laser pointed at nadir. When the laser is pointed to within a few degrees of nadir, Eq. (2.19) can be approximated by

$$\sigma_P \text{ (mbar)} \simeq \frac{0.212 \sin E}{f(\lambda_1) - f(\lambda_2)} \sigma_{\Delta R} \text{ (mm)} \quad . \tag{2.24}$$

3. STATISTICS OF THE DETECTED SIGNAL

3.1 Introduction

The accuracy of the differential propagation time measurement depends upon the temporal characteristics of the reflected pulses and the timing algorithms employed in the receiver. The temporal characteristics of the reflected pulses are closely related to the statistics of the speckle fields, which are generated after the transmitted signals are reflected by the targets of interest. Due to the nature of the target surface profiles, the resultant speckle can either be fully developed or partially developed. Consequently, the corresponding detected signals will have different statistics with respect to different target surface profiles. In this chapter, both the fully and partially developed speckle statistics will be discussed.

3.2 Statistics of the Reflected Signals from the Diffuse Targets

When the target surface is rough on the optical scale, and when sufficiently large numbers of independent scattering areas exist within the laser footprint, then the reflected speckle field is usually regarded as fully developed and follows circular complex Gaussian statistics [Goodman, 1965 and 1975]. Gardner [1982] and Tsai and Gardner [1982] have investigated the temporal characteristics of optical pulses that were reflected from both the diffuse ground targets and the ocean. For normal incidence of the laser beam on the target and direct detection of the reflected pulses, the conditional mean detected signal ($\langle S(t)\rangle$) and the autocovariance function ($\langle C_S(t_1,t_2)\rangle$) are given respectively by

$$\langle S(t)\rangle = \langle N\rangle \int d^2\underline{\rho}\; b_2(\underline{\rho},z)\; |f(t - \psi(\underline{\rho}))|^2 * h(t) \quad , \tag{3.1}$$

and

$$C_S(t_1,t_2) = \langle N\rangle \int d^2\underline{\rho}\; b_2(\underline{\rho},z) \int_{-\infty}^{\infty} d\tau |f(\tau - \psi(\underline{\rho}))|^2\; h(t_1 - \tau)\; h(t_2 - \tau)$$

$$+ \langle N\rangle^2 K^{-1} \int d^2\underline{\rho}\; b_4(\underline{\rho},z)\; g(t_1 - \psi(\underline{\rho}))\; g(t_2 - \psi(\underline{\rho})) \tag{3.2}$$

where

$$b_n(\underline{\rho},z) = |a(\underline{\rho},z)|^n\; \beta_r^{n/2}(\underline{\rho}) \;/\; \int d^2\underline{\rho}\; |a(\underline{\rho},z)|^n\; \beta_r^{n/2}(\underline{\rho}) \quad , \tag{3.3}$$

$$\psi(\underline{\rho}) = \frac{2z}{c} + \frac{\rho^2}{cz} - \frac{2\xi(\underline{\rho})}{c} \quad , \tag{3.4}$$

$$g(t) = |f(t)|^2 * h(t) \quad , \tag{3.5}$$

$$K = A_R(\lambda z)^{-2}\; [\int d^2\underline{\rho}\; |a(\underline{\rho},z)|^2]^2 \;/\; \int d^2\underline{\rho}\; |a(\underline{\rho},z)|^4 \quad , \tag{3.6}$$

$$\langle N\rangle = \frac{\eta}{hf}\; \beta_r^o\; Q\; T_a^{\,2}\; A_R\; z^{-2} \quad , \tag{3.7}$$

$$\beta_r^o = \int d^2\underline{\rho}\; |a(\underline{\rho},z)|^2\; \beta_r(\underline{\rho}) \;/\; \int d^2\underline{\rho}\; |a(\underline{\rho},z)|^2 \tag{3.8}$$

with

$\underline{\rho}$ = (x,y) = horizontal coordinate vector on the target surface measured from the center of the footprint,

$a(\underline{\rho},z)$ = complex amplitude cross-section of the laser footprint,

$\beta_r(\underline{\rho})$ = power reflection coefficient of the target,

β_r^o = average power reflectivity of the target within the footprint,

$\xi(\underline{\rho})$ = surface profile of the target,

z = target distance,

c = velocity of light,

$|f(t)|^2$ = transmitted laser pulse intensity,

$h(t)$ = impulse response of the receiver electronics,

A_R = area of the receiver aperture,

λ = laser wavelength,

Q = total energy transmitted per laser pulse,

T_a = one-way intensity transmittance of the atmosphere,

η = quantum efficiency of the photodetector, and

hf = energy of one signal photon.

Throughout this thesis the spatial integrals are assumed to be evaluated over the entire $\underline{\rho}$ plane. The pulse propagation time (ψ) is a function of the surface profile of the target $\xi(\underline{\rho})$ within the laser footprint which is generally unknown and may be considered to be random. The first term in ψ is the nominal round-trip propagation time from the ranging system to the center of the target. The second term is the additional delay due to the curvature of the laser wavefront, and the last term is due to the range spread of the target. $\langle N \rangle$ is the expected number of detected signal photons per received pulse. K is the signal-to-noise ratio of the speckle which can also be regarded as the number of speckle correlation cells averaged by the receiver aperture. K is equal to or greater than one and typically is much larger than one. The first term in Eq. (3.2) is due to the shot-noise, while the second term is due to the speckle.

3.3 Statistics of the Reflected Signals from the Cube Corner Reflector (CCR) Arrays

Most optically rough targets with sufficiently large numbers of independent scattering areas will yield the signals statistics that were described in Section 3.2. However, there are targets of interest which do not fall into this category, and the resultant statistics of the reflected signals can be quite different. One important example is the Laser Geodynamic Satellite (Lageos) - the first space target devoted exclusively to Laser ranging. Lageos is a passive, long-lived target with well defined orbit [Fitzmaurice, et al., 1977]. It is a 60-cm diameter sphere orbiting at an altitude of 5900 km. Its surface is covered with 426 cube corner reflectors (CCR) to retrodirect any incident optical signal. Because of the relatively small number of point reflectors on Lageos, the reflected electrical field does not exhibit Gaussian statistics, and the resultant speckle is the so-called "partially developed" speckle [Goodman, 1975].

The reflected electric field from any CCR array consists of the coherent addition of the reflected electric field components from CCR's at various ranges within the array. The phase angles associated with these field components are in general random. If the range or height difference between two or more CCR's is shorter than the transmitted pulse width, the reflected pulses will overlap in time at the receiver, resulting in either constructive or destructive interference depending on the relative phase difference. In this case the detected power at the receiver will vary randomly from pulse to pulse as the relative phase changes due to changing target orientation. This coherent interference can introduce random fluctuations in the detected pulse shape, and consequently, increase the range error [Bufton, et al., 1977].

The mean detected signal and the signal autocovariance for reflections from a CCR array can be derived by using the discrete facet model for specular reflections, the Fresnel diffraction formula and Campbell's Theorem [Papoulis, 1974]. The detailed calculations are shown in Appendix A. The results are [Im and Gardner, 1985]

$$\langle S(t)\rangle = \langle N\rangle \sum_{m=1}^{M} B_2(\underline{\rho}_m, z) \left| f(t - \psi(\underline{\rho}_m)) \right|^2 * h(t) \quad , \tag{3.9}$$

and

$$\begin{aligned} C_S(t_1,t_2) = {} & \langle N\rangle \sum_{m=1}^{M} B_2(\underline{\rho}_m, z) \int_{-\infty}^{\infty} d\tau \left| f(\tau - \psi(\underline{\rho}_m)) \right|^2 h(t_1 - \tau)\, h(t_2 - \tau) \\ & + \langle N\rangle^2 K^{-1} \sum_{\substack{m=1 \\ m\neq n}}^{M} \sum_{n=1}^{M} B_4(\underline{\rho}_m, \underline{\rho}_n, z, \lambda) \int_{-\infty}^{\infty} d\tau_1 \, f(\tau_1 - \psi(\underline{\rho}_m)) \\ & \cdot f^*(\tau_1 - \psi(\underline{\rho}_n))\, h(t_1 - \tau_1) \int_{-\infty}^{\infty} d\tau_2 \, f^*(\tau_2 - \psi(\underline{\rho}_m)) \\ & \cdot f(\tau_2 - \psi(\underline{\rho}_n))\, h(t_2 - \tau_2) \end{aligned} \tag{3.10}$$

where

$$B_2(\underline{\rho}_m, z) = \sigma_m \left| a(\underline{\rho}_m, z) \right|^2 \Big/ \sum_{m=1}^{M} \sigma_m \left| a(\underline{\rho}_m, z) \right|^2 \quad , \tag{3.11}$$

$$B_4(\underline{\rho}_m,\underline{\rho}_n,z,\lambda) = \frac{\sigma_m\ \sigma_n\ |a(\underline{\rho}_m,z)|^2\ |a(\underline{\rho}_n,z)|^2\ W^2(\underline{\rho}_m,\underline{\rho}_n,z,\lambda)}{\sum_{\substack{m=1\\ m\neq n}}^{M}\ \sum_{n=1}^{M} \sigma_m\ \sigma_n\ |a(\underline{\rho}_m,z)|^2\ |a(\underline{\rho}_n,z)|^2\ W^2(\underline{\rho}_m,\underline{\rho}_n,z,\lambda)\ \gamma(\underline{\rho}_m,\underline{\rho}_n)} \quad , \tag{3.12}$$

$$K = \frac{\left[\sum_{m=1}^{M} \sigma_m\ |a(\underline{\rho}_m,z)|^2 \int_{-\infty}^{\infty} dt\ |f(t)|^2\right]^2}{\sum_{\substack{m=1\\ m\neq n}}^{M}\ \sum_{n=1}^{M} \sigma_m\ \sigma_n\ |a(\underline{\rho}_m,z)|^2\ |a(\underline{\rho}_n,z)|^2\ W^2(\underline{\rho}_m,\underline{\rho}_n,z,\lambda)\ \gamma(\underline{\rho}_m,\underline{\rho}_n)} \quad , \tag{3.13}$$

$$\langle N\rangle = \frac{\eta}{hf}\ GQ\ T_a^2\ A_R\ z^{-2} \quad , \tag{3.14}$$

$$G = \sum_{m=1}^{M} \sigma_m\ |a(\underline{\rho}_m,z)|^2\ /\ \int d^2\underline{\rho}\ |a(\underline{\rho},z)|^2 \quad , \tag{3.15}$$

$$\gamma(\underline{\rho}_m,\underline{\rho}_n) = \left|\int_{-\infty}^{\infty} dt\ f(t-\psi(\underline{\rho}_m))\ f^*(t-\psi(\underline{\rho}_n))\right|^2 \quad , \tag{3.16}$$

$$\sigma_m = \beta_{r_m}\ A_m^2\ /\ \lambda^2 \quad , \tag{3.17}$$

$$W(\underline{\rho}_m,\underline{\rho}_n,z,\lambda) = \frac{J_1[2(\lambda z)^{-1}\ (\pi A_R)^{1/2}|\underline{\rho}_m - \underline{\rho}_n|]}{[(\lambda z)^{-1}\ (\pi A_R)^{1/2}|\underline{\rho}_m - \rho_n|]} \tag{3.18}$$

with

$\underline{\rho}_m$ = horizontal coordinate vector of the m-th CCR,

M = number of CCR's in the array,

A_m = effective reflecting area of the m-th CCR,

β_{r_m} = power reflectivity of the m-th CCR, and

G = gain of the CCR array.

J_1 is the Bessel function of the first kind of the first order. σ_m is the effective lidar cross-section when the specular reflection from the m-th CCR is redirected toward the receiver [Fitzmaurice et al., 1977]. The effective lidar cross-section of the CCR's at optical wavelengths is usually very large ($\sim 10^6$ m^2). The effective reflecting area (A_m) is a function of the orientation of each CCR and is generally smaller than the actual surface area. The speckle SNR is dependent on both the optical wavelength and the range distance. The coherent interference factor ($\gamma(\underline{\rho}_m, \underline{\rho}_n)$) is the time integral of the product of two transmitted pulse envelopes that are separated by the differential time delay $\psi(\underline{\rho}_m) - \psi(\underline{\rho}_n)$. By referring to Eq. (3.4), the differential time delay is directly proportional to the height variations between two CCR's ($\xi(\underline{\rho}_m) - \xi(\underline{\rho}_n)$). Therefore, when the two CCR's are separated sufficiently in range, $\gamma(\underline{\rho}_m, \underline{\rho}_n)$ is zero. When they lie on the same plane, $\gamma(\underline{\rho}_m, \underline{\rho}_n)$ is one. $W(\underline{\rho}_m, \underline{\rho}_n, z, \lambda)$ is the aperture weighing factor. When the range distance is long so that each individual CCR cannot be resolved by the receiving telescope, W is approximately equal to one. However, for short distance ranging, individual CCR may be resolved and W may be significantly less than one.

Equations (3.9) through (3.18) are valid for ranging to CCR array at any arbitrary distance. However, for most practical applications the range distances are on the order of 10^3-10^4 km so that the following inequality

$$|\underline{\rho}_m - \underline{\rho}_n| << \frac{\lambda z}{4(\pi A_R)^{1/2}} \qquad \forall\ m,n \tag{3.19}$$

is satisfied. In this case, W is approximately 1 and Eqs. (3.12) and (3.13) can be simplified to

$$B_4(\underline{\rho}_m,\underline{\rho}_n,z) \cong \frac{\sigma_m\ \sigma_n\ |a(\underline{\rho}_m,z)|^2\ |a(\underline{\rho}_n,z)|^2}{\sum_{\substack{m=1\\ m\neq n}}^{M}\ \sum_{n=1}^{M} \sigma_m\ \sigma_n\ |a(\underline{\rho}_m,z)|^2\ |a(\underline{\rho}_n,z)|^2\ \gamma(\underline{\rho}_m,\underline{\rho}_n)}\ , \tag{3.20}$$

and

$$K = \frac{\left[\sum_{m=1}^{M} \sigma_m\ |a(\underline{\rho}_m,z)|^2 \int_{-\infty}^{\infty} dt\ |f(t)|^2\right]^2}{\sum_{\substack{m=1\\ m\neq n}}^{M}\ \sum_{n=1}^{M} \sigma_m\ \sigma_n\ |a(\underline{\rho}_m,z)|^2\ |a(\underline{\rho}_n,z)|^2\ \gamma(\underline{\rho}_m,\underline{\rho}_n)} \tag{3.12}$$

respectively. Therefore, at reasonably long range, the speckle SNR for reflection from a CCR array is independent of the optical wavelength, but is affected strongly by the coherent interference. In this regard, the speckle SNR for reflections from a CCR array is quite different from that for reflections from a diffuse target. The speckle SNR for reflection from a CCR array and its importance in laser ranging applications will be discussed in more detail in Chapter 5.

3.4 Gaussian Model for the Transmitted Pulse Intensity and Receiver Impulse Response

If the transmitted pulse intensity ($|f(t)|^2$) and receiver impulse response (h(t)) are modeled as Gaussian functions of time, $\langle S(t)\rangle$ and

$C_S(t_1,t_2)$ for the reflected signals from both the diffuse target and CCR array can be simplified to give

$$\langle S(t)\rangle = \langle N\rangle\, f_S(t)\ , \tag{3.22}$$

and

$$C_S(t_1,t_2) = \langle N\rangle\, G(\sqrt{2}\,\sigma_h,\ t_1 - t_2)\, f_S\left(\frac{t_1 + t_2}{2}\right) + \langle N\rangle^2\, K^{-1}\, G(\sqrt{2}\,\sigma_g,\ t_1 - t_2)\, f_{SP}\left(\frac{t_1 + t_2}{2}\right) \tag{3.23}$$

where

$$f_S(t) = \begin{cases} \int d^2\underline{\rho}\ b_2(\underline{\rho},z)\ G(\sigma_g,\ t - \psi(\underline{\rho})) & \text{diffuse target} \\ \sum_{m=1}^{M} B_2(\underline{\rho}_m,z)\ G(\sigma_g,\ t - \psi(\underline{\rho}_m)) & \text{CCR array,} \end{cases} \tag{3.24}$$

$$f_{SP}(t) = \begin{cases} \int d^2\underline{\rho}\ b_4(\underline{\rho},z)\ G(\sigma_g/\sqrt{2},\ t - \psi(\underline{\rho})) & \text{diffuse target} \\ \sum_{m=1}^{M}\sum_{\substack{n=1 \\ m\neq n}}^{M} B_4(\underline{\rho}_m,\underline{\rho}_n,z)\ G\left(\sigma_g/\sqrt{2},\ t - \frac{\psi(\underline{\rho}_m) + \psi(\underline{\rho}_n)}{2}\right)\cdot \gamma(\underline{\rho}_m,\underline{\rho}_n) & \text{CCR array,} \end{cases} \tag{3.25}$$

$$\gamma(\underline{\rho}_m,\underline{\rho}_n) = \exp\left\{-\frac{[\psi(\underline{\rho}_m) - \psi(\underline{\rho}_n)]^2}{4\sigma_f^2}\right\} , \tag{3.26}$$

$$G(\sigma,t) = (\sqrt{2\pi}\ \sigma)^{-1} \exp\ [-t^2/2\sigma^2] , \tag{3.27}$$

$$\sigma_g^2 = \sigma_h^2 + \sigma_f^2 . \tag{3.28}$$

$f_S(t)$ is the normalized waveform of the mean detected signal. $f_{SP}(t)$ is the normalized waveform of the speckle induced variance of the received signal. Both $f_S(t)$ and $f_{SP}(t)$ are functions of the target geometry. σ_f and σ_h are the rms widths of the transmitted pulse intensity ($|f|^2$) and the receiver impulse response (h), respectively. σ_g is the rms width of the reflected pulse intensity from a nondispersive point target. In deriving Eq. (3.23), we have used the fact that the width of the detected signal is large compared to both σ_f and σ_h. We can see from Eq. (3.23) that shot noise has a correlation length of about $2\sqrt{2}\ \sigma_h$, and speckle has a correlation length of about $2\sqrt{2}\ \sigma_g$. By referring to Eqs. (3.4) and (3.26), $\gamma(\underline{\rho}_m,\underline{\rho}_n)$ is significant when the following condition is satisfied:

$$\psi(\underline{\rho}_m) - \psi(\underline{\rho}_n) = -\frac{\rho_m^2 - \rho_n^2}{cz} + \frac{2}{c}[\xi(\underline{\rho}_m) - \xi(\underline{\rho}_n)] < 2\sqrt{2}\ \sigma_f . \tag{3.29}$$

Since the optical beam curvature effect (ρ_m^2/cz) is very small, we have equivalently

$$[\xi(\underline{\rho}_m) - \xi(\underline{\rho}_n)] < 2\ c\sigma_f . \tag{3.30}$$

Inequality (3.30) simply states that only the CCR's that are separated in range by less than the width of the transmitted pulse will interfere with each other. Therefore, short laser pulses must be used in order to minimize speckle. In this case, interference only occurs when two or more CCR's happen to lie on the same horizontal plane. Equations (3.22) and (3.23) will be used in subsequent chapters to analyze the receiver's timing performance.

4. COMPARISON OF THE ML ARRIVAL TIME ESTIMATORS IN THE PRESENCE OF BACKGROUND NOISE

4.1 Introduction

In addition to the effects of atmospheric refraction and turbulence, the performance of laser ranging systems is also limited by the presence of noise. The problem of estimating the arrival (propagation) time of laser pulses in the presence of both shot noise and background noise has been investigated by Bar-David [1969, 1975]. Under the assumptions that the envelope of the transmitted pulse is piecewise differentiable and that the speckle noise is negligible, Bar-David derived the Maximum-Likelihood (ML) estimator, which consisted of correlating the received signal with the logarithm of the mean received signal and searching for the peak of the correlation function. This estimator is optimal if the target surface is assumed to be optically flat or if the range spread of the target is smaller than the laser pulse width. However, for the extended diffuse target where the range spread is larger than the transmitted pulse width, the width of the received pulse will be longer than the correlation length of the speckle induced fluctuation. As a consequence, the time resolved speckle will cause random small scale fluctuations within the received pulse and introduce additional errors in the estimate of the arrival time. In this case, Bar-David's estimator will no longer be optimal. In a recent paper, Tsai and Gardner [1985] studied the ML estimator of the pulse arrival times in the presence of both shot noise and time-resolved speckle. Their results show that, under the background-noise-free condition, the accuracy of the ML estimator improves directly with the width of the receiver observation

interval when the received signal is large. Thus, their estimator appears to perform better than Bar-David's estimator at high signal levels over the optically rough targets. However, as the width of the observation interval increases, the background noise which enters the receiving telescope becomes significant and may affect the accuracy improvement of this new ML estimator. The following analysis investigates the performances of both ML estimators on the arrival time estimation in the presence of background noise, and the results obtained should be more suitable for realistic ranging applications.

4.2 Statistics of Signal and Noise

In a direct-detection laser ranging system geometry, the reflected laser pulses are detected by a receiving telescope and the photodetector. The detector output is then filtered and sampled periodically at an interval T equal to the inverse of the filter bandwidth. Thus the sampled values are proportional to the number of photons detected in consecutive time bins of width T, and the receiver observations can be modeled as a photocount vector $\underline{k}$,

$$\underline{k} = (k_1, k_2, \ldots, k_n) \tag{4.1}$$

where k_i is the photocount within the i-th time bin of width T. k_i in general consists of both the signal photocount (k_{s_i}) and the background noise photocount (k_{b_i}). That is,

$$k_i = k_{S_i} + k_{b_i} \quad , \qquad i=1,\ldots,n. \tag{4.2}$$

The statistics of k_{S_i} are related to the signal energy W_{S_i} received during the i-th time bin. For reflection from diffuse targets and in the presence of fully developed speckle, it has been shown that W_{S_i} is approximately gamma distributed [Goodman, 1973 and 1975], obeying the probability density function

$$p(W_{S_i}) = [\Gamma(M_i)W_{S_i}]^{-1} [M_i W_{S_i}/\langle W_{S_i}\rangle]^{M_i} \exp[-M_i W_{S_i}/\langle W_{S_i}\rangle] \ , \tag{4.3}$$

where $\langle W_{S_i}\rangle$ is the mean signal energy in the i-th time bin. M_i is the speckle signal-to-noise ratio in the i-th time bin, which is defined as the square of the mean divided by the variance

$$M_i = \langle W_{S_i}\rangle^2 \ / \ \mathrm{var}(W_{S_i}). \tag{4.4}$$

The mean and variance of W_{S_i} have been derived by Gardner [1982] for reflections from rough diffuse targets. They are given by

$$\langle W_{S_i}\rangle = \langle Q_S\rangle \int_{(i-1)T}^{iT} dt \int d^2\underline{\rho}\ b_2(\underline{\rho},z) \ | \ f(t - \psi(\underline{\rho}))|^2 \tag{4.5}$$

and

$$\mathrm{var}(W_{S_i}) = \langle Q_S \rangle^2 K^{-1} \int_{(i-1)T}^{iT} dt_1 \int_{(i-1)T}^{iT} dt_2 \int d^2\underline{\rho}\; b_4(\underline{\rho},z) \left| f(t_1-\psi(\underline{\rho})) \right|^2 \cdot \left| f(t_2-\psi(\underline{\rho})) \right|^2 \tag{4.6}$$

where $\langle Q_S \rangle$ is the expected received signal energy per pulse. The remaining quantities were defined in Chapter 3.2. Without loss of generality, we have assumed the bandwidth of the photodetector to be much larger than the bandwidth of the transmitted signals in both Eqs. (4.5) and (4.6).

For a Gaussian-shaped transmitted pulse intensity with RMS width σ_f, Eqs. (4.5) and (4.6) can be simplified so that

$$\langle W_{S_i} \rangle \cong \langle Q_S \rangle F_S(iT)T \tag{4.7}$$

and

$$\mathrm{var}(W_{S_i}) \cong \langle Q_S \rangle^2 K^{-1} F_{SP}(iT)T \ , \tag{4.8}$$

where

$$F_S(t) = \int d^2\underline{\rho}\; b_2(\underline{\rho},z)\; G(\sigma_f,\; t - \psi(\underline{\rho})) \tag{4.9}$$

and

$$F_{SP}(t) = \int d^2\underline{\rho}\; b_4(\underline{\rho},z)\; G(\sigma_f/\sqrt{2},\; t - \psi(\underline{\rho})). \tag{4.10}$$

$F_S(t)$ is the normalized waveform of the mean received signal prior to sampling and $F_{SP}(t)$ is the normalized waveform of the speckle induced variance of the received signal prior to sampling. They both are functions of the target geometry. In deriving Eqs. (4.7) and (4.8), we have made the assumption that the width of the time bin T is long compared with the width of the transmitted pulse, but it is short compared to the widths of F_S and F_{SP}. For the photodetector with finite bandwidth, σ_f must be replaced by $(\sigma_f + \sigma_d)^{1/2}$ in both Eqs. (4.9) and (4.10) where σ_d is the RMS width of the impulse response of the photodetector.

By using Eqs. (4.7) and (4.8), M_i can be expressed as

$$M_i = K\, F_S^2(iT)T \;/\; F_{SP}(iT)\ . \tag{4.11}$$

M_i may be thought of as the number of speckle correlation cells within the receiver aperature during the i-th time bin. For targets where the range spread is large compared to the transmitted pulse width, M_i will change with time as different regions of the target are illuminated by the propagating pulse. At the receiver, the speckle correlation area is inversely related to the area of illumination on the target. If only one point is illuminated on the target, the speckle correlation area is infinite and M_i is one. When a large number of points are simultaneously illuminated, the speckle will be fully developed and M_i will begin to increase. When the target is completely illuminated by the laser footprint, M_i will be equal to K. Typically, M_i will be approximately one near the leading and trailing edges of the received pulse and larger than one near the center of the pulse. For targets with large range spread, typically only a part of the target area is illuminated within one time bin and M_i will be smaller than K.

Since W_{S_i} is gamma distributed with parameter M_i, the distribution of k_{S_i} can be shown to have a probability density function given by [Goodman, 1965]

$$p(k_{S_i}) = \frac{\Gamma(k_{S_i} + M_i)}{\Gamma(k_{S_i} + 1)\ \Gamma(M_i)} \left[1 + \frac{M_i}{\langle k_{S_i} \rangle}\right]^{-k_{S_i}} \left[1 + \frac{\langle k_{S_i} \rangle}{M_i}\right]^{-M_i} \tag{4.12}$$

where

$$\langle k_{S_i} \rangle = \frac{\eta}{hf} \langle W_{S_i} \rangle = \langle N \rangle\ F_S(iT)\ T \tag{4.13}$$

with $\langle N \rangle$ being defined in Chapter 3.2 as the number of expected photons per received pulse. If both k_{S_i} and M_i at each time bin are integers, the function given by Eq. (4.12) is negative binomial. Therefore, the variance of k_{S_i} is

$$\mathrm{var}(k_{S_i}) = \langle k_{S_i} \rangle + \langle k_{S_i} \rangle^2 / M_i \quad . \tag{4.14}$$

For most optical receivers, the target-reflected laser pulses are usually much broader than the transmitted pulses. Therefore, the width of time bin, T, is larger than the transmitted pulse width. In this case, the signal photocounts from different time bins are statistically independent. The joint density function of $\underline{k}_S$ is therefore

$$p(\underline{k}_S) = \prod_{i=1}^{n} p(k_{S_i}) \tag{4.15}$$

and the cross covariance is

$$\mathrm{cov}(k_{S_i}, k_{S_j}) = \begin{cases} \mathrm{var}(k_{S_i})\ \delta_{i,j} & i = j \\ 0 & i \neq j \end{cases} \quad . \tag{4.16}$$

Background noise is mainly due to the undesirable background radiation entering the receiving telescope. External noise can arise from any background

sources including the sun, the moon, and the stars. Often a more important source of noise may be sunlight reflected directly off the target itself. All such backgrounds are thermal in origin. Mandel [1959] has shown that thermal background noise produces Poisson distributed noise photocounts when the receiver time bin width T is large compared to the background noise coherence time. In this case, the background noise probability density function is given by

$$p(k_{b_i}) = \frac{\langle k_{b_i} \rangle^{k_{b_i}}}{k_{b_i}!} \exp[-\langle k_{b_i} \rangle] \tag{4.17}$$

where

$$\langle k_{b_i} \rangle = \mathrm{var}(k_{b_i}) = \lambda_b T \tag{4.18}$$

and λ_b is the average background noise photocount rate.

Under the assumptions that the noise photocounts are mutually independent at different time bins, and that they are statistically uncorrelated with the signal photocount at every time bin, we can derive the second order statistics as

$$\mathrm{cov}(k_{b_i}, k_{b_j}) = \begin{cases} \mathrm{var}(k_{b_i})\, \delta_{i,j} & i = j \\ 0 & i \neq j \end{cases}, \tag{4.19}$$

and

$$\mathrm{cov}(k_{S_i}, k_{b_j}) = 0 \qquad i,j, \tag{4.20}$$

respectively.

4.3 Estimation of Arrival Time

In laser ranging applications, the arrival time of the reflected pulse, denoted by τ, is of interest. In this case, Eq. (4.12) can be written

explicitly as

$$p(\underline{k}_S|\tau) = \prod_{i=1}^{n} \frac{\Gamma(k_{S_i} + M_i(\tau))}{\Gamma(k_{S_i} + 1)\,\Gamma(M_i(\tau))} \left[1 + \frac{M_i(\tau)}{\langle k_{S_i}(\tau)\rangle}\right]^{-k_{S_i}} \left[1 + \frac{\langle k_{S_i}(\tau)\rangle}{M_i(\tau)}\right]^{-M_i(\tau)} . \tag{4.21}$$

The Maximum-Likelihood (ML) estimate of the arrival time is the value of τ which maximizes $[p(\underline{k}_S|\tau)]$, or equivalently, $\ln[p(k_S|\tau)]$. That is

$$\hat{\tau}_{SPEC} = \arg \max_{\tau}[\ln p(\underline{k}_S|\tau)] \quad , \tag{4.22}$$

where $\arg \max_{x} [F(x)]$ denotes the argument x which maximizes F(x). By substituting Eq. (4.21) into Eq. (4.22) and making the assumption that the received pulse always stays within the observation interval for all values of τ so that there are no end effects, the estimator given by Eq. (4.22) reduces to [Tsai and Gardner, 1985]

$$\hat{\tau}_{SPEC} = \arg \max[H(\tau)] \tag{4.23}$$

where

$$H(\tau) = \sum_{i=1}^{n} \left(k_{S_i} + M_i(\tau) - \frac{1}{2}\right) \ln(k_{S_i} + M_i(\tau)) - \sum_{i=1}^{n} k_{S_i} \ln\left[1 + \frac{M_i(\tau)}{\langle k_{S_i}(\tau)\rangle}\right] . \tag{4.24}$$

In deriving Eqs. (4.23) and (4.24), we have made use of the following approximation

$$\ln \Gamma(x) = (x - 1/2) \ln x - x + 1/2\,(\ln 2\pi) \qquad x >> 1 . \tag{4.25}$$

In the absence of background noise, Eqs. (4.23) and (4.24) describe an optimal estimating scheme. This estimator emphasizes signal counts in the tails of the received pulse where the speckle is less severe. Therefore, in

the large signal limit, the accuracy of this estimator improves as the width of the observation interval (nT) increases. However, when the background noise is present, its effects will be significant in the tails of the received pulse where the signal counts are low. Consequently, we would expect the improvement on the performance of this estimator to be offset somewhat by the effects of background noise when the observation interval is large.

In the presence of background noise, Eq. (4.24) becomes

$$H(\tau) = \sum_{i=1}^{n} \left(k_i + M_i(\tau) - \frac{1}{2}\right) \ell n(k_i + M_i(\tau)) - \sum_{i=1}^{n} k_i \ell n\left[1 + \frac{M_i(\tau)}{\langle k_{S_i}(\tau)\rangle}\right] \tag{4.26}$$

where ki is given by Eq. (4.2).

Notice that by replacing Eq. (4.24) by Eq. (4.26) the estimator has become suboptimal.

Assuming that the maximum value that has been chosen using $\hat{\tau}_{SPEC}$ is in the correct neighborhood of the actual arrival time, τ_o, the variance of this estimator can be calculated in terms of the first two derivatives of $H(\tau)$, evaluated at the actual arrival time of the pulse. This method of calculation has been used in similar problems [Helstrom, 1960]. If $H(\tau)$ is twice differentiable about τ_o, then $H(\tau)$ can be expanded by Taylor series to become

$$\dot{H}(\tau) = \dot{H}(\tau_o) + (\tau - \tau_o)\ddot{H}(\tau_o) + \ldots \tag{4.27}$$

where the dot $(\cdot)$ has been used to denote the time derivative. By the definition of $\hat{\tau}_{SPEC}$,

$$0 = \dot{H}(\hat{\tau}_{SPEC}) = \dot{H}(\tau_o) + (\hat{\tau}_{SPEC} - \tau_o)\ddot{H}(\tau_o) + \ldots \tag{4.28}$$

from which it follows that the error of this estimator is

$$\hat{\tau}_{SPEC} - \tau_o \cong - \frac{\dot{H}(\tau_o)}{\ddot{H}(\tau_o)} \tag{4.29}$$

provided $\ddot{H}(\tau_o) \neq 0$. This constraint excludes pulses which have constant slopes such as the rectangular and triangular pulses from the analysis.

If we assume that the shot noise and speckle are not severe so that $\langle \ddot{H}(\tau_o) \rangle^2 >> \text{var}[\ddot{H}(\tau_o)]$, then the bias and variance of this estimator can be written as

$$\langle \hat{\tau}_{SPEC} - \tau_o \rangle = - \langle \dot{H}(\tau_o) \rangle \; / \; \langle \ddot{H}(\tau_o) \rangle \tag{4.30}$$

and

$$\text{var}(\hat{\tau}_{SPEC}) = \text{var}[\dot{H}(\tau_o)] \; / \; \langle \ddot{H}(\tau_o) \rangle^2 \; . \tag{4.31}$$

In these equations, the expectations are over the observation vector $\underline{k}$.

By using Eqs. (4.13) through (4.20), it can be shown that $\langle \dot{H}(\tau_o) \rangle$ is zero. Therefore, $\hat{\tau}_{SPEC}$ estimator is unbiased. The variance of $\dot{H}(\tau_o)$ can be calculated to give

$$\text{var}[H(\tau_o)] = \sum_{i=1}^{n} \frac{\langle \dot{k}_{S_i} \rangle^2}{\langle k_{S_i} \rangle \left[1 + \dfrac{\langle k_{S_i} \rangle}{M_i} \right]} + \sum_{i=1}^{n} \frac{\langle k_{b_i} \rangle \langle \dot{k}_{S_i} \rangle^2}{\langle k_{S_i} \rangle^2 \left[1 + \dfrac{\langle k_{S_i} \rangle}{M_i} \right]^2} \; . \tag{4.32}$$

The first term in Eq. (4.32) is the variances due to the combined effects of the shot-noise and speckle in the background-noise-free situation; the second term is the additional error due to the presence of background noise.

$\langle \ddot{H}(\tau_o) \rangle$ can be calculated to give

$$\langle \ddot{H}(\tau_o) \rangle = - \sum_{i=1}^{n} \frac{\langle \dot{k}_{S_i} \rangle^2}{\langle k_{S_i} \rangle \left[1 + \dfrac{\langle k_{S_i} \rangle}{M_i} \right]} \; . \tag{4.33}$$

Notice that $\langle \ddot{H}(\tau_o) \rangle$ does not depend on the background noise count ($\langle K_{b_i} \rangle$). Finally by substituting these results into Eq. (4.31), we have for the variance of the $\hat{\tau}_{SPEC}$ estimator

$$\text{var}(\hat{\tau}_{SPEC}) = \sigma^2_{\tau_{SPEC}} = \left\{ \sum_{i=1}^{n} \frac{\langle \dot{k}_{S_i} \rangle^2}{\langle k_{S_i} \rangle \left(1 + \frac{\langle k_{S_i} \rangle}{M_i} \right)} \right\}^{-1}$$

$$+ \left\{ \sum_{i=1}^{n} \frac{\langle k_{b_i} \rangle \langle \dot{k}_{S_i} \rangle^2}{\langle k_{S_i} \rangle^2 \left(1 + \frac{\langle k_{S_i} \rangle}{M_i} \right)^2} \right\} \left\{ \sum_{i=1}^{n} \frac{\langle \dot{k}_{S_i} \rangle^2}{\langle k_{S_i} \rangle \left(1 + \frac{\langle k_{S_i} \rangle}{M_i} \right)} \right\}^{-2} \qquad (4.34)$$

$$= \left\{ \sum_{i=1}^{n} \frac{\dot{F}_S T}{\frac{F_S}{\langle N \rangle} + \frac{F_{SP}}{K}} \right\}^{-1} + \left\{ \frac{\lambda_b}{\langle N \rangle^2} \sum_{i=1}^{n} \frac{\dot{F}_S^2 T}{\left[\frac{F_S}{\langle N \rangle} + \frac{F_{SP}}{K} \right]^2} \right\} \left\{ \sum_{i=1}^{n} \frac{\dot{F}_S T}{\frac{F_S}{\langle N \rangle} + \frac{F_{SP}}{K}} \right\}^{-2} .$$

The first term in Eq. (4.34) is the MS timing error in the background-noise-free situation. The second term arises due to the presence of background noise.

As a comparison, the ML estimator derived by Bar-David [1969] considered both the shot noise and background noise. Therefore, it is optimal in situations where speckle noise is negligible. Mathematically, it can be written as

$$\hat{\tau}_{SHOT} = \arg \max_{\tau} \sum_{i=1}^{n} k_i \, \ell n \langle k_i(\tau) \rangle \quad . \qquad (4.35)$$

By employing the same procedure used above, we find it to be unbiased, and the variance in the presence of speckle is given by

$$\text{var}(\tau_{SHOT}) = \sigma^2_{\tau_{SHOT}} = \left\{ \sum_{i=1}^{n} \frac{\langle \dot{k}_{S_i} \rangle^2}{\langle k_{S_i} \rangle + \langle k_{b_i} \rangle} \right\}^{-1}$$

$$+ \left\{ \sum_{i=1}^{n} \frac{\langle \dot{k}_{S_i} \rangle^2}{M_i \left[1 + \frac{\langle k_{b_i} \rangle}{\langle k_{S_i} \rangle} \right]^2} \right\} \left\{ \sum_{i=1}^{n} \frac{\langle \dot{k}_{S_i} \rangle^2}{\langle k_{S_i} \rangle + \langle k_{b_i} \rangle} \right\}^{-2} \qquad (4.36)$$

$$= \frac{1}{\langle N \rangle} \left\{ \sum_{i=1}^{n} \frac{\dot{F}_S^2 T}{F_S + \frac{\lambda_b}{\langle N \rangle}} \right\}^{-1} + \frac{1}{K} \left\{ \sum_{i=1}^{n} \frac{F_{SP} \dot{F}_S^2 T}{\left(F_S + \frac{\lambda_b}{\langle N \rangle} \right)^2} \right\} \left\{ \sum_{i=1}^{n} \frac{\dot{F}_S^2 T}{F_S + \frac{\lambda_b}{\langle N \rangle}} \right\}^{-2} .$$

When the speckle noise is small compared to shot noise (i.e., when $K \gg \langle N \rangle$), and when there is no background noise (i.e., $\lambda_b = 0$), both Eqs. (4.34) and (4.36) reduce to

$$\sigma^2_{\tau_{SPEC}} = \sigma^2_{\tau_{SHOT}} = \left\{ \sum_{i=1}^{n} \frac{\langle \dot{k}_{S_i} \rangle^2}{\langle k_{S_i} \rangle} \right\}^{-1} + \sum_{i=1}^{n} \frac{\langle \dot{k}_{S_i} \rangle^2}{M_i} \Bigg/ \left\{ \sum_{i=1}^{n} \frac{\langle \dot{k}_{S_i} \rangle^2}{\langle k_{S_i} \rangle} \right\}^{-2} . \qquad (4.37)$$

4.4 Timing Performance for Diffuse Flat Target

To illustrate quantitatively the effects of background noise, we shall look at some specific target configurations and evaluate their corresponding timing variances. In the first example we consider pulse reflections from an infinite flat diffuse target. We also assume that the target surface is normal to the ray of laser incidence (Fig. 4.1 with $\phi = 0$). When the laser beam is incident normally onto the target surface, the broadening of the received pulse is due to the wavefront curvature of the laser beam.

To simplify the mathematics, we assume that the power reflectivity is uniform over the entire footprint, and that the laser footprint has a Gaussian cross-section

$$|a(\underline{\rho}, z)|^2 = Q(2\pi z^2 \tan^2 \theta_T)^{-1} \exp(-\rho^2 / 2z^2 \tan^2 \theta_T) \qquad (4.38)$$

where Q is the transmitted laser pulse energy, and θ_T is the RMS laser beam

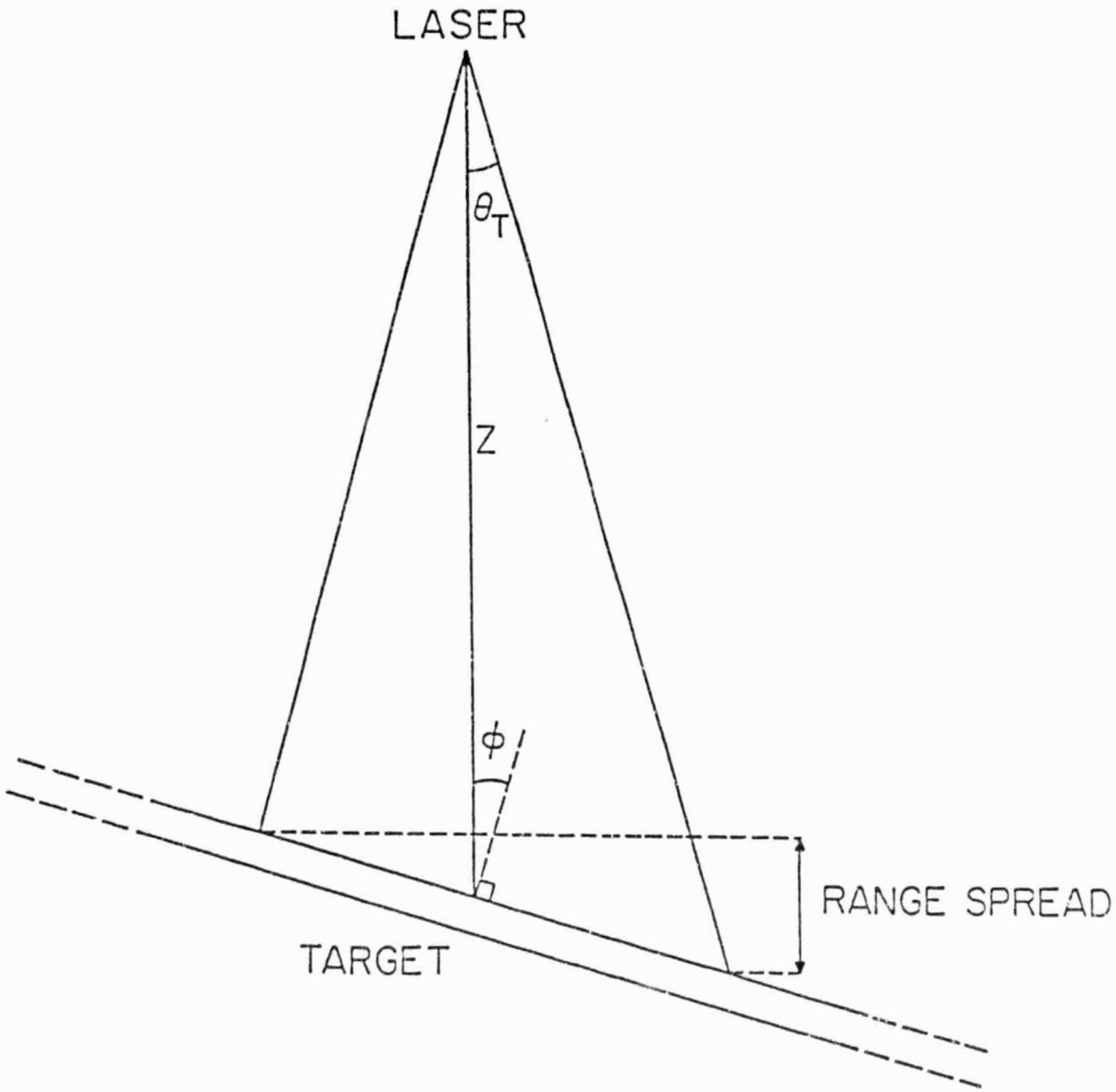

Fig. 4.1. Geometries of the infinite flat diffuse target and the laser ranging system.

divergence angle. In this case, the speckle SNR for the entire observation interval (K) can be calculated using Eq. (3.6) to give

$$K = \pi A_R \left(2 \tan \theta_T / \lambda\right)^2 . \tag{4.39}$$

For normal incidence, the mean received signal and the waveform of the speckle variance at each time bin, F_S and F_{SP}, can be calculated to give

$$F_S(iT) = \frac{c}{4z \tan^2 \theta_T} \exp\left[\frac{c^2\sigma_f^2}{8z^2 \tan^4 \theta_T} - \frac{c(iT - 2z/c)}{2z \tan^2 \theta_T}\right] \cdot \operatorname{erfc}\left[\frac{c\sigma_f}{2\sqrt{2}\, z \tan^2 \theta_T} - \frac{(iT - 2z/c)}{\sqrt{2}\sigma_f}\right] \tag{4.40}$$

and

$$F_{SP}(iT) = \frac{c}{2z \tan^2 \theta_T} \exp\left[\frac{c^2\sigma_f^2}{4z^2 \tan^4 \theta_T} - \frac{(iT - 2z/c)}{z \tan^2 \theta_T}\right] \cdot \operatorname{erfc}\left[\frac{c\sigma_f}{2z \tan^2 \theta_T} - \frac{(iT - 2z/c)}{\sigma_f}\right] , \tag{4.41}$$

respectively. Equations (4.40) and (4.41) are plotted in Figs. 4.2 and 4.3, respectively, for three different laser beam divergence angles. We can see that the leading edges of F_S and F_{SP} are sharp and undistorted. However, the trailing edges are broadened by the beam curvature effect.

The speckle SNR at each time bin (Mi) is given by

$$Mi = \frac{KCT}{8z \tan^2 \theta_T} \operatorname{erfc}^2\left[\frac{c\sigma_f}{2\sqrt{2}\, z \tan^2 \theta_T} - \frac{iT - 2z/c}{\sqrt{2}\, \sigma_f}\right] \Big/ \left[\operatorname{erfc} \frac{c\sigma_f}{2z \tan^2 \theta_T} - \frac{iT - 2z/c}{\sigma_f}\right] \tag{4.42}$$

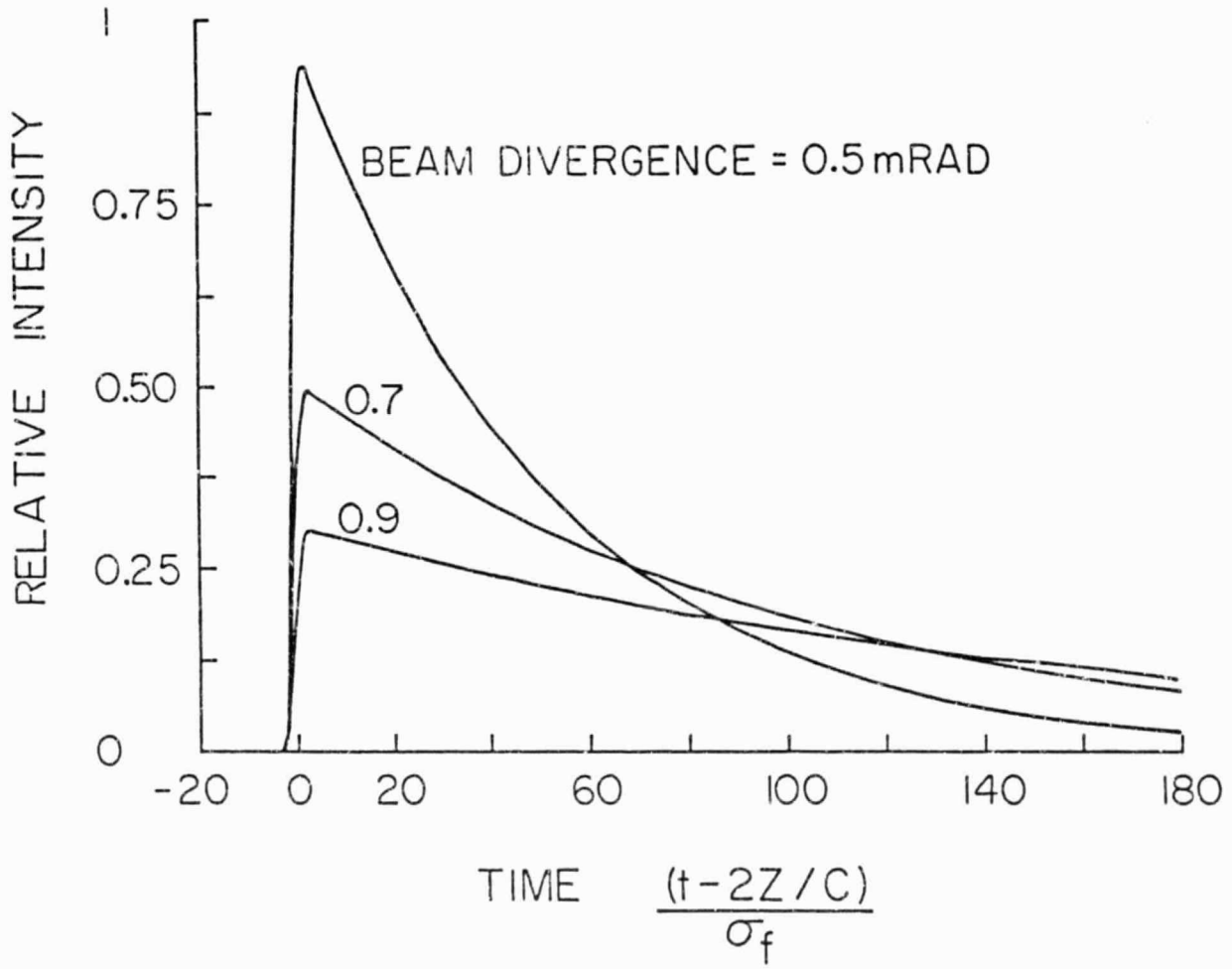

Fig. 4.2. Mean received waveform for normal incidence on an infinite flat diffuse target. (z = 500 km, $c\sigma_f$ = 0.5 cm, A_R = 100 cm^2, λ = 1.064 μm).

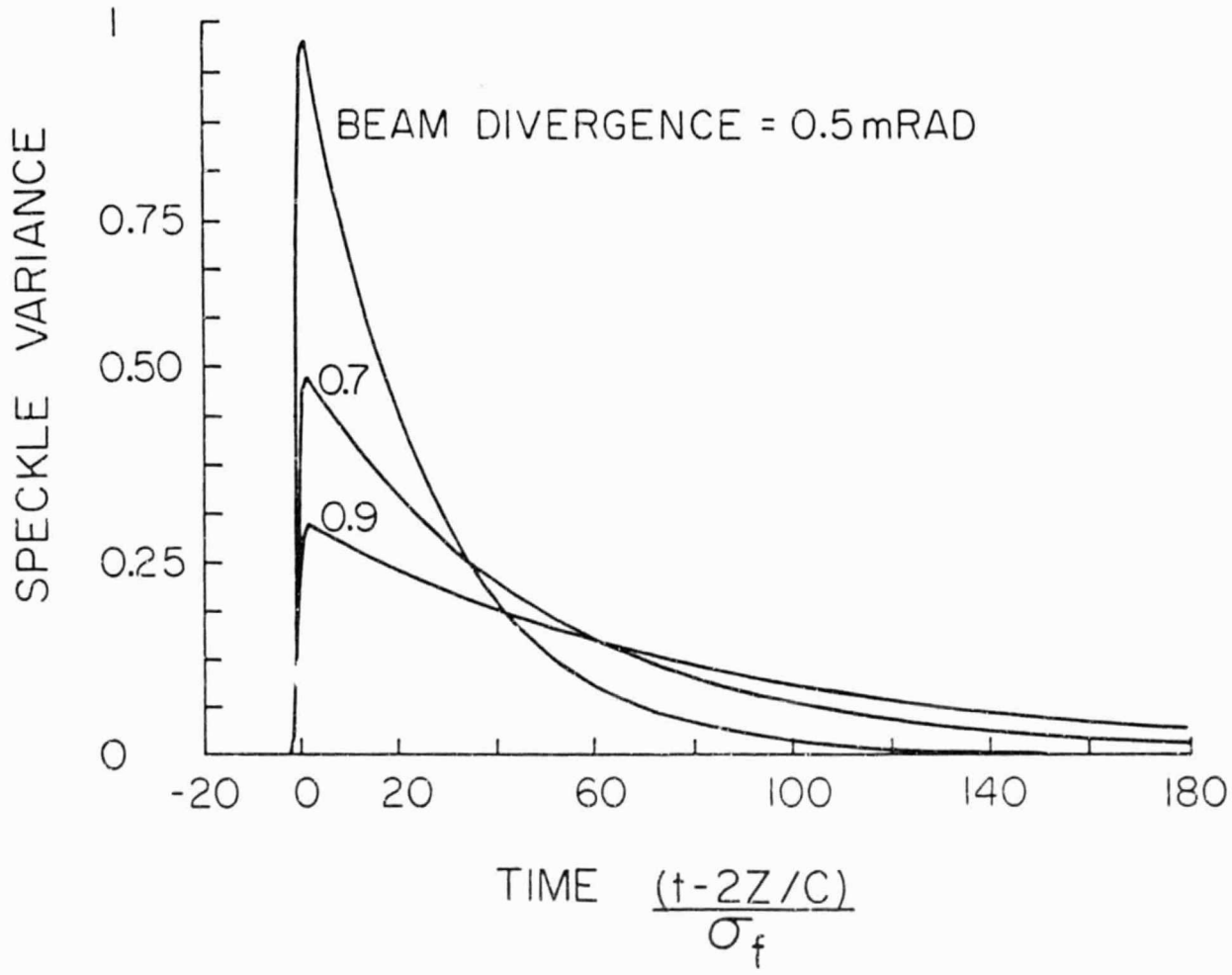

Fig. 4.3. Speckle variance for normal incidence on an infinite flat diffuse target (z = 500 km, $c\sigma_f$ = 0.5 cm, A_R = 100 cm^2, λ = 1.064 μm).

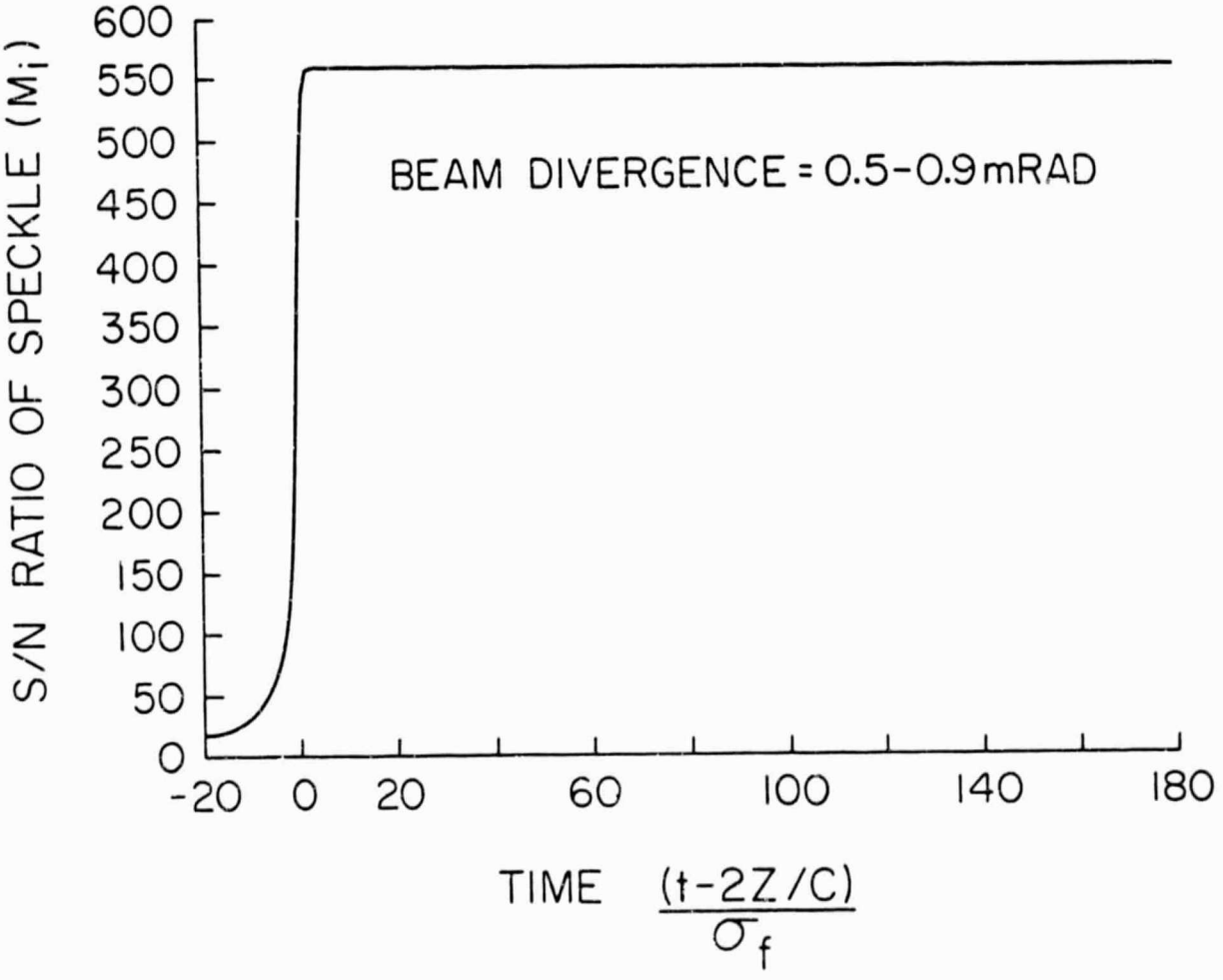

Fig. 4.4. Speckle SNR for normal incidence on an infinite flat diffuse target. (z = 500 km, $c\sigma_f$ = 0.5 cm, A_R = 100 cm^2, λ = 1.064 μm).

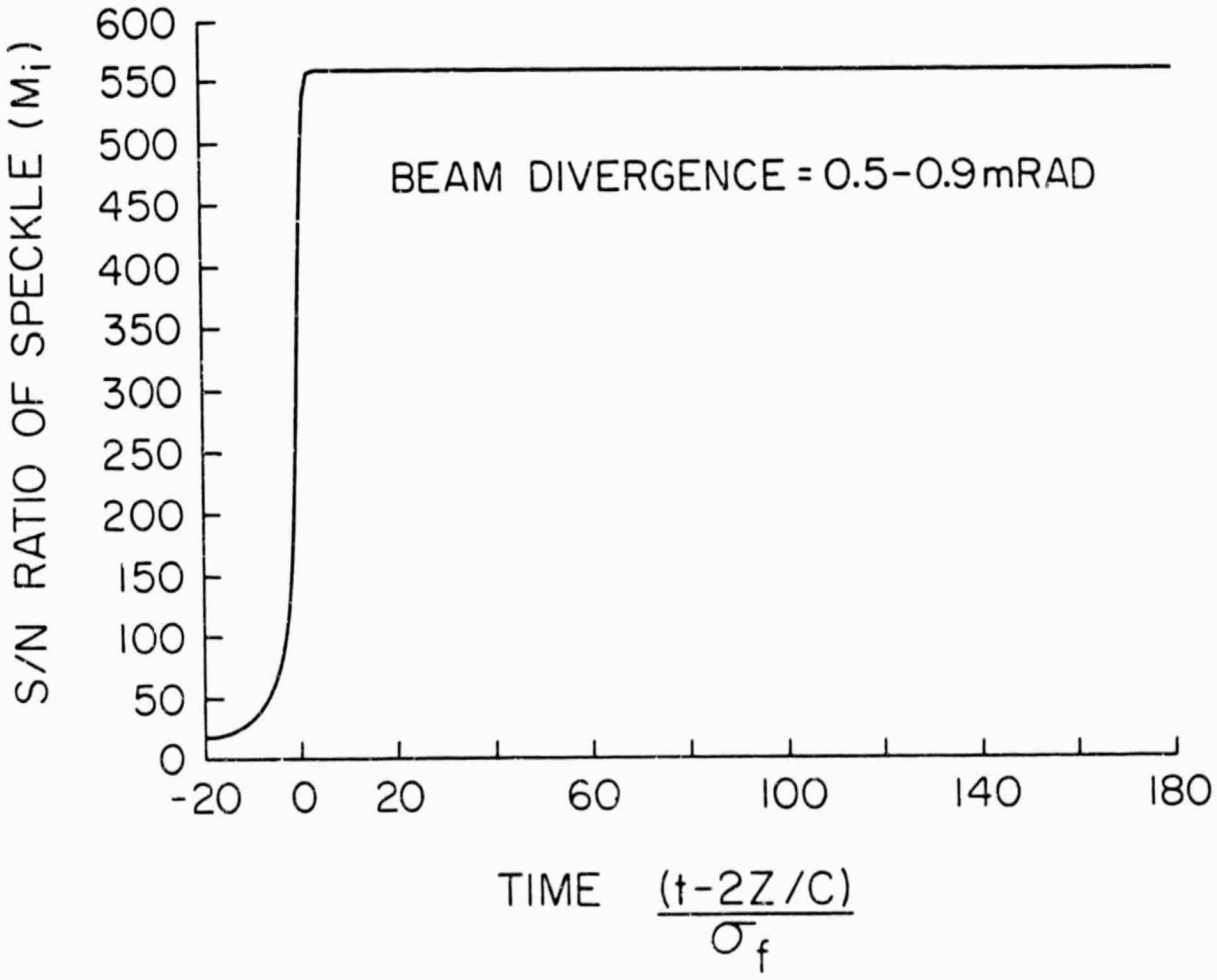

Fig. 4.4. Speckle SNR for normal incidence on an infinite flat diffuse target. (z = 500 km, $c\sigma_f$ = 0.5 cm, A_R = 100 cm^2, λ = 1.064 μm).

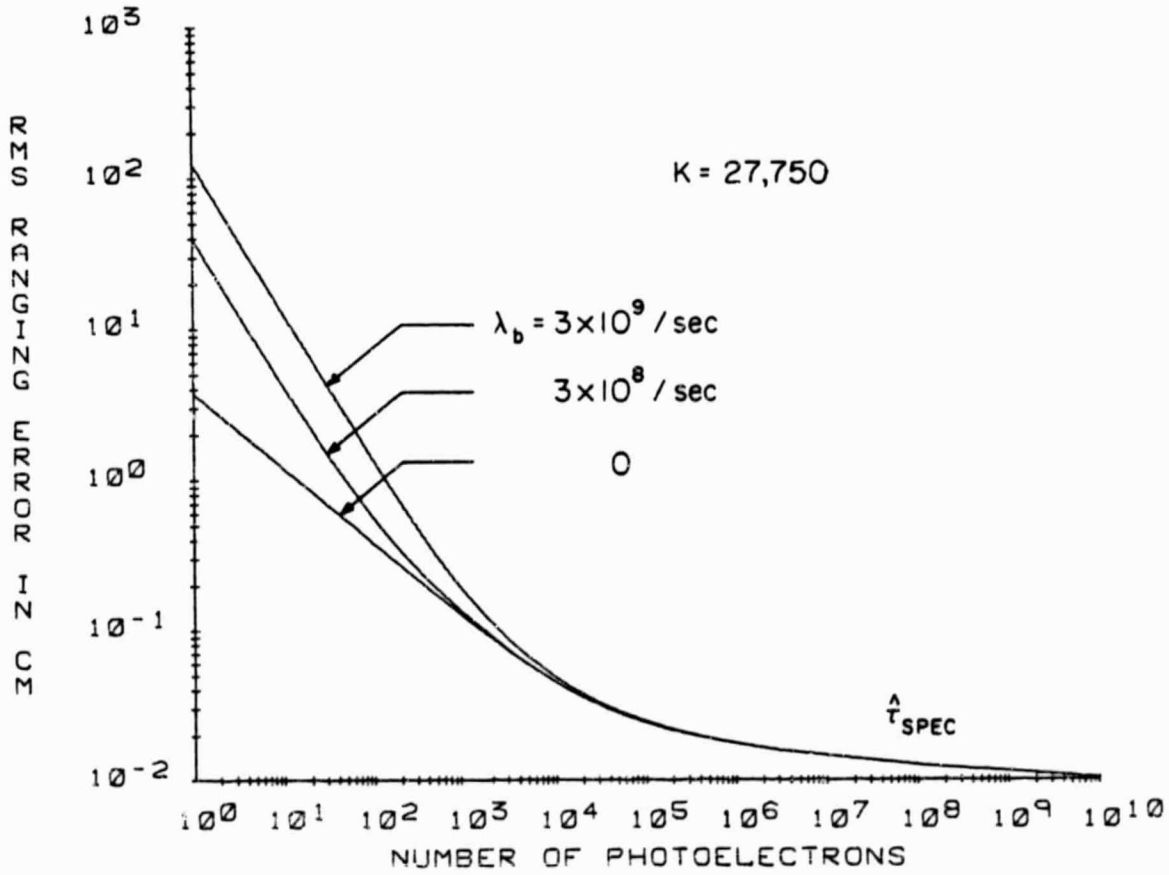

Fig. 4.5. RMS ranging error using $\hat{\tau}_{SPEC}$ estimator for normal incidence on an infinite flat diffuse target. (z = 500 km, θ_T = 0.5 mrad, $c\sigma_f$ = 0.5 cm, A_R = 100 cm^2, λ = 1.064 μm).

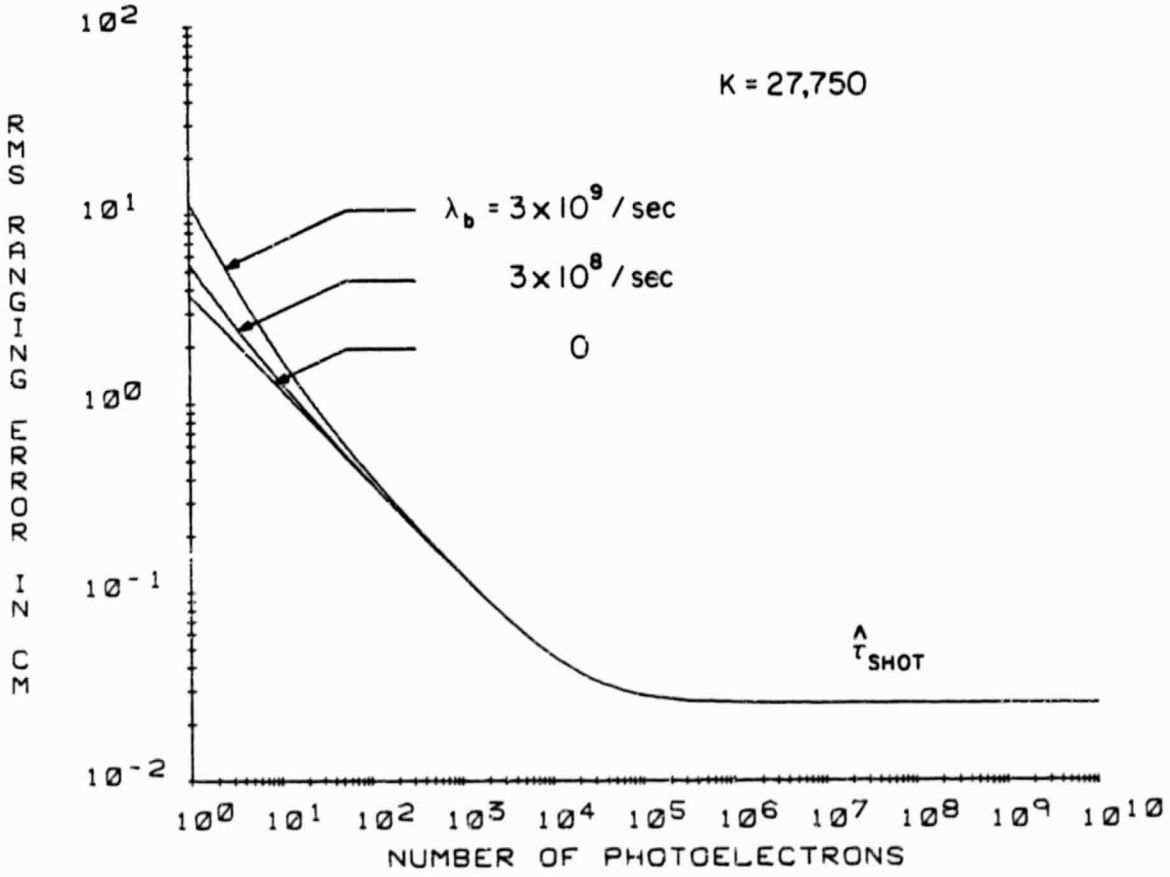

Fig. 4.6. RMS ranging error using $\hat{\tau}_{SHOT}$ estimator for normal incidence on an infinite flat diffuse target. (z = 500 km, θ_T = 0.5 mrad, $c\sigma_f$ = 0.5 cm, A_R = 100 cm^2, λ = 1.064 μm).

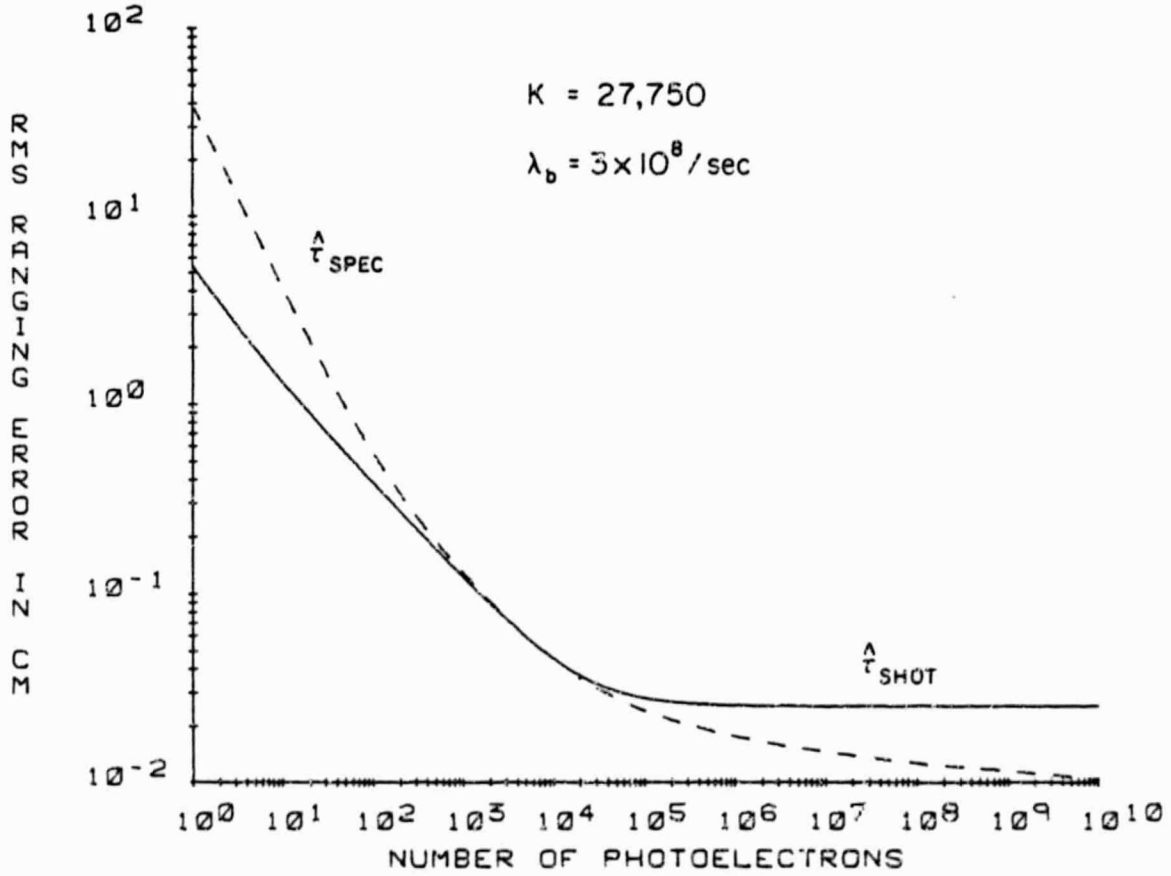

Fig. 4.7. Comparison of the RMS ranging errors using $\hat{\tau}_{SPEC}$ and $\hat{\tau}_{SHOT}$ estimators for normal incidence on an infinite flat diffuse target. (z = 500 km, θ_T = 0.5 mrad, $c\sigma_f$ = 0.5 cm, A_R = 100 cm^2, λ = 1.064 μm).

$\hat{\tau}_{SPEC}$ estimator. However, at high signal level where the speckle dominates, the $\hat{\tau}_{SPEC}$ estimator performs considerably better than the $\hat{\tau}_{SHOT}$ estimator. Consequently, in applications where the signal level is expected to be low, $\hat{\tau}_{SHOT}$ estimator should be used to estimate the pulse arrival times. On the other hand, in applications where speckle is expected to be the dominated factor, $\hat{\tau}_{SPEC}$ must be used to minimize the timing error.

For non-normal incidence on an infinite flat target the broadening of the received signal is dominated by the range spread of the target. This range spread arises because the target in this case is tilted with respect to the optical axis (refer to Fig. 4.1). By neglecting the beam curvature effects, F_S and F_{SP} are given approximately by

$$F_S(iT) = G(\sigma_T,\ iT - 2z/c) \tag{4.44}$$

and

$$F_{SP}(iT) = G(\sigma_T/\sqrt{2},\ iT - 2z/c) \tag{4.45}$$

where

$$\sigma_T = \left[\sigma_f^2 + \frac{4z^2 \tan^2 \theta_T \tan^2 \phi}{c}\right]^{1/2} . \tag{4.46}$$

ϕ is the incidence angle of the laser beam with respect to the target surface normal. From Eqs. (4.44) and (4.46), both the mean received signal and the speckle variance are Gaussian in shape with the RMS width σ_T. The pulse width consists of the transmitted pulse width (σ_f) and the effects of the range spread of the target $2z \tan \theta_T \tan \phi$ [Gardner,1982]. The value of M_i in this case is given by

$$M_i = K\ T\ /\ 2\sqrt{\pi}\ \sigma_T . \tag{4.47}$$

Again, M_i is constant with time (i). Equations (4.44) and (4.45) are plotted in Figs. 4.8 and 4.9 for three different incidence angles. By comparing

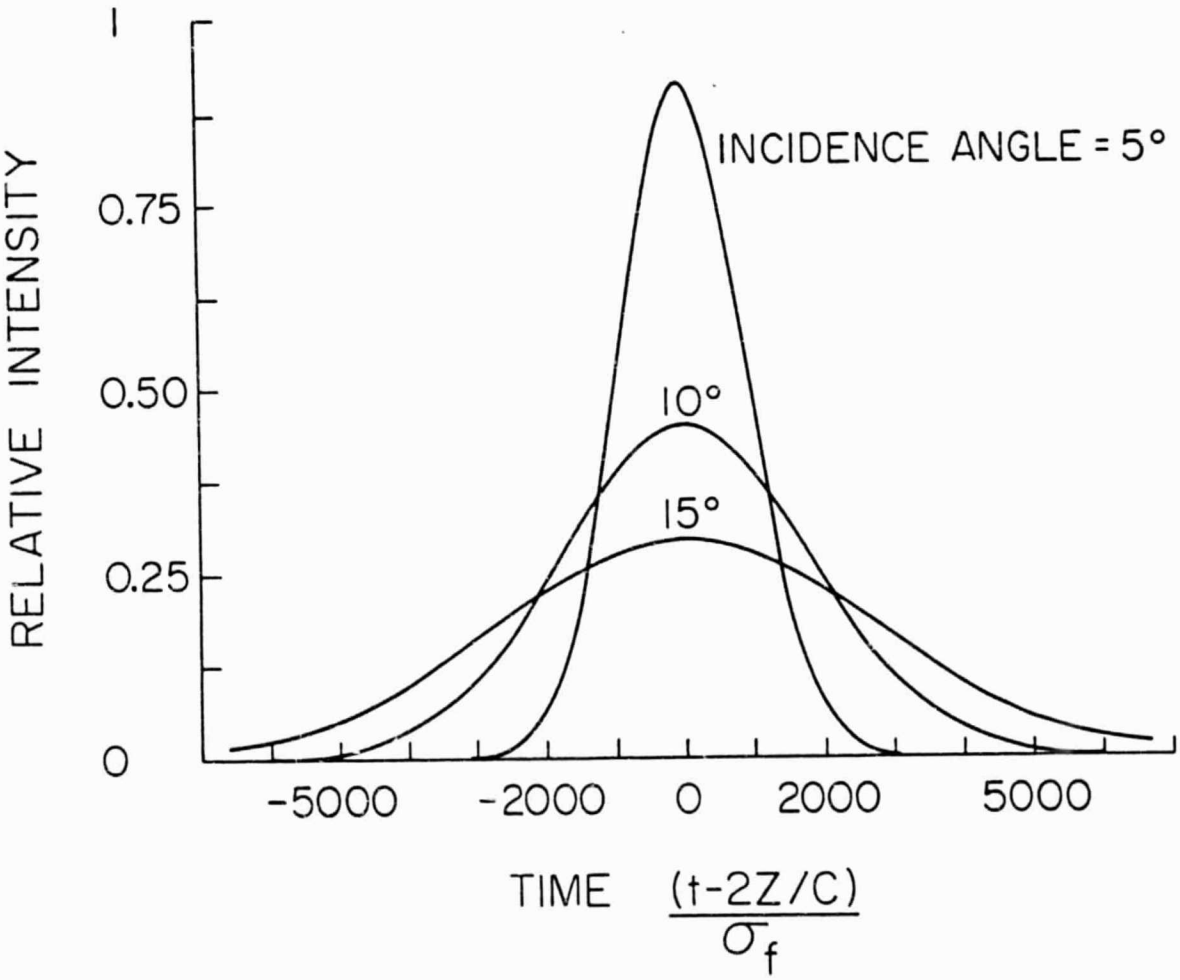

Fig. 4.8. Mean received waveform for non-normal incidence on an infinite flat diffuse target. (z = 500 km, θ_T = 0.1 mrad, $c\sigma_f$ = 0.5 cm, A_R = 100 cm^2, λ = 1.064 μm).

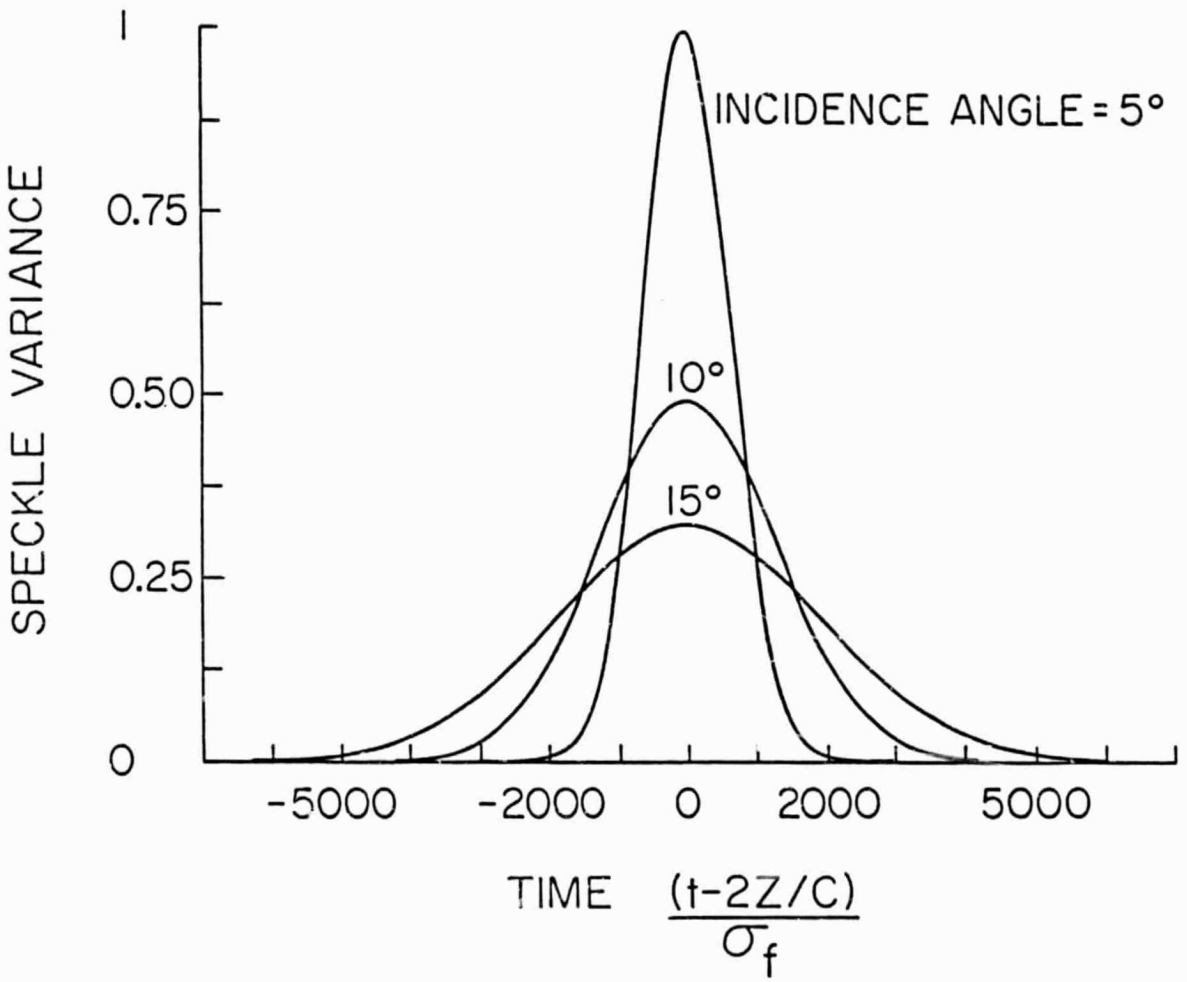

Fig. 4.9. Speckle variance for non-normal incidence on an infinite flat diffuse target (z = 500 km, θ_T = 0.1 mrad, $c\sigma_f$ = 0.5 cm, A_R = 100 cm^2, λ = 1.064 μm).

Fig. 4.8 with Fig. 4.2, we can see that the received signal in the non-normal incidence case is much broader in width than that in the normal incidence case. Consequently, we would expect the timing error to be larger in the tilted target configuration [Tsai and Gardner, 1985].

The variance of the $\hat{\tau}_{SPEC}$ estimator is given approximately by

$$\sigma^2_{\tau_{SPEC}} \cong \frac{\sigma_T^2}{\langle N \rangle} \frac{1}{g_1(\langle N \rangle, K)} + \frac{\lambda_b \sigma_T^3}{\langle N \rangle^2} \frac{g_2(\langle N \rangle, K)}{g_1^2(\langle N \rangle, K)} \tag{4.48}$$

where

$$g_1(\langle N \rangle, K) = \frac{1}{\sqrt{2\pi}} \int_{-\frac{nT}{2\sigma_T}}^{\frac{nT}{2\sigma_T}} dy \frac{y^2 e^{-y^2/2}}{1 + \sqrt{2}\ \langle N \rangle\ K^{-1}\ e^{-y^2/2}} \quad , \tag{4.49}$$

and

$$g_2(\langle N \rangle, K) = \int_{-\frac{nT}{2\sigma_T}}^{\frac{nT}{2\sigma_T}} dy \frac{y^2}{(1 + \sqrt{2}\ \langle N \rangle\ K^{-1}\ e^{-y^2/2})^2} \quad . \tag{4.49}$$

$nT/2\sigma_T$ is the ratio between the width of the observation interval and the RMS full width of the received signal. Consequently, we would expect this ratio to be on the order of three in order for the receiver to sample to entire pulse. Because the MS timing error given by Eq. (4.48) depends on g_1 and g_2, which in turn depend on this ratio, the timing error will depend on the width of the observation interval (nT). Because nT also determines the amount of background noise allowed to the receiver, so it is a very important factor in determining the timing performance of the $\hat{\tau}_{SPEC}$ estimator.

Equation (4.48) is plotted versus $\langle N \rangle$ in Fig. 4.10 for $nT = 14\ \sigma_T$ and for three different values of λ_b in order to illustrate the effect of background noise on the performance of the $\hat{\tau}_{SPEC}$ estimator. In Fig. 4.11 Eq. (4.48) is plotted for three different values of $nT/2\sigma_T$ in order to show the significance of the observation interval width at both the low and high signal levels.

In the shot noise limited region, that is , when $\langle N \rangle \ll K$, Eq. (4.48) can be simplified to

$$\sigma^2_{\tau_{SPEC}} \approx \frac{\sigma_T^2}{\langle N \rangle}\left[1 + \frac{2}{3}\lambda_b \frac{\sigma_T}{\langle N \rangle}\left(\frac{nT}{2\sigma_T}\right)^3\right], \qquad \langle N \rangle \ll K \quad . \tag{4.51}$$

According to Eq. (4.51), the timing error by using $\hat{\tau}_{SPEC}$ estimator will decrease as the signal strength increases at low signal level. In the absence of background noise, the timing performance is only limited by the pulse width (or the bandwidth) of the received signal. But when the background noise is present, the timing performance will be degraded inversely with both the background noise count rate and the observation interval width. These effects can be seen from both Figs. 4.10 and 4.11 in the small signal region. Because $\sigma^2_{\tau_{SPEC}}$ is straightly increasing with respect to nT, and therefore, the observation interval width must be chosen to be as small as possible in order to minimize the timing error. It should be noted that the observation interval cannot be chosen to be smaller than the pulse length of the received signal ($\sim 6\sigma_T$). When nT is smaller than $6\sigma_T$, Eq. (4.51) is no longer valid. However, it is easy to show that the timing error in this case will increase as the observation interval width is reduced.

In the speckle limited region, that is, when $\langle N \rangle \gg K$, the MS timing error using $\hat{\tau}_{SPEC}$ is bounded below by

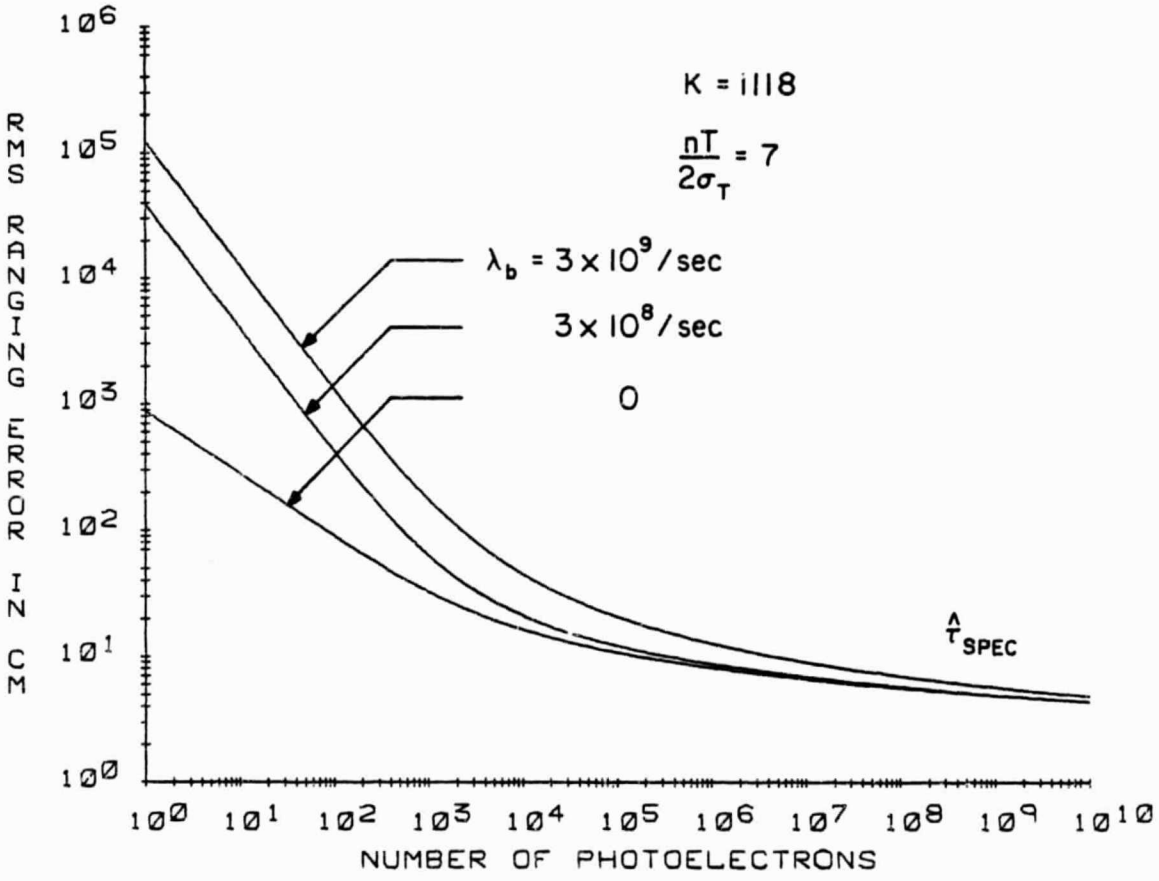

Fig. 4.10. RMS ranging error using $\hat{\tau}_{SPEC}$ estimator for non-normal incidence on an infinite flat diffuse target. ($z = 500$ km, $\theta_T = 0.1$ mrad, $\phi = 0.5°$, $c\sigma_f = 0.5$ cm, $A_R = 100$ cm^2, $\lambda = 1.064$ μm, $nT/2\sigma_T = 7$).

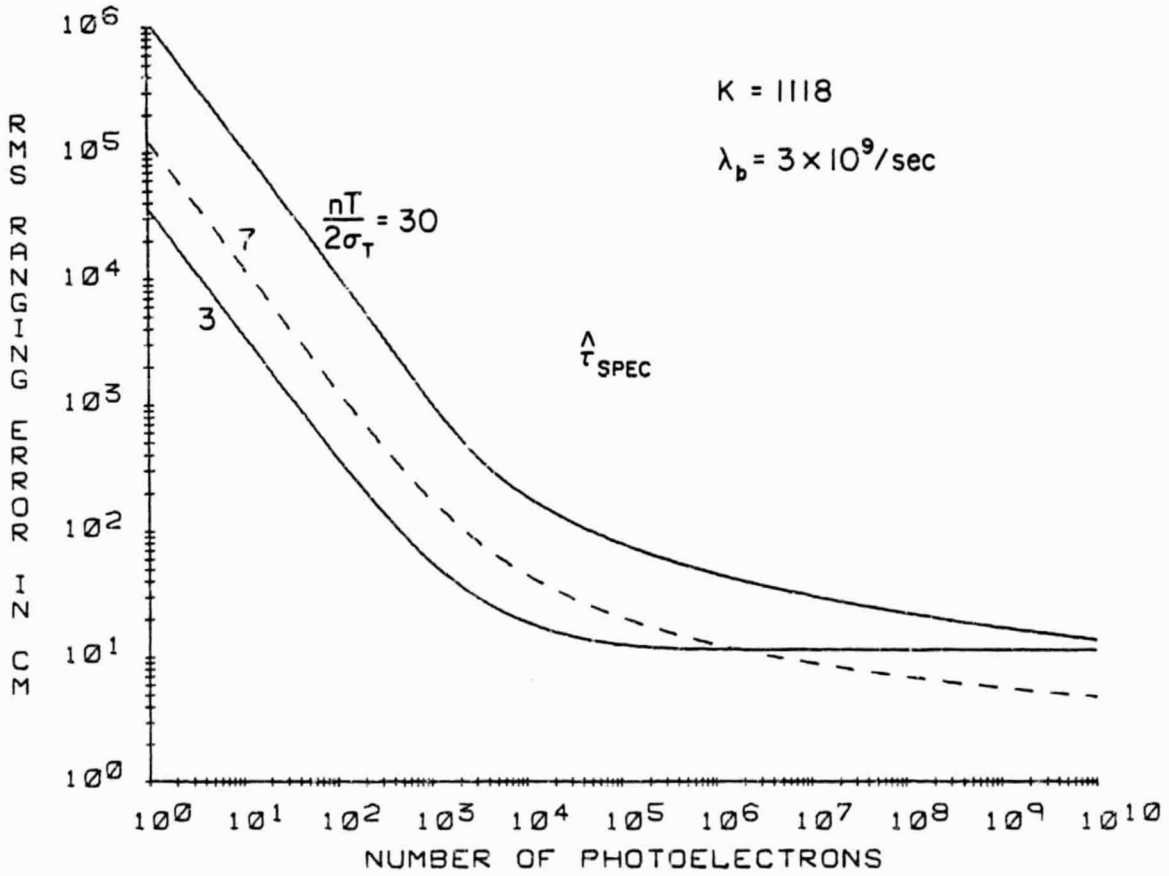

Fig. 4.11. Dependence of RMS ranging error on the observation interval width by using $\hat{\tau}_{SPEC}$ estimator and for non-normal incidence on an infinite flat diffuse target. (z = 500 km, θ_T = 0.1 mrad, ϕ = 0.5°, $c\sigma_f$ = 0.5 cm, A_R = 100 cm^2, λ = 1.064 μm).

$$\sigma_{\tau_{SPEC}} > 3\sqrt{\pi}\ \frac{\sigma_T^2}{K}\left(\frac{2\sigma_T}{nT}\right)^3 + \frac{9\pi}{4}\frac{\lambda_b\,\sigma_T^3}{\langle N\rangle^2}\, e^{\left(\frac{nT}{2\sigma_T}\right)^2}\left(\frac{2\sigma_T}{nT}\right)^6\left[2\left(\frac{nT}{2\sigma_T}\right) - 1\right] \qquad (4.52)$$

$$\langle N\rangle >> K \ .$$

When both λ_b and nT are small, the first term in Ineq. (4.52) dominates, and the timing error will decrease as the observation interval width increases. However, as nT is increased, the exponential term will eventually dominate such that the second term exceeds the first term. In this case, any further increase in nT would result in the increase of timing error. This effect is illustrated by Fig. 4.11 at the large signal region. By applying L'Hopital's rule, it can be shown that

$$\lim_{nT\to\infty} \sigma^2_{\tau_{SPEC}} > \frac{12\pi}{5}\frac{\lambda_b\,\sigma_T^3}{\langle N\rangle^2}\left(\frac{nT}{2\sigma_T}\right) e^{\left(\frac{nT}{2\sigma_T}\right)^2} \ . \qquad (4.53)$$

Consequently, it is theoretically possible for the timing error of $\hat{\tau}_{SPEC}$ estimator to approach infinity when the observation interval width is exceedingly large. In general, an optimal width can be determined by using conventional optimization technique.

In Fig. 4.12, the RMS timing error is plotted versus $nT/2\sigma_T$ for different values of $\langle N\rangle$ and for the typical satellite laser ranging parameters. According to this figure, the optimal width of observation interval is between 4 and 6, this corresponds to the full width of a Gaussian pulse at the 5% point. Consequently, nT must be chosen to be not more than the pulsewidth of the received signal in order to obtain the optimal performance. Fortunately, the rate of increase of the timing error with respect to the observation interval width is relatively slow, and therefore, we would not expect significant reduction on the timing performance of $\hat{\tau}_{SPEC}$ when the chosen observation interval width is a few times larger than the optimal width.

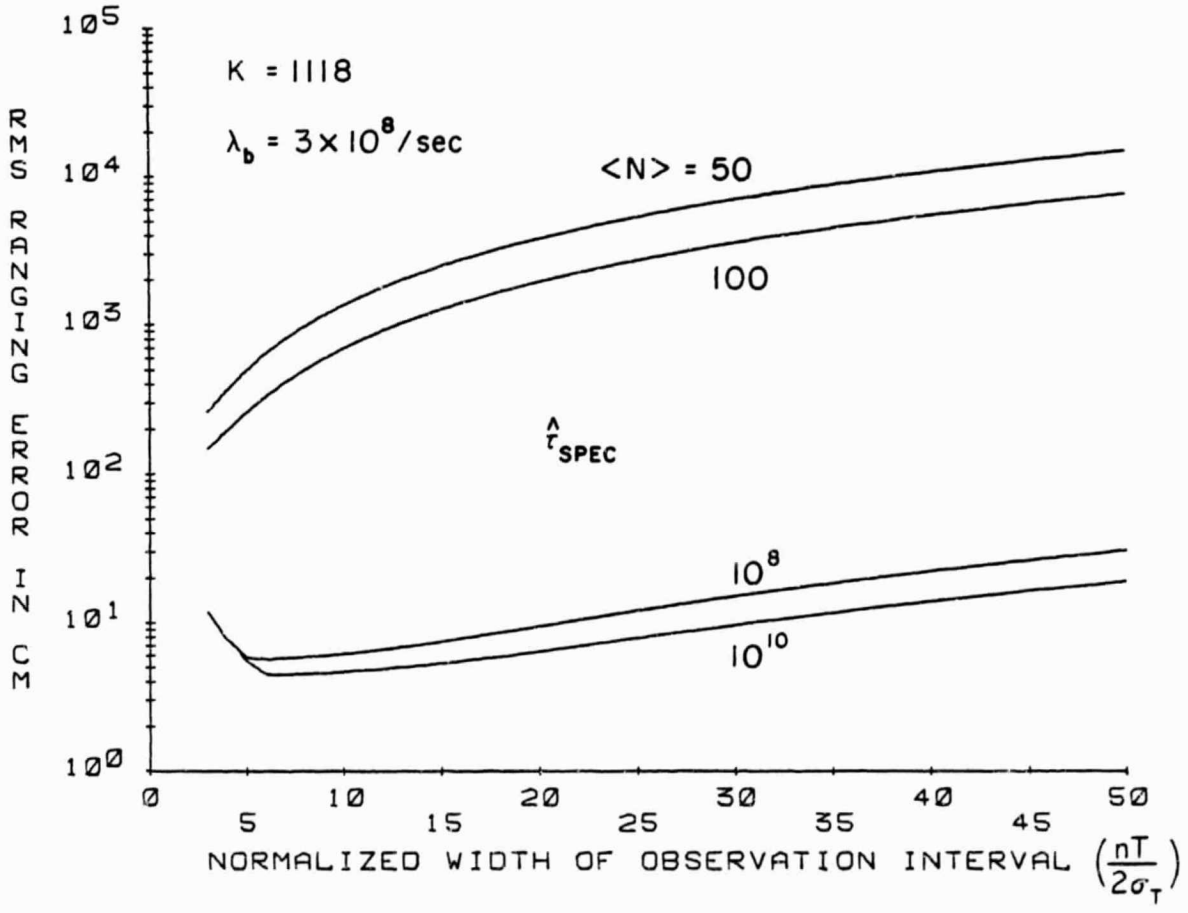

Fig. 4.12. RMS ranging error versus width of observation interval using $\hat{\tau}_{SPEC}$ estimator for non-normal incidence on an infinite flat diffuse target. (z = 500 km, θ_T = 0.1 mrad, ϕ = 0.5°, $c\sigma_f$ = 0.5 cm, A_R = 100 cm^2, λ = 1.064 μm).

The timing variance of the $\hat{\tau}_{SHOT}$ estimator can be calculated using Eqs. (4.36), (4.44) and (4.45) to give

$$\hat{\tau}_{SHOT} = \frac{\sigma_T^2}{\langle N \rangle} \frac{1}{g_3(\langle N \rangle, K)} + \frac{\sigma_T^2}{K} \frac{g_4(\langle N \rangle, K)}{g_3^2(\langle N \rangle, K)} \tag{4.54}$$

where

$$g_3(\langle N \rangle, K) = \frac{1}{\sqrt{2\pi}} \int_{-\frac{nT}{2\sigma_T}}^{\frac{nT}{2\sigma_T}} \frac{y^2 \, e^{-y^2/2} \, dy}{1 + \sqrt{2\pi} \, \lambda_b \, \sigma_T \, \langle N \rangle^{-1} \, e^{y^2/2}} \tag{4.55}$$

and

$$g_4(\langle N \rangle, K) = \frac{1}{\sqrt{\pi}} \int_{-\frac{nT}{2\sigma_T}}^{\frac{nT}{2\sigma_T}} \frac{y^2 \, e^{-y^2} \, dy}{(1 + \sqrt{2\pi} \, \lambda_b \, \sigma_T \, \langle N \rangle^{-1} \, e^{y^2/2})^2} \quad . \tag{4.56}$$

Equation (4.54) is plotted versus $\langle N \rangle$ in Fig. 4.13 for different values of λ_b. It is also plotted in Fig. 4.14 for different values of $nT/2\sigma_T$.

In the shot noise limited region, Eq. (4.54) reduces to

$$\sigma^2_{\hat{\tau}_{SHOT}} \cong \frac{4\sqrt{\pi} \, \lambda_b \, \sigma_T^3}{\langle N \rangle^2} \qquad \langle N \rangle << K \quad . \tag{4.57}$$

Therefore, in the low signal limit, the timing error for the $\hat{\tau}_{SHOT}$ estimator will increase directly with the background noise photocount rate. However, Eq. (4.57) does not depend on nT, and therefore, will not change even if the observation interval width is increased. These effects are clearly shown by Figs. 4.13 and 4.14 at the small signal level. Also, this MS error has a $\langle N \rangle^{-2}$ dependence instead of the $\langle N \rangle^{-1}$ dependence as in the background-noise-free situation.

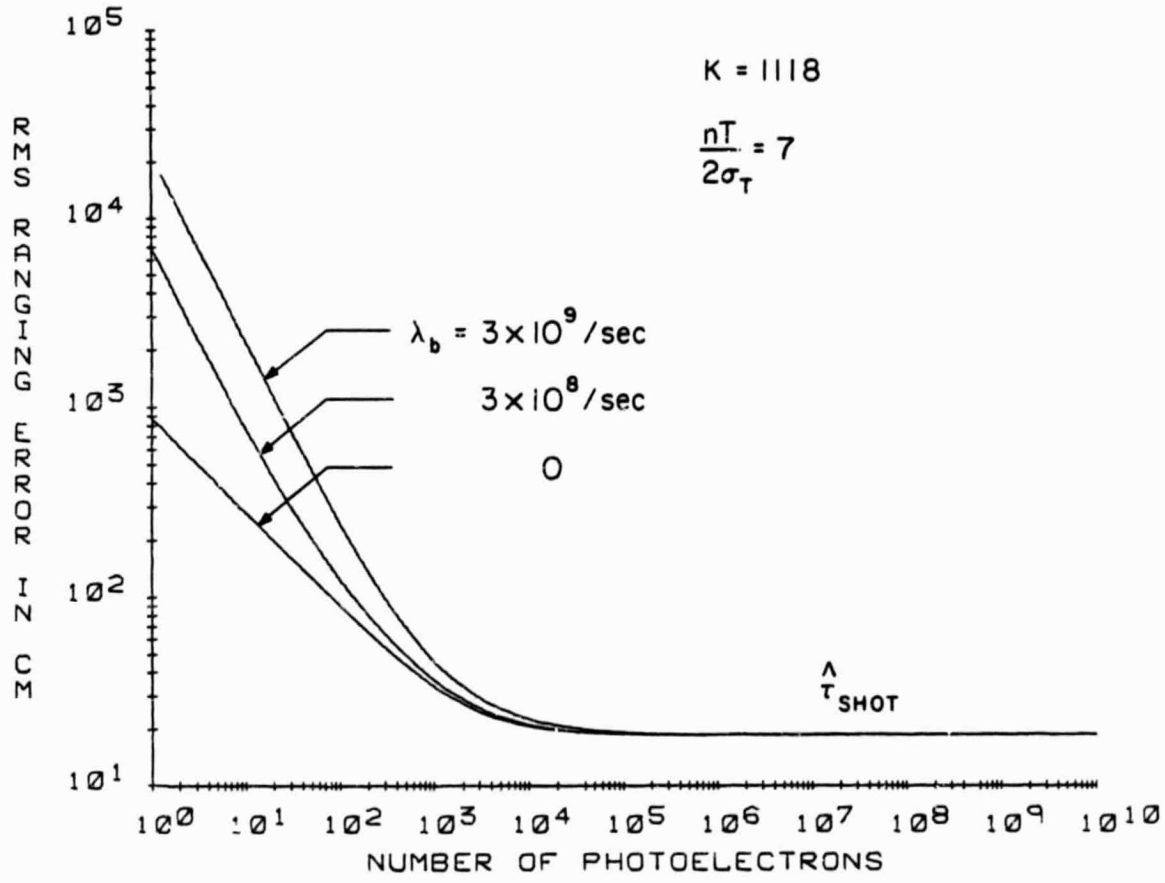

Fig. 4.13. RMS ranging error using $\hat{\tau}_{SHOT}$ estimator for non-normal incidence on an infinite flat diffuse target (z_2 = 500 km, θ_T = 0.1 mrad, ϕ = 5°, $c\sigma_f$ = 0.5 cm, A_R = 100 cm^2, λ^2= 1.064 μm, $nT/2\sigma_T$ = 7).

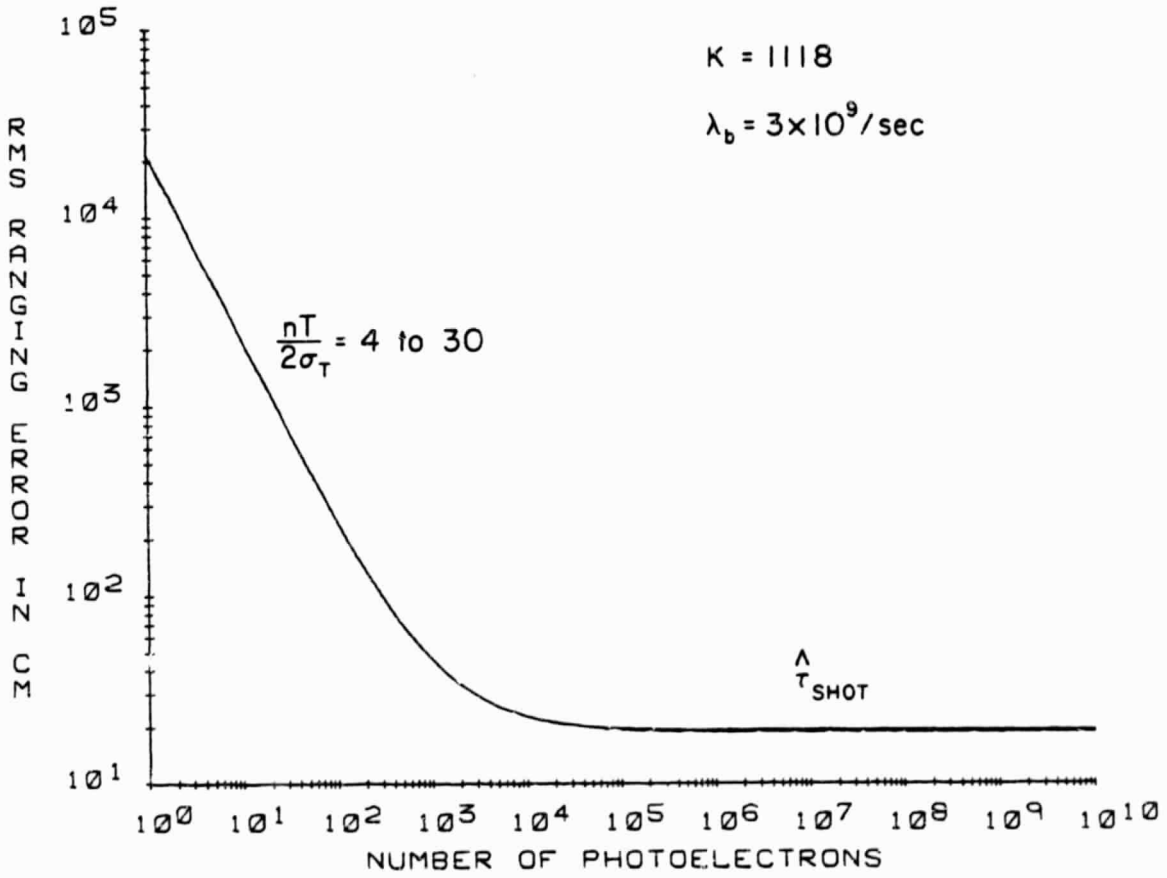

Fig. 4.14. Dependence of RMS ranging error on the observation interval width by using $\hat{\tau}_{SHOT}$ estimator and for non-normal incidence on an infinite flat diffuse target. (z = 500 km, θ_T = 0.1 mrad, ϕ = 0.5°, $c\sigma_f$ = 0.5 cm, A_R = 100 cm^2, λ = 1.064 μm).

In the speckle limiting region, Eq. (4.54) reduces to

$$\sigma^2_{\tau_{SHOT}} \cong \frac{\sigma_T^2}{2K} \qquad \langle N \rangle << K \quad . \qquad (4.58)$$

From Eq. (4.58), the timing performance of $\hat{\tau}_{SHOT}$ does not depend on either the background noise or the observation interval width. In this region, however, the speckle effects become significant. Consequently, the performance of this estimator will saturate at high signal level.

To compare the performance of these two estimators on the tilted diffuse flat target, both Eqs. (4.48) and (4.54) are plotted in Fig. 4.15 for $b = 3x10^8$/sec. The results show that within normal background noise level, the performance of the $\hat{\tau}_{SHOT}$ estimator is better than that of the $\hat{\tau}_{SPEC}$ estimator at low signal level. However, at high signal level, the $\hat{\tau}_{SPEC}$ estimator will perform better than the $\hat{\tau}_{SHOT}$ estimator.

4.5 Discussion

In laser ranging applications, shot noise, speckle and background noise introduce ranging errors, thus, limit the ranging (timing) accuracy of the receiver. In this chapter, two Maximum-likelihood arrival time estimators were investigated in order to understand their performances under the influence of the background noise. Bar-David's $\hat{\tau}_{SHOT}$ estimator takes into account both shot noise and background noise, and therefore, its performance is relatively less sensitive to the addition of background noise. However, at high signal level, its performance is limited by the time resolved speckle. On the other hand, Tsai and Gardner's $\hat{\tau}_{SPEC}$ estimator considers both shot noise and speckle. Consequently, it performs better than $\hat{\tau}_{SHOT}$ at high signal level where the speckle is the dominated error source, but it is subject in a greater extent to the addition of background noise. Also, this estimator is dependent

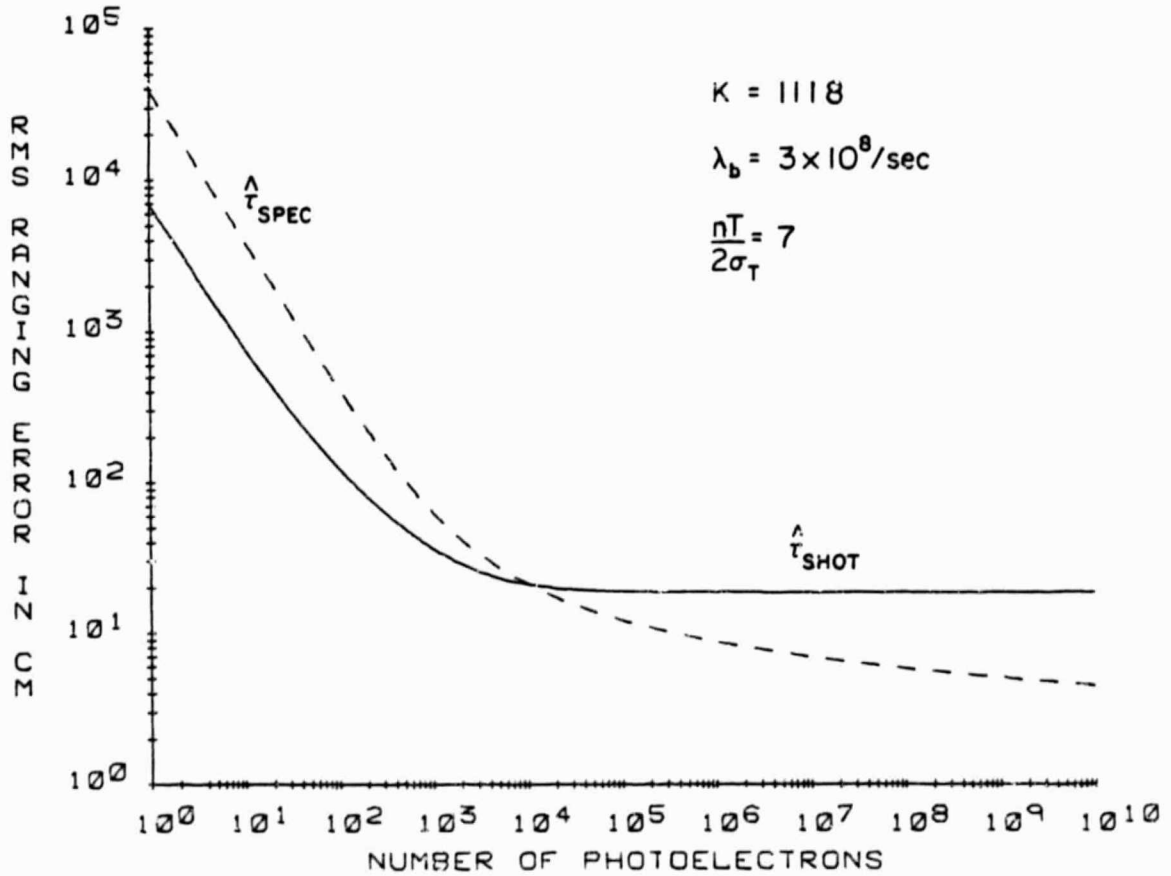

Fig. 4.15. Comparison of the RMS ranging errors using $\hat{\tau}_{SPEC}$ and $\hat{\tau}_{SHOT}$ estimators for non-normal incidence on an infinite flat diffuse target. (z = 500 km, θ_T = 0.1 mrad, ϕ = 0.5°, $c\sigma_f$ = 0.5 cm, A_R = 100 cm^2, λ = 1.064 μm).

on the width of the observation interval, especially at low signal level. At high signal level, its performance will be degraded slightly when the width of the observation interval is large compared to the pulse width of the received signal.

Background noise effect appears to be most sigificant at low signal level in the estimation of the arrival time. At high signal level, however, its effect is negligible. In normal background noise level, $\hat{\tau}_{SHOT}$ estimator will perform better than $\hat{\tau}_{SPEC}$ estimator at low signal level, but $\hat{\tau}_{SPEC}$ estimator will perform better at high signal level.

5. TWO-COLOR CROSS-CORRELATION ALGORITHM

5.1 Introduction

In satellite laser ranging applications where it is impossible or too expensive to obtain accurate meteorological information around the ranging sites, or in applications where optical pathlengths at two frequencies are necessary in order to obtain the appropriate parameter information, such as the surface pressure, it is desirable to measure the difference in the round-trip propagation time between pulses that were transmitted simultaneously at two optical frequencies. The Maximum-Likelihood estimators described in Chapter 4 can be used to determine the differential arrival time of the detected pulses in two-color ranging. Unfortunately, implementation of the ML estimators requires a prior knowledge of the mean detected pulse shape, and therefore, can only be used in applications where the target profiles and orientations are known. In most cases of interest, however, the mean pulse shapes will not be known and suboptimal estimators must be used.

The centroid estimator is easy to implement and is optimum for Gaussian pulses when speckle is negligible. Unfortunately, most of the reflected pulses from realistic targets are non-Gaussian and asymmetric, which reduces the effectiveness of the centroid estimator. Iyer [1976] has proposed a leading-edge threshold detection technique which registers the arrival time the instant that the output of the optical detection system exceeds a preset threshold. Receivers of this type are frequently used in laser ranging applications. However, this algorithm introduces a signal dependent bias which must be compensated in high precision ranging applications.

In this chapter a two-color cross correlation technique is being studied; the results will be applied to the pulse reflections from ground diffuse targets, earth-orbiting CCR arrays, and ocean.

5.2 Cross-Correlation Algorithm

In a two-color ranging system, the laser pulses of two different wavelengths are transmitted simultaneously. If the two beams are aligned so that their footprints overlap, the mean reflected pulse shapes will be almost identical. An effective technique for estimating the differential arrival time that takes advantage of this pulse similarity is calculation of the peak of the cross-correlation function of the two detected signals. This correlation estimator can be written mathematically as [Gardner et al., 1983]

$$\hat{\tau}_{COR} = \arg \max_{\tau} \left[\int_{-\infty}^{\infty} dt \; S_1(t) \; S_2(t + \tau) \right] = \arg \max_{\tau} \left[R_{12}(\tau) \right] \quad , \quad (5.1)$$

where S_1 and S_2 are the detected signals at wavelengths λ_1 and λ_2, respectively, $R_{12}(\tau)$ is the cross-correlation function of these two signals, τ is the differential arrival time, and $\hat{\tau}_{COR}$ is its estimate using the correlation algorithm.

To analyze the performance of the correlation estimator, we must linearize R_{12} around the actual differential arrival time (τ_o) by using a Taylor series expansion. This method depends upon the underlying assumption that R_{12} is differentiable. Therefore, we shall exclude from the analysis detected signals which would give rise to a non-differentiable R_{12} such as rectangular pulses. With the assumption that the shot noise and speckle are not severe so that

$$\text{var}\,[\ddot{R}_{12}(\tau_o)] << E^2\,[\ddot{R}_{12}(\tau_o)] \quad , \tag{5.2}$$

the bias ($E(\Delta\tau_{COR})$) and the variance ($\sigma^2_{\tau_{COR}}$) of the correlation estimator can be calculated to give

$$E[\Delta\tau_{COR}] = E[\hat{\tau}_{COR} - \tau_o] = -E[\dot{R}_{12}(\tau_o)]/E[\ddot{R}_{12}(\tau_o)] \tag{5.3}$$

and

$$\sigma^2_{\tau_{COR}} = E[(\hat{\tau}_{COR} - \tau_o)^2] = E[\dot{R}^2_{12}(\tau_o)]/E^2[\ddot{R}_{12}(\tau_o)] \quad . \tag{5.4}$$

Eq. (5.4) gives the lower bound of the correlation estimator. The actual timing variance is expected to be higher depending upon the actual SNR. When the SNR is high, however, the actual timing variance will approach this bound asymptotically.

By noting that both the speckle and the shot noise induced fluctuations are uncorrelated at the two frequencies, we can express the bias and the variance of the correlation estimator in terms of the mean and autocorrelation functions of S_1 and S_2. That is,

$$E[\Delta\tau_{COR}] = -\int_{-\infty}^{\infty} dt\, \langle S_1(t)\rangle \langle \dot{S}_2(t+\tau_o)\rangle \Big/ \left\{\int_{-\infty}^{\infty} dt\, \langle S_1(t)\rangle \langle \ddot{S}_2(t+\tau_o)\rangle\right\} \quad , \tag{5.5}$$

$$\sigma^2_{\tau_{COR}} = \frac{\dfrac{\partial^2}{\partial\tau_1\partial\tau_2} \int_{-\infty}^{\infty} dt_1 \int_{-\infty}^{\infty} dt_2\, R_{S_1}(t_1,t_2)\, R_{S_2}(t_1+\tau_1, t_2+\tau_2)\Big|_{\tau_1=\tau_2=\tau_o}}{\int_{-\infty}^{\infty} dt\, \langle S_1(t)\rangle \langle \ddot{S}_2(t+\tau_o)\rangle^2} \tag{5.6}$$

where

$$R_{S_i}(t_1,t_2) = C_{S_i}(t_1,t_2) + \langle S_i(t_1)\rangle\langle S_i(t_2)\rangle \ , \qquad i=1,2. \tag{5.7}$$

The mean (Eq. (3.22)) and autocovariance function (Eq. (3.23)) at the two frequencies are related by

$$\langle S_i(t)\rangle = \langle N_i\rangle \ f_S(t - (i-1)\tau_o) \qquad i=1,2 \tag{5.8}$$

and

$$C_{S_i}(t_1,t_2) = \langle N_i\rangle \ G(\sqrt{2}\ \sigma_h, t_1 - t_2) \ f_S\left(\frac{t_1 + t_2}{2} - (i-1)\tau_o\right)$$

$$+ \langle N_i\rangle^2 K_i^{-1} \ G(\sqrt{2}\ \sigma_g, \ t_1 - t_2) \ f_{SP}\left(\frac{t_1 + t_2}{2} - (i-1)\tau_o\right) \ , \ i=1,2, \tag{5.9}$$

respectively. By substituting Eq. (5.8) into Eq. (5.5), it is easy to show that the correlation estimator is unbiased. Since this estimator cross correlates the two noise corrupted signals, the peak of the cross correlation function will shift randomly and introduce a timing error. In order to analyze the characteristics of this timing error, Eq. (5.6) is expanded using Eq. (5.7) to give

$$\sigma^2_{\tau_{COR}} = \frac{\dfrac{\partial^2}{\partial\tau_1\partial\tau_2} \int_{-\infty}^{\infty} dt_1 \int_{-\infty}^{\infty} dt_2 \ \langle S_1(t_1)\rangle\langle S_1(t_2)\rangle\langle S_2(t_1 + \tau_1)\rangle\langle S_2(t_2 + \tau_2)\rangle \Big|_{\tau_1=\tau_2=\tau_o}}{\int_{-\infty}^{\infty} dt \ \langle S_1(t)\rangle \ \langle \ddot{S}_2(t + \tau_o)\rangle^2}$$

$$+\frac{\dfrac{\partial^2}{\partial\tau_1\partial\tau_2}\left\{\int_{-\infty}^{\infty}dt_1\int_{-\infty}^{\infty}dt_2\,\langle S_1(t_1)\rangle\langle S_1(t_2)\rangle\,C_{S_2}(t_1+\tau_1,t_2+\tau_2)\right\}\Big|_{\tau_1=\tau_2=\tau_o}}{\left\{\int_{-\infty}^{\infty}dt\,\langle S_1(t)\rangle\,\langle\ddot{S}_2(t+\tau_o)\rangle\right\}^2}$$

$$+\frac{\dfrac{\partial^2}{\partial\tau_1\partial\tau_2}\left\{\int_{-\infty}^{\infty}dt_1\int_{-\infty}^{\infty}dt_2\,C_{S_1}(t_1,t_2)\,\langle S_1(t_1+\tau_1)\rangle\langle S_2(t_2+\tau_2)\rangle\right\}\Big|_{\tau_1=\tau_2=\tau_o}}{\left\{\int_{-\infty}^{\infty}dt\,\langle S_1(t)\rangle\,\langle\ddot{S}_2(t+\tau_o)\rangle\right\}^2} \qquad (5.10)$$

$$+\frac{\dfrac{\partial^2}{\partial\tau_1\partial\tau_2}\left\{\int_{-\infty}^{\infty}dt_1\int_{-\infty}^{\infty}dt_2\,C_{S_1}(t_1,t_2)\,C_{S_2}(t_1+\tau_1,t_2+\tau_2)\right\}\Big|_{\tau_1=\tau_2=\tau_o}}{\left\{\int_{-\infty}^{\infty}dt\,\langle S_1(t)\rangle\langle\ddot{S}_2(t+\tau_o)\rangle\right\}^2}\ .$$

The first term on the right side of Eq. (5.10) equals the square of the bias, so that it is zero. The second and the third terms are the first-order errors involving the cross-correlations of the mean of S_1 and the fluctuating portion of S_2, and vice versa. The last term is the second-order error involving the cross-correlations of the fluctuating portions of both S_1 and S_2. Notice that the first-order errors will be the total error for an estimator that correlates the detected signals with their corresponding means. From this point of view, the second-order error is an additional error incurred when the mean pulse shapes are not known, which is the case in most applications.

Because of the random nature of most of the target surface profiles, f_S and f_{SP} are generally very difficult to evaluate, and numerical computation is usually required to determine the timing error given by Eq. (5.10). It is more convenient to express the timing error in the frequency domain. By substituting Eqs. (5.8) and (5.9) into Eq. (5.10) and Fourier transforming the various terms, the mean-square (MS) timing error can be expressed in terms of the bandwidth of the detected signal. The result is [Im and Gardner, 1985]

$$\sigma_{\tau_{COR}}^2 = \left(\frac{1}{\langle N_1\rangle} + \frac{1}{\langle N_2\rangle}\right)\frac{\alpha_1}{2B_S^2} + \left(\frac{1}{K_1} + \frac{1}{K_2}\right)\frac{\alpha_2}{2B_S^2}$$

$$+ \frac{\sqrt{\pi}}{2\sqrt{2}\,B_S^4 \int_{-\infty}^{\infty} d\omega\,|\phi_S(\omega)|^2}\left\{\frac{\sigma_h^{-2} - B_S^2}{\langle N_1\rangle\langle N_2\rangle\sigma_h}\right. \tag{5.11}$$

$$+ \frac{\alpha_3(\sigma_g^{-2} - B_{SP}^2)}{K_1K_2\sigma_g} + \frac{\alpha_4\left(\dfrac{1}{\sigma_h^2 + \sigma_f^2/2} - B_x^2\right)}{\langle N_1\rangle K_2(\sigma_h^2 + \sigma_f^2/2)^{1/2}}$$

$$\left. + \frac{\alpha_4\left(\dfrac{1}{\sigma_h^2 + \sigma_f^2/2} - B_x^2\right)}{\langle N_2\rangle K_1(\sigma_h^2 + \sigma_f^2/2)^{1/2}}\right\}$$

where

$$B_S^2 = \int_{-\infty}^{\infty} d\omega\ \omega^2\ |\phi_S(\omega)|^2 \ /\ \int_{-\infty}^{\infty} d\omega\ |\phi_S(\omega)|^2 \quad , \tag{5.12}$$

$$B_{SP}^2 = \int_{-\infty}^{\infty} d\omega\ \omega^2\ |\phi_{SP}(\omega)|^2 \ /\ \int_{-\infty}^{\infty} d\omega\ |\phi_{SP}(\omega)|^2 \quad , \tag{5.13}$$

$$B_x^2 = \int_{-\infty}^{\infty} d\omega\ \omega^2 \phi_S^*(\omega)\phi_{SP}(\omega) \ /\ \int_{-\infty}^{\infty} d\omega\ \phi_S^*(\omega)\phi_{SP}(\omega) \quad , \tag{5.14}$$

$$\alpha_1 = \frac{\int_{-\infty}^{\infty} d\omega\ \omega^2 \phi_S^*(\omega)\ [\phi_S(\omega) * \phi_S(\omega)]}{\int_{-\infty}^{\infty} d\omega\ \omega^2\ |\phi_S(\omega)|^2 \ \int_{-\infty}^{\infty} d\omega\ |\phi_S(\omega)|^2} \quad , \tag{5.15}$$

$$\alpha_2 = \frac{2\ \int_{-\infty}^{\infty} d\omega\ \phi_{SP}^*(\omega)\ [j\omega\phi_S(\omega) * j\omega\phi_S(\omega)]}{\int_{-\infty}^{\infty} d\omega\ \omega^2\ |\phi_S(\omega)|^2 \ \int_{-\infty}^{\infty} d\omega\ |\phi_S(\omega)|^2} \quad , \tag{5.16}$$

$$\alpha_3 = \int_{-\infty}^{\infty} d\omega\ |\phi_{SP}(\omega)|^2 \ /\ \int_{-\infty}^{\infty} d\omega\ |\phi_S(\omega)|^2 \quad , \tag{5.17}$$

$$\alpha_4 = \int_{-\infty}^{\infty} d\omega\ \phi_S^*(\omega)\ \phi_{SP}(\omega) \ /\ \int_{-\infty}^{\infty} d\omega\ |\phi_S(\omega)|^2 \quad , \tag{5.18}$$

$$\phi_S(\omega) = \int_{-\infty}^{\infty} dt\ f_S(t)\ \exp(-j\omega t) \tag{5.19}$$

and

$$\phi_{SP}(\omega) = \int_{-\infty}^{\infty} dt\ f_{SP}(t)\ \exp(-j\omega t) \quad . \tag{5.20}$$

B_S is the RMS bandwidth of the mean detected signal, B_{SP} is the RMS bandwidth of the speckle variance waveform, B_X is the RMS 'cross-bandwidth' between the mean detected signal and speckle variance. Since f_S and f_{SP} involve the convolution of the transmitted pulse and the receiver impulse response, the RMS bandwidths B_S, B_{SP} and B_X are always larger than σ_h^{-1}. The α_i's are dimensionless factors which typically vary between 1 and 2 depending on the surface profile.

In Eq. (5.11), the terms involving $\langle N_i \rangle^{-1}$ are the first-order shot-noise contributions to the timing error due to the correlation between the mean signal at one frequency and the shot-noise induced fluctuating component of the detected signal at the other frequency, and vice versa. The terms involving K_i^{-1} are the first-order speckle-noise contributions to the timing error due to the correlation between the mean signal at one frequency and the speckle induced fluctuating component of the detected signal at the other frequency, and vice versa. The term involving $(\langle N_1 \rangle \langle N_2 \rangle)^{-1}$ is the second-order shot-noise contribution due to the correlation between the shot-noise induced fluctuating components of the detected signals at the two frequencies. The term involving $(K_1 K_2)^{-1}$ is the second-order speckle-noise contribution due to the correlation between the speckle induced fluctuating components of the detected signals at the two frequencies. The last two terms involving $(\langle N_1 \rangle K_2)^{-1}$ and $(\langle N_2 \rangle K_1)^{-1}$ are the second-order errors due to the correlation between the shot-noise induced fluctuating component of the detected signal at one frequency and the speckle induced fluctuating component of the detected signal at the other frequency, and vice versa.

The first-order errors depend on the bandwidth of the mean detected signal, which is related to the target surface profile and to the beam curvature. The second-order errors depend on the difference between the

receiver bandwidth and the bandwidths that are related to the detected signal. It should be emphasized that each of the differences in the second-order terms are strictly positive. When the receiver bandwidth is very large, the timing error is dominated by the second-order shot-noise effect. On the other hand, when the receiver bandwidth is very small, the bandwidth of the mean detected signal will also be very small. Consequently, the first-order errors will dominate the overall timing error. In these two extreme cases, however, the overall timing error is likely to be very large. Fortunately, the first-order errors are less sensitive to the change in receiver bandwidth than the second-order errors, and the second-order errors can be reduced to negligible levels by reducing the receiver bandwidth before the first-order errors diverge significantly. In general, there is an optimum receiver bandwidth which minimizes the overall timing error for a given set of received pulses.

The timing error of the correlation receiver is inversely proportional to the signal bandwidth. This is expected since high bandwidth signals will contain fine scale structure which improve the performance of the correlation timing algorithm. At low signal levels, the timing performance is dominated by either the first-order or the second-order shot-noise effect depending upon the difference in the bandwidths of the receiver and the mean detected signals. In either case, the timing error will decrease as the received signal strength increases. At high signal levels, however, the speckle becomes significant, and it places the fundamental limit on the timing accuracy of the correlation receiver.

5.3 Pulse Reflections from Infinite Diffuse Flat Targets

To illustrate quantitatively the timing performance of the correlation receiver and its dependence on the target profile, we shall look at specific target configurations. In the first example we consider pulse reflections from an infinite flat diffuse target. This is a good model for reflections from ground targets. When the laser beam is incident normally on a flat surface, the reflected pulses are broadened by the wavefront curvature of the laser beam. However, this effect is usually small for typical beam divergences. When the laser beam is incident at an angle ϕ with respect to the surface normal (refer to Fig. 4.1), a range spread will be introduced by the diffuse target. The amount of range spread for a given target depends on ϕ and the illuminated surface area. For an infinite flat target at a range z from the ranging system, and for laser beam divergence angle θ_T, the RMS range spread is approximately 2 z tan θ_T tan ϕ [Gardner, 1982]. The range spread induced broadening of a received pulse can significantly reduce the signal bandwidth, and, as indicated in Section 5.2, will degrade the timing performance of the correlation receiver.

To simplify the mathematics, we assume that the power reflectivity is uniform over the entire footprint, and that the laser footprint has a Gussian cross-section

$$|a(\underline{\rho},z)|^2 = Q(2\pi\, z^2 \tan^2\theta_T)^{-1} \exp(-\rho^2/2z^2 \tan^2\theta_T) \qquad (5.21)$$

where Q is the transmitted laser pulse energy. f_S and f_{SP} can now be calculated by using Eqs. (3.3), (3.4), (3.24), (3.25) for the diffuse

target. By neglecting the curvature effects, we obtain

$$f_S(t) = G(\sigma_S,\ t - 2z/c) \tag{5.22}$$

and

$$f_{SP}(t) = G(\sigma_S/\sqrt{2},\ t - 2z/c) \tag{5.23}$$

with

$$\sigma_S = (\sigma_f^2 + \sigma_h^2 + \sigma_r^2)^{1/2} = (\sigma_g^2 + \sigma_r^2)^{1/2} \quad , \tag{5.24}$$

$$\sigma_r = 2\ z\ \tan\ \theta_T\ \tan\ \phi\ /c \quad . \tag{5.25}$$

σ_S is the width of the reflected pulse from the flat diffuse target for the case of non-normal incidence. σ_r is the range spread induced pulse broadening. f_S and f_{SP} are plotted in Figs. 5.1 and 5.2 respectively for the nominal ranging system parameters and three different incidence angles. We can see that both f_S and f_{SP} are significantly broadened even for a very small incidence angle. The number of speckle correlation cells can be calculated by using Eqs. (3.6) and (3.21):

$$K_i = \pi\ A_R(2\ \tan\ \theta_T/\lambda_i)^2 \ . \tag{5.26}$$

Typically, K_i is of the order of a few hundred or more. The MS timing error can be calculated by substituting the Fourier tranforms of Eqs. (5.22) and (5.23) into Eqs. (5.11) through (5.20). The results are

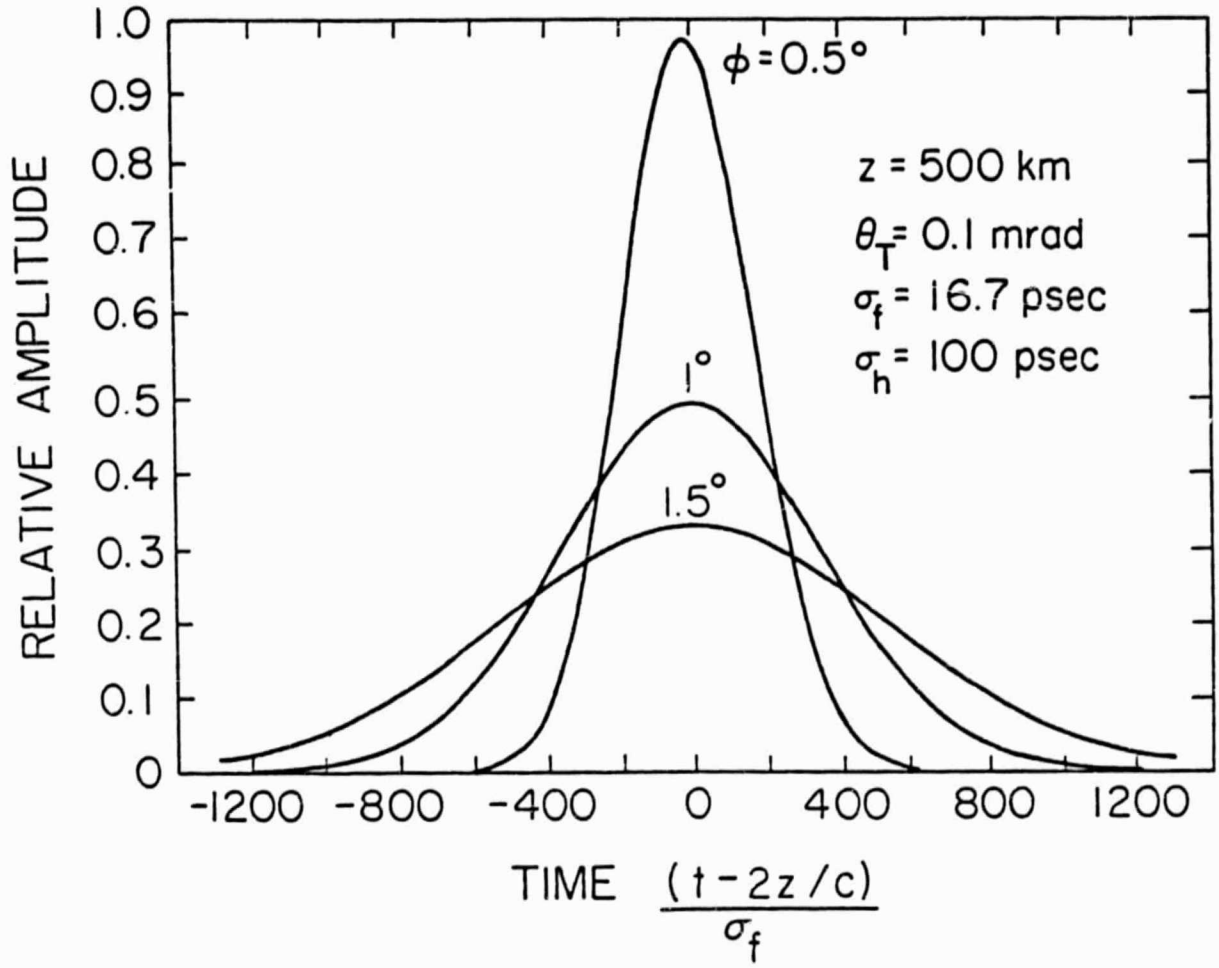

Fig. 5.1. Mean detected signal waveform ($f_S(t)$) for non-normal incidence on an infinite flat diffuse target. (z = 500 km, θ_T = 0.1 mrad, σ_f = 16.7 psec, σ_h = 100 psec).

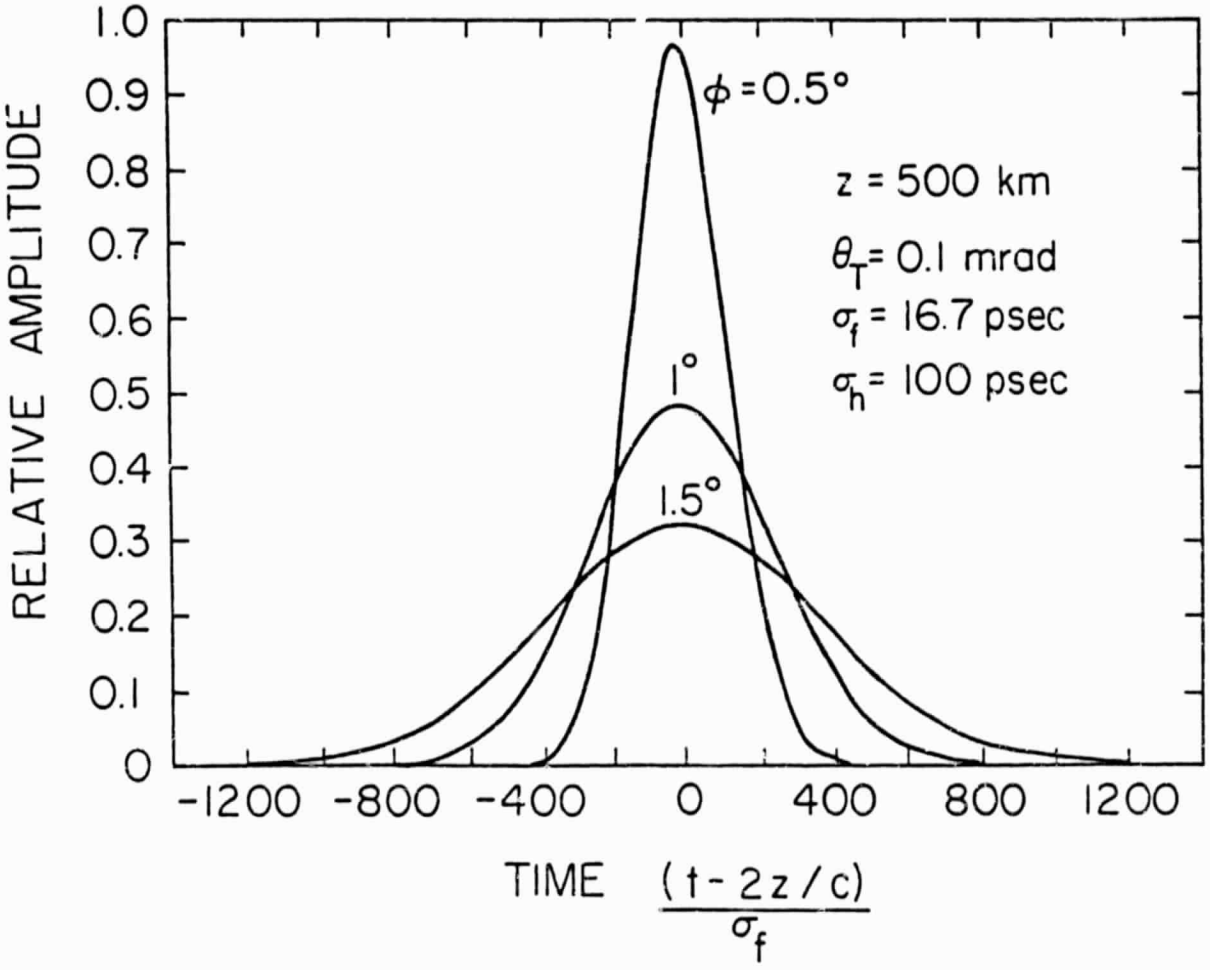

Fig. 5.2. Speckle variance ($f_{SP}(t)$) for non-normal incidence on an infinite flat diffuse target. (z = 500 km, θ_T = 0.1 mrad, σ_f = 16.7 psec, σ_h = 100 psec)

$$\sigma_{\tau_{COR}}^2 = \frac{8}{3\sqrt{3}}\left(\frac{1}{\langle N_1\rangle} + \frac{1}{\langle N_2\rangle}\right)\sigma_S^2 + \sqrt{2}\left(\frac{1}{K_1} + \frac{1}{K_2}\right)\sigma_S^2$$

$$+ \frac{\sigma_S^5\,(1 - \sigma_h^2/2\sigma_S^2)}{\sqrt{2}\,\langle N_1\rangle\langle N_2\rangle\sigma_h^3} + \frac{\sigma_S^5\,(1 - \sigma_g^2/\sigma_S^2)}{K_1K_2\,\sigma_g^3} \qquad (5.27)$$

$$+ \frac{4}{\sqrt{3}}\left(\frac{1}{\langle N_1\rangle K_1} + \frac{1}{\langle N_2\rangle K_1}\right)\frac{\sigma_S^5\left(1 - \frac{\sigma_g^2 + \sigma_h^2}{3\sigma_S^2}\right)}{(\sigma_g^2 + \sigma_h^2)^{3/2}}$$

From Eq. (5.27), we can see that the first-order timing errors of the correlation receiver increase directly with σ_S, which in turn is directly proportional to the range spread of the target σ_r, the transmitted pulse width σ_f, and the width of the receiver impulse response σ_h. The second-order errors are inversely related to σ_h. Since $\sigma_S > \sigma_g > \sigma_h$, the second-order errors will always exist in this receiver. The timing performance for this configuration is plotted against the expected signal strength $\langle N_1\rangle = \langle N_2\rangle = \langle N\rangle$ in Fig. 5.3 for the same ranging parameters used in Figs. 5.1 and 5.2. The plotted result shows that the timing error can be quite large due to the range spread effect. The curves saturate at high signal levels because of the speckle.

At low signal levels, the timing error of the correlation receiver is dominated by the shot-noise contributions, and Eq. (5.27) can be written approximately as

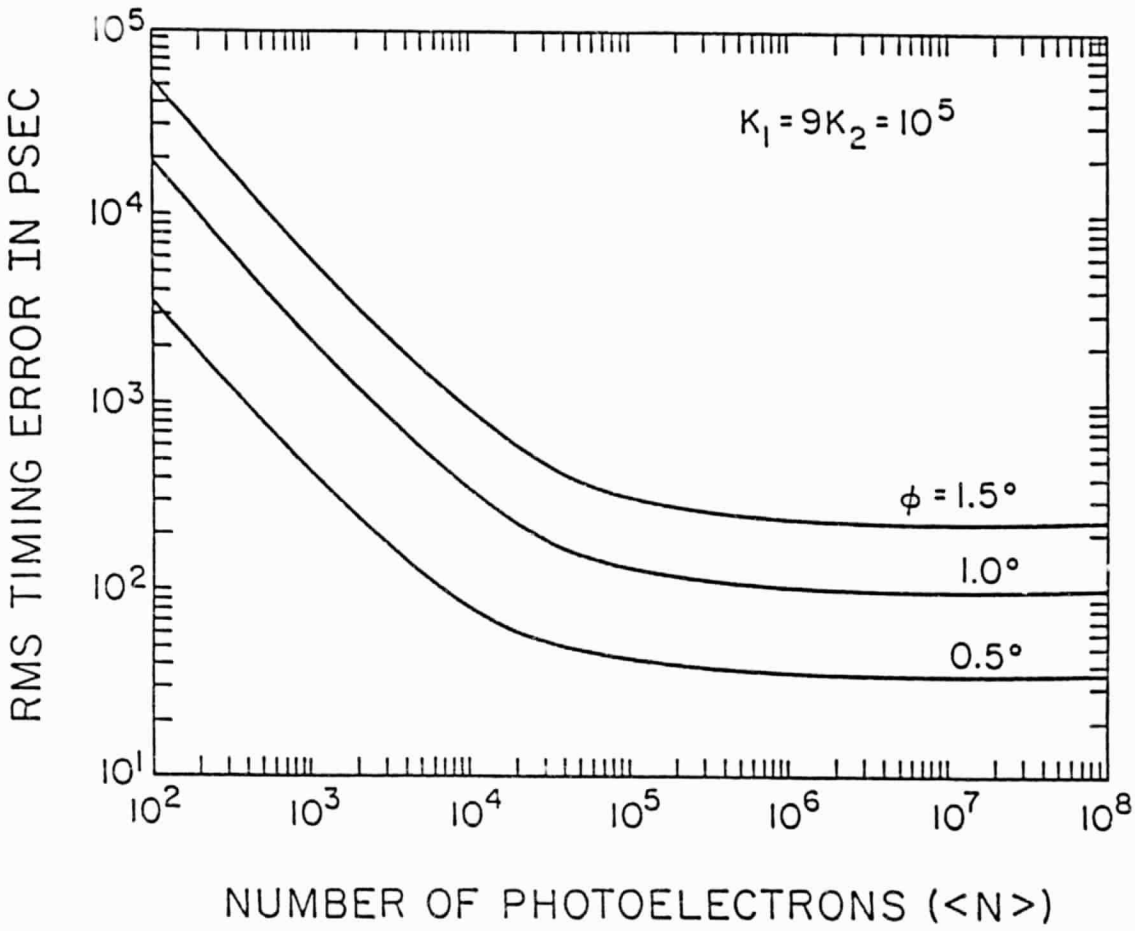

Fig. 5.3. RMS differential timing error versus received signal strength for pulse reflections from an infinite flat diffuse target using the correlation estimator (z = 500 km, θ_T = 0.1 mrad, σ_f = 16.7 psec, σ_n = 100 psec, λ_1 = 0.355 μm, λ_2 = 1.064 μm, A_R = 0.1 m^2).

$$\sigma_{\tau_{COR}}^2 \simeq \frac{4}{3\sqrt{3}} \left(\frac{1}{\langle N_1 \rangle} + \frac{1}{\langle N_2 \rangle}\right) \frac{1}{B_S^2} + \frac{B_R(2B_R^2 - B_S^2)}{4\sqrt{2}\,\langle N_1 \rangle \langle N_2 \rangle B_S^5}, \quad \langle N_i \rangle \ll K_i \tag{5.28}$$

where

$$B_S = (\sqrt{2}\,\sigma_S)^{-1} = [2(\sigma_f^2 + \sigma_h^2 + \sigma_r^2)]^{-1/2} ,$$

$$B_R = (\sqrt{2}\,\sigma_h)^{-1} .$$

B_S is the RMS bandwidth of the mean detected signal, and B_R is the RMS receiver bandwidth. In this region, if the receiver bandwith is large, the second-order shot-noise effect is the most significant error source, and the timing error of the correlation receiver can be very large. On the other hand, when the receiver bandwidth is small, the first-order shot-noise effect dominates, and the timing error of the correlation reciever in this case is likely to be smaller. In Fig. 5.3, we chose the parameters so that $B_R \gg B_S$. Therefore, the RMS timing error curves decrease according to $\langle N \rangle^{-1}$ when $\langle N \rangle \ll K_i$.

At high signal levels, the speckle noise dominates, and the timing error of the correlation receiver can be written approximately as

$$\sigma_{\tau_{COR}}^2 \simeq \frac{1}{\sqrt{2}} \left(\frac{1}{K_1} + \frac{1}{K_2}\right) \frac{1}{B_S^2} + \frac{B_{PT}(B_{PT}^2 - B_S^2)}{2K_1K_2B_S^5}, \quad \langle N_i \rangle \gg K_i \tag{5.29}$$

where

$$B_{PT} = (\sqrt{2}\ \sigma_g)^{-1} = [2(\sigma_h^2 + \sigma_f^2)]^{-1/2} \quad . \tag{5.30}$$

B_{PT} is the RMS bandwidth of the point target response of the system. In this region, the shot-noise effect is negligible. This behavior is illustrated by the saturated (flat) regions of the three curves shown in Fig. 5.3. As we can see, the speckle noise places a fundamental limit on the accuracy of the differential arrival time estimation. Unlike the second-order shot-noise error, the second-order speckle-noise error will saturate at a finite level even if B_R approaches infinity ($\sigma_h \to 0$). This is due to the fact that the correlation length of the speckle-induced fluctuation in the received signal is $2\sqrt{2}(\sigma_h^2 + \sigma_f^2)^{1/2}$ (refer to Eq. (3.23)), so even if σ_h is very small, there is still a small amount of correlation left on the speckle-induced fluctuating components of the received signals, and this prevents the timing error from diverging.

The effect of receiver bandwidth on the timing performance of the correlation receiver can be illustrated by plotting in Fig. 5.4 the timing error versus the normalized receiver bandwidth ($B_R/\hat{B}_S$) for three different values of $\langle N \rangle$ and for $K_1 = 9K_2 = 10^5$. $\hat{B}_S = [2(\sigma_f^2 + \sigma_r^2)]^{-1/2}$ is the RMS bandwidth of the received signal prior to detection and therefore does not depend upon the receiver bandwidth. The upper curve ($\langle N \rangle = 500$) corresponds to the case of shot-noise-limited differential timing error. When $B_R \gg \hat{B}_S$, the second-order shot-noise effect dominates, and the overall timing error increases with increasing receiver bandwidth. Consequently, the timing performance can be improved by reducing the receiver bandwidth. On the other hand, when $B_R \ll \hat{B}_S$, the first-order effect dominates, and the timing error decreases as the receiver bandwidth increases. We can see that the

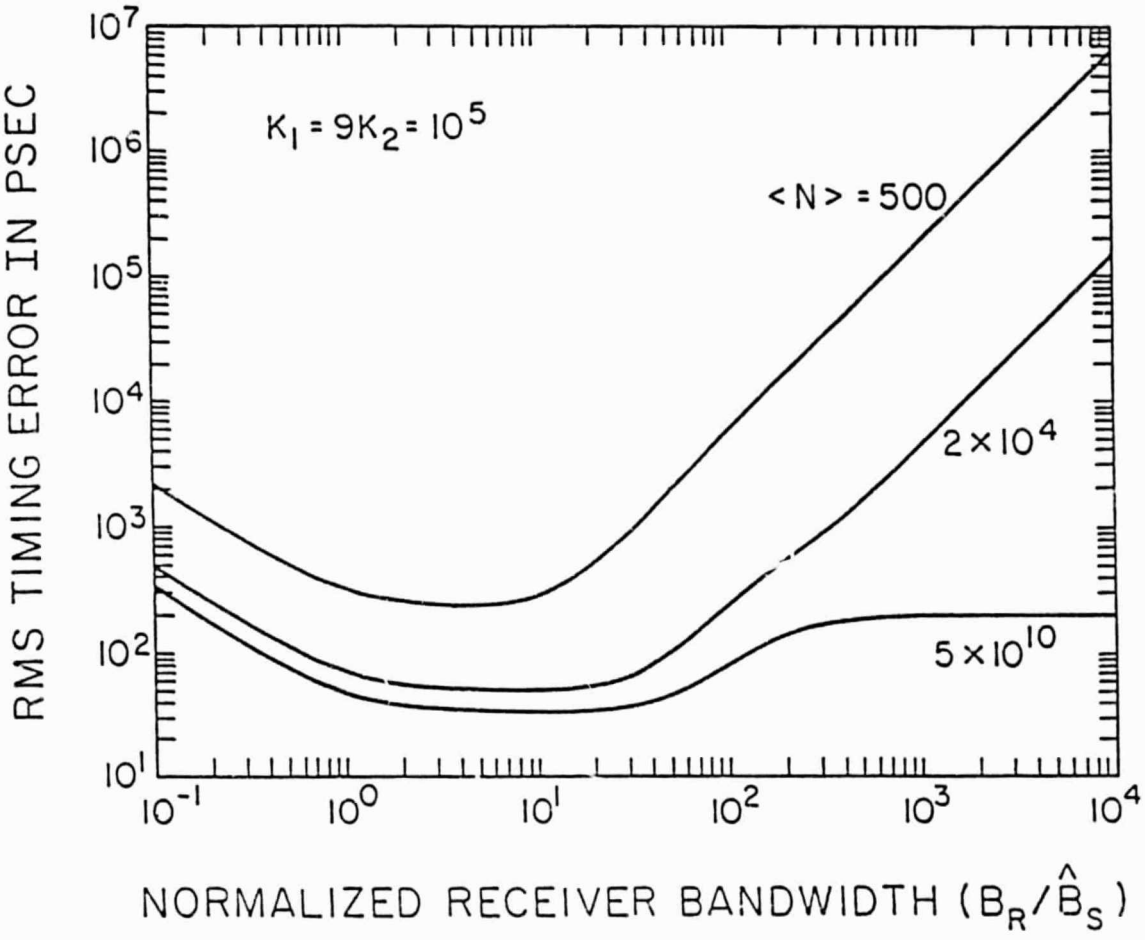

Fig. 5.4. RMS differential timing error versus normalized receiver bandwidth ($B_R/\hat{B}_S$) for pulse reflections from an infinite flat diffuse target using the correlation estimator. B_R is the receiver bandwidth, and $\hat{B}_S$ is the signal bandwidth prior to detection. (z = 500 km, θ_T = 0.1 mrad, σ_f = 16.7 psec, ϕ = 0.5°, λ_1 = 0.355 μm, λ_2 = 1.064 μm, A_R = 0.1 m^2)

minimum timing error occurs somewhere between these two extremes. The middle curve ($\langle N \rangle = 2 \times 10^4$) corresponds to the case where the shot-noise and speckle contributions to the timing error are almost equal. In this case the dependence of the timing error on B_R is almost the same as for the upper curve. The bottom curve ($\langle N \rangle = 5 \times 10^{10}$) corresponds to the timing error in the speckle-limited region. This curve has almost the same basic characteristics as the other two curves except when the receiver bandwidth is very large. When $B_R \gg \hat{B}_S$, the timing error saturates because the second-order speckle-noise error is much less sensitive to the change of B_R for reasons discussed earlier.

To illustrate the effects of speckle in the differential arrival time estimation, the RMS timing error is plotted versus the signal strength $\langle N \rangle$ for different sets of K_i's in Fig. 5.5. The flat regions in this figure correspond to the speckle-limited regions. We can see that the timing error increases as the speckle SNR decreases. When the K_i's approach infinity, the ranging system operates in the shot-noise-limited region and so the timing accuracy is always improved as the received signals become stronger. At low signal levels, the second-order shot noise is the most significant error source so the curve has a $\langle N \rangle^{-1}$ dependence. At high signal levels, the first-order shot noise is the most significant error source, so the curve has a $\langle N \rangle^{-1/2}$ dependence. However, for all finite values of K_i's, the timing accuracy will saturate when $\langle N \rangle = K_i$. According to Eq. (5.26), we can minimize the speckle effect by increasing either the laser beam divergence angle (θ_T) or the area of the receiver aperture (A_R), or both. However, the expression in Eq. (5.27) contains terms that are proportional to $\tan^2\theta_T$. Consequently, the timing error will increase by increasing

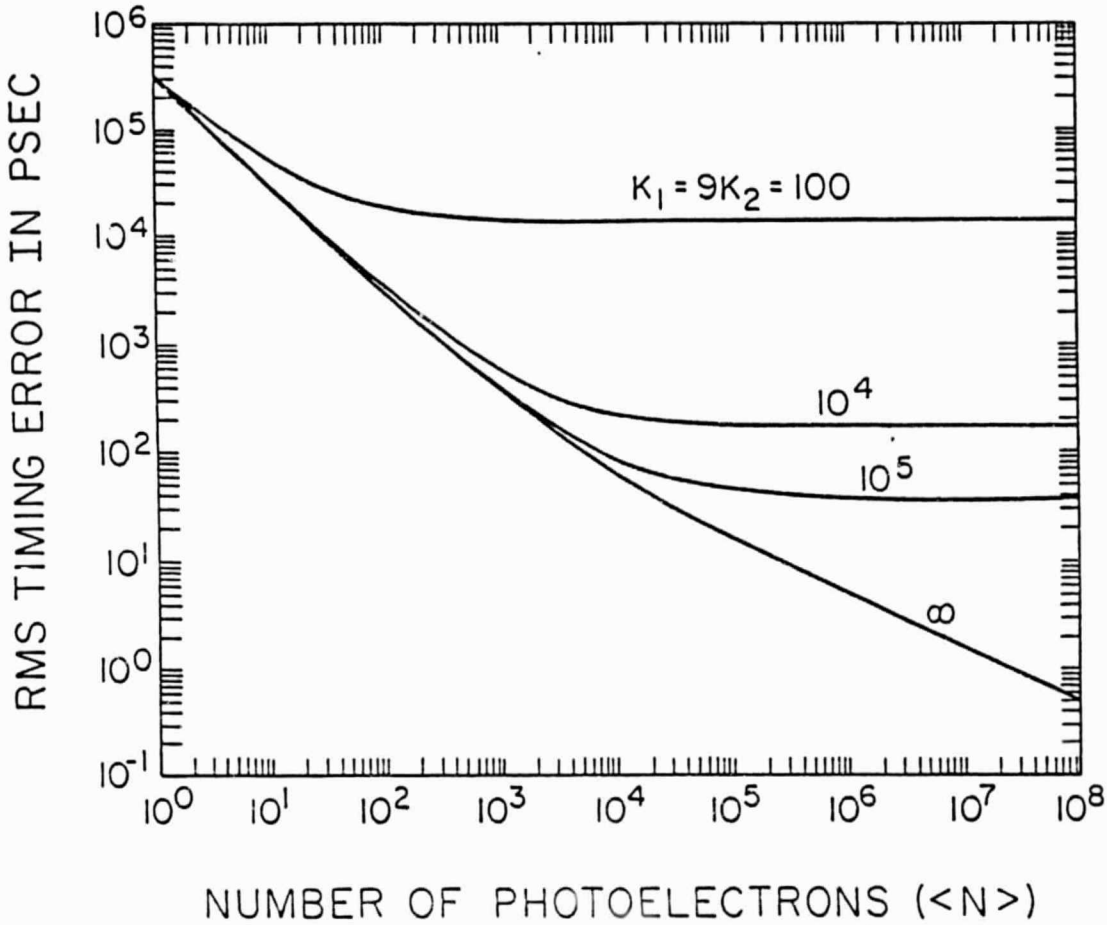

Fig. 5.5. RMS differential timing error versus received signal strength for pulse reflections from an infinite flat diffuse target using correlation estimator (z = 500 km, θ_T = 0.1 mrad, σ_f = 16.7 psec, σ_h = 100 psec, ϕ = 0.5°, λ_1 = 0.355 μm, λ_2 = 1.064 μm).

θ_T even though the K_i's increase. The only effective way to reduce the speckle-noise contribution is to increase the area of the receiver aperture. In fact, the increase in aperture size will also reduce the shot-noise contribution because $\langle N \rangle$ is also proportional to A_R.

It is interesting to compare the performance of the correlation estimator with that of the optimal ML estimator. By using the fact that both the shot-noise and speckle induced signal fluctuations at the two frequencies are uncorrelated, the ML estimator of the two-color differential arrival time can be expressed as [Tsai and Gardner, 1985]

$$\sigma_{\tau_{ML}}^2 = \left[\int_{-\infty}^{\infty} \frac{\dot{f}_S^2(t)dt}{\langle N_1 \rangle^{-1} f_S(t) + K_1^{-1} f_{SP}(t)} \right]^{-1} + \left[\int_{-\infty}^{\infty} \frac{\dot{f}_S^2(t)dt}{\langle N_2 \rangle^{-1} f_S(t) + K_2^{-1} f_{SP}(t)} \right]^{-1} \tag{5.31}$$

$$= \sigma_S^2 \left[\frac{1}{\langle N_1 \rangle \, g(\langle N_1 \rangle, K_1)} + \frac{1}{\langle N_2 \rangle \, g(\langle N_2 \rangle, K_2)} \right]$$

where

$$g(\langle N_i \rangle, K_1) = \frac{1}{\sqrt{2\pi}} \int_{-\infty}^{\infty} dy \; \frac{y^2 \exp(-y^2/2)}{1 + \sqrt{2}\, \langle N_i \rangle \, K_i^{-1} \exp(-y^2/2)}, \quad i=1,2 \; . \tag{5.32}$$

The timing error for the ML estimator consists only of first-order errors and so its dependence on the receiver bandwidth is only through σ_S. Both Eqs. (5.29) and (5.32) are plotted versus the expected signal strength $\langle N_1 \rangle = \langle N_2 \rangle = \langle N \rangle$ in Fig. 5.6 for comparison.

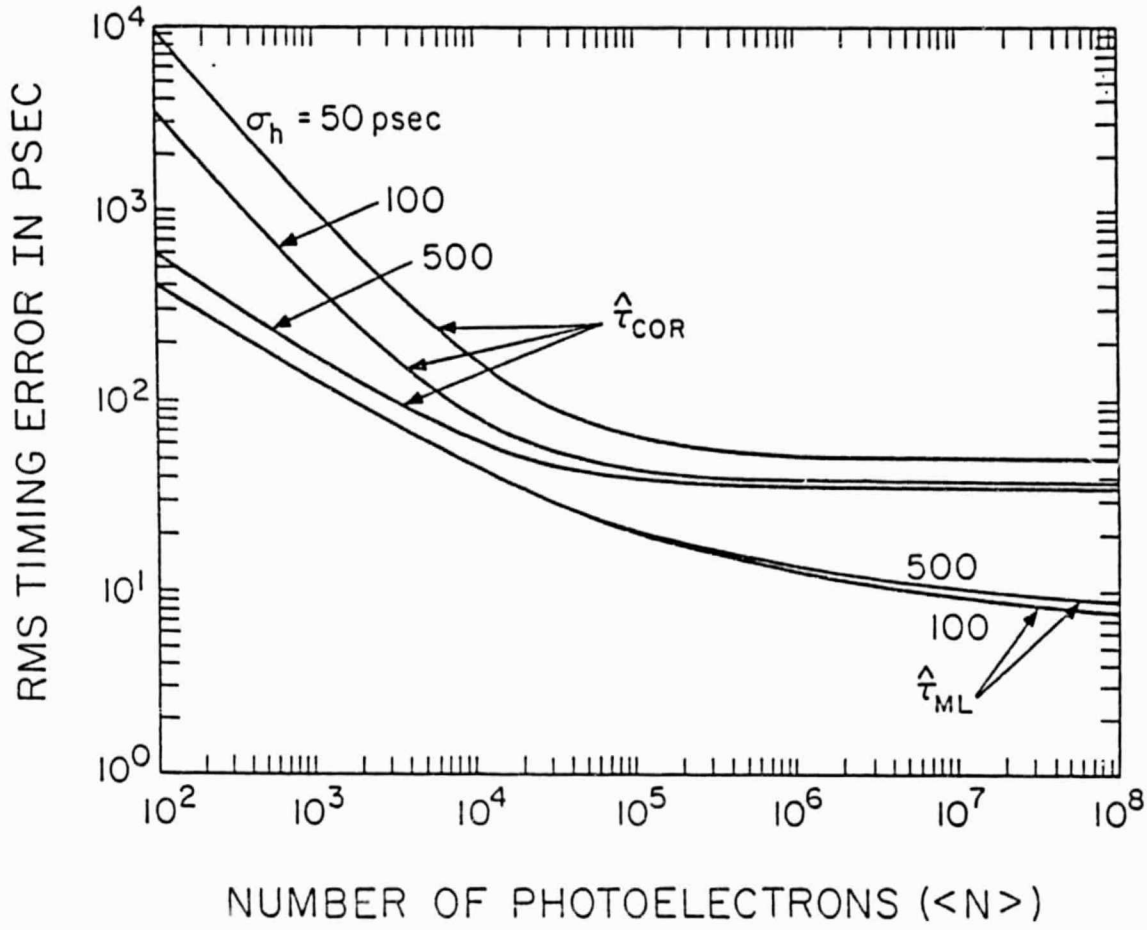

Fig. 5.6. Comparison of the RMS differential timing errors using the correlation estimator ($\hat{\tau}_{COR}$) and Maximum-Likelihood (ML) estimator ($\hat{\tau}_{ML}$) for pulse reflections from an infinite flat diffuse target. (z = 500 km, θ_T = 0.1 mrad, σ_f = 16.7 psec, ϕ = 0.5°, λ_1 = 0.355 μm, λ_2 = 1.064 μm, A_R = 0.1 m^2, $K_1 = 9K_2 = 10^5$)

In the shot-noise-limited region ($\langle N \rangle \ll K_i$), the RMS timing errors of the ML estimator have an $\langle N \rangle^{-1/2}$ dependence as expected and are quite insensitive to the change in B_R. Whereas, the rms timing errors of the correlation estimator when $B_R \gg B_S$ (σ_h = 50 psec, 100 psec) have an $\langle N \rangle^{-1}$ dependence due to the dominance of the second-order shot-noise error contribution. When B_R is reduced (σ_h = 500 psec), the second-order contribution is less dominant and the overall timing error decreases as $\langle N \rangle^{-1/2}$. In fact, the timing accuracy of the correlation estimator is comparable to that of the ML estimator when B_R is chosen properly.

In the speckle-limited region ($\langle N \rangle \gg K_i$), however, we cannot gain much improvement by reducing the receiver bandwidth because speckle-noise contribution is much less sensitive to the change of B_R. In this region, the ML estimator will perform consistently better than the correlation estimator.

5.4 Reflections from the Flat Cube-Corner Reflector (CCR) Arrays

As the second example, we now consider a flat CCR array. The geometry and the orientation of the array is shown graphically in Fig. 5.7. The array has p CCR's in each row and q CCR's in each column. We shall assume the spacing d to be uniform between adjacent CCR's in each row and in each column on the array, and the laser beam to be incident onto the target at an angle ϕ with respect to the target normal. The orientation of the array is such that the CCR's in each column are at the same range (height). This target configuration is similar to the CCR arrays on the Geodetic Earth Orbiting Satellite 1 and 2 (Geos-1 and -2) and the lunar arrays.

For typical target ranges, the surface area of the CCR array is usually much smaller than the size of the laser footprint, and hence, we shall

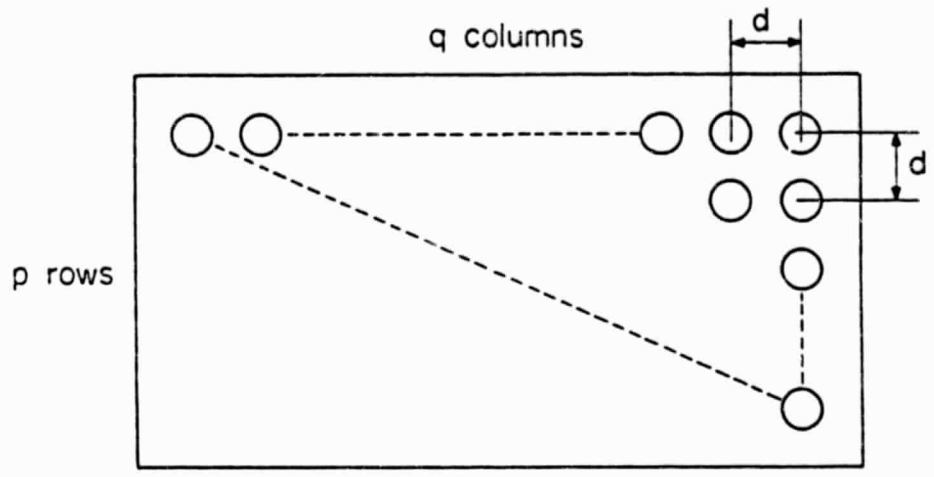

(a) bottom view

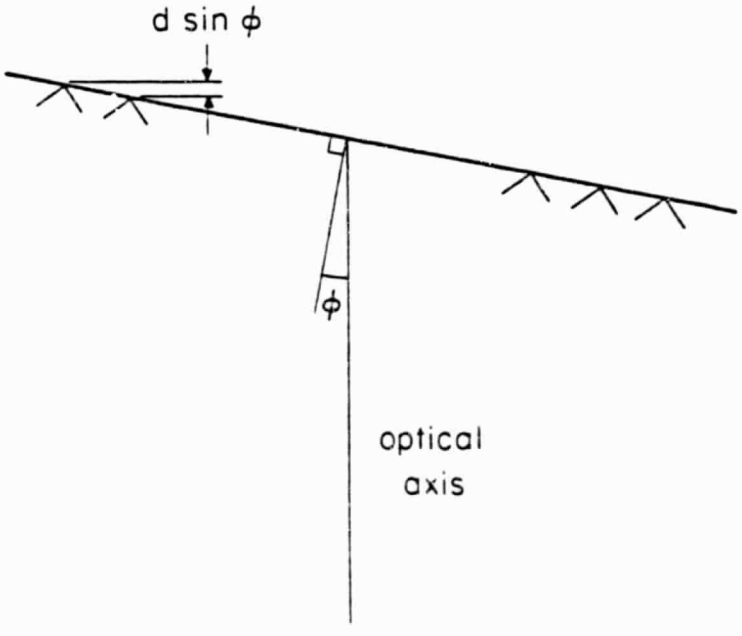

(b) side view

Fig. 5.7. Geometry of the flat CCR array.

assume the laser cross-section ($|a|^2$) within the illuminated array to be uniform. Furthermore, we shall also assume the power reflectivities (β_{r_m}'s) and the effective reflecting surface areas (A_m's) of all the CCR's on the array to be equal.

The total reflected electric field from a CCR array consists of the coherent additions of the field components due to the reflections from all the illuminated CCR's within the laser footprint. Due to the facts that the array is rough on the optical scale and that the range is continually changing, there will be slight variations in the apparent positions of the CCR's on the array. If the CCR array is macroscopically flat and normal to the optical axis ($\phi = 0°$), the distances traveled by the reflected field components back to the receiver plane may differ by several laser wavelengths. As a consequence, the phase angles of the field components are random and mutually independent. This effect generates a partially developed speckle field. The dephased components will introduce coherent interference in the received signal power. On the other extreme, if the flat array is illuminated at a non-normal incidence angle so that the range difference between any two CCR's on the array is larger than the width of the transmitted laser pulse, then the received signal will consist of a train of non-overlapping pulses. In this case, the effect of coherent interference is negligible. In practice, the amount of interference will be somewhere between these two extremes. As expected, the partially developed speckle will introduce an additional error in the range measurements.

The effect of coherency is given in Chapter 3 by the coherent interference factor $\gamma(\underline{\rho}_m, \underline{\rho}_n)$. The parameter which is most sensitive to this effect is the speckle SNR (K_i). Because K_i for satellite altitude ranging (Eq. (3.21)) is independent of the optical wavelengths, we shall let

$K_1 = K_2 = K$. By substituting Eq. (3.26) into Eq. (3.21) and using the above assumptions on the target parameters, K can be expressed as

$$K = \frac{M^2}{\sum_{\substack{m=1 \\ m\neq n}}^{M} \sum_{n=1}^{M} \gamma(\underline{\rho}_m, \underline{\rho}_n)} = \frac{M^2}{\sum_{\substack{m=1 \\ m\neq n}}^{M} \sum_{n=1}^{M} \exp\left[-\left(\frac{\psi(\underline{\rho}_m) - \psi(\underline{\rho}_n)}{2\sigma_f}\right)^2\right]} \tag{5.33}$$

where $M=p\cdot q$ is the total number of CCR's in the array, and $\psi(\underline{\rho}_m) - \psi(\underline{\rho}_n)$ is given by Eq. (3.29), and $\underline{\rho}_m$ is the transverse coordinate vector of the mth CCR measured with respect to the center of the laser cross-section. Since the range delay due to beam wave curvature effects is small, Eq. (5.33) can be simplified to give

$$K \cong \frac{M^2}{\sum_{\substack{m=1 \\ m\neq n}}^{M} \sum_{n=1}^{M} \exp\left[-\left(\frac{\xi(\underline{\rho}_m) - \xi(\underline{\rho}_n)}{c\sigma_f}\right)^2\right]} \quad . \tag{5.34}$$

For the target configuration given by Fig. 5.7, K can be expressed in terms of the CCR's spacing and incidence angle:

$$K = \frac{(pq)^2}{2p^2 \sum_{m=1}^{q} (q-m)e^{-(m\beta)^2} + p^2q - pq} \tag{5.35}$$

where

$$\beta = d \sin\phi / (c\sigma_f) \quad . \tag{5.36}$$

β is the ratio between the range difference among CCR's on adjacent columns and the transmitted pulse width. When $\beta = 0$ (normal incidence), Eq. (5.35) reduces to

$$K = pq / (pq-1) = M / (M-1) \qquad \text{for } \beta = 0. \tag{5.37}$$

In this case, K is always between 1 and 2 for $M > 1$. This low speckle SNR makes speckle averaging impossible and is a consequence of the relatively small area of the CCR array. In other words, the speckle correlation area of the reflected field at the receiver plane is so large that only a few speckle cells fall within the receiver aperture. On the other hand, when $d \sin \phi$ is much longer than the transmitted pulse width ($c\sigma_f$), Eq. (5.35) can be reduced to

$$K = pq / (p-1) = M / (p-1), \qquad \text{for } \beta \gg 1. \tag{5.38}$$

According to Eq. (5.38), K can be very large if the CCR array consists of many widely spaced columns and only a few rows. In fact, if $p = 1$, then $K \to \infty$ because in this case the reflected pulses from each CCR do not overlap in time at the receiver so there is no speckle induced interference. In reality, however, we would expect p and q to be equal and on the order of 5 to 10. Consequently, K will be somewhere between 1 and 10. Eq. (5.35) is plotted in Fig. 5.8 versus the horizontal spacing (d) of the CCR's within the array for different incidence angles and for p=4 and q=3.

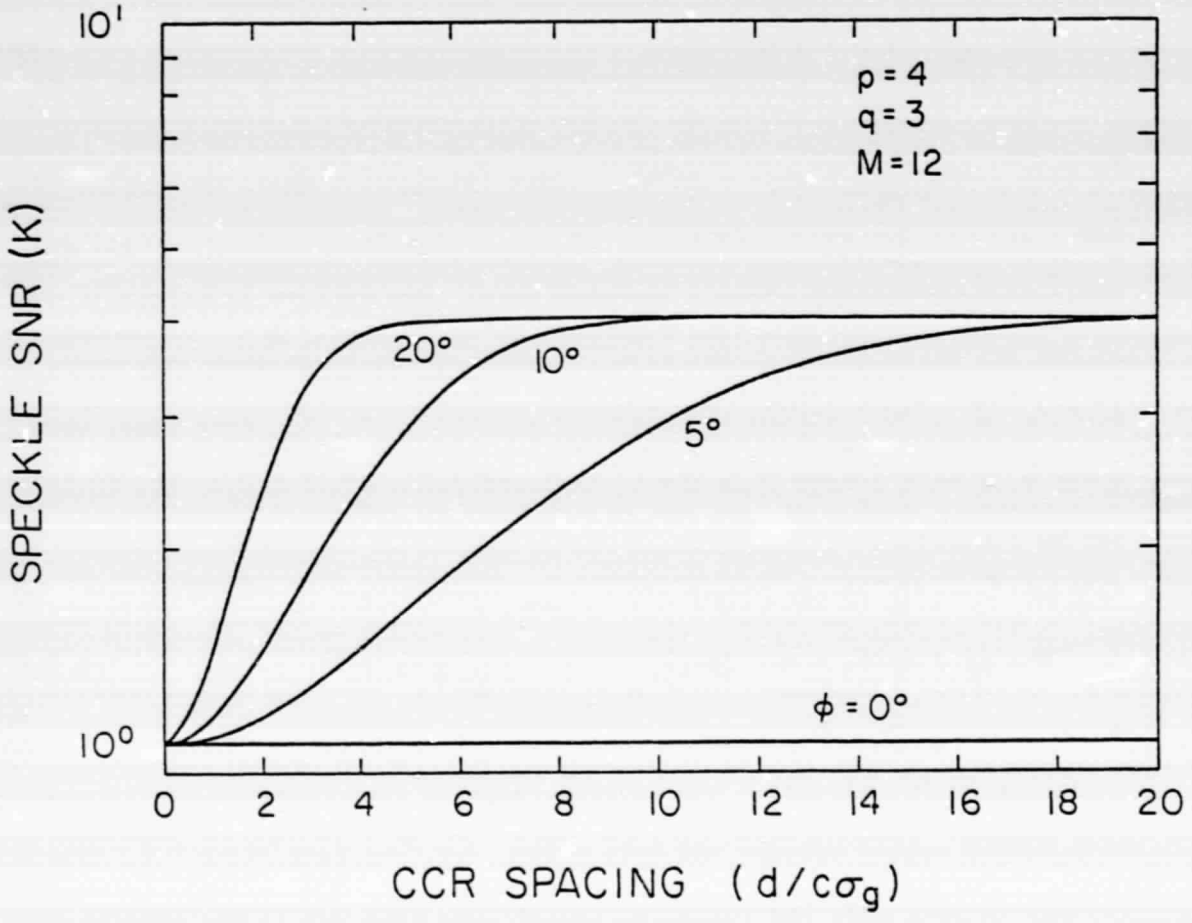

Fig. 5.8. Speckle SNR (K) versus relative spacing of the CCR array ($d/c\sigma_g$). Note that the relative range difference between CCR's at adjacent columns is ($d/c\sigma_g$) sin ϕ where $c\sigma_g$ is the point target pulse length. (z = 500 km, θ_T = 0.1 mrad, σ_f = 33 psec, σ_h = 33 psec, $c\sigma_g$ = 1.4 cm, p = 4, q = 3)

C-2

The mean detected signal bandwidth can be calculated by using Eqs. (3.4), (3.24), (5.12) and (5.19). By neglecting beam curvature effects, the signal bandwidth has the form

$$B_S^2 = B_{PT}^2 (1 - \alpha_d) = \frac{1}{2\sigma_g^2} (1 - \alpha_d) \tag{5.39}$$

where

$$\alpha_d = \frac{2 \sum_{m=1}^{M} \sum_{n=1}^{M} \left[\frac{\xi(\rho_m) - \xi(\rho_n)}{c\sigma_g} \right]^2 \exp\left[- \left[\frac{\xi(\rho_m) - \xi(\rho_n)}{c\sigma_g} \right]^2 \right]}{\sum_{m=1}^{M} \sum_{n=1}^{M} \exp\left[- \left[\frac{\xi(\rho_m) - \xi(\rho_n)}{c\sigma_g} \right]^2 \right]} . \tag{5.40}$$

$(1-\alpha_d)$ is the bandwidth degradation factor and it is always between 0 and 1. For normal incidence, the reflected signal components from different CCR's will overlap in time almost perfectly. Consequently, α_d is essentially zero, and the bandwidth of the reflected signal from the CCR array is the same as that from a point target. When the range difference between CCR's is on the same order of magnitude as the width of the point target response ($c\sigma_g$), the signal components overlap partially and the total signal pulse is broadened. In this case, we expect degradation in the detected signal bandwidth, and the amount of degradation depends on how much the range difference between CCR's differs from $c\sigma_g$. When the range difference is longer than $c\sigma_g$, the detected signal consists of a train of non-overlapping pulses reflected from different CCR's. Although the detected signal is broadened in time, the bandwidth is still the same as that for a single pulse.

The mean detected signal bandwidth for the configuation given in Fig. 5.7 can be expressed as

$$B_S^2 = \frac{1}{2\sigma_g^2}\left[1 - \frac{4\sum_{m=1}^{q}(m\beta_1)^2 (q-m)\, e^{-(m\beta_1)^2}}{2\sum_{m=1}^{q}(q-m)\, e^{-(m\beta_1)^2} + q}\right] \tag{5.41}$$

where

$$\beta_1 = d \sin\phi / c\sigma_g \tag{5.42}$$

is the ratio between the range difference among CCR's on adjacent columns and the width of the point target response. Eq. (5.41) is plotted in Fig. 5.9 versus the spacing of the array for different incidence angles ϕ and for p=4 and q=3. As predicted, the maximum bandwidth is obtained when ϕ=0 or when the range difference (d sin ϕ) is large compared with $c\sigma_g$. When d sin ϕ is on the same order of magnitude as $c\sigma_g$, however, the bandwidth is degraded by almost a factor of 2.

The rms bandwidth of the speckle variance (B_{SP}) and the cross-bandwidth (B_X) can be calculated by similar procedures. However, they both involve multiple summations, and numerical computations are usually required. Numerical results for B_{SP} and B_X are plotted in Fig. 5.10 and 5.11, respectively, for the same parameters used in Fig. 5.9. Both B_{SP} and B_X have characteristics similar to that of the signal bandwidth B_S.

The timing performance when ranging to the CCR array can now be calculated by using the above results for the speckle SNR and the various bandwidth parameters. Because the speckle noise contamination on the

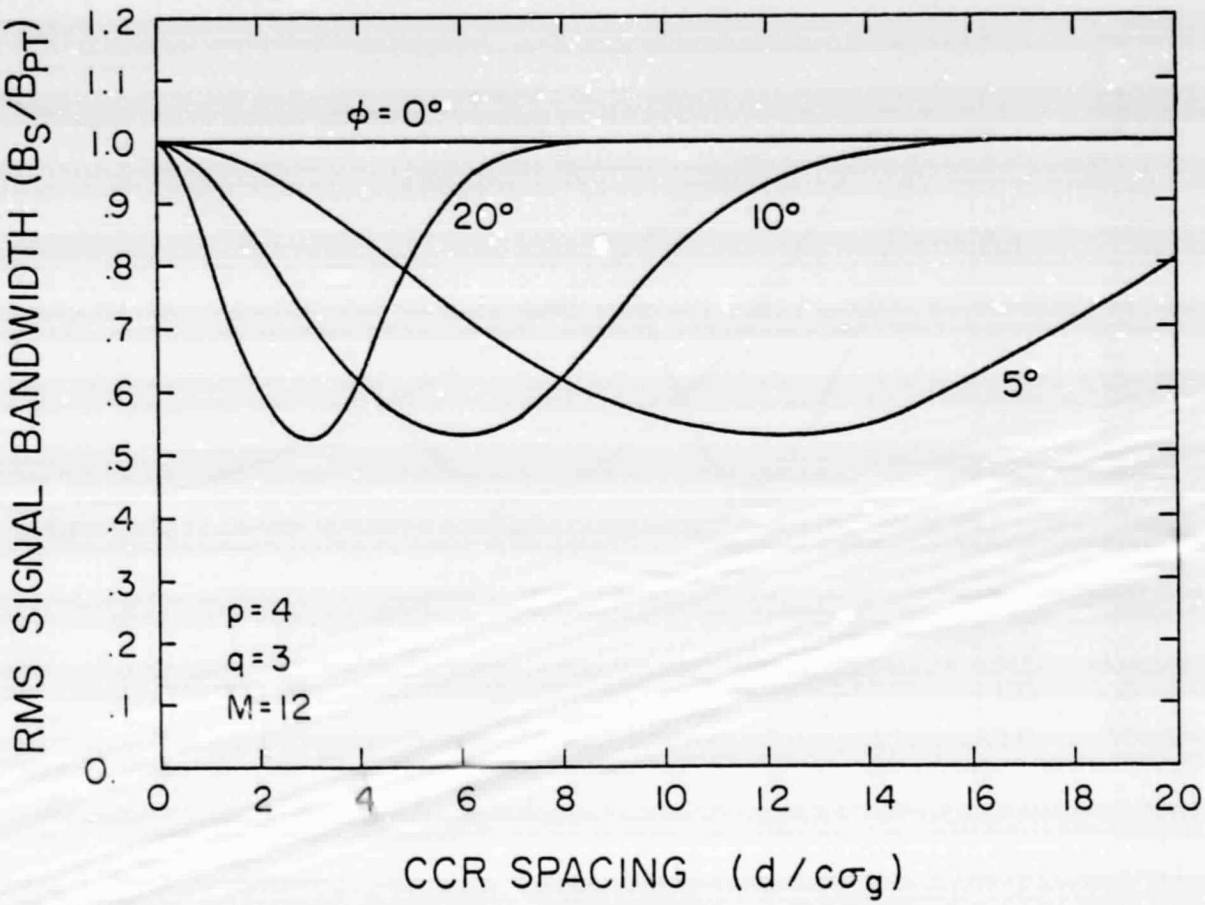

Fig. 5.9. Normalized RMS detected signal bandwidth (B_S/B_{PT}) versus relative spacing of the CCR array ($d/c\sigma_g$). Note that the relative range difference between CCR's at adjacent columns is ($d/c\sigma_g$) sin ϕ where $c\sigma_g$ is the point target pulse length. (z = 500 km, θ_T = 0.1 mrad, σ_f = 33 psec, σ_h = 33 psec, $c\sigma_g$ = 1.4 cm, p = 4, q = 3)

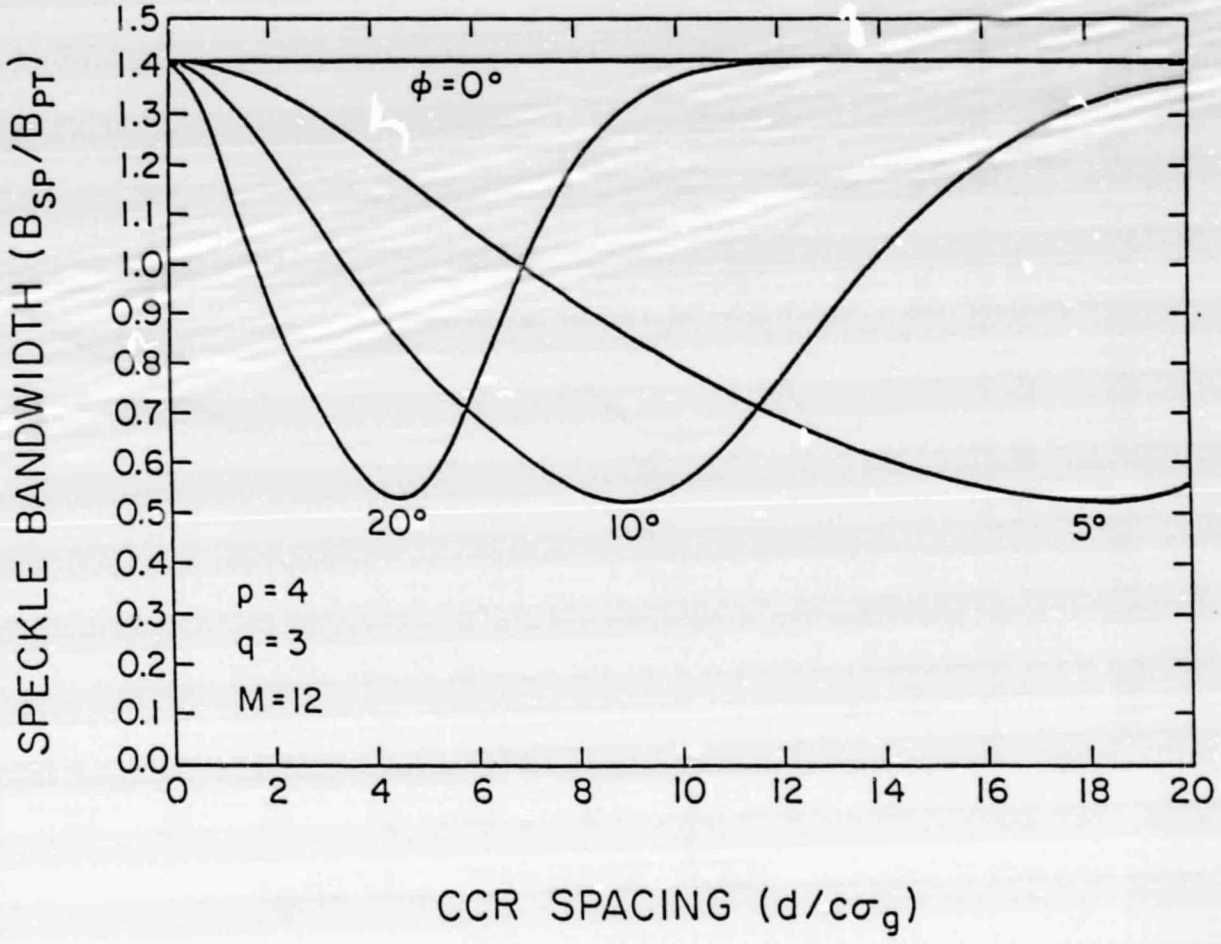

Fig. 5.10. Normalized RMS bandwidth of the speckle variance (B_{SP}/B_{PT}) versus relative spacing of the CCR array ($d/c\sigma_g$). Note that the relative range difference between CCR's at adjacent columns is ($d/c\sigma_g$) sin ϕ where $c\sigma_g$ is the point target pulse length. (z = 500 km, θ_T = 0.1 mrad, σ_f = 33 psec, σ_h = 33 psec, $c\sigma_g$ = 1.4 cm, p = 4, q = 3)

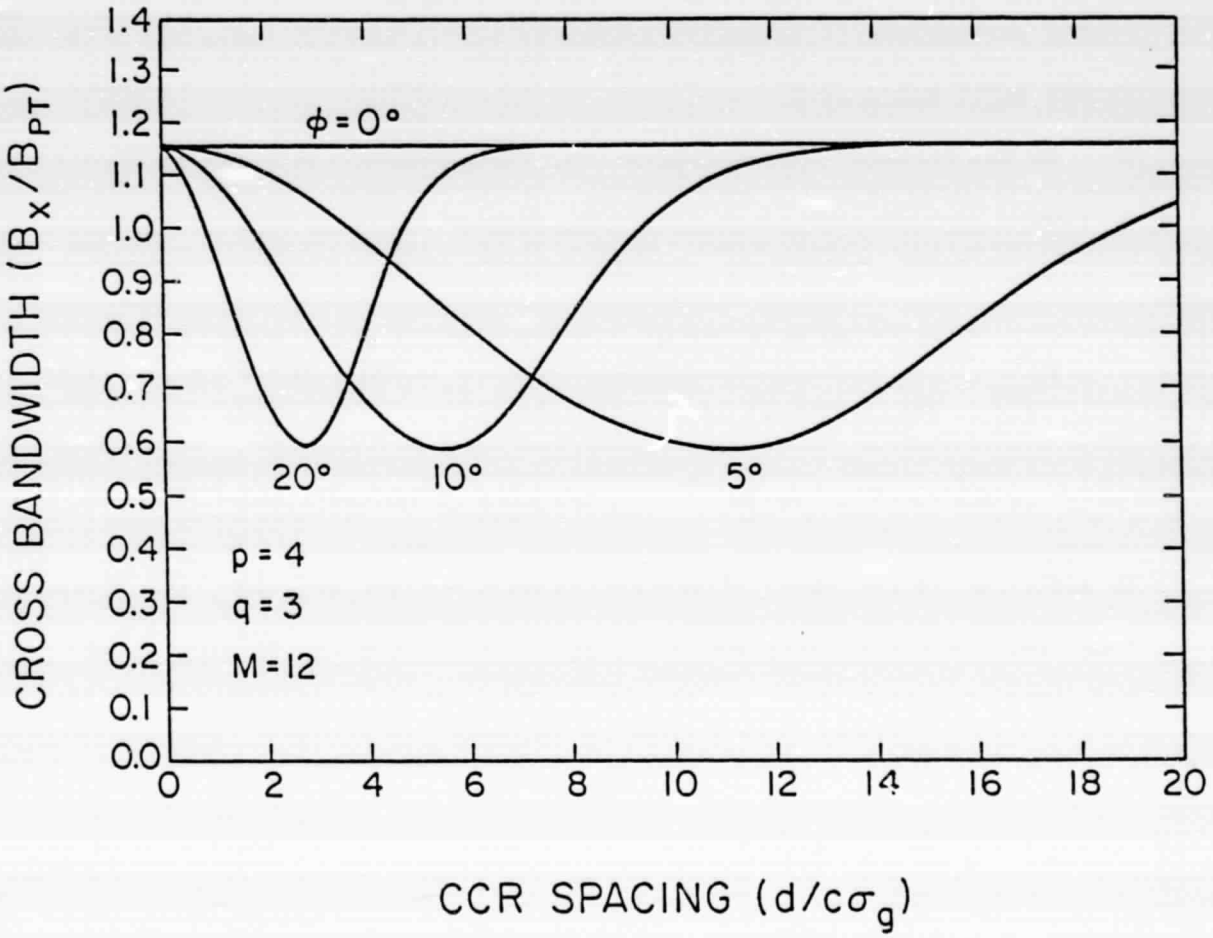

Fig. 5.11. Normalized RMS cross-bandwidth (B_X/B_{PT}) versus relative spacing of the CCR array ($d/c\sigma_g$). Note that the relative range difference between CCR's at adjacent columns is ($d/c\sigma_g$) sin ϕ where $c\sigma_g$ is the point target pulse length. (z = 500 km, θ_T = 0.1 mrad, σ_f = 33 psec, σ_h = 33 psec, $c\sigma_g$ = 1.4 cm, p = 4, q = 3)

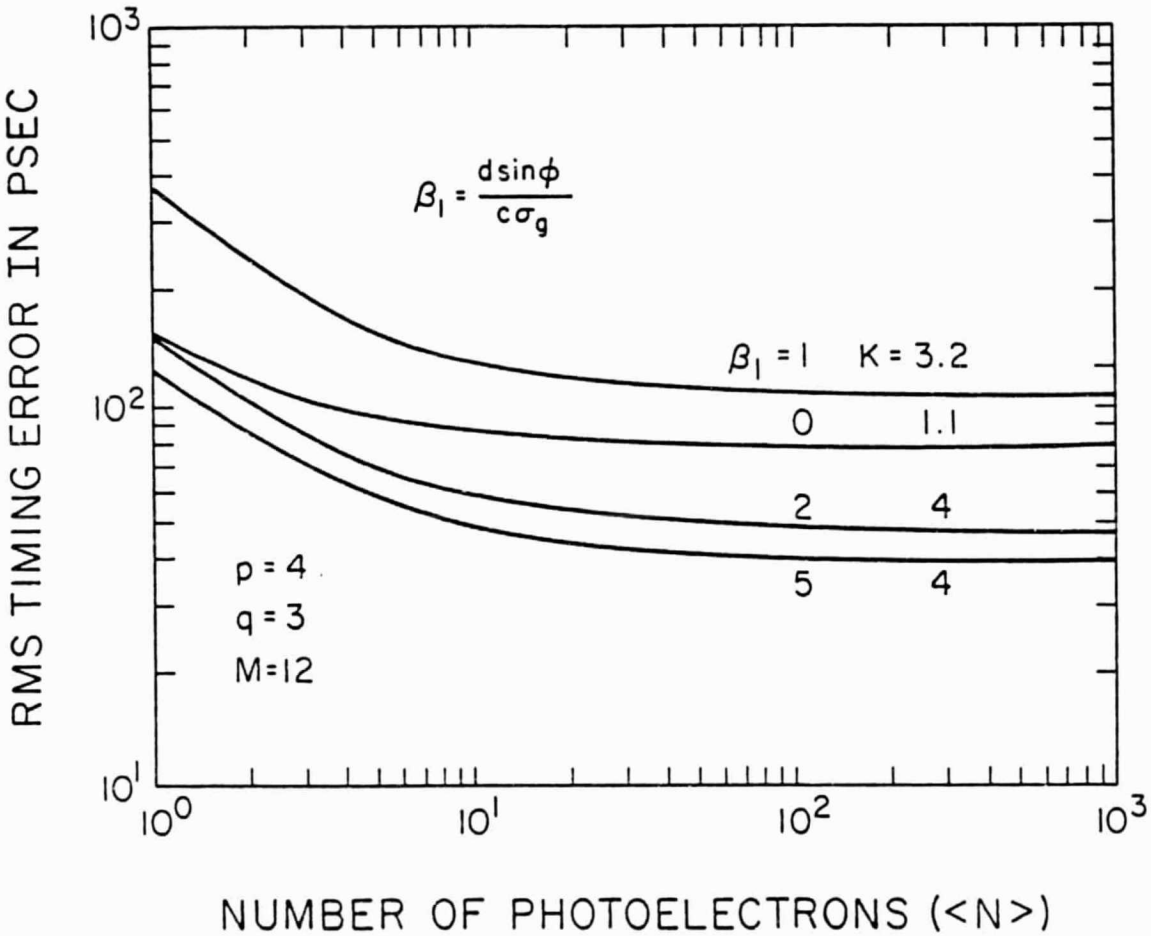

Fig. 5.12. RMS differential timing error versus received signal strength for pulse reflections from a CCR array. Note that β_1 is the relative range difference between CCR's at adjacent columns. (z = 500 km, θ_T = 0.1 mrad, σ_f = 33 psec, σ_h = 33 psec, $c\sigma_g$ = 1.4 cm, p = 4, q = 3)

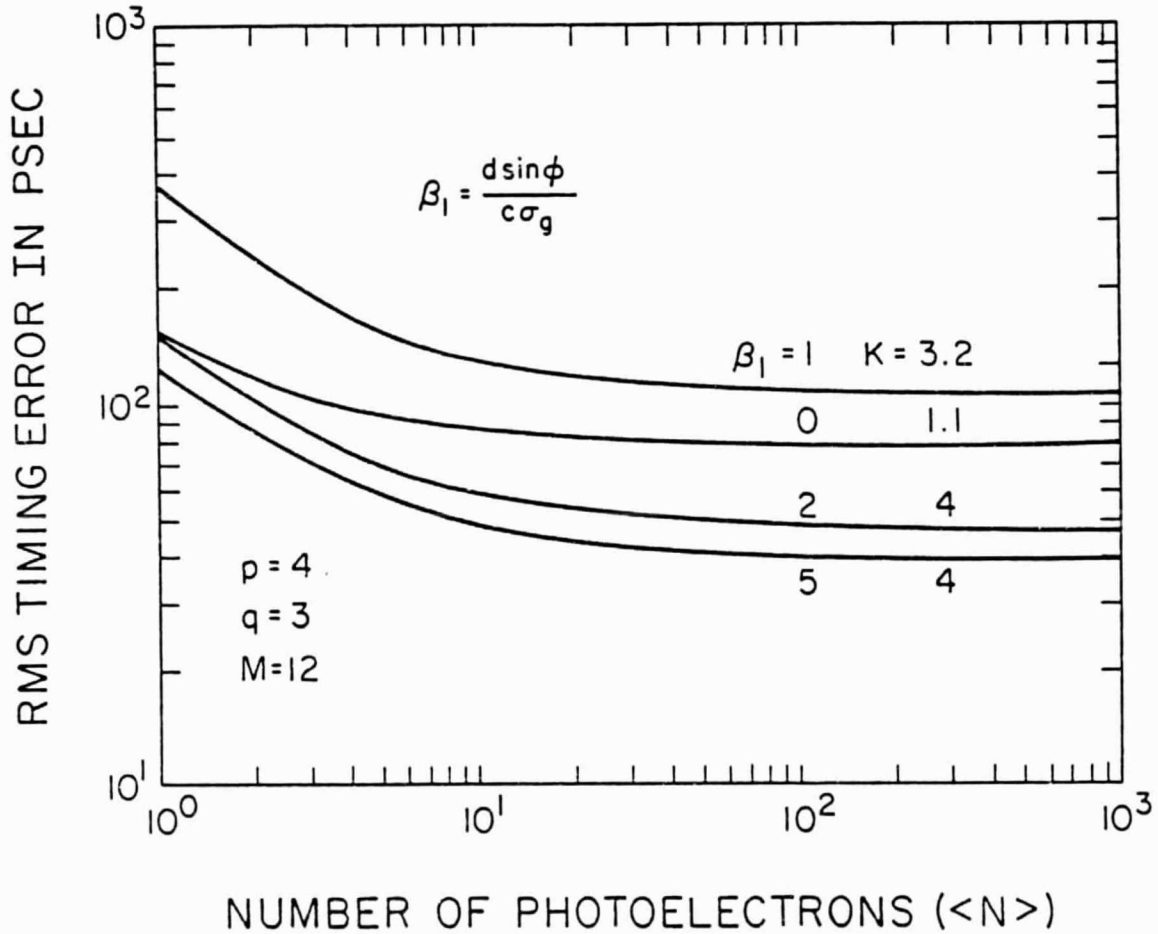

Fig. 5.12. RMS differential timing error versus received signal strength for pulse reflections from a CCR array. Note that β_1 is the relative range difference between CCR's at adjacent columns. (z = 500 km, θ_T = 0.1 mrad, σ_f = 33 psec, σ_h = 33 psec, $c\sigma_g$ = 1.4 cm, p = 4, q = 3)

In order to improve the ranging accuracy, very narrow transmitted pulses and receivers of very high resolution must be used. One important consequence is that the detected signal strength has very little effect on ranging accuracy. Thus, the design of two-color satellite ranging systems is dominated by the transmitted pulselength, pulse repetition rate and receiver bandwidth and not the detected signal strength.

The above results can give us some insights on the timing accuracy when ranging to Lageos. Lageos is a 60-cm diameter sphere that is covered by 426 CCR's. The spacing between adjacent CCR's is on the order of 10° arc-length with respect to the center of the satellite [Fitzmaurice et al., 1977]. This corresponds to about 5.2 cm. The corresponding range difference between adjacent CCR's is approximately 4.5 mm, which is typically much smaller than the transmitted pulsewidth. Consequently, K is small, and the ranging accuracy to Lageos is also limited by the width of the detected signal pulse.

5.5 Pulse Reflections from the Ocean

The reflection of laser pulses from the ocean is due mainly to scattering by randomly distributed specular points on the ocean surface. These reflected pulses are broadened due to the differences in wave height ($\xi(\underline{\rho})$) at various points within the laser footprint. The wave height at any given point on the ocean is the result of many wave components that have been generated by the wind in different regions and have propagated to the point of observation. Therefore, for footprint area which is large compared to the longest waves on the ocean, the central limit theorem can be used to argue that the surface profile of the ocean at the point of observation is Gaussian distributed. Under this assumption, the expected received signal

can be calculated by taking the expectation of Eq. (3.1) over the probability distribution of the Gaussian surface profile ξ. In Fig. 5.13, the mean received signal by using the Gaussian ocean model is plotted for five different laser beam divergence. As the beam divergence increases, the trailing edge of the pulse is broadened by the wavefront curvature effects, and the return pulse becomes asymmetric.

The pulse shape computed using the Gaussian assumption will accurately predict the actual pulse shapes whenever the laser footprint is large compared to the ocean wave periods. However, when the footprint is small, the local probability distribution of surface profile within the footprint can be considerably different from a Gaussian. Sea wave records often reveal a sinusoidal or trochoidal profile for the dominant long-period waves. In these areas, the surface profile is more suitably modeled as a large amplitude sinusoid or trochoid wave with superimposed small amplitude disturbances (capillary waves) of short correlation length. For the one-dimensional sinusoidal wave model, the ocean surface profile can be represented by [Kinsman, 1965]

$$\xi(\underline{\rho}) = A \cos \left(\frac{2\pi}{\Lambda} x + \phi_p \right) + \xi_1(\underline{\rho}) \tag{5.45}$$

where A is the amplitude of the sinusoidal wave, Λ is its period, ϕ_p is the phase angle, and $\xi_1(\underline{\rho})$ is the small-scale disturbances. In Fig. 5.14, an expected received signal using this model is computed numerically for the case when the laser is pointed off nadir by 1°. The results reveal multiple glints (high frequency components) due to the specular reflections from successive wave crests and wave troughs. Crest reflections are responsible for

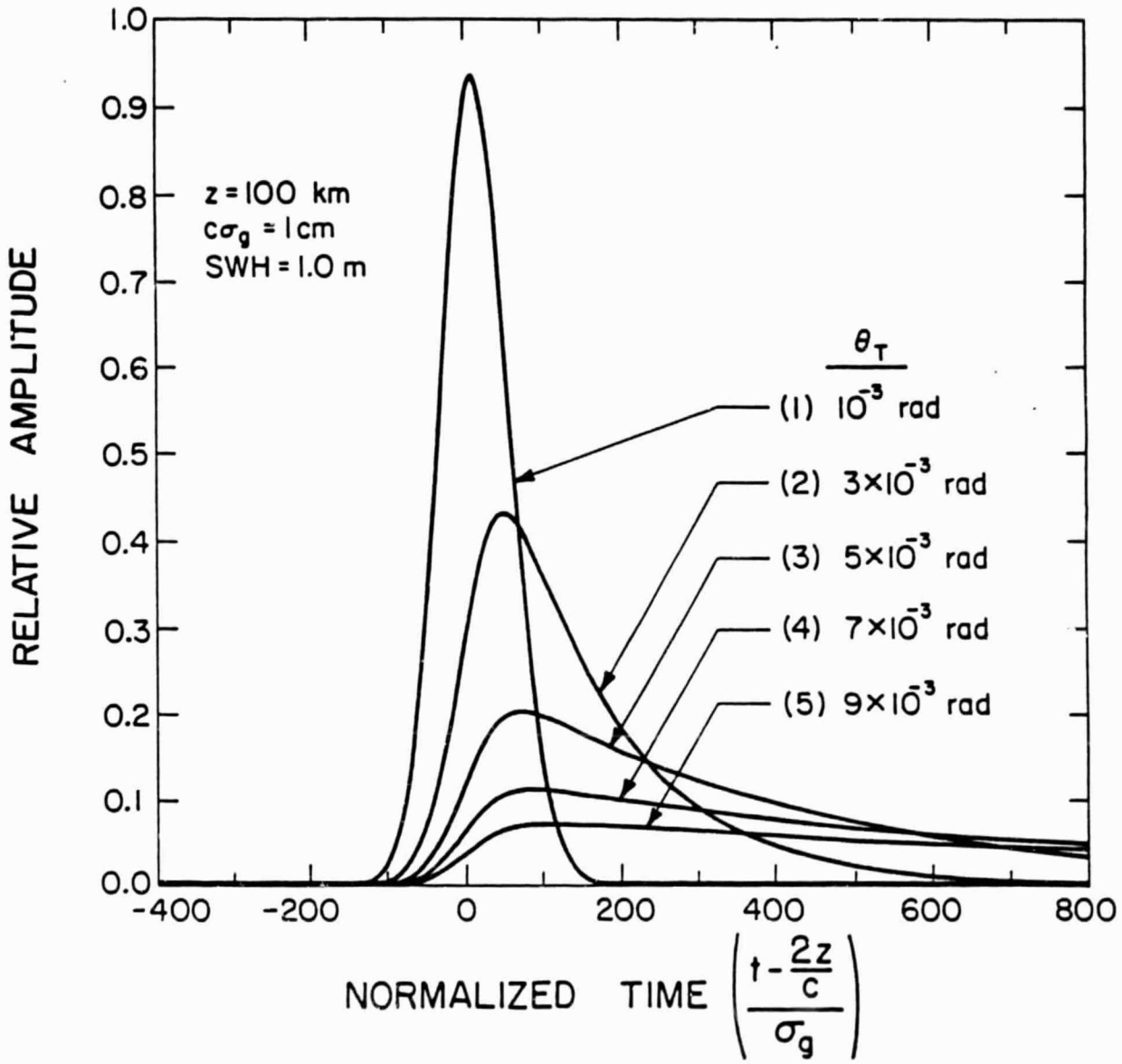

Fig. 5.13. Mean received pulse shapes for reflection from an ocean whose wave height is Gaussian distributed. The laser altimeter is pointed at nadir, and the significant wave height (SWH) is 1 m.

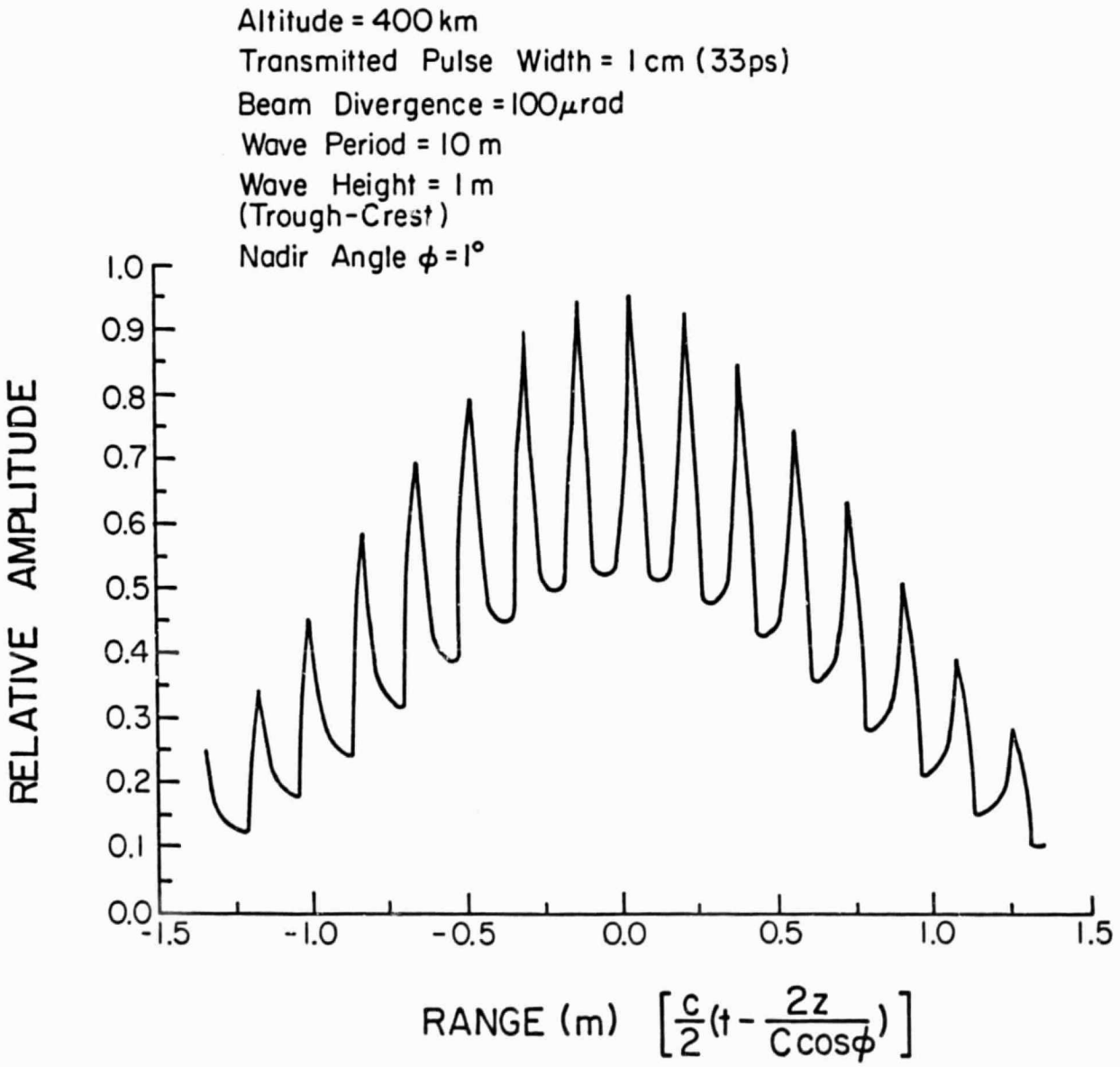

Fig. 5.14. Mean received pulse shape for reflection from an ocean that has sinusoidal profile. The nadir angle is 1°. The wave height is 1 m (trough to crest) and the wave period is 10 m. The structure is caused by the reflections from successive wave crests and troughs.

the sharp peaks in the first half of the pulse, while trough reflections are responsible for the structure in the second half. The sharpness of the glints is related to the beam divergence and the ocean parameters.

Because of the dynamic and random nature of the ocean, the surface profile is not a perfect Gaussian or sinusoid. The Gaussian model and the sinusoidal wave model can be viewed as the two extremes. The actual received pulse shapes are likely to lie somewhere between the broad, smooth pulse and the highly structured shapes. However, the received pulses are expected to exhibit fine scale structure due to strong specular reflections within the laser footprint. This structure, which increases the signal bandwidth, is an important factor in achieving picosecond timing accuracies.

To illustrate the effects of surface profile on bandwidth (or the sharpness of the glints), the MS bandwidth is calculated in Appendix B for a Gaussian distributed profile under the conditions that the profile correlation length (L) is much less or greater than the footprint radius. The results are

$$B_S^2 = \begin{cases} \Delta_1 \,/\, \sigma_g^{\,2} & L \geq z \tan \theta_T \\ \\ \Delta_1 \,/\, (\sigma_g^2 + 4\, \sigma_\xi^2/c^2) & L \ll z \tan \theta_T \quad , \end{cases} \tag{5.46}$$

where

$$\Delta_1 = \frac{\gamma_1\, e^{-\gamma_1^2}}{\sqrt{\pi}\ \mathrm{erfc}(\gamma_1)} - \gamma_1^2 \quad , \tag{5.47}$$

$$\gamma_1 = \begin{cases} \dfrac{c\sigma_g}{2\ z\ \tan\ \theta_T}\ (2\ \sigma_\xi^2/L^2 + \tan^2\theta_T)^{-1/2} & L \geq z\ \tan\ \theta_T \\ \\ \dfrac{c}{2\ z\ \tan^2\theta_T}\ (\sigma_g^2 + 4\ \sigma_\xi^2/c^2)^{1/2} & L \ll z\ \tan\ \theta_T \end{cases} \tag{5.48}$$

and σ_ξ is the RMS wave height of the ocean. When $L \geq z \tan \theta_T$, if the received pulse shapes are dominated by beam curvature ($\tan \theta_T$ is large) or surface effects (σ_ξ is large), γ_1 will be small. If the curvature and surface effects are negligible, γ_1 will be large. On the other hand, when $L \ll z \tan \theta_T$, γ_1 will be large when σ_ξ is large. In these two limiting cases, γ_1 simplifies to

$$\Delta_1 = \begin{cases} \dfrac{\gamma_1}{\sqrt{\pi}} & \gamma_1 \ll 1 \\ \\ \dfrac{1}{2} & \gamma_1 \gg 1 \quad . \end{cases} \tag{5.49}$$

The other parameters such as the MS speckle bandwidth B_{SP}^2 and the cross bandwidth B_X^2 can also be calculated using a similar procedure. The results are tabulated in Table 5.1.

To evaluate the expression for the timing error, we shall use the assumption that $c\sigma_g \ll \sigma_\xi < z \tan \theta_T$. For large footprints the solution for

TABLE 5.1.

EXPRESSIONS OF THE QUANTITIES WHICH ARE NEEDED FOR EVALUATING THE TIMING VARIANCE OF THE OCEAN-REFLECTED PULSES BY A CORRELATION RECEIVER

	SMALL FOOTPRINT ($L \gg z \tan \theta_T$)	LARGE FOOTPRINT ($L \ll z \tan \theta_T$)
Δ_i	$\dfrac{\gamma_i e^{-\gamma_i^2}}{\sqrt{\pi}\,\mathrm{erfc}(\gamma_i)} - \gamma_i^2$	$i = 1,2,3$
$\langle B^2 \rangle$	$\dfrac{\Delta_1}{\sigma_g^2}$	$\dfrac{\Delta_1}{\left(\sigma_g + \frac{4}{c^2}\sigma_\xi^2\right)}$
$\langle B_{SP} \rangle^2$	$\dfrac{2\Delta_2}{\sigma_g^2}$	$\dfrac{\Delta_2}{\left(\frac{\sigma_g^2}{2} + \frac{4\sigma_\xi^2}{c^2}\right)}$
$\langle B_x \rangle^2$	$\dfrac{4\Delta_3}{3\sigma_g^2}$	$\dfrac{\Delta_3}{\left(\frac{3}{4}\sigma_g^2 + \frac{4\sigma_\xi^2}{c^2}\right)}$
γ_1	$\dfrac{c\sigma_g}{2z \tan \theta_T}\left(\dfrac{2\sigma_\xi^2}{L^2} + \tan^2 \theta_T\right)^{-1/2}$	$\dfrac{c}{2z \tan^2 \theta_T}\left(\sigma_g^2 + \dfrac{4\sigma_\xi^2}{c^2}\right)^{1/2}$
γ_2	$\dfrac{c\sigma_g}{2\sqrt{2}\, z \tan \theta_T}\left(\dfrac{\sigma_\xi^2}{L^2} + \tan^2 \theta_T\right)^{-1/2}$	$\dfrac{c}{2z \tan^2 \theta_T}\left(\dfrac{\sigma_g^2}{2} + \dfrac{4\sigma_\xi^2}{c^2}\right)^{1/2}$
γ_3	$= \dfrac{\sqrt{3}\, c\sigma_g}{4z \tan \theta_T}\left(\dfrac{3\sigma_\xi^2}{L^2} + \dfrac{\tan^2 \theta_T}{2}\right)^{-1/2}$	$= \dfrac{c}{\sqrt{2}\, z \tan^2 \theta_T}\left(\dfrac{3}{4}\sigma_g^2 + \dfrac{4\sigma_\xi^2}{c^2}\right)^{1/2}$
$\langle \int d\omega \lvert \phi_S(\omega) \rvert^2 \rangle$	$\pi \gamma_1 e^{\gamma_1^2}\,\mathrm{erfc}(\gamma_1)\,\sigma_g^{-1}$	$\pi \gamma_1 e^{\gamma_1^2}\,\mathrm{erfc}(\gamma_1)\left(\sigma_g^2 + \dfrac{4\sigma_\xi^2}{c^2}\right)^{-1/2}$
$\langle \alpha_3 \rangle$	$= \sqrt{2}$	$= 1$
$\langle \alpha_4 \rangle$	$= \dfrac{2}{\sqrt{3}}$	$= 1$
$\langle \alpha_1 \rangle, \langle \alpha_2 \rangle$	$1 \le \langle \alpha_1 \rangle, \langle \alpha_2 \rangle \le 2$	

$L \ll z \tan \theta_T$ is probably the most applicable. The MS timing error in this case is

$$\sigma_{\tau_{COR}}^2 \geq \left(\frac{1}{\langle N_1 \rangle} + \frac{1}{\langle N_2 \rangle}\right) \frac{4\alpha_1 \sigma_\xi^2}{c^2} + \left(\frac{1}{K_1} + \frac{1}{K_2}\right) \frac{4\alpha_2 \sigma_\xi^2}{c^2} \qquad L \ll z \tan \theta_T. \tag{5.50}$$

Since the second-order errors are not included, so Ineq. (5.50) only serves as the lower bound of the timing error. Because the ocean height is typically of the order of tens of centimeters or greater, σ_ξ/c will usually be a few nanosecond or more. Consequently, picosecond timing accuracy is probably not feasible when the footprint is large.

When the laser footprint is small, the solution for $L \geq z \tan \theta_T$ is probably the most applicable, and the MS timing error in this case is

$$\sigma_{\tau_{COR}} \simeq \left(\frac{1}{\langle N_1 \rangle} + \frac{1}{\langle N_2 \rangle}\right) \frac{4}{3\sqrt{3}\, B_S^2} + \left(\frac{1}{K_1} + \frac{1}{K_2}\right) \frac{\sqrt{2}}{2B_S^2}$$

$$+ \frac{\sqrt{2}\,\sigma_g}{B^4} \left[\frac{\sigma_h^{-2} - B_S^2}{\langle N_1 \rangle \langle N_2 \rangle \sigma_h} + \frac{\sqrt{2}\,(\sigma_g^{-2} - 2B_S^2)}{K_1 K_2 \sigma_g} \right. \tag{5.51}$$

$$\left. + \frac{\frac{2}{\sqrt{3}} \left(\frac{1}{\sigma_h^2 + \sigma_f^2/2} - \frac{\sqrt{2}}{3} B_S^2 \right)}{\langle N_1 \rangle K_2 \left(\sigma_h^2 + \sigma_f^2/2\right)^{1/2}} + \frac{\frac{2}{\sqrt{3}} \left(\frac{1}{\sigma_h^2 + \sigma_f^2/2} - \frac{\sqrt{2}}{3} B_S^2 \right)}{\langle N_2 \rangle K_1 \left(\sigma_h^2 + \sigma_f^2/2\right)^{1/2}} \right]$$

$L \geq z \tan \theta_T$

where

$$B_S \cong \frac{c\,L}{2\sqrt{2}\pi\,\sigma_\xi \sigma_g\, z \tan\theta_T} \quad . \tag{5.52}$$

B_S^2 is the MS bandwidth of the signals that are reflected from the ocean. From Eqs. (5.51) and (5.52), we can see that when the footprint is small and the surface correlation length is large, picosecond timing accuracy is possible if the bandwidth of the receiver is chosen properly so that it is not too large compared to the signal bandwidth. The effect of the receiver bandwidth on the timing accuracy for the ocean reflected pulses is similar to that in the diffuse target reflection situation. Consequently, the analysis on the effects of receiver bandwidth given in Section 5.3 can apply in the ocean reflection case.

When the ocean surface correlation length is very large so that $L >> z \tan\theta_T$, the ocean surface within the laser footprint is essentially flat. In this case, the MS timing error is

$$\sigma_{\tau_{COR}}^2 = \left(\frac{1}{\langle N_1 \rangle} + \frac{1}{\langle N_2 \rangle} \right) \frac{8\sigma_g^2}{3\sqrt{3}} + \left(\frac{1}{K_1} + \frac{1}{K_2} \right) \sqrt{2}\,\sigma_g^2$$

$$+ \sqrt{2}\,\sigma_g^5 \left[\frac{\frac{1}{\sigma_h^2} - \frac{1}{2\sigma_g^2}}{\langle N_1 \rangle \langle N_2 \rangle \sigma_h} + \frac{\frac{1}{\sigma_h^2 + \sigma_f^2/2} - \frac{2}{3\sigma_g^2}}{\langle N_1 \rangle K_2 \left(\sigma_h^2 + \sigma_f^2/2\right)^2} \right]^{1/2} + \tag{5.53}$$

$$+\frac{\dfrac{1}{\sigma_h^2 + \sigma_f^2/2} - \dfrac{2}{3\sigma_g^2}}{\langle N_2 \rangle K_1 \left(\sigma_h^2 + \sigma_f^2/2\right)^{1/2}}\Bigg] \cdot \qquad L >> z \tan \theta_T$$

Notice that Eq. (5.53) is primarily the MS timing error for reflections from many specular points over a flat surface. This is expected because the ocean with very long surface correlation length behaves like a mirror within the laser footprint.

In order to illustrate the effect of ocean surface correlation length (L) on the performance of the correlation estimator, the RMS timing error is plotted versus the normalized surface correlation length in Fig. 5.15 for three different values of RMS ocean wave height (σ_ξ). The plotted results show that picosecond timing accuracy is achievable over regions where L is at least an order of magnitude larger than the laser footprint. When L is very large, the timing errors saturate at the lowest possible level.

In Fig. 5.16, the RMS timing error is plotted versus the expected signal strength for three different sets of speckle SNR (K_i's) and when L is twenty times the footprint radius. The results show that the timing accuracy improves as the signal strength and speckle SNR increases.

The timing accuracy of the ocean reflection using the sinusoidal wave model cannot be evaluated to closed form. Numerical results are plotted versus the expected signal strength in Fig. 5.17 for several values of speckle SNR $K_1 = K_2 = K$. The system and ocean parameters correspond to the expected received pulse shape plotted in Fig. 5.14. Again, the timing

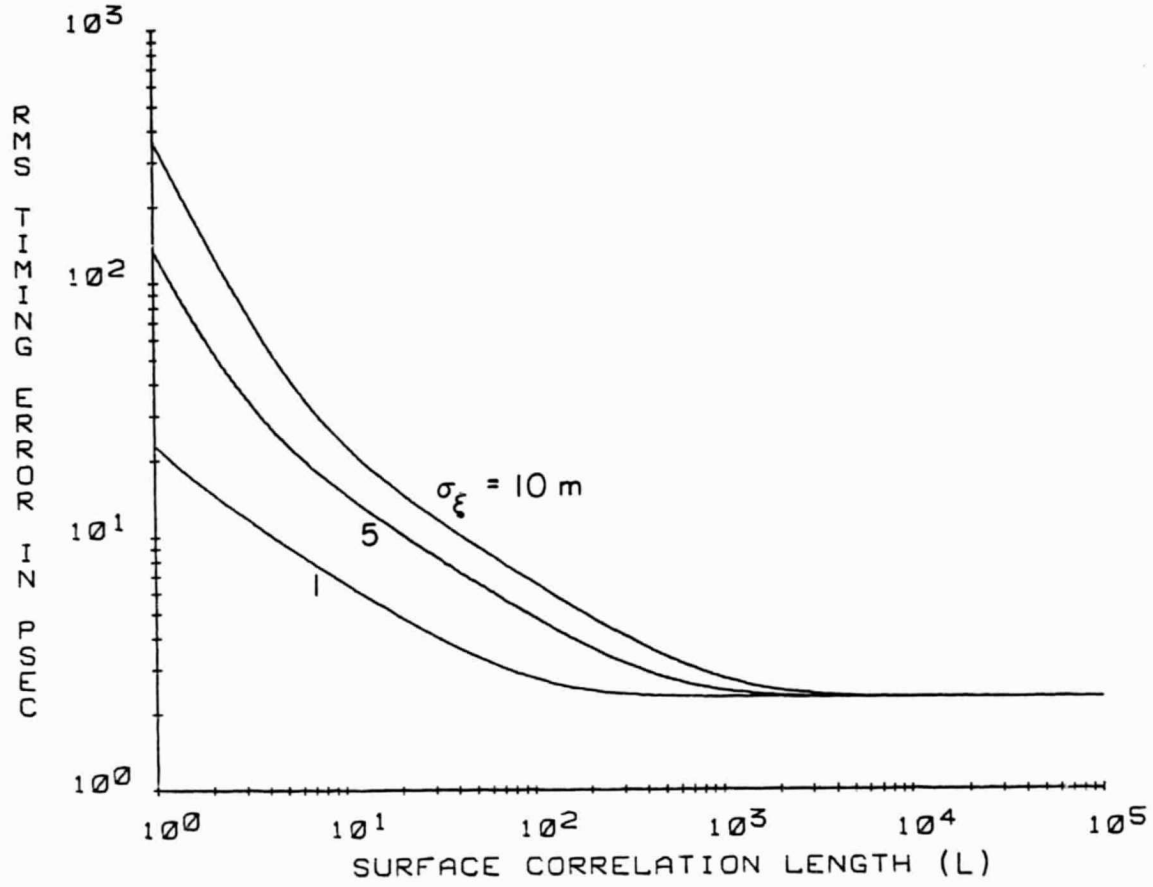

Fig. 5.15. RMS differential timing error versus surface correlation length for the pulse reflections from a Gaussian ocean. (z = 400 km, θ_T = 0.1 mrad, σ_f = 33 psec, σ_h = 100 psec, λ_1 = 0.355 μm, λ_2 = 1.064 μm, ϕ = 0, $K_1 = 9K_2 = 10^5$, $\langle N_1 \rangle = \langle N_2 \rangle = 10^4$).

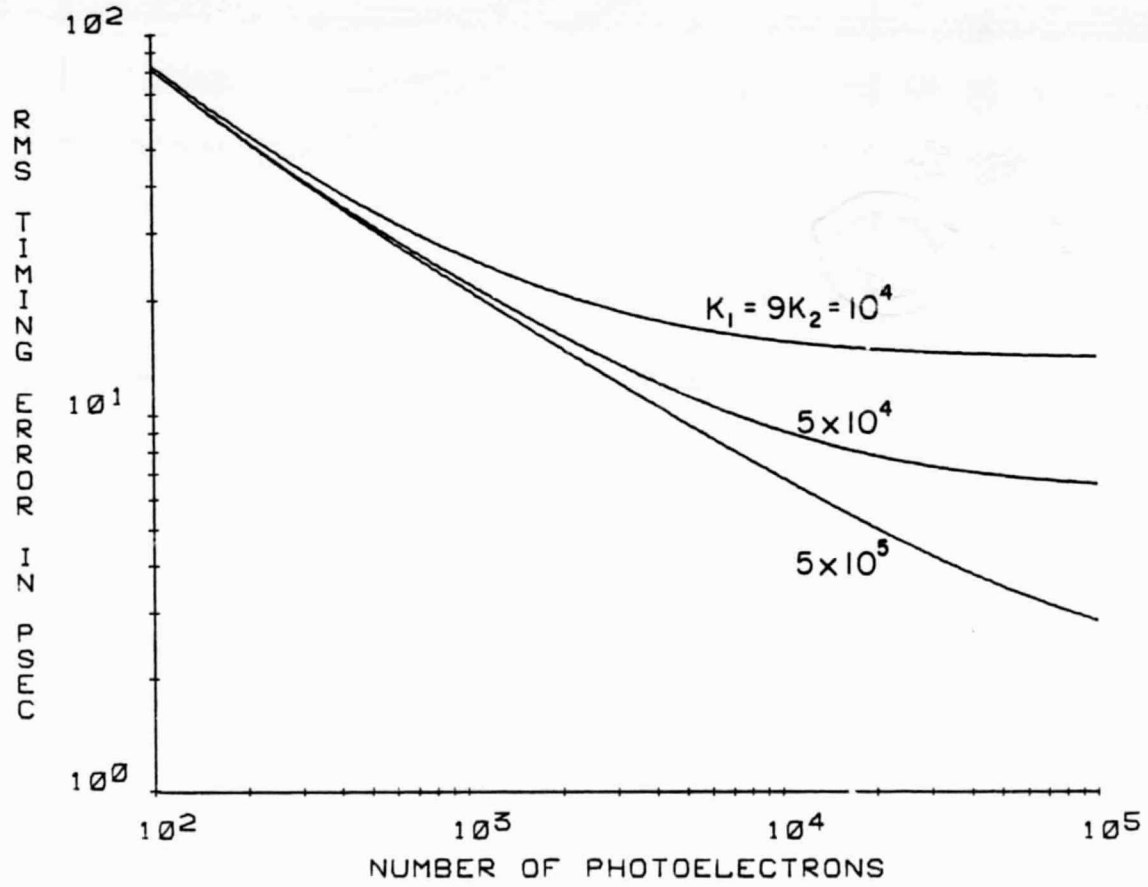

Fig. 5.16. RMS differential timing error versus received signal strength for the pulse reflections from a Gaussian ocean. (z = 400 km, θ_T = 0.1 mrad, σ_f = 33 psec, σ_h = 100 psec, λ_1 = 0.355 μm, λ_2 = 1.064 μm, ϕ = 0, σ_ξ = 3 m).

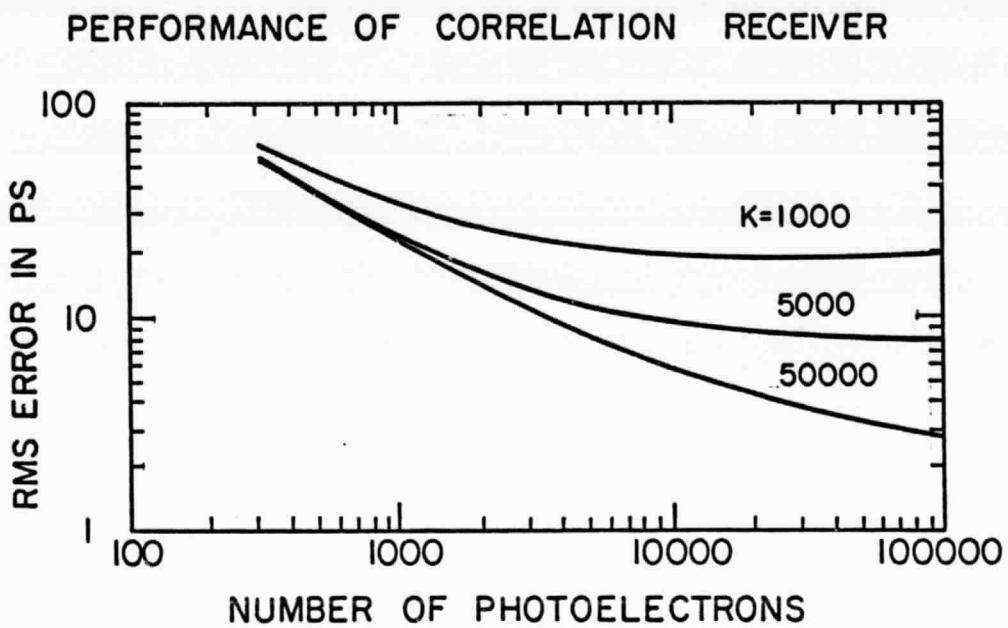

Fig. 5.17. RMS differential timing error versus received signal strength for the pulse reflections from a sinusoidal ocean. The mean received pulse shape is plotted in Fig. 5.14.

accuracy improves as the signal strength and speckle SNR increase. The system and ocean parameters in both Figs. 5.16 and 5.17 are deliberately chosen to be very close to each other in order to compare the timing accuracies by using different ocean wave models. Although one was obtained through bandwidth analysis while the other through numerical computation, the results are very similar. According to these results, it is evident that the timing accuracy depends only on the bandwidth (or the sharp glint) of the reflected signal regardless of which ocean model that we assume. In both figures, picosecond timing accuracies appear to be feasible when the expected photocounts for both pulses approach a few thousand. The timing accuracy can be improved further by averaging the measurements from many shots. It should be emphasized that these results are only estimates of the expected timing accuracy. The actual receiver performance will depend on the local surface profile within the laser footprint.

5.6 Discussion

Pulsed two-color laser ranging systems can be used to determine the atmospheric delay by measuring the difference in propagation times between two optical pulses that are transmitted simultaneously at two different frequencies. However, proper design of the receiver timing algorithm is necessary in order to obtain picosecond differential timing accuracies which are required for most applications. In this chapter, the cross-correlation technique is used to estimate the differential propagation time between pulses which are reflected from CCR arrays and diffuse targets. The performance of the correlation technique is analyzed by considering both speckle and shot noise. The accuracy of this estimator is, in general, a function of the detected signal strength, speckle SNR, receiver bandwidth and the detected signal bandwidth.

Pulse reflections from various targets were analyzed in order to evaluate quantitatively the performance of this estimator. For the flat diffuse targets, the timing accuracy is highly dependent on the receiver bandwidth and the characteristics of the time-resolved speckle. At low signal levels, it was shown that the timing performance of the correlation estimator is comparable to that of the optimal Maximum-likelihood (ML) estimator when the receiver bandwidth is chosen to match the bandwidth of the target reflected pulses. At high signal levels, however, time-resolved speckle places a fundamental limit on the performance of the correlation estimator. For the cube corner reflector arrays, the timing performance is dominated by partially developed speckle so that the differential propagation time cannot be resolved to better than the pulsewidth of the received signals. For the ocean, the timing accuracy is highly dependent on the ocean surface correlation length and the bandwidth of the receiver. It was shown that picosecond timing accuracy is only feasible over regions where the surface correlation length is larger than the laser footprint radius. Based upon these analytical results, it appears the overall performance of two-color satellite laser ranging systems is dominated by the receiver bandwidth, transmitted laser pulsewidth, and pulse repetition rate, and not by the detected signal strength.

6. SYSTEM ALIGNMENT EFFECTS

6.1 Introduction

In the preceding chapter we described the performance of the correlation estimator under ideal situations. That is, we assumed that the two laser beams were perfectly aligned, that the beam divergence angles associated with the two operating frequencies were identical, and that there was no displacement between the transmitter and the receiver. In actual practice, however, not all the above assumptions will be satisfied, and as the result the timing accuracy we obtain may be degraded. In this chapter we investigate the system alignment effects on the performance of a two-color laser ranging system.

6.2 Correlation Coefficient and Mean Square Error

One of the basic assumptions used in applying the correlation timing estimator is that the return signals at two frequencies have similar pulse shapes. In practice, however, the return pulses may not always be identical. This could be due to misalignment at the transmitter or due to atmospheric turbulence. Any decorrelation of the pulse shape will, in general, degrade the performance of the correlation estimator.

The correlation coefficient between the received signals at the two frequencies can be defined as

$$\rho_{12}(\tau) = \frac{\int_{-\infty}^{\infty} S_1(t)\, S_2(t+\tau)\, dt}{\left[\int_{-\infty}^{\infty} S_1^2(t)dt \int_{-\infty}^{\infty} S_2^2(t+\tau)dt\right]^{1/2}} \quad . \tag{6.1}$$

When the two signals are identical in shape, ρ_{12} has a maximum value of one at $\tau = \tau_o$, where τ_o is the difference between the propagation times of the two signals. ρ_{12} is in general random due to the random nature of the received signals. The expected value of ρ_{12} is approximately given by

$$\langle \rho_{12}(\tau) \rangle \cong \frac{\int_{-\infty}^{\infty} \langle S_1(t)\, S_2(t+\tau) \rangle\, dt}{\left[\int_{-\infty}^{\infty} dt_1 \int_{-\infty}^{\infty} dt_2 \langle S_1^2(t_1)\, S_2^2(t_2+\tau) \rangle\right]^{1/2}} . \tag{6.2}$$

Using the fact that the shot noise and speckle are uncorrelated at the two frequencies, the expected value of ρ_{12} can be simplified to

$$\langle \rho_{12}(\tau) \rangle = \frac{\int_{-\infty}^{\infty} \langle S_1(t) \rangle \langle S_2(t+\tau) \rangle\, dt}{\left[\int_{-\infty}^{\infty} dt_1 \int_{-\infty}^{\infty} dt_2\, R_{S_1}(t_1,t_1)\, R_{S_2}(t_2+\tau,\, t_2+\tau)\right]^{1/2}} . \tag{6.3}$$

When the signals are not identical, Eqs. (5.8) and (5.9) become

$$\langle S_i(t) \rangle = \langle N_i \rangle\, f_{S_i}(t - (i-1)\, \tau_o) \qquad i=1,2, \tag{6.4}$$

and

$$\begin{aligned} C_{S_i}(t_1,t_2) = {} & \langle N_i \rangle\, G(\sqrt{2}\,\sigma_h,\, t_1-t_2)\, f_{S_i}\left(\frac{t_1+t_2}{2} - (i-1)\,\tau_o\right) \\ & + \langle N_i \rangle^2 K_i^{-1} G(\sqrt{2}\,\sigma_g,\, t_1-t_2)\, f_{SP_i}\left(\frac{t_1+t_2}{2} - (i-1)\,\tau_o\right) \qquad i=1,2 \end{aligned} \tag{6.5}$$

where f_{S_i} and f_{SP_i} are the normalized received signal and speckle variance at wavelength λ_i, respectively. By substituting Eqs. (6.4) and (6.5) into Eq. (6.3) and using Parseval's Theorem, we can express $\langle \rho_{12}(\tau) \rangle$ at $\tau = \tau_o$ in terms of the frequency spectrum of the mean received signals as

$$\langle \rho_{12}(\tau_o) \rangle = \frac{\int_{-\infty}^{\infty} d\omega \; \phi_{S_1}^{*}(\omega) \; \phi_{S_2}(\omega)}{\left[\prod_{i=1}^{2} \left(\frac{\sqrt{\pi}}{\langle N_i \rangle \sigma_h} + \frac{\sqrt{\pi}}{K_i \sigma_g} + \int_{-\infty}^{\infty} d\omega \; |\phi_{S_i}(\omega)|^2 \right) \right]^{1/2}} \tag{6.6}$$

where

$$\phi_{S_i}(\omega) = \int_{-\infty}^{\infty} f_{S_i}(t) \; e^{-j\omega t} \, dt \quad . \tag{6.7}$$

When the mean received signals at the two frequencies are different, the MS timing error of the correlation receiver becomes

$$\sigma_{\tau_{12}}^2 = \frac{4\pi^2 \int_{-\infty}^{\infty} d\omega_1 \int_{-\infty}^{\infty} d\omega_2 \; \hat{R}_{S_1}(\omega_1, \omega_2) \; \hat{R}_{S_2}(\omega_1, \omega_2) \; e^{-j(\omega_1 + \omega_2)\tau_o}}{\langle N_1 \rangle^2 \langle N_2 \rangle^2 \left[\int_{-\infty}^{\infty} d\omega \; \omega^2 \; \phi_{S_1}^{*}(\omega) \; \phi_{S_2}(\omega) \right]^2} \quad . \tag{6.8}$$

The numerator of Eq. (6.8) can be expressed in terms of the Fourier transforms of the expected signals and the speckle variances as

$$4\pi^2 \int_{-\infty}^{\infty} d\omega_1 \int_{-\infty}^{\infty} d\omega_2 \hat{R}_{S_1}(\omega_1,\omega_2)\, \hat{R}_{S_2}(\omega_1,\omega_2)\, e^{-j(\omega_1+\omega_2)\tau_o}$$

$$= - \langle N_1\rangle^2 \langle N_2\rangle^2 \left[\int_{-\infty}^{\infty} d\omega\, \omega\, \phi_{S_1}^*(\omega)\, \phi_{S_2}(\omega) \right]^2$$

$$+ \langle N_1\rangle\langle N_2\rangle^2 \int_{-\infty}^{\infty} d\omega\, \phi_{S_1}^*(\omega) \left[j\omega\, \phi_{S_2}(\omega) * j\omega\, \phi_{S_2}(\omega) \right]$$

$$+ \langle N_1\rangle^2\langle N_2\rangle \int_{-\infty}^{\infty} d\omega\, \phi_{S_2}^*(\omega) \left[j\omega\, \phi_{S_1}(\omega) * j\omega\, \phi_{S_1}(\omega) \right]$$

$$+ \frac{\langle N_1\rangle^2\langle N_2\rangle^2}{K_1} \int_{-\infty}^{\infty} d\omega\, \phi_{SP_1}^*(\omega) \left[j\omega\, \phi_{S_2}(\omega) * j\omega\, \phi_{S_2}(\omega) \right]$$

$$+ \frac{\langle N_1\rangle^2\langle N_2\rangle^2}{K_2} \int_{-\infty}^{\infty} d\omega\, \phi_{SP_2}^*(\omega) \left[j\omega\, \phi_{S_1}(\omega) * j\omega\, \phi_{S_1}(\omega) \right]$$

$$+ \frac{\sqrt{\pi}\, \langle N_1\rangle\langle N_2\rangle}{4\sqrt{2}\, \sigma_h} \left\{ \frac{1}{\sigma_h^2} \int_{-\infty}^{\infty} d\omega\, \phi_{S_2}^*(\omega)\, \phi_{S_1}(\omega) - \int_{-\infty}^{\infty} d\omega\, \omega^2\, \phi_{S_2}^*(\omega)\, \phi_{S_1}(\omega) \right\}$$

$$+ \frac{\sqrt{\pi}\, \langle N_1\rangle^2\langle N_2\rangle^2}{4\sqrt{2}\, \sigma_g\, K_1\, K_2} \left\{ \frac{1}{\sigma_g^2} \int_{-\infty}^{\infty} d\omega\, \phi_{SP_2}^*(\omega)\, \phi_{SP_1}(\omega) - \int_{-\infty}^{\infty} d\omega\, \omega^2\, \phi_{SP_2}^*(\omega)\, \phi_{SP_1}(\omega) \right\}$$

$$+ \frac{\sqrt{\pi}\, \langle N_1\rangle\langle N_2\rangle^2}{4\, (\sigma_h^2 + \sigma_g^2)^{1/2}\, K_2} \left\{ \frac{2}{2\sigma_h^2 + \sigma_f^2} \int_{-\infty}^{\infty} d\omega\, \phi_{S_1}^*(\omega)\, \phi_{SP_2}(\omega) - \int_{-\infty}^{\infty} d\omega\, \phi_{S_1}^*(\omega)\, \phi_{SP_2}(\omega) \right\}$$

$$+\frac{\sqrt{\pi}\,\langle N_1\rangle^2\langle N_2\rangle}{4\,(\sigma_h^2+\sigma_g^2)^{1/2}K_1}\left\{\frac{2}{2\sigma_h^2+\sigma_f^2}\int_{-\infty}^{\infty}d\omega\;\phi_{S_2}^{*}(\omega)\;\phi_{SP_1}(\omega)-\int_{-\infty}^{\infty}d\omega\;\phi_{S_2}^{*}(\omega)\;\phi_{SP_1}(\omega)\right\} \tag{6.9}$$

where

$$\phi_{SP_i}(\omega)=\int_{-\infty}^{\infty}dt\;\; f_{SP_i}(t)\;e^{-j\omega t}\quad,\qquad i=1,2\;. \tag{6.10}$$

The first term in Eq. (6.10) equals the square of the bias. The next four terms are the first-order terms involving the cross correlations of the mean of S_1 and the fluctuating portion of S_2, and vice versa. The last four terms are the second-order terms involving the cross correlations of the fluctuating portions of the two signals.

6.3 Geometry

The geometry of the ranging system is illustrated in Fig. 6.1. The laser beams at two different wavelengths are transmitted from the system simultaneously. Laser beam 1 is incident on the target surface at an angle ϕ, and beam 2 is incident on the target surface at an angle $\phi + \Delta\phi$. $\Delta\phi$ is the difference in incidence angles between the two beams due to misalignment. Throughout the analysis, the incident angles are assumed to be small so that the shadowing effects can be neglected. The expressions for the means and covariance of the received signals involve 2-D integrations over the planes that are transverse to the direction of propagations. Therefore, we need to determine the apparent distances (z_i) and the apparent surface profiles ($\xi(\underline{\rho}_i)$) in terms of z and $\xi(\underline{\rho})$. From simple geometrical considerations, we have

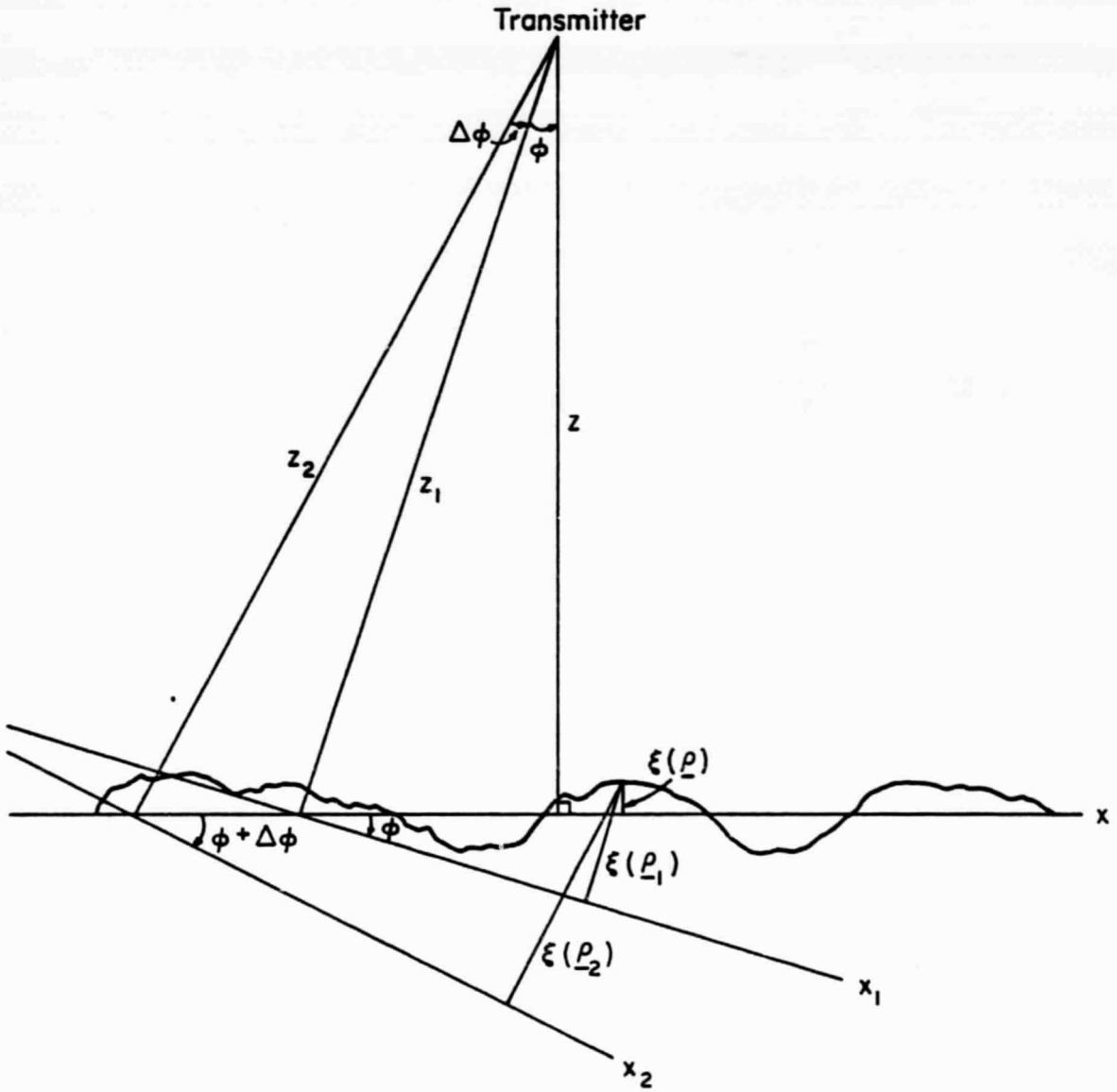

Fig. 6.1. Geometry of the two-color laser ranging system with angular offset.

$$z_i = z \,/\, \cos(\phi + (i-1)\Delta\phi) \quad , \qquad i=1,2, \tag{6.11}$$

$$x_i = x\cos(\phi + (i-1)\Delta\phi) - \xi(\underline{\rho})\sin(\phi + (i-1)\Delta\phi) \tag{6.12}$$

$$\simeq x\cos(\phi + (i-1)\Delta\phi) \quad , \qquad i=1,2$$

$$y_i = y \quad , \qquad i=1,2, \tag{6.13}$$

$$\xi(\underline{\rho}_i) = x\sin(\phi + (i-1)\Delta\phi) + \xi(\underline{\rho})\cos(\phi + (i-1)\Delta\phi), \quad i=1,2. \tag{6.14}$$

The laser intensity footprints at the two wavelengths are assumed to be Gaussian,

$$|a(\underline{\rho}_i,z)|^2 = \frac{Q}{2\pi\sigma_i^2} \exp\left[-\frac{\rho_i^2}{2\sigma_i^2}\right] , \tag{6.15}$$

where

$$\sigma_i = z\tan(\theta_T + (i-1)\Delta\theta_T) \,/\, \cos(\phi + (i-1)\Delta\phi) \quad . \tag{6.16}$$

σ_i is the footprint radius measured at the $e^{-1/2}$ point on the $\underline{\rho}_i$ plane. In Eq. (6.15), we have assumed that laser beam 1 has a divergence angle of θ_T and beam 2 has a divergence angle $(\theta_T + \Delta\theta_T)$. $\Delta\theta_T$ is the difference in divergence angles between the two beams.

The power spectra of the normalized received signals can be calculated by using Eq. (3.24), Eq. (6.7), Eqs. (6.11) through (6.15) as

$$|\phi_{S_i}(\omega)|^2 \cong \frac{e^{-\omega^2\sigma_g^2}}{4\pi^2\sigma_i^4} \int d^2\underline{\rho}_a \int d^2\underline{\rho}_b \exp\left[-\frac{(x_a^2 + x_b^2)\cos^2[\phi + (i-1)\Delta\phi]}{2\sigma_i^2}\right] \cdot$$

$$\cdot \exp\left[-\frac{y_a^2 + y_b^2}{2\sigma_i^2}\right] \exp\left[-j\frac{\omega\cos\phi}{cz}(x_a^2\cos^2\phi - x_b^2\cos^2\phi + y_a^2 - y_b^2)\right] \tag{6.17}$$

$$\cdot \langle \exp\left\{j\frac{2\omega}{c}\cos\phi\,[\xi(\underline{\rho}_a) - \xi(\underline{\rho}_b)]\right\} \rangle$$

where $\underline{\rho}_a = (x_a, y_a)$ and $\underline{\rho}_b = (x_b, y_b)$.

For the Gaussian target surface profile with RMS surface roughness σ_ξ, the ensemble average in (6.17) becomes

$$\langle \exp\left\{j\frac{2\omega}{c}\cos\phi\,[\xi(\underline{\rho}_a) - \xi(\underline{\rho}_b)]\right\} \rangle = e^{-\frac{4\omega^2\cos^2\phi\,\sigma_\xi^2}{c^2}[1 - R_\xi(\underline{\rho}_a, \underline{\rho}_b)]} \tag{6.18}$$

where $R_\xi(\underline{\rho}_a, \underline{\rho}_b)$ is the normalized autocorrelation function of the surface profile. If the correlation length of the target surface (L) is large compared to the laser footprint radius, $R_\xi(\underline{\rho}_a, \underline{\rho}_b)$ can be approximated as

$$R_\xi(\underline{\rho}_a, \underline{\rho}_b) = 1 - \frac{(\underline{\rho}_a - \underline{\rho}_b)^2}{2L^2} \quad . \tag{6.19}$$

Substituting Eq. (6.19) into Eq. (6.11) and carrying out the integration, we

have

$$|\phi_{S_i}(\omega)|^2 \cong \frac{e^{-\omega^2\sigma_g^2}}{1 + \beta_i\omega^2} \quad , \qquad i=1,2 \tag{6.20}$$

where

$$\beta_i = \frac{8\sigma_\xi^2\sigma_i^2}{c^2L^2} + \frac{4\sigma_i^4}{c^2z^2} \quad , \qquad i=1,2 \quad . \tag{6.21}$$

The cross spectrum between the two signals ($\phi_{S_1}^*\phi_{S_2}$) can be calculated using a similar approach with slight modifications of the expected phase function. Due to the difference in incidence angles at the two propagation paths, the laser foortprints do not overlap completely, and $R_\xi(\underline{\rho}_a,\underline{\rho}_b)$ must be modified so that

$$R_\xi(\underline{\rho}_a,\underline{\rho}_b) = 1 - \frac{\{x_a - x_b + z\,[\tan(\phi+\Delta\phi) - \tan\phi]\}^2 + (y_a-y_b)^2}{2L^2} \quad . \tag{6.22}$$

After carrying out the integration, we have

$$\phi_{S_1}^*(\omega)\,\phi_{S_2}(\omega) \cong (1 + \beta_{12}\omega^2)^{-1} \exp\left\{ -\omega^2\left[\sigma_g^2 + \frac{2\sigma_\xi^2 z^2 \sin^2\Delta\phi}{c^2L^2\cos^2\phi\,\cos^2(\phi+\Delta\phi)}\right]\right\} \tag{6.23}$$

$$\cdot\exp\left[\frac{8\omega^4\sigma_\xi^4 z^2\,\sin^2\Delta\phi\,(\sigma_1^2 + \sigma_2^2)}{c^4L^4\,\cos^2\phi\,\cos^2(\phi+\Delta\phi)\,(1 + \beta_{12}\omega^2)}\right]$$

where

$$\beta_{12} = \frac{4\,\sigma_\xi^2\,(\sigma_1^2 + \sigma_2^2)}{c^2L^2} + \frac{4\,\sigma_1^2\,\sigma_2^2}{c^2z^2} \quad . \tag{6.24}$$

The expected correlation coefficient can now be evaluated by substituting Eqs. (6.20) and (6.23) into Eq. (6.6). Numerical results are plotted versus different system parameters in Figs. 6.2 and 6.3. In these results, we let $\phi = 0$ because it is the most common viewing configuration in satellite laser ranging. Similar results would be obtained when ϕ is nonzero but small. In Fig. 6.2, $\langle\rho_{12}\rangle$ is plotted against $\Delta\theta_T/\theta_T$ for different values of misalignment angles $\Delta\phi$ and for a target surface correlation length which is on the same order of magnitude as the smaller footprint. We can see that the maximum correlation can be obtained when both $\Delta\theta_T$ and $\Delta\phi$ are zero; that is, when the two beams have the same divergence and they are aligned so that the laser footprint intensities are identical. This maximum value, however, is less than unity because of the decorrelation of the signals due to shot noise and speckle (refer to Eq. (6.6)). When the two beams are misaligned, the footprints overlap only partially, which results in differences in received pulse shapes and a decorrelation of the two signals. The peak correlation at each curve corresponds to the situation in which the largest possible overlap area is attained.

In Fig. 6.3 $\langle\rho_{12}\rangle$ is plotted versus the target surface correlation length and for $\Delta\theta_T = 0$ (equal divergence of the two beams). When the magnitude of the surface correlation length is on the same order as the size of the footprint, the degree of correlation is roughly proportional to the overlap

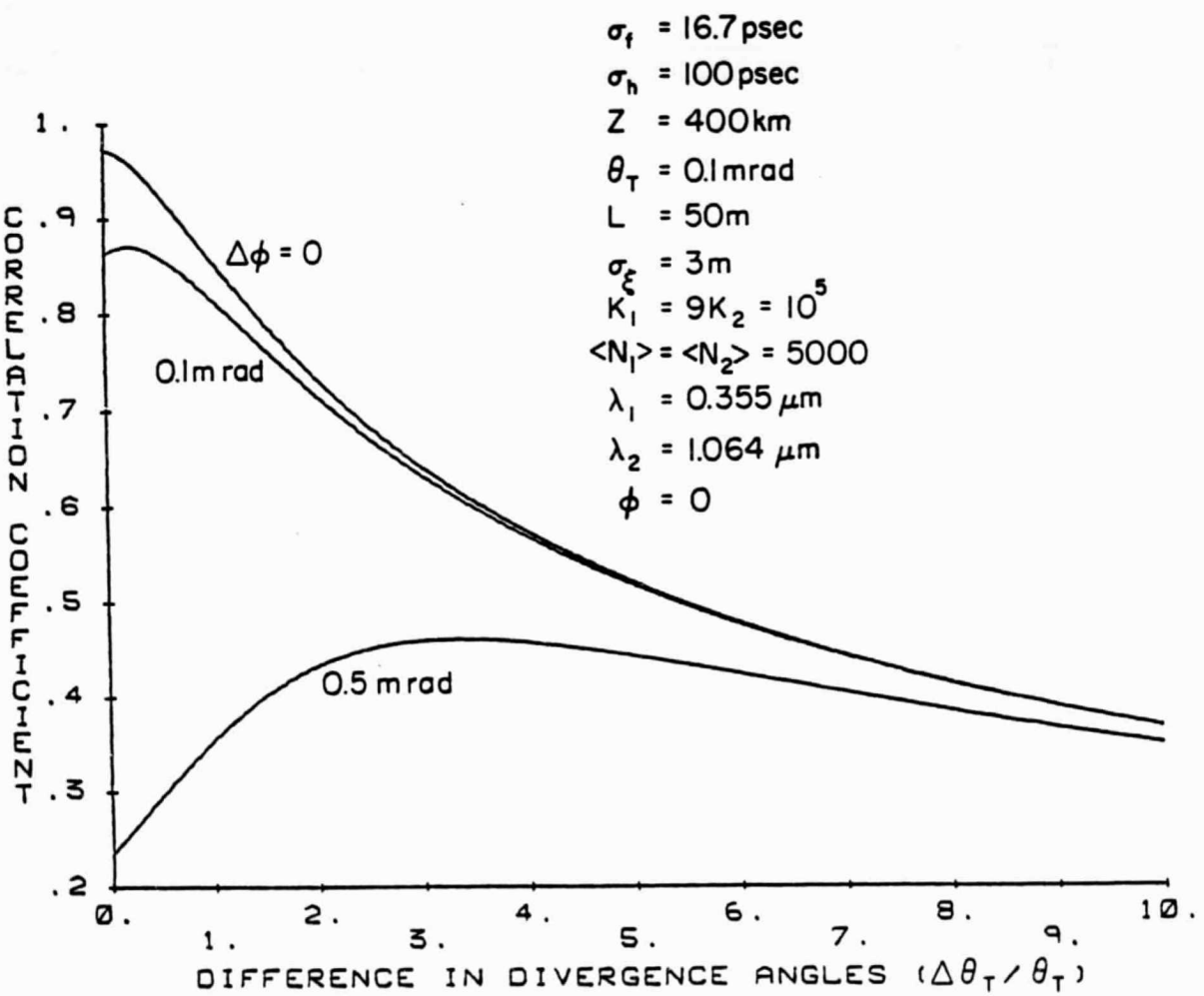

Fig. 6.2. Mean correlation coefficient versus difference in divergence angles.

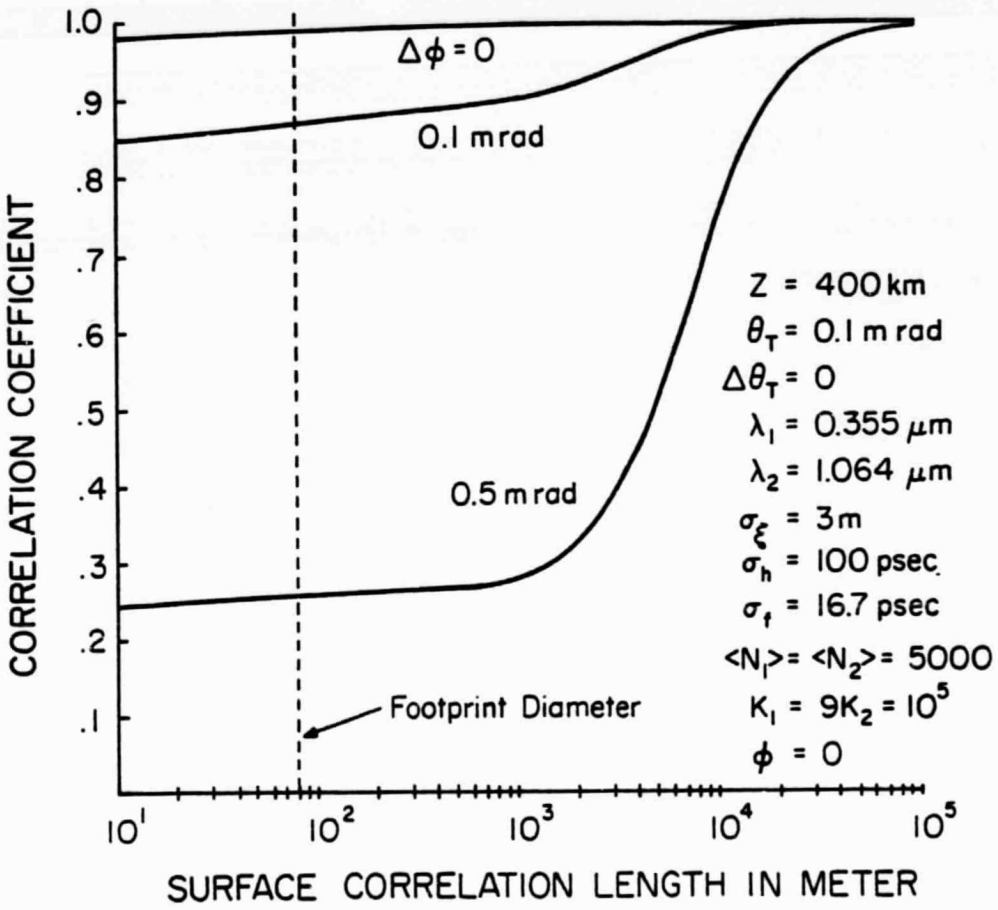

Fig. 6.3. Mean correlation coefficient versus target surface correlation length.

area. Consequently, the top curve, which corresponds to the largest overlap area, has the highest correlation. When the surface correlation length is very large (flat surface), the intensities reflected from different regions of the surface are identical. In this case, high correlation can always be achieved regardless of how well the two footprints overlap.

In Chapter 5, it was shown that the timing performance of the correlation algorithm depends on the ratio of the receiver bandwidth (B_R) to the expected signal bandwidth (B_S). Since this algorithm depends on how well the two signals are correlated, we could expect the correlation coefficient to exhibit the same dependence. We shall illustrate this point by means of a simple example. Let us assume that the received signals have Gaussian pulse shapes and that there are no system alignment errors. In this case,

$$f_{S_i}(t) = \frac{1}{\sqrt{2\pi}\ \sigma_S} \exp\left[- \frac{(t - 2\ z/c)^2}{2\ \sigma_S^2} \right] \qquad i=1,2 \tag{6.25}$$

where

$$\sigma_S = (\sigma_f^2 + \sigma_h^2 + \sigma_r^2)^{1/2} \quad .$$

σ_S is the RMS pulse width of the received signal at both wavelengths and σ_r is pulse broadening due to the target range spread. It follows from Eq. (6.25) that B_S and B_R are

$$B_S = \frac{1}{\sqrt{2}\sigma_S} = \frac{1}{\sqrt{2}\ (\sigma_h^2 + \sigma_f^2 + \sigma_r^2\ )^{1/2}}$$

and

$$B_R = \frac{1}{\sqrt{2}\sigma_h} \quad ,$$

respectively. By substituting Eq. (6.25) into (6.16), we have

$$\langle \rho_{12}(\tau_o) \rangle = \frac{1}{\left[\prod_{i=1}^{2} \left(1 + \frac{\sigma_S}{K_i \sigma_g} + \frac{\sigma_S}{\langle N_i \rangle \sigma_h}\right) \right]^{1/2}} \quad . \tag{6.26}$$

When ranging to diffuse targets at satellite altitudes, K_i is much larger than $\langle N_i \rangle$. If we let $\langle N_1 \rangle = \langle N_2 \rangle = \langle N \rangle$, Eq. (6.26) can be simplified to

$$\langle \rho_{12}(\tau_o) \rangle \cong \frac{\langle N \rangle}{\langle N \rangle + \frac{\sigma_S}{\sigma_h}} = \frac{\langle N \rangle}{\langle N \rangle + \frac{B_R}{B_S}} \quad . \tag{6.27}$$

Notice that the receiver bandwidth B_R is always greater than the detected signal bandwidth B_S. According to Eq. (6.27), B_R must not be too large compared to B_S in order to obtain high correlation between the two signals. This is the same conclusion reached in Chapter 5.

The numerical results for the MS timing error are plotted versus the signal strength in Figs. 6.4 and 6.5 for different ranging parameters. For simplicity, we have assumed the signal strengths at the two wavelengths are equal. In Fig. 6.4 we assume the two beams are aligned but their divergence angles are different. The bottom curve ($\Delta\theta_T = 0$) corresponds to the case of complete overlap of the laser footprints (no system error). As

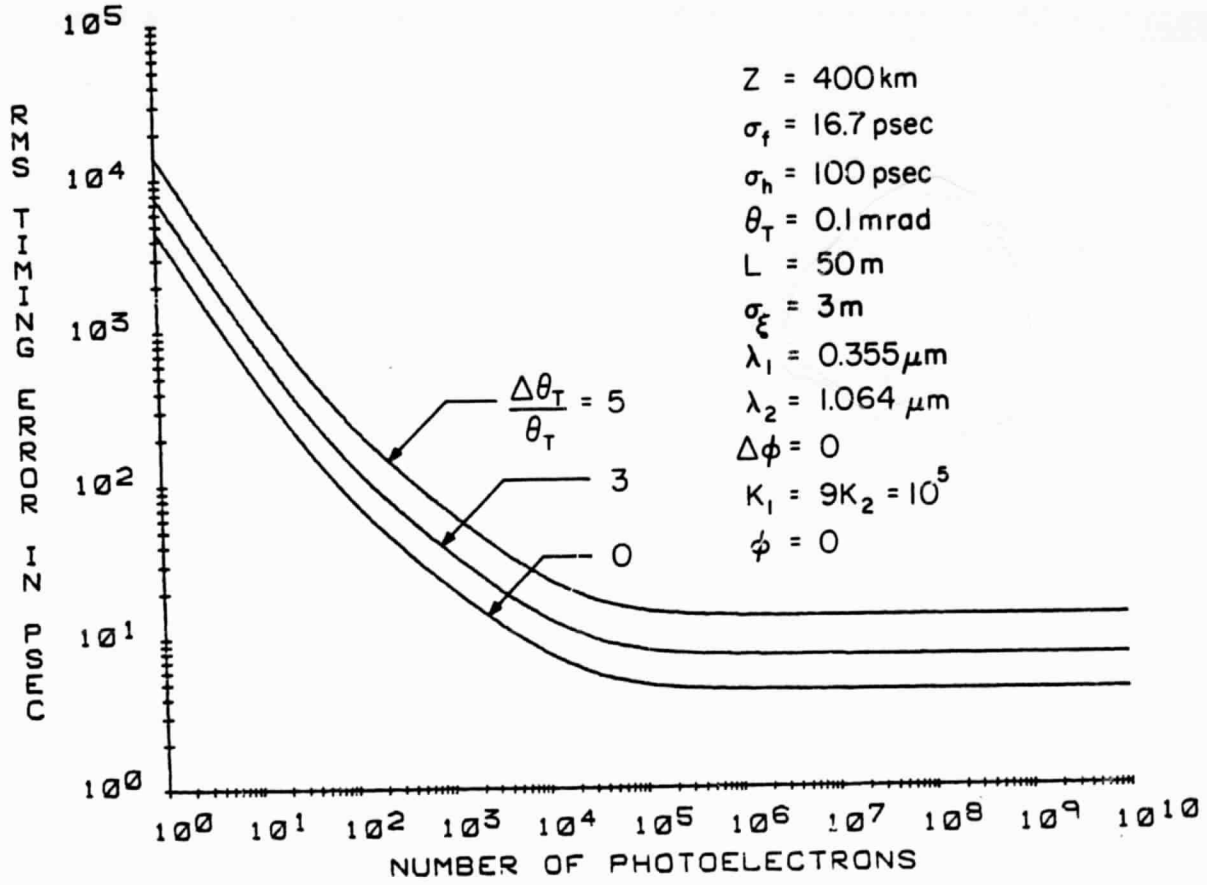

Fig. 6.4. RMS differential timing error versus expected signal strength when the divergence angles of the two transmitted laser beams are different. The ranging system is pointed at nadir.

expected, the timing error increases with increasing $\Delta\theta_T$. This additional error is partly due to the slight difference in signal intensities introduced by different footprint areas, and partly due to the broadening of one of the received signals. However, this additional error is usually small.

In Fig. 6.5 we assume the two beams have equal divergences but they are misaligned. The remaining parameters are the same as those used in Fig. 6.4. As we can see, the additional error due to misalignment is considerably larger than that due to differences in divergence. The middle curve corresponds to the case of partial overlap of the beams, and the additional error due to this slight misalignment is not very severe. The top curve corresponds to the case at which the two beams illuminate different parts of the target surface. Since the surface correlation length is finite, the reflected signal intensities at the two wavelengths are considerably different. Consequently, the performance of the correlation receiver in this case is degraded considerably.

6.4 Return Signals for Coaxial and Noncoaxial Systems with Central Obstruction

For the laser ranging systems, the recieved signal is given by the link equation

$$\langle N \rangle = \frac{\eta}{hf} \beta_r^o Q T_a^2 A_R z^{-2} \tag{6.28}$$

where Q is the average transmitted pulse energy, η is the quantum efficiency of the receiving system, hf is the signal photon energy, T_a is the two-way atmospheric transmittance, β_r^o is the average power reflectivity of the target, A_R is the receiver aperture area, and z is the range distance. In most cases, however, not all the light collected by the telescope is detected by the detector. Signal power is normally lost by two mechanisms.

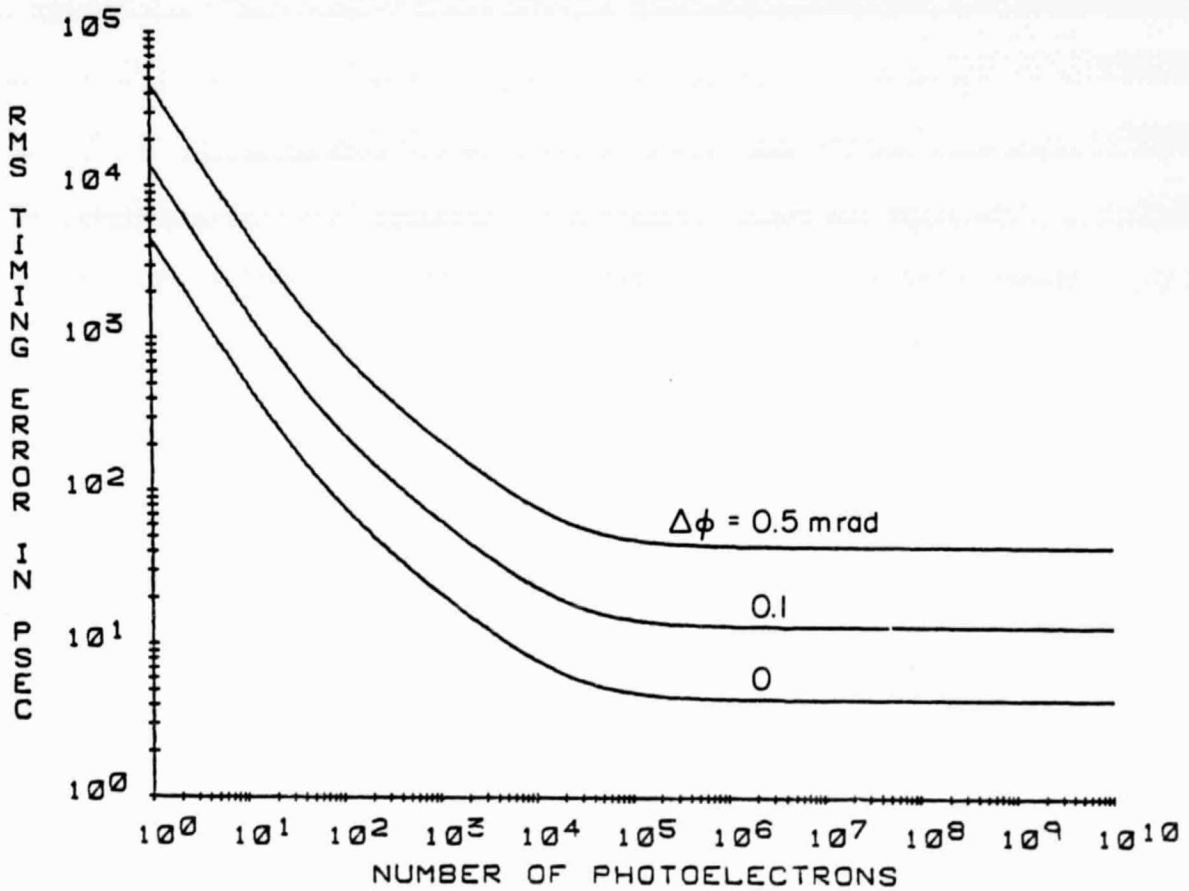

Fig. 6.5. RMS differential timing error versus expected signal strength when the two transmitted laser beams are misaligned. The divergence angles of the two beams are equal, and the remaining parameters correspond to those given in Fig. 6.4.

First, the overlap of the transmitted beam with the receiver's field-of-view (FOV) is often incomplete as in noncoaxial systems or in systems with shadowing of the main mirror by a central obstruction, e.g., a secondary mirror. Second, because the telescope is focused at infinity, light backscattered from targets at small and medium distances is not focused in the focal plane. Both effects give rise to a deviation of the detector power from the z^{-2} dependence as given by the link equation.

To study the return signals for coaxial and noncoaxial systems, we assume a target with uniform reflectivity and negligible range spread. The analysis here closely follows that of [Harms et al., 1978, 1979].

The geometry of the receiving optics is given by Fig. 6.6. Let r_p and r_b be the radii of the primary mirror and central obstruction, respectively. The detector is situated on the optical axis, at a distance D behind the primary lens, while the obstruction or secondary mirror of the telescope is located at a distance S_b in front of the lens. The primary lens forms an image of the target on the image plane. For the target at distance z, the image is located at distance I(z) behind the lens, where I(z) is related to z by the thin lens formula

$$1/I(z) + 1/z = 1/f \quad , \tag{6.29}$$

and f is the focal length of the primary lens.

The light backscattered from a point $\underline{\rho}_o$ on the target is focused onto the image plane resulting in an irradiance $dS(\underline{\rho}_i, z)$ at point $\underline{\rho}_i$, where $\underline{\rho}_i = \underline{\rho}_o\ I(z)/z$. A pencil of light backscattered to a surface element dA around $\underline{\rho}_i$ will illuminate an annulus in the detector plane around $\underline{\rho}_d$ with an irradiance of

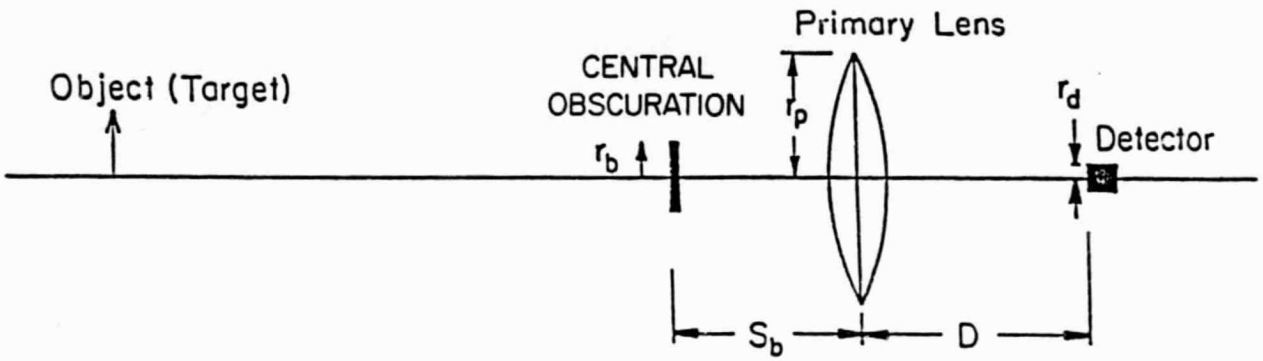

Fig. 6.6. Geometry of the receiving optics.

$$dS(\underline{\rho}_d, z) = \frac{dS(\underline{\rho}_i, z)dA}{\pi r_c^2 (1 - r_b^2/r_p^2)} \tag{6.30}$$

where $S(\underline{\rho}_d, z)$ and $S(\underline{\rho}_i, z)$ are the irradiances in the detector and image plane, respectively. The size of the annulus can be calculated by using geometric optics. The ray tracing of the reflected light is given by Fig. 6.7. From this figure, $\underline{\rho}_d$ is related to $\underline{\rho}_i$ by

$$\underline{\rho}_d = \frac{D}{I(z)} \underline{\rho}_i \quad , \tag{6.31}$$

and the outer radius of the annulus r_c is related to r_p by

$$r_c = r_p \frac{I(z) - D}{I(z)} \quad . \tag{6.32}$$

The total irradiance at the detector plane is provided by all the pencils of rays for which the principal rays intersect the detector plane within a circle around $\underline{\rho}_d$ with radius r_c excluding those rays within a circle with radius $r_c\, r_b / r_p$. The corresponding marginal points in the image plane form an annulus with an outer radius r_m given by

$$r_m = r_c \frac{I(z)}{D} \tag{6.33}$$

and an inner radius equal to $r_m r_b / r_p$.

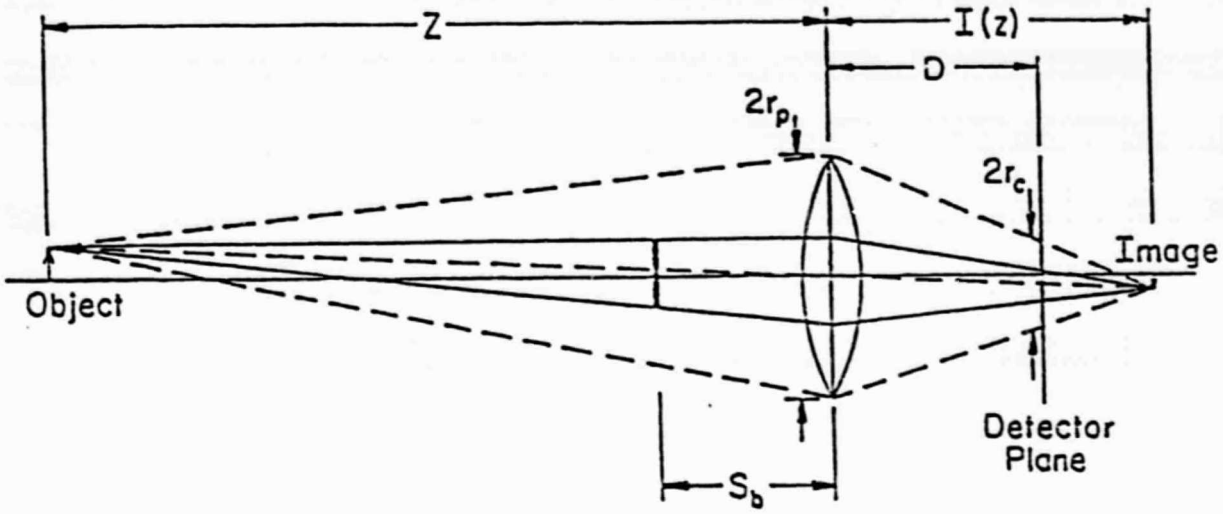

(a) RAY TRACING OF THE REFLECTED LIGHT

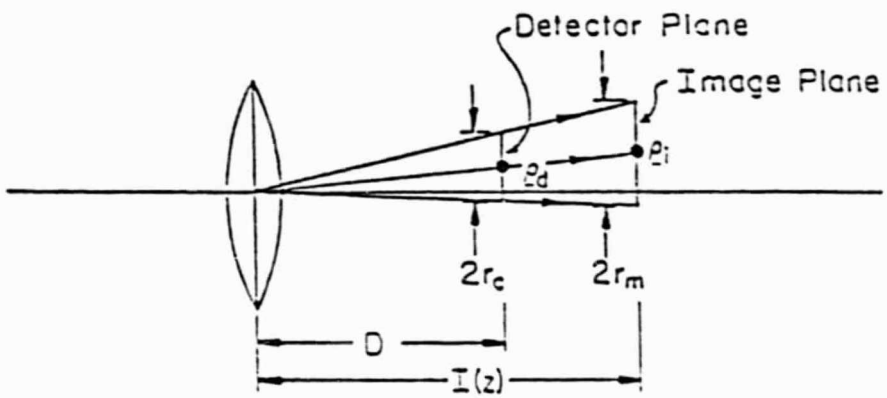

(b) GEOMETRIES OF THE DETECTOR AND IMAGE PLANES

Fig. 6.7. Shadowing in the detector plane due to central obstruction.

In the noncoaxial systems, the position of the transmitted beam relative to the receiver axis varies with distance z. Fig. 6.8 shows the geometrical arrangements of the transmitter and receiver in a noncoaxial ranging system. The detector defines the optical (z) axis of the receiver, the y axis points toward the transmitter, and the x axis is perpendicular to both. The transmitted beam and receiver axes are inclined toward each other by a small angle δ with a separation d at z = 0. Therefore, the y-coordinate of the beam center at any distance z is given by

$$a_o(z) = d - \delta z \tag{6.34}$$

Because of the displacement, the total irradiance distributions on both the image plane and the detector plane are no longer symmetric around the receiver axis. Instead, they are symmetric around a parallel axis whose y-coordinate is displaced from the receiver axis by the amount

$$a(z) = \frac{I(z)}{z}(d - \delta z) \quad . \tag{6.35}$$

By assuming a Gaussian footprint with radius z tan θ_T at the $e^{-1/2}$ point, and using Eq. (6.35), the irradiance at the image plane is given by

$$S(\underline{\rho}_i, z) = \frac{\pi(r_p^2 - r_b^2)}{z^2} P_o T_a^2 \beta_r \frac{1}{2\pi\sigma_I^2} e^{-\frac{x_i^2 + (y_i - a(z))^2}{2\sigma_I^2}} \tag{6.36}$$

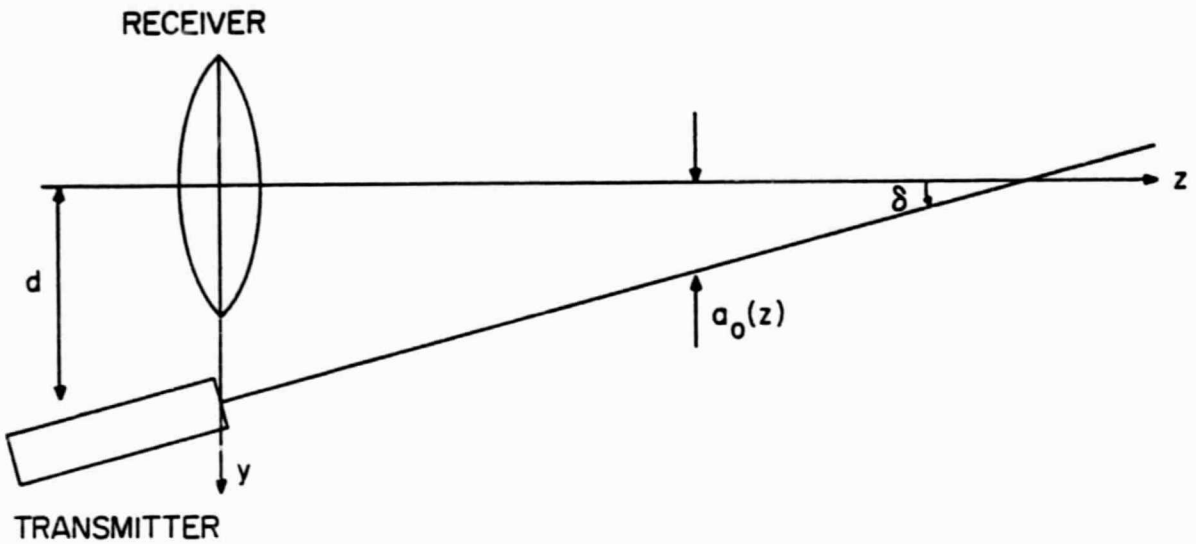

Fig. 6.8. Configuration of the transmitter and the receiver.

where

$$\sigma_I = z \tan \theta_T \frac{I(z)}{z} \approx I(z) \tan \theta_T \quad , \tag{6.37}$$

$\underline{\rho}_i = (x_i, y_i)$, and P_o is the average transmitted power.

By using Eqs. (6.30) and (6.36), we can express the irradiance at the detector plane as

$$S(\underline{\rho}_d, z) = \frac{P_o \beta_r^o T_a^2 r_p^2}{2\pi z^2 \sigma_I^2 r_c^2} \iint A(r_m, \frac{I}{D}\underline{\rho}_d) \,/\, A(r_m \frac{r_b}{r_p}, \frac{I}{D}\underline{\rho}_d) \cdot dxdy \exp\left[-\frac{x^2 + (y - a(z))^2}{2\sigma_I^2}\right] \tag{6.38}$$

where $A(r_m, \frac{I}{D}\underline{\rho}_d)/A(r_m \frac{r_b}{r_p}, \frac{I}{D}\underline{\rho}_d)$ denotes the integration region - an annulus with outer radius r_m, and inner radius $r_m \frac{r_b}{r_p}$ and centered around $\frac{I}{D}\underline{\rho}_d$.

By making changes of variable, we can write

$$S(\underline{\rho}_d, z) = \frac{P_o \beta_r^o T_a^2 r_p^2}{2\pi z^2 \sigma_I^2 r_c^2} \iint A(r_m, \underline{0}) \,/\, A(r_m \frac{r_b}{r_p}, \underline{0}) \cdot dxdy \exp\left[-\frac{(x - \frac{I}{D} x_d)^2 + (y - a(z) - \frac{I}{D} y_d)^2}{2\sigma_I^2}\right] . \tag{6.39}$$

The average detected power is given by

$$P(z) = \int d\underline{\rho}_d \; S(\underline{\rho}_d, z) = \int_0^{2\pi} d\phi \int_0^{r_d} \rho_d \; d\rho_d \; S(\underline{\rho}_d, z) \tag{6.40}$$

where r_d is the radius of the detector. By using the assumption that $d \ll z\, r_d / D$, Eq. (6.40) can be evaluated to give

$$P(z) = \frac{2\pi P_o \beta_r^o T_a^2 r_p^2}{r_c^2 z^2 \sigma_I^2} \; e^{-\frac{a^2(z)}{2\sigma_I^2}} \int_0^{r_d} d\rho_d \; \rho_d \; e^{-\frac{I^2 \rho_d^2}{2\sigma_I^2 D^2}} \tag{6.41}$$

$$\cdot \int_{r_m \frac{r_b}{r_p}}^{r_m} d\rho \; \rho \; e^{-\rho^2/2\sigma_I^2} \; I_o\left(\frac{I \; \rho \; \rho_d}{D \; \sigma_I^2}\right)$$

where I_o is the modified Bessel function of the first kind and zero order. Again, by making changes of variables, we have

$$P(z) = \frac{2\pi P_o T_a^2 \beta_r^o}{\left(1 - \frac{z}{f} + \frac{z}{D}\right)^2 z^4 \tan^2\theta_T} e^{-\frac{(d - \delta z)^2}{2z^2\tan^2\theta_T}} \int_0^{r_d \frac{z}{D}} d\rho_d \, \rho_d \, e^{-\rho_d^2/2z^2\tan^2\theta_T}$$

$$\cdot \int_{r_b \left|1 - \frac{z}{f} + \frac{z}{D}\right|}^{r_p \left|1 - \frac{z}{f} + \frac{z}{D}\right|} d\rho \, \rho \, e^{-\rho^2/2z^2\tan^2\theta_T} I_o\left(\frac{\rho \, \rho_d}{z^2\tan^2\theta_T}\right) . \qquad (6.42)$$

The expected signal strength is then

$$\langle N \rangle = \frac{\eta}{hf} Q \, T_a^2 \beta_r^o \frac{2\pi}{\left(1 - \frac{z}{f} + \frac{z}{D}\right)^2 z^4 \tan^2\theta_T} e^{-\frac{(d - \delta z)^2}{2z^2\tan^2\theta_T}} \qquad (6.43)$$

$$\cdot \int_0^{r_d \frac{z}{D}} d\rho_d \, \rho_d \, e^{-\rho_d^2/2z^2\tan^2\theta_T} \int_{r_b \left|1 - \frac{z}{f} + \frac{z}{D}\right|}^{r_p \left|1 - \frac{z}{f} + \frac{z}{D}\right|} d\rho \, \rho \, e^{-\rho^2/2z^2\tan^2\theta_T} I_o\left(\frac{\rho \, \rho_d}{z^2\tan^2\theta_T}\right) .$$

If the radius of the detector r_d is very large, i.e., $r_d >> z \tan \theta_T$, Eq. (6.43) can be simplified to

$$\langle N \rangle \simeq \frac{\eta}{hf} Q T_a^2 \beta_r^o \frac{\pi(r_p^2 - r_b^2)}{z^2} e^{-\frac{(d - \delta z)^2}{2z^2 \tan^2 \theta_T}} . \tag{6.44}$$

In Eq. (6.44), the term $(r_p^2 - r_b^2)$ includes the effect of central obstruction; the exponential term includes the effect of separation between transmitter and receiver. It can be seen that the familiar link equation can be deduced for the coaxial system when the detector size is large, except that in this case the effective receiver aperture is being reduced by the obstruction. For the noncoaxial systems, on the other hand, the received signal strength can be considerably different from that predicted by the link equation.

6.5 Numerical Results

For the coaxial systems, the change in the return signal strength is mainly due to central obstruction and finite detector size. In Fig. 6.9 the received signal strength is plotted versus altitude for the coaxial system without central obstruction and for different detector radii. The telescope is assumed to be focused at infinity. When the detector is very large, the result reduces to the familiar link equation so that there is a z^{-2} dependence. For a finite detector size, signals at close distances are partially detected because the target is not focused on the detector. In Fig. 6.10, we show the results for the system with central obstruction. For large detector size, the return signal is uniformly reduced in proportion to the smaller effective receiver area. However, the z^{-2} dependence is

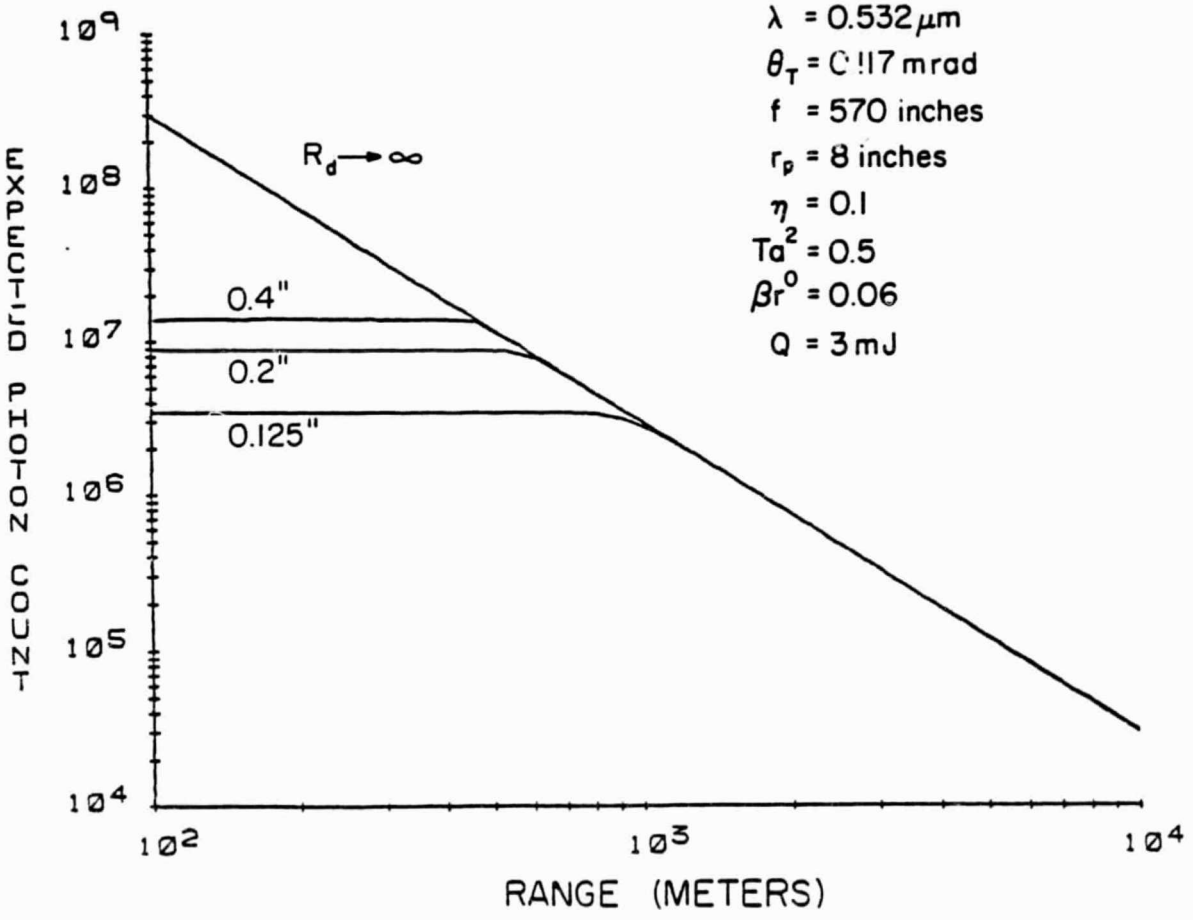

Fig. 6.9. Expected signal photocount versus range for the coaxial system without central obstruction. Telescope is focussed at infinity.

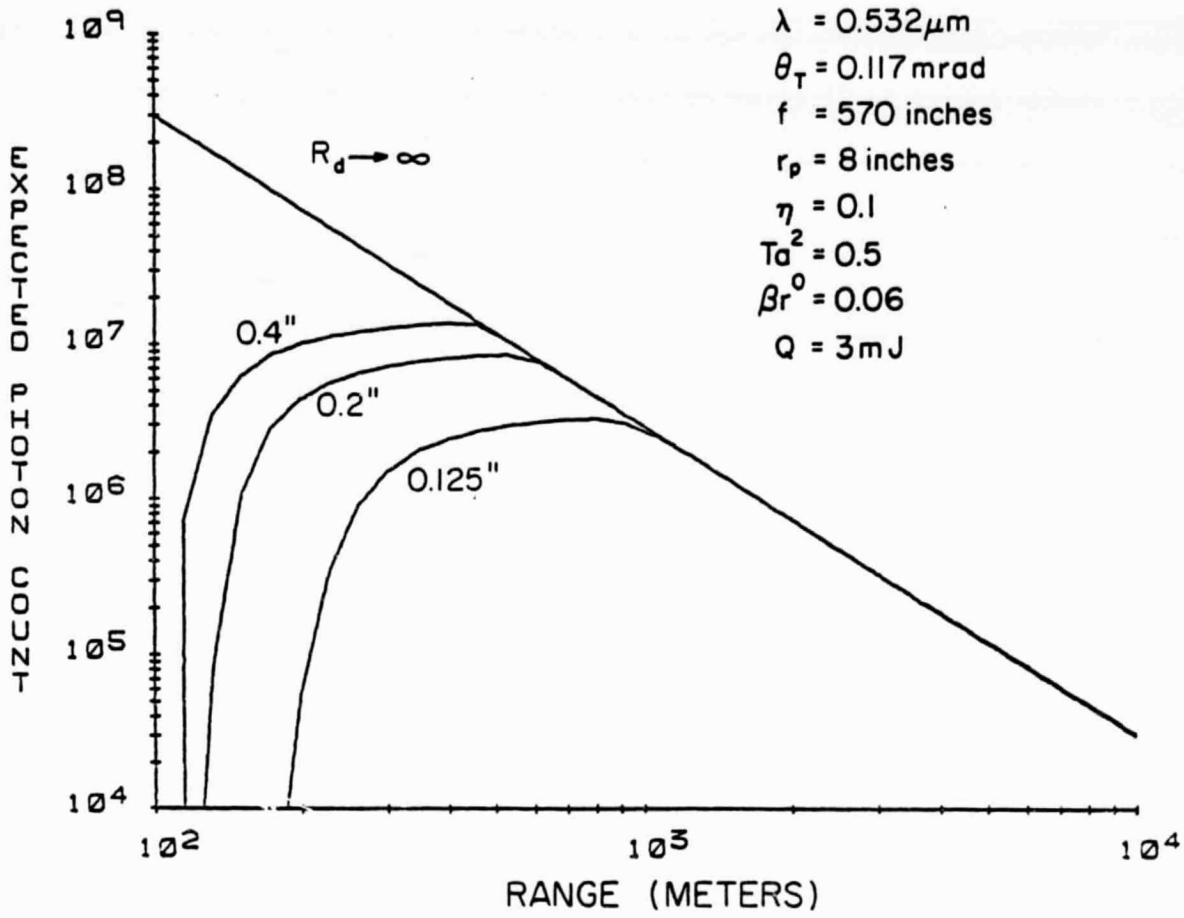

Fig. 6.10. Expected signal photocount versus range for the coaxial system with central obstruction. Telescope is focussed at infinity.

maintained because all the energy collected by the telescope is detected (Eq. (6.44) with $d = \delta = 0$). For small detectors, on the other hand, the signals reflected from targets at close distances are reduced appreciably because the obstruction causes a shaded region in the detector plane. This shaded region is directly related to the size of the obstruction.

In the noncoaxial systems, the change in return signal strength is mainly due to the relative orientation between the transmitter and receiver. Fig. 6.11 shows the received signal strength as a function of distance for a system separation (d) of 9 inches and for different inclination angles δ. In this figure, we do not include the effect of obscuration. For comparison, the results from the standard link equation and the signal levels of a corresponding coaxial system are also given. It can be seen from the figure that even for the modest separation of the transmitter and receiver, only the signals of limited range region are detected by the receiver. The strongest signals are detected from the distances where the laser footprints and the receiver FOV's completely overlap each other. The signal levels fall off rapidly as the overlapping areas decrease. The distance at which a peak signal can be detected decreases with increasing inclination angle δ.

In Fig. 6.12 the signal strength is plotted versus distance for the noncoaxial system with central obstructon. The parameter used in this figure is the same as that in Fig. 6.11. We can see the central obstruction reduces the signal level uniformly at large ranges. In addition, the return signals from short distances are reduced in strength due to the shadowing in the detector. However, the effect is relatively minor compared to the effect of system separation.

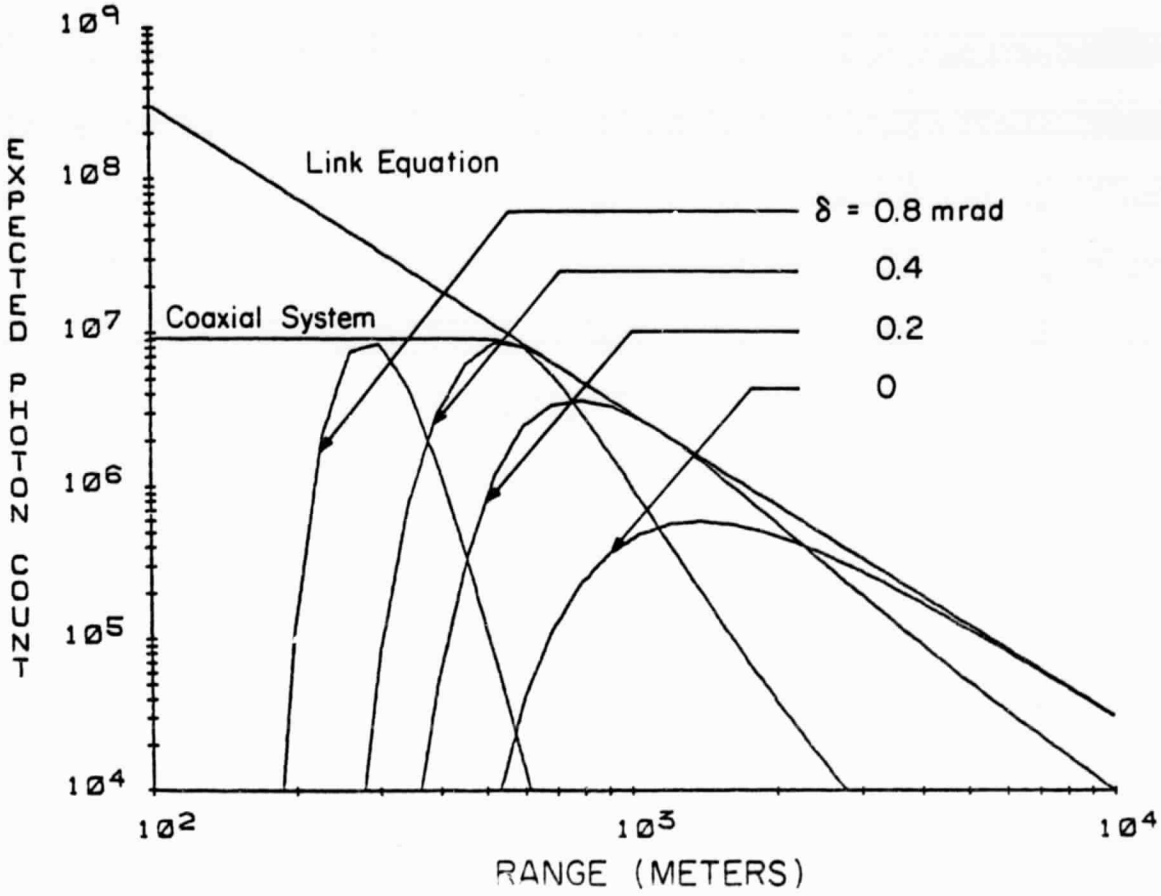

Fig. 6.11. Expected signal photocount versus range for the noncoaxial system without central obstruction. Telescope is focussed at infinity. The transmitter and receiver are separated by 9 inches. The remaining parameters correspond to those given in Fig. 6.9.

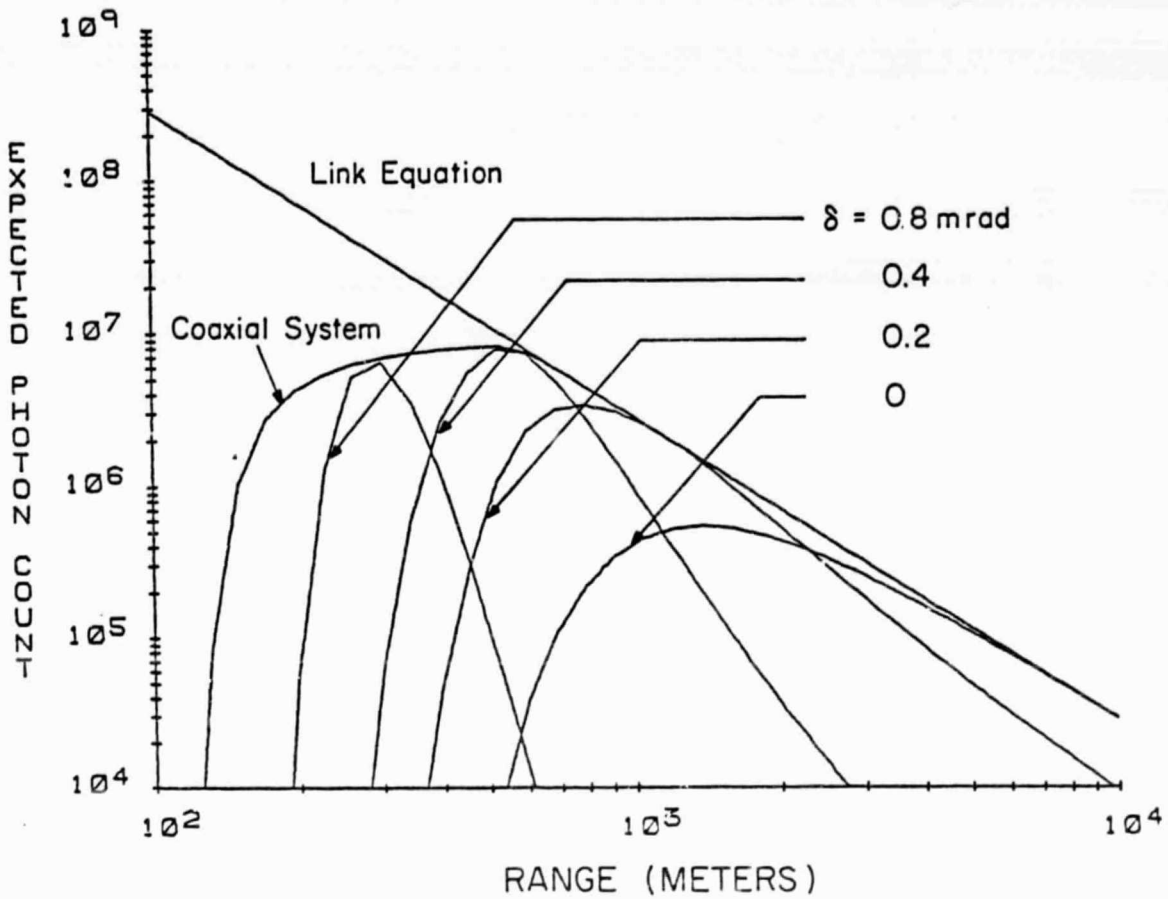

Fig. 6.12. Expected signal photocount versus range for the noncoaxial system with central obstruction. Telescope is focussed at infinity. The transmitter and receiver are separated by 9 inches. The remaining parameters correspond to those given in Figure 6.10.

In Fig. 6.13, the received signal strength is plotted versus the displacement d for the system with central obstruction and with parallel axes ($\delta = 0$). This system, although ideally matched at infinity (complete overlap), suffers from a strong reduction of the near range signals. This reduction of the near range signals is not due to the obstruction, but is the result of incomplete overlap between the transmitter and receiver at close distances. Consequently, this system is suitable for satellite distance ranging, but not so for airborne ranging.

6.6 Conclusion

In this chapter the system alignment effects on the performance of two-color laser ranging systems were investigated. When the transmitted laser beams at two wavelengths have different beam divergences and/or are misaligned, the correlation between the two signals is reduced considerably. Consequently, the timing performance of the correlation receiver is degraded. The degradation is particularly severe when the two beams are misaligned. It was also shown that the expected correlation coefficient depends on the expected signal strength and the relative magnitude between the receiver bandwidth and the bandwidth of the mean signal. The best correlation can be obtained when there is no system error, when the signal strength is high, and when the receiver bandwidth is only slightly larger than the signal bandwidth.

The effects of the central obstruction on return signal strengths were also investigated. In coaxial systems, the central obstruction is more important to signals from short distances because it causes a shaded region in the detector plane and results in appreciable reduction in signal level. For large distances the obstruction gives rise to a uniform reduction of the signal level. In noncoaxial systems, the suppression of return signals is

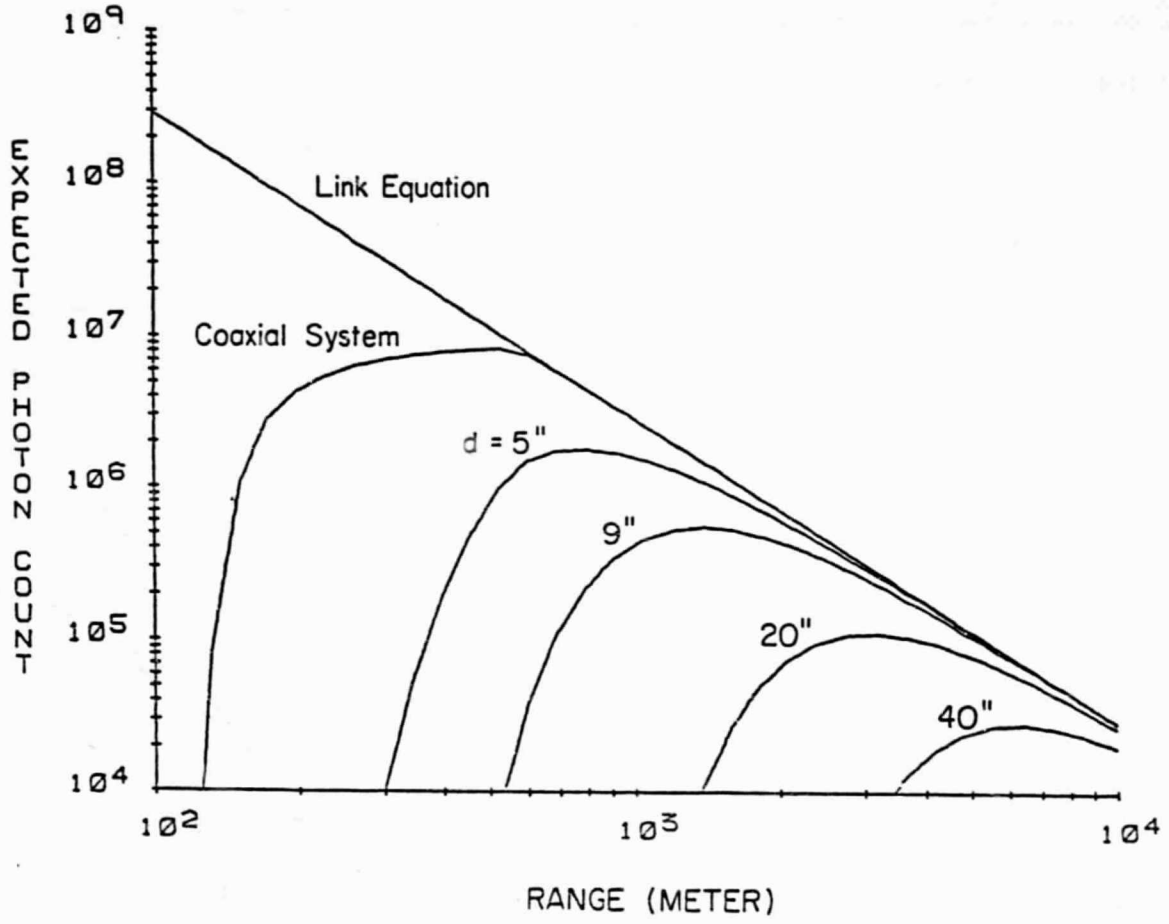

Fig. 6.13. Expected signal photocount versus range for the noncoaxial ranging system with parallel transmitter and receiver axes ($\delta = 0$). Telescope is focussed at infinity. The remaining parameters correspond to those given in Figure 6.10.

primarily due to the incomplete overlap of the transmitted beam with the receiver's field-of-view. Noncoaxial systems with parallel axes suffer from considerable loss in signal return at small to medium distances and approach the coaxial signal for long distance. The obstruction effect of the receiver appears to be less significant as compared to the effects of the geometrical arrangements in the noncoaxial systems. The advantage of using the noncoaxial systems is that the unwanted signals (such as background noise) can be compressed by choosing the system separation and inclination angle carefully so that complete overlap between the laser footprint and the receiver FOV occurs only at the target plane.

7. HORIZONTAL PATH RANGING EXPERIMENTS

7.1 Introduction

Parallel with the theoretical research on the pulsed two-color laser ranging, an experimental program has been administrated by NASA-Goddard Space Flight Center (GSFC) to determine the performance of the available system hardware and identify possible hardware limitations in the past five years. By using a mode-locked ND:YAG laser transmitter and a photomultiplier-based receiving system, Abshire [1982] first demonstrated that differential timing accuracies of a few picosecond was achievable when ranging to a single cube corner reflector over a horizontal path of 500 m. In March of 1983, we conducted a single-color horizontal path experiment at GSFC to study the speckle effects and timing accuracies by ranging to a flat diffuse target and a ocean-simulated target [Im, et al, 1983]. Our results showed that single shot accuracies of 90 to 40 psec, respectively, were acheiveable for these two targets. In September of 1983, the first two-color airborne experiment was conducted by ranging to the ocean [Abshire, et al., 1984, Tsai and Gardner, 1984]. The results indicated high correlation between the returns at the two wavelengths, and the single shot accuracy approaching 40 psec was achievable.

The above experimental results indicate that the two-color laser ranging technique is feasible. Yet, the ranging accuracy at that time was limited by the relatively long impulse response time (500 psec) of the system electronics. For the technique to apply to satellite laser ranging, a receiver of much higher time resolution is desirable. In late 1983, a dual-channel streak camera of 5-psec time resolution was interfaced into the ranging system by the NASA personnels. In February and April of 1985, a

series of horizontal path experiments were conducted using the new system. The main objective of these experiments was to verify the theory behind the cross-correlation differential timing algorithm (Chapter 5). In this Chapter, the experimental measurements will be presented and compared with the theory.

7.2 Review of Theory

In a two-color pulsed laser ranging system, the laser pulses of two different wavelengths are transmitted simultaneously. Due to the difference in refractive indices of the atmosphere at different optical frequencies, the two pulses will arrive at the target surface at different times. If the laser intensity cross-sections at the two wavelengths are approximately equal, the mean reflected pulse shapes detected by the receiver will be very similar. Therefore, the difference between the roundtrip propagation times of the two signals can be estimated by cross-correlating the detected pulses and searching for the peak of the correlation function. Mathematically, the cross-correlation estimator can be written as [Im and Gardner, 1985]

$$\hat{\tau}_{COR} = \arg \max_{\tau} \left[\int_{-\infty}^{\infty} dt \; S_1(t) \; S_2(t + \tau) \right] = \arg \max_{\tau} \left[R_{12}(\tau) \right] . \qquad (7.1)$$

S_1 and S_2 are the detected signals at wavelengths λ_1 and λ_2, respectively. $R_{12}(\tau)$ is the cross-correlation function of these two signals. τ is the differential propagation time, and $\hat{\tau}_{COR}$ is its estimate using the correlation algorithm. $\arg \max_{x} (f(x))$ is used to denote the argument x that maximizes f(x).

The performance of the correlation estimator was derived in Chapter 5. This estimator is unbiased, and the MS timing error is highly dependent on the bandwidth of the mean received signal, receiver bandwidth, expected signal strength and the time-resolved speckle.

The bandwidth of the received signal is inversely related to the time extent of the received signal, which in turn is related to the ranging geometry and the reflecting properties of the target surface. When ranging to a diffuse target, the reflected signals are broadened mainly due to the range spread of the target. When ranging to a specular target such as a cube corner reflector (CCR) array, the reflected signals contain sharp glints which characterize the point target response of the ranging system. The signal statistics for these two target configurations were given in Chapter 3. For the experimental work reported here, we are primarily interested in the pulse reflections from a tilted diffuse flat target board with its surface area larger than the size of the laser footprint, and from a tilted CCR array with its surface area much smaller than the size of the laser footprint. The latter configuration is of particular interest because CCR arrays have been deployed on satellites (LAGEOS and GEOS) and the moon and are routinely used as targets for geodetic measurements. By assuming Gaussian models for the receiver impulse response and the transmitted signal intensity, the expected received signals for these two target configurations can be expressed as

$$\langle S(t) \rangle = \begin{cases} \dfrac{\langle N \rangle}{\sqrt{2\pi}\,\sigma_S} e^{-t^2/2\sigma_S^2} & \text{for tilted diffuse flat target} \\ \dfrac{\langle N \rangle}{\sqrt{2\pi}\,\sigma_g} \sum_{m=1}^{M} \exp\left\{ - \dfrac{[t - 2\xi(\underline{\rho}_m)/c]^2}{2\,\sigma_g^2} \right\} & \text{for tilted CCR array} \end{cases} \tag{7.2}$$

where

$$\sigma_S = (\sigma_g^2 + \sigma_r^2)^{1/2} = (\sigma_f^2 + \sigma_h^2 + \sigma_r^2)^{1/2} \tag{7.3}$$

is the RMS pulse width of the detected singal that has been reflected from a tilted diffuse flat target, and σ_r is the pulse broadening due to the range spread of the target. The remaining quantities were defined in Chapter 5. According to Eq. (7.2), the mean received signal reflected from a tilted diffuse flat target is Gaussian shaped, while the mean received signal reflected from a CCR array consists of a train of narrow pulses with widths equal to the point target response of the receiver. Each pulse corresponds to reflections from one CCR. When $\xi = 0$, the individual pulses merge to form a single pulse. When $0 < \xi < c\sigma_g$, the pulses overlap partially which results in broadening of the overall pulse shape and a reduction in signal bandwidth. When $\xi > c\sigma_g$, the pulses do not overlap so that the signal bandwidth is equivalent to that of a single pulse. The RMS pulse width of the reflected signal from the CCR array can be calculated from Eq. (7.2) as

$$\sigma_S^2 \cong \sigma_g^2 + \frac{4}{c^2 M} \sum_{m=1}^{M} (\xi(\underline{\rho}_m) - \bar{\xi})^2 \qquad \text{for CCR array} \qquad (7.4)$$

where $\bar{\xi}$ is the average range of the CCR array

$$\bar{\xi} = \frac{1}{M} \sum_{m=1}^{M} \xi(\underline{\rho}_m) \quad . \qquad (7.5)$$

The power spectrum of the mean recieved signal ($|\Phi_S(\omega)|^2$) is particularly useful in determining the mean signal bandwidth. It can also provide information on the photocount of the mean pulse measurements provided the system is properly calibrated. $|\Phi_S(\omega)|^2$ is defined as

$$|\Phi_S(\omega)|^2 = \left| \int_{-\infty}^{\infty} S(t)\, e^{-j\omega t}\, dt \right|^2 \quad . \qquad (7.6)$$

For the flat diffuse target and the CCR array, Eq. (7.5) can be evaluated explicitly using Eqs. (7.2) and (7.3) to give

$$|\Phi_S(\omega)|^2 = \begin{cases} \langle N\rangle^2 \, |G(\omega)|^2 \, e^{-\omega^2\sigma_r^2} \\ \qquad\qquad - \omega^2\sigma_S^2 \qquad\qquad \text{tilted diffuse flat target} \\ = \langle N\rangle^2 \, e \\ \\ \dfrac{\langle N\rangle^2}{M^2} \, |G(\omega)|^2 \sum_{m=1}^{M} \sum_{n=1}^{M} \cos\left[\dfrac{2\omega}{c}\left(\xi(\underline{\rho}_m) - \xi(\underline{\rho}_n)\right)\right] \\ \qquad\qquad\qquad\qquad \text{tilted CCR array} \\ \qquad\qquad - \omega^2\sigma_g^2 \\ = \dfrac{\langle N\rangle^2}{M^2} \, e \qquad \sum_{m=1}^{M} \sum_{n=1}^{M} \cos\left[\dfrac{2\omega}{c}\left(\xi(\underline{\rho}_m) - \xi(\underline{\rho}_n)\right)\right] \end{cases} \tag{7.7}$$

where

$$|G(\omega)|^2 = |H(\omega)|^2 \, |F(\omega)|^2 \quad . \tag{7.8}$$

$G(\omega)$ is the Fourier transform of the system point target response, $H(\omega)$ is the transfer function of the receiver, and $F(\omega)$ is the Fourier transform of the transmitted signal. It follows from Eq. (7.7) that the MS bandwidth of the mean received signal (B_S) is

$$B_S^2 = \begin{cases} \dfrac{1}{2\sigma_S^2} & \text{tilted diffuse flat target} \\ \dfrac{1}{2\sigma_g^2}\,[1 - \alpha_d] & \text{tilted CCR array} \end{cases} \qquad (7.9)$$

where $(1-\alpha_d)$ is the bandwidth degradation factor derived in Eq. (5.40). It takes on values between 0 and 1. When the pulse reflections from different CCR's completely overlap ($\xi = 0$) or when they are completely separated ($\xi > c\sigma_g$) in time, σ_d is zero and the bandwidth is equal to that of a single pulse. When the pulse train overlaps partially ($0 < \xi < c\sigma_g$), the mean signal bandwidth is reduced because $(1- \alpha_d)$ is less than 1.

When the range spread of the target is larger than the correlation length of the speckle induced fluctuations, the time-resolved speckle will cause small-scale fluctuations within the detected pulse and distort its shape. In this case, it may be difficult to extract the mean signal from the measured data accurately. We can, however, obtain a biased estimate of the mean signal power spectrum by averaging the power spectra of the measured pulses. This technique is particularly useful in situations where the mean signal is not known a priori such as ranging to dynamic targets. The expected power spectrum of the received signal is defined as

$$E[\,|S(\omega)|^2] = \langle |S(\omega)|^2 \rangle \qquad (7.10)$$

where $S(\omega)$ is the Fourier tranform of the $S(t)$. After expansion, we have

$$\langle |S(\omega)|^2 \rangle = \int_{-\infty}^{\infty} \int_{-\infty}^{\infty} dt_1 dt_2 \, \langle S(t_1)\, S(t_2) \rangle \, e^{-j\omega(t_1 - t_2)} \tag{7.11}$$

$$= \int_{-\infty}^{\infty} \int_{-\infty}^{\infty} dt_1 dt_2 \, [C_S(t_1,t_2) - \langle S(t_1) \rangle \langle S(t_2) \rangle] \, e^{-j\omega(t_1 - t_2)}$$

where C_S is given by Eq. (3.23) and is the covariance of $S(t)$. From Eqs. (3.22) and (3.23), it follows that

$$\langle |S(\omega)|^2 \rangle = \langle N \rangle |H(\omega)|^2 + \langle N \rangle^2 K^{-1} |G(\omega)|^2 + |\Phi_S(\omega)|^2 \tag{7.12}$$

where $|H|^2$ and $|G|^2$ are the power spectrum of $h(t)$ and $g(t)$, respectively, and K is the speckle SNR. As can be seen from Eq. (7.12), $\langle |S|^2 \rangle$ is a noisy estimate of $|\Phi|^2$. The first term is due to shot noise, and the second term is due to speckle. These two terms are most significant at high frequencies. To reliably estimate $|\Phi_S|^2$, the signal must be large compared to the shot noise and speckle level. After combining Eqs. (7.7) and (7.12), we have

$$\langle |S(\omega)|^2 \rangle = \begin{cases} \langle N \rangle |H(\omega)|^2 + \langle N \rangle^2 \, |G(\omega)|^2 \left[\frac{1}{K} + e^{-\omega^2 \sigma_r^2} \right] \\ \qquad \text{tilted diffuse flat target} \\ \\ \langle N \rangle |H(\omega)|^2 + \langle N \rangle^2 \, |G(\omega)|^2 \cdot \\ \qquad \text{tilted CCR array} \cdot \\ \left\{ \frac{1}{K} + \frac{1}{M^2} \sum_{m=1}^{M} \sum_{n=1}^{M} \cos \left[\frac{2\omega}{c} \left(\xi(\underline{\rho}_m) - \xi(\underline{\rho}_n) \right) \right] \right\} \end{cases} \tag{7.13}$$

For the diffuse target, $|\Phi_S|^2$ can be estimated accurately at the frequency range

$$\omega < \begin{cases} \left(\dfrac{\ell n \langle N \rangle}{\sigma_S^2 - \sigma_h^2} \right)^{1/2} & K >> \langle N \rangle \\ \left(\dfrac{\ell n\ K}{\sigma_S^2 - \sigma_g^2} \right)^{1/2} & K << \langle N \rangle \quad . \end{cases} \tag{7.14}$$

We can see from Ineq. (7.14) that $\langle |S(\omega)|^2 \rangle$ can estimate $|\Phi_S|^2$ accurately when $\langle N \rangle$ and K are large, and when the received signals have narrow pulse widths. For the CCR array, accurate estimate of $|\Phi_S|^2$ can only be achieved when the array surface is normal to the optical axis such that

$$\xi(\underline{\rho}_m) - \xi(\underline{\rho}_n) = 0 \qquad \forall\ m,n, \tag{7.15}$$

and when both $\langle N \rangle$ and K are large. When the array is tilted, there will always be some frequency components

$$\omega = \frac{k\pi c}{4\ (\xi(\underline{\rho}_m) - \xi(\underline{\rho}_n))} \qquad k=1,2,\ldots \tag{7.16}$$

that fall below the shot noise level and cannot be estimated.

The various parameters mentioned in this section will be compared with the experimental measurements in subsequent sections.

7.3 Experimental Configuration

The major elements comprising the two-color laser ranging system used during the experiments were a mode-locked, frequency-triple ND:YAG laser transmitter and an image-intensified streak camera-based receiver.

The laser transmitter assembly is given in Fig. 7.1. When the laser is triggered, its flashlamps are fired, and the 1.064-μm radiation rapidly increases within the oscillator cavity. This cavity contains both a dye cell to force mode-locking, and an etalon to control the width of the oscillator pulse. The optical output from the oscillator contains 6 to 12 of these pulses with a pulse separation time of 7 nsec. The Pockels cell is triggered by the oscillator output pulse train. It and the output polarizer pass only a single output pulse and attenuate the remaining input pulses by 20 times. The energy of the selected pulse is then increased by ten times in the amplifier assembly. This output pulse is then input to the frequency doubler and the tripler subsequently which convert part of its energy to 0.532 and 0.355 μm. The nominal laser output is 6 mJ at 1.064 μm, 3 mJ at 0.532 μm, and 1 mJ at 355 μm. The three output pulses are coincident in time and exit the transmitter simultaneously.

The streak-camera-based receiver uses the swept-image converter to provide psec response time, which is about 15 times faster than the transmitted pulse widths. The operation of the linear scan streak camera is shown in Fig. 7.2. The incident optical pulse illuminates the photocathode and frees photoelectrons from its rear surface. These photoelectrons are accelerated rapidly by a mesh electrode and are deflected vertically by a fast electrical sweep. This results in a time-to-space mapping of the electron stream. The resulting electron distribution impinges on the microchannel plate, which preserves the spatial distribution and amplifies it. The amplified electron

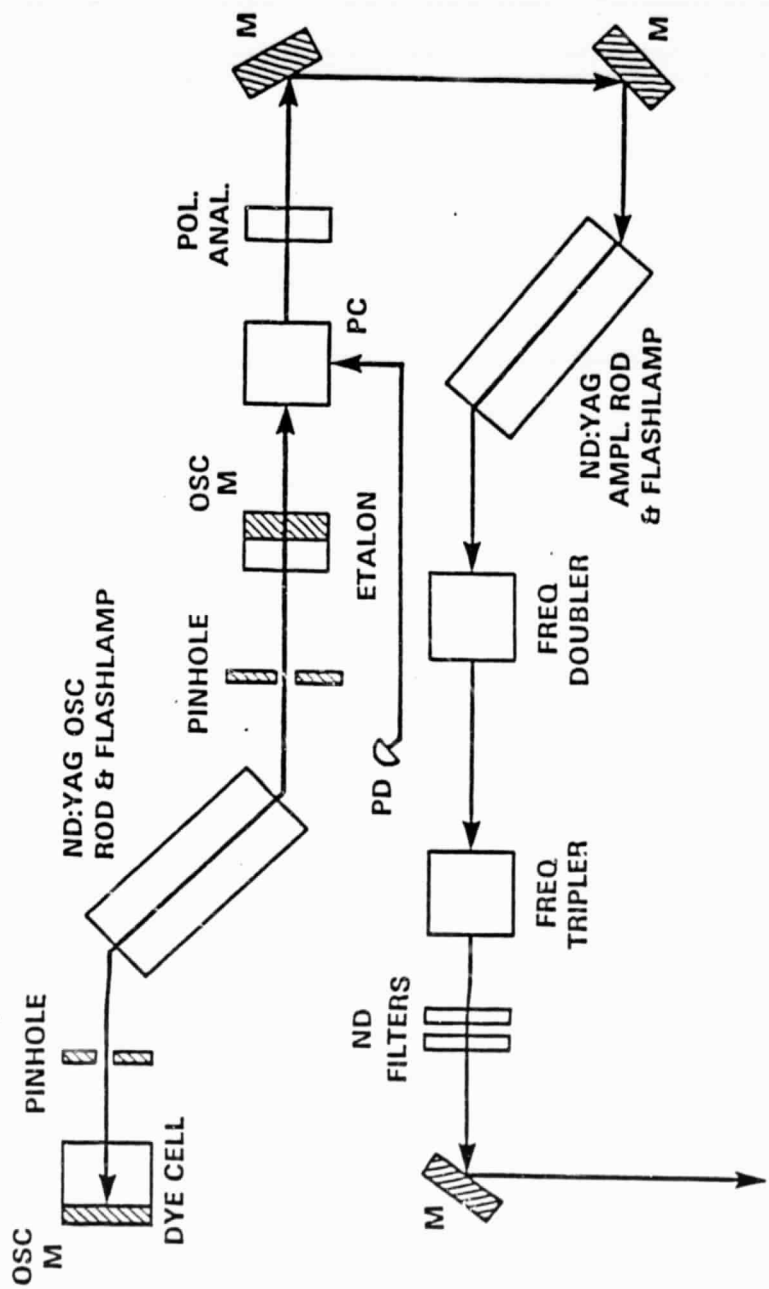

Fig. 7.1. Dye modelocked, frequency-tripled ND:YAG laser transmitter.

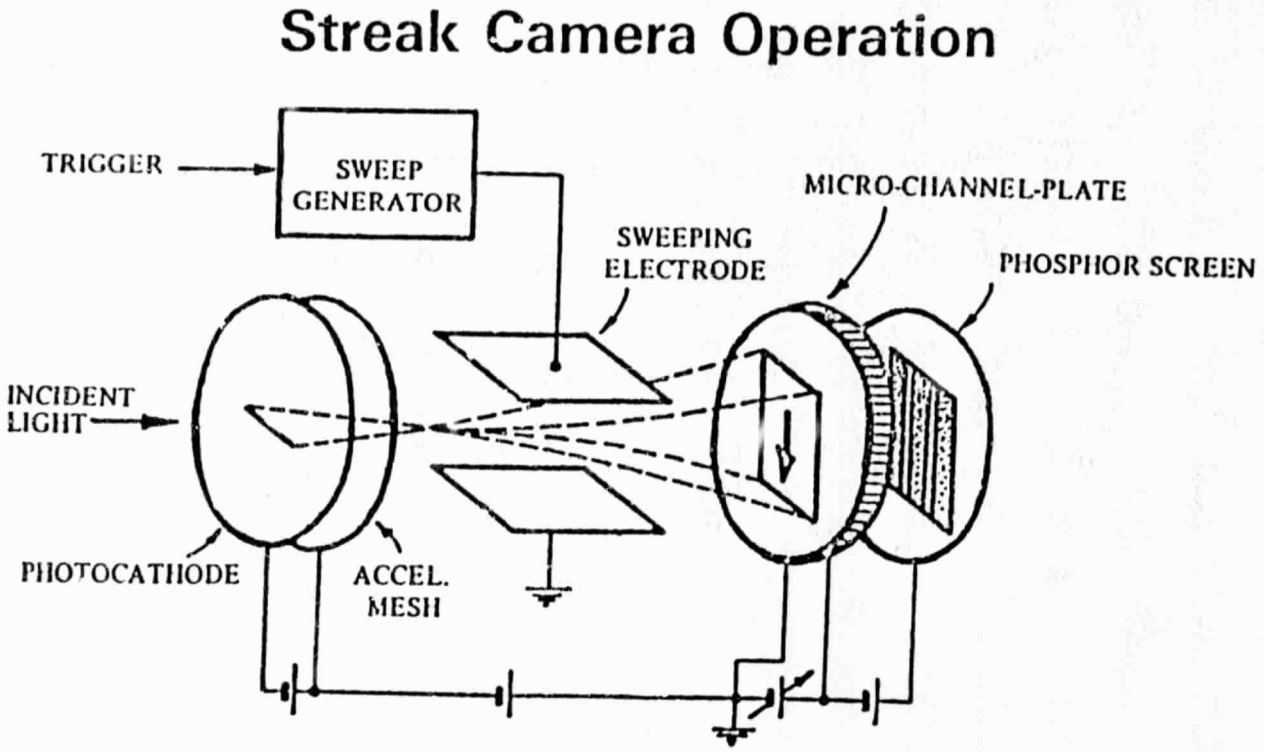

Fig. 7.2. Operation of a typical linear scan streak camera.

bundle exits the rear of the plate and is accelerated into a phosphor screen. This produces a weak optical image whose spatial intensity distribution is proportional to the temporal intensity distribution of the illuminating pulse. An intensified video camera reads out this image, and a digitizer-microprocessor system converts it back to an intensity versus time profile.

The ranging system configuration used during the CCR array test is shown in Fig. 7.3. During the diffuse target test a different transmitter-telescope orientation was used. This new subsystem is shown inside the circle, which replaces the subsystem within the dashed box. However, the principal operation of these two systems are identical. The system parameters are listed in Table 7.1.

The systems were operated in the following manner. The 30 psec (FWHM) pulses at both 0.532 and 0.355 μm from the YAG laser first entered the transmit beam alignment system to eliminate the angular offset due to the nonlinear action of the angle-matched $KD^{*}P$ frequency doubling and tripling crystals inside the laser. Four percent of the aligned signal energy was then reflected by a beam splitter into the reference path to start the timing system and to determine the system delay. The remaining signals at the two wavelengths were directed to the target along a horizontal path. The optical returns from the targets were collected by the receiver telescope. They were reimaged by an eyepiece, which relayed the focal point to the start of the optical delay system. At this point, a beamsplitter reflected part of the optical signals into a photomultiplier, whose output was used to trigger the streak camera and to stop the timing system. The remainder of the reflected energy at each wavelength entered the 40 nsec imaging delay line. This additional delay allowed enough time for the

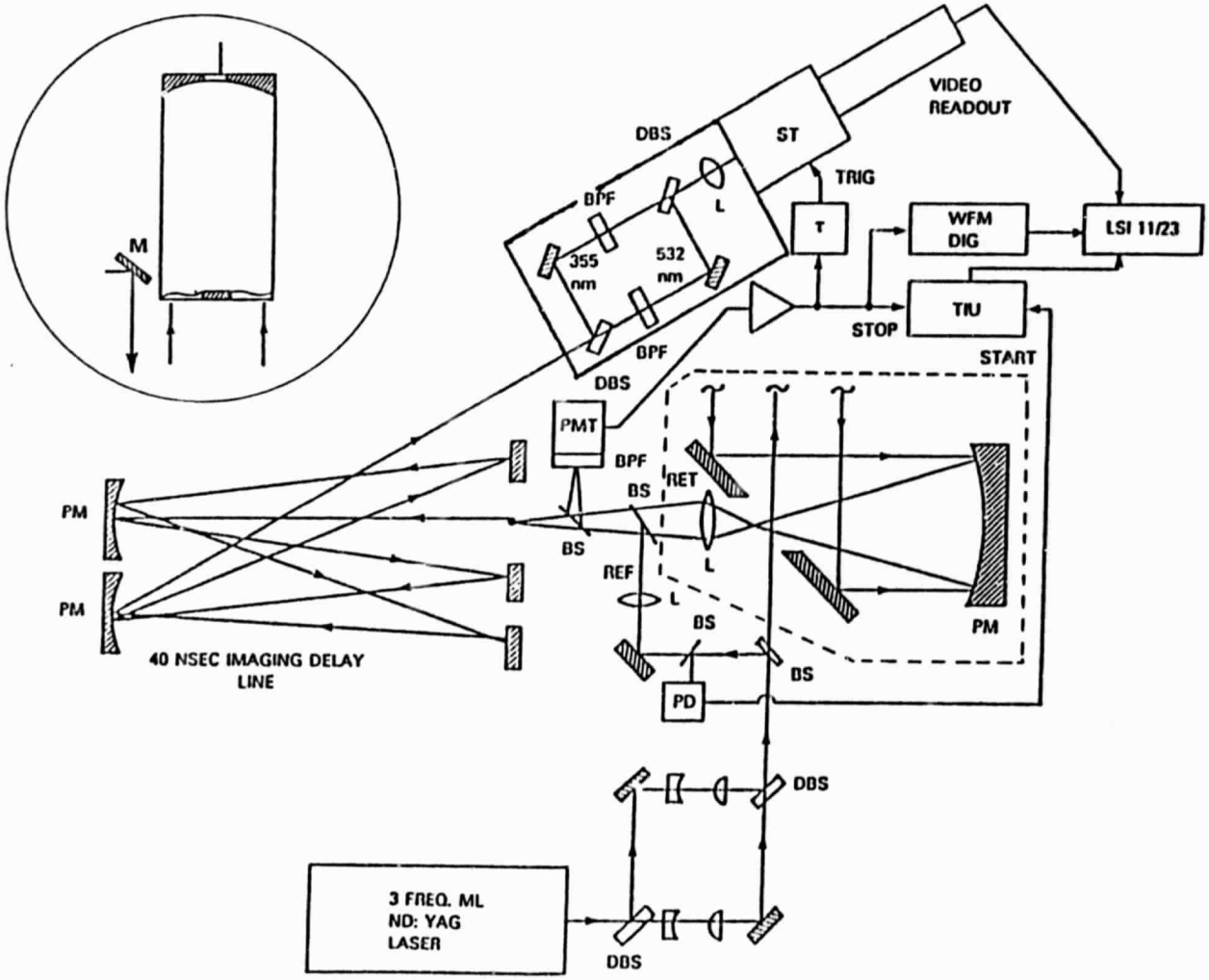

Fig. 7.3. The pulsed, two-color laser ranging systems used during the CCR array and diffuse target experiments.

TABLE 7.1.

SYSTEM PARAMETERS FOR THE TWO-COLOR LASER RANGING SYSTEMS
USED DURING THE HORIZONTAL PATH EXPERIMENTS

System Parameters
Horizontal Path experiments

Laser	:	Quantel YG40 - Mode Locked ND:YAG nominal 30 psec pulse (FWHM) 0.3 mJ at 0.532 μm, 0.5 mJ at 0.355 μm
Telesccpes	:	CCR Array Test - 460 cm^2 area, 91 cm focal length Diffuse Target Test - 891 cm^2 area, 391 cm focal length
Mirrors	:	Double Dielectric maximum reflections at both 0.355 and 0.532 μm
Photomultiplier	:	Hamamatsu R1294, Dual MCP, QE = 4%
Optical Delay	:	White Cell, 8 passes, 40 nsec
Streak Camera	:	Hamamatsu C1370, 5 psec resolution, 85 psec impulse response
TIU	:	HP 5370A, 100 psec accuracy
Computer	:	DEC LSI 11/23, Dual floppy disks

streak camera to eliminate any possible transient effects. The signals from the delay system then entered a light-tight enclosure, where the 0.355-μm pulse was reflected from a dichroic beam splitter, while the 0.532-μm pulse passed through it. The pulse in each path then passed through a bandpass filter for background noise rejection. They were then recombined by a second dichroic and were focused into the streak camera photocathode. The slight offset in the focussed spots due to the path splitting permitted the streak camera to record the two pulses simultaneously. The streak camera outputs were electronically read out by the video camera, and were recorded onto floppy disk for off-line processing.

7.4 Experimental Results for the CCR Array Targets

The cube-corner reflector (CCR) array test was conducted at NASA-Goddard Space Flight Center during February 26 and 27, 1985. Arrays of four CCR's with two different orientations with respect to the optical axis were used. These target geometries are illustrated in Fig. 7.4. The dimensions given in the figure are accurate to within ±0.5 mm (±1.6 psec) on both the length and the depth of the arrays. The first array was orientated such that the target surface was normal to the optical axis. The second array was tilted so that the range spacing between adjacent CCR's was 4 mm. The one-way range for both target configurations was 389 meters. The RMS impulse response time of the streak camera receiver(σ_h) was 27.7 psec. The laser beam divergence angles at both wavelengths were 0.1 mrad full width at the 10% point (0.233 mrad RMS). The nominal transmitted pulse width at each wavelength was 30 psec FWHM (12.7 psec RMS).

The return pulse pairs obtained during the experiment were grouped into sets of 50 to 100 measurements. Typical pulse returns at 0.355- and 0.532- μm from the normal and tilted CCR arrays are shown in Figs. 7.5 and

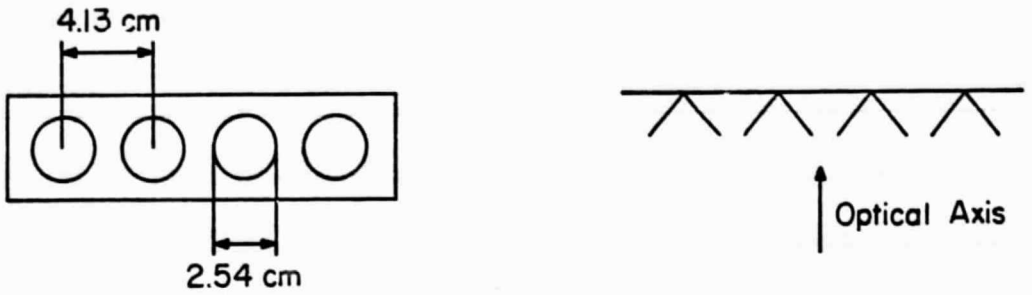

(a) Normal Cube Corner Array

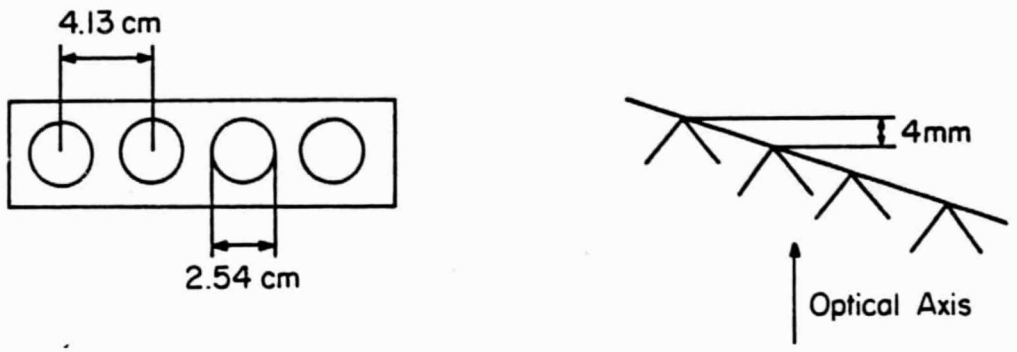

(b) Tilted Cube Corner Array

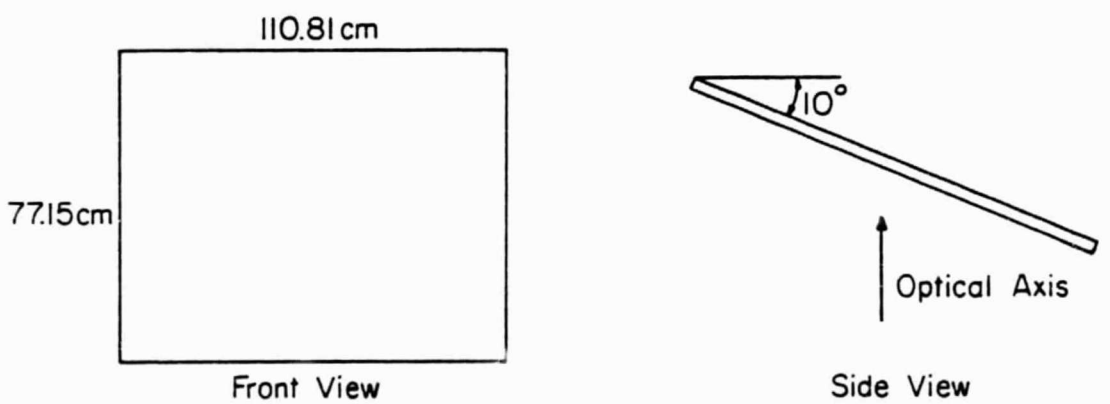

(c) Diffuse Target Board

Fig. 7.4. Geometries of the range targets.

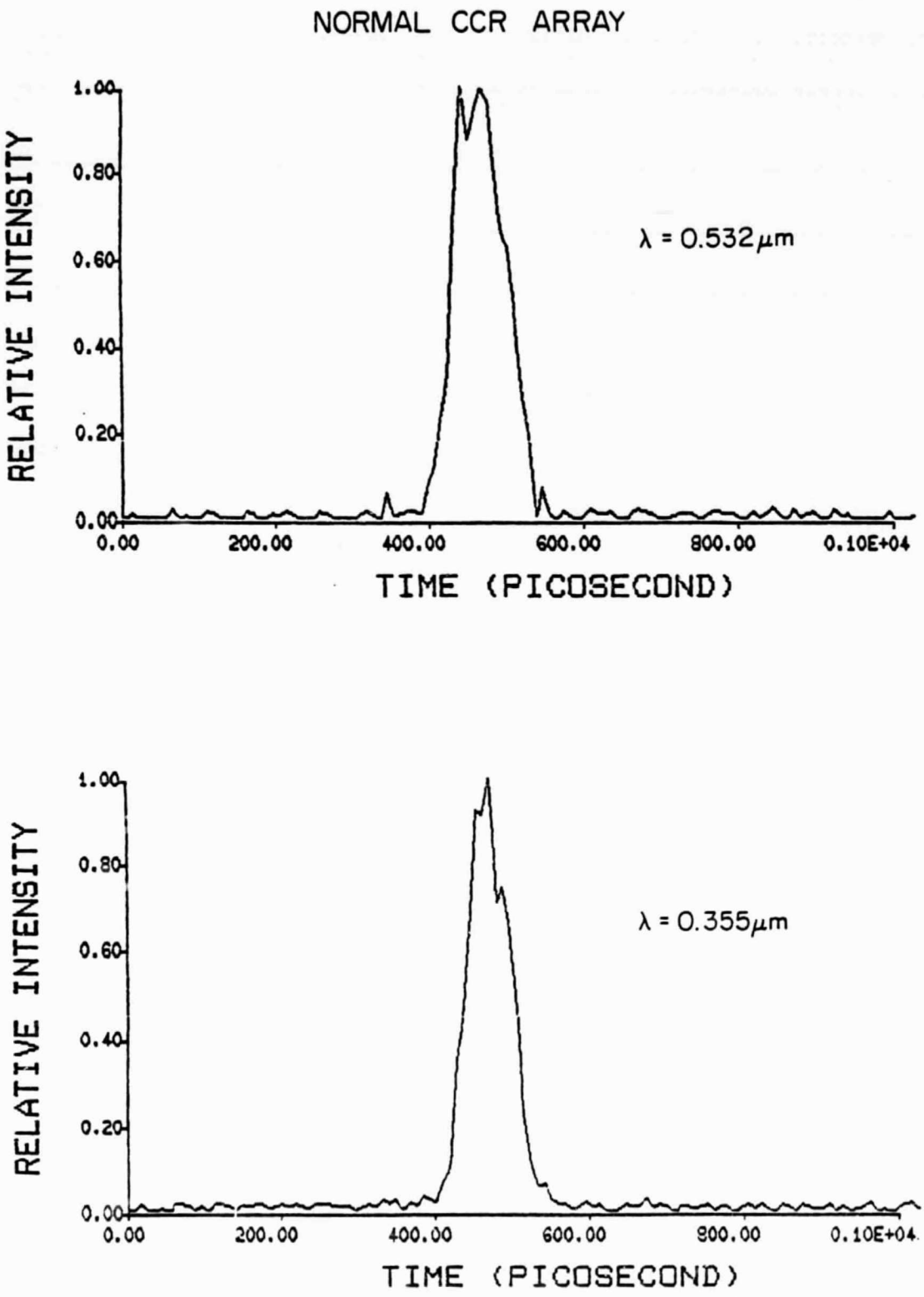

Fig. 7.5. Waveforms of the typical pulsed signals at 0.532 and 0.355 μm reflected from the normal CCR array.

7.6, respectively. With the picosecond time resolution capability of the streak camera receiver, the small-scale structure within a single pulse can be observed. This structure is due primarily to speckle induced fluctuation which results from the coherent interference of the pulses reflected from different CCR's. From Eq. (3.23) the speckle correlation length is $\sqrt{2}\ \sigma_g$, which is much shorter than the range spreads of the pulse returns from the tilted array. Consequently, the time-resolved speckle induced fluctuation in these pulses are particularly severe as shown in Fig. 7.6.

By using Eq. (7.2) and the system parameters, the mean signal at each wavelength for the normal array should be Gaussian shaped with an RMS width of 30.5 psec. The mean signal for the tilted array should consist of four partially overlapped pulses with their peaks separated by 27 psec. The RMS width of the tilted target is 42.8 psec by using Eq. (7.4).

The mean waveforms in each data set were computed by averaging the measured waveforms. To compensate for the random time jitter of the receiver, the measured waveforms were aligned using a correlation technique. This was done by first selecting a reference pulse pair which had the highest intensity return at 0.355 μm. The remaining pulse pairs were shifted with respect to this reference pair such that the cross-correlation functions were maximized. An apparent mean pulse pair was computed by averaging the shifted waveforms. The shifted pulse pairs were then windowed, correlated, and shifted with respect to this mean and a new mean pulse pair was calculated. This iteration procedure was terminated when no further shifting was required to maximize the correlation function. Normally two to three iterations were required in order to determine the true mean waveforms.

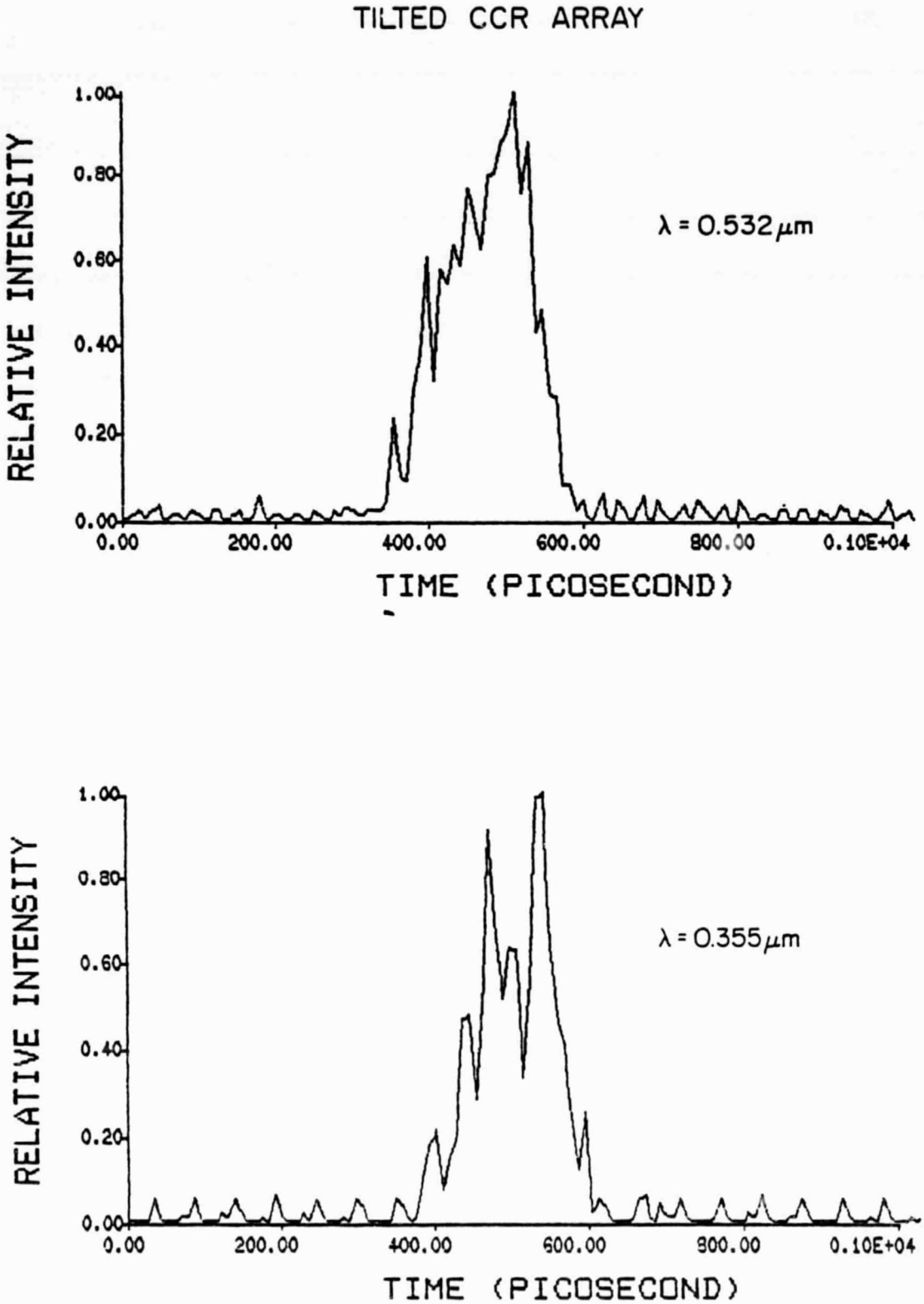

Fig. 7.6. Waveforms of the typical pulsed signals at 0.532 and 0.355 μm reflected from the tilted CCR array.

The waveforms of the typical mean signals for the normal array are shown in Fig. 7.7. As predicted, these waveforms are approximately Gaussian shaped. The widths at the $e^{-1/2}$ point for the 0.532 and 0.355 μm are 68 and 61 psec, respectively, which are approximately equal to twice the predicted RMS pulse width. Fig. 7.8 shows the typical mean signals for the tilted array. These pulses exhibit some sharp glints that correspond to the reflections from CCR's at different range. The spacings between these glints are between 27 and 30 psec as predicted, and the width at the $e^{-1/2}$ point is 102 psec for the mean return at each wavelength.

The measured mean pulse widths on each data set are listed in the second and third columns of Table 7.2. For the normal array, the measured mean pulse widths at 0.532 μm are between 26 and 36 psec, with an average value of 31.4 psec. The measured mean pulse widths at 0.355 μm are between 25 and 33 psec, with an average of 29.2 psec. Both these values are very close to the predicted value of 30.5 psec. For the tilted array, the measured mean pulse widths at both 0.532 μm and 0.355 μm are between 37 and 53 psec, with the average widths of 44.6 psec and 44.7 psec, respectively. Again, both these values agree well with the predicted width of 42.7 psec.

The power spectra of the mean signal measurements ($|\Phi_S(\omega)|^2$) were computed using a 512-point FFT. The spectra of the mean signals shown in Fig. 7.7 for the normal array are plotted in Fig. 7.9. The theoretical prediction using Eq. (7.7) is

$$|\Phi_S(\omega)|^2 = \langle N \rangle^2 \, e^{-\omega^2(\sigma_h^2 + \sigma_f^2)} \quad . \tag{7.17}$$

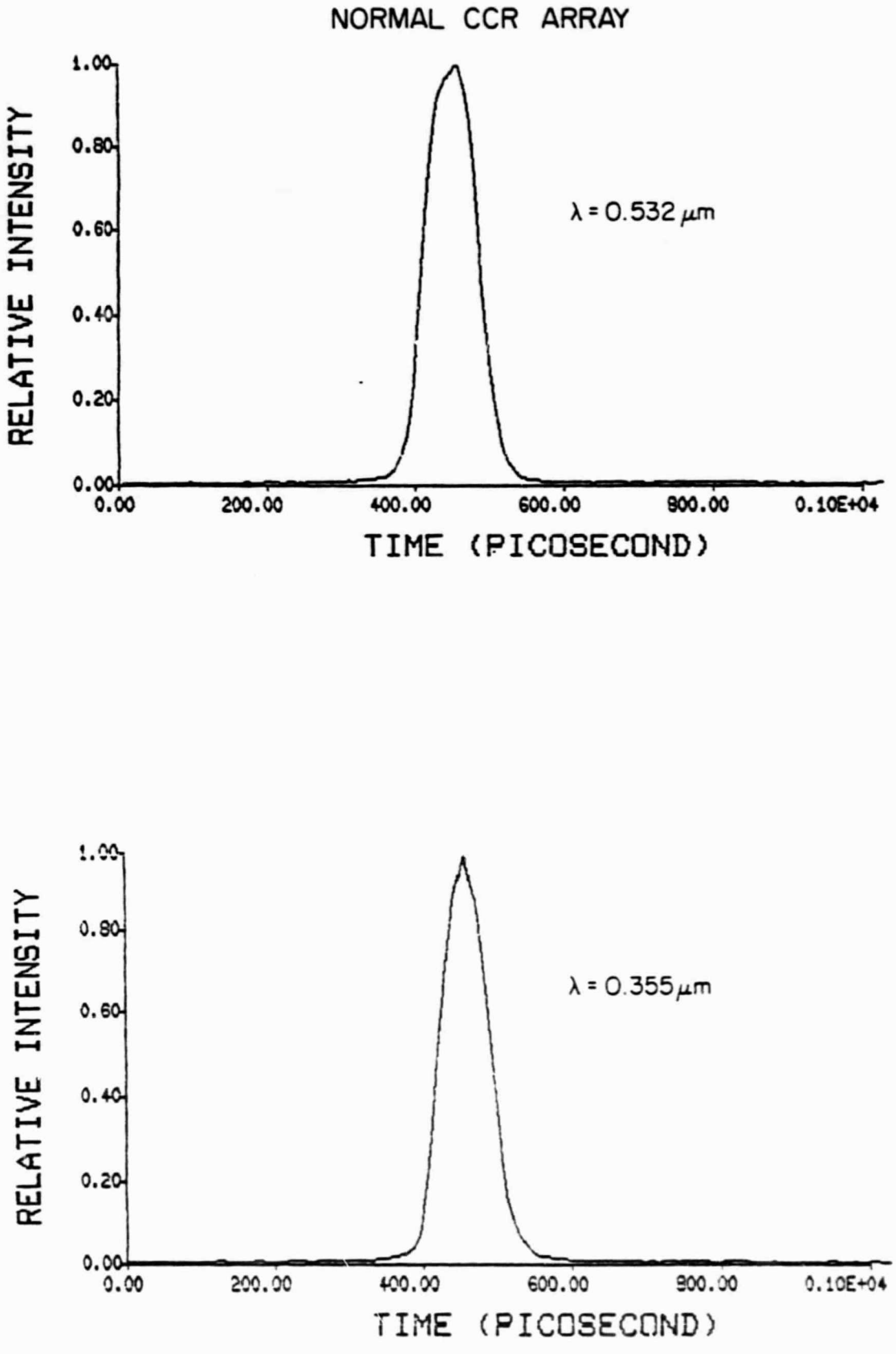

Fig. 7.7. Waveforms of the typical mean pulsed signals at 0.532 and 0.355 μm reflected from the normal CCR array.

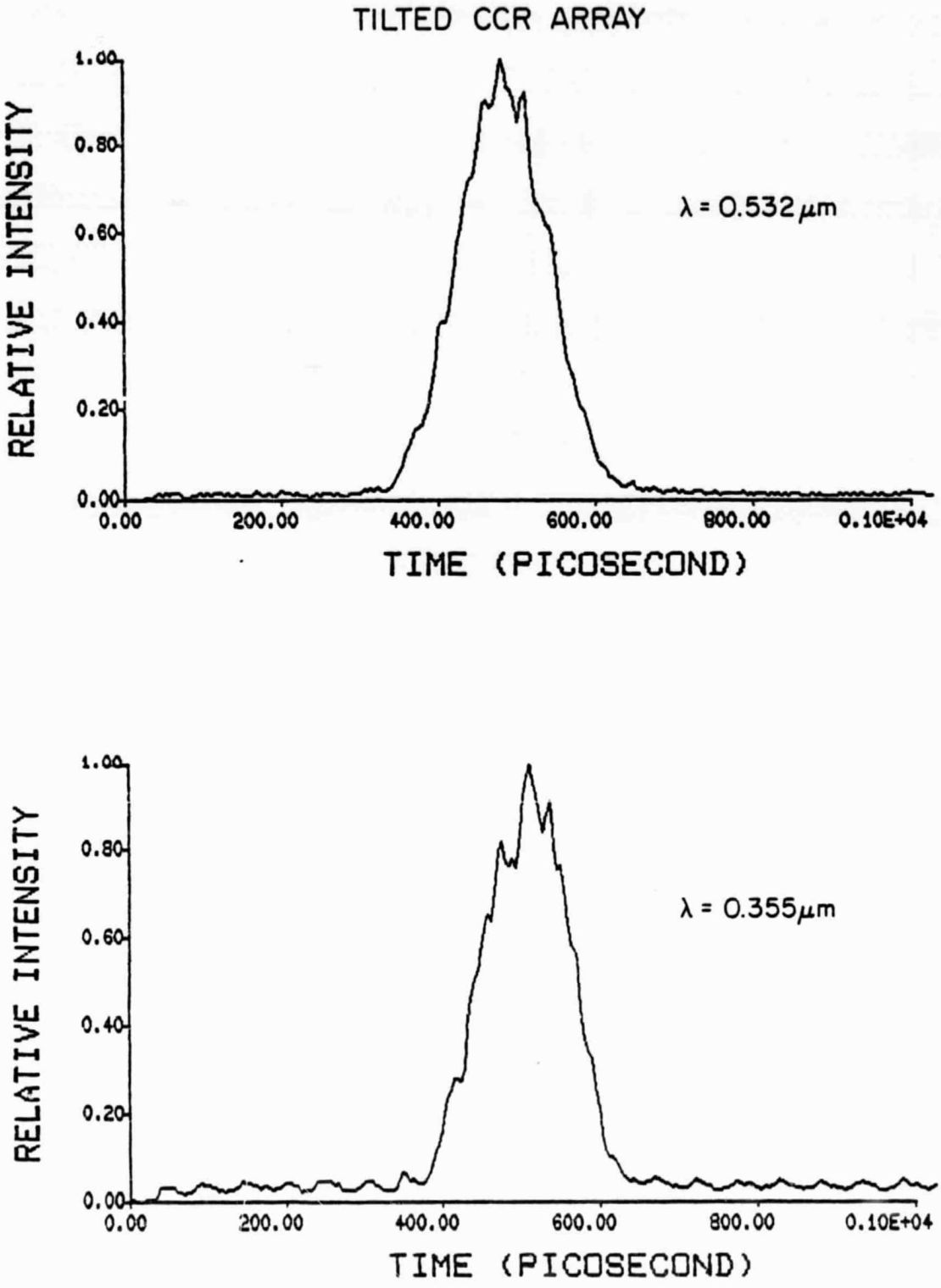

Fig. 7.8. Waveforms of the typical mean pulsed signals at 0.532 and 0.355 μm reflected from the tilted CCR array.

TABLE 7.2.

PULSE WIDTH AND BANDWIDTH MEASUREMENTS FOR THE PULSE REFLECTIONS FROM BOTH THE NORMAL AND TILTED CCR ARRAY

NORMAL CCR ARRAY

	Mean pulse width (psec)		RMS bandwidth (GHz)	
set no.	0.355 μm	0.532 μm	0.355 μm	0.532 μm
1	35.6±1.0	30.5±1.0	3.93±0.07	3.59±0.07
2	31.5	29.5	3.73	4.20
3	28.5	29.5	4.07	3.39
4	35.6	30.5	3.86	3.39
5	31.5	33.6	3.39	2.44
6	30.5	25.4	4.15	3.12
7	26.4	25.4	3.95	3.52
average	31.4	29.2	3.87	3.38

TILTED CCR ARRAY

	Mean pulse width (psec)		RMS bandwidth (GHz)	
set no.	0.355 μm	0.532 μm	0.355 μm	0.532 μm
1	52.9±1.0	52.9±1.0	2.04±0.07	2.24±0.07
2	50.8	47.8	2.44	2.76
3	38.8	38.5	2.56	2.44
4	40.8	39.6	2.04	1.69
5	42.5	43.7	2.82	2.32
6	37.1	37.6	2.49	2.08
7	45.3	46.8	2.04	1.76
8	49.3	50.1	1.82	2.20
average	44.7	44.6	2.28	2.19

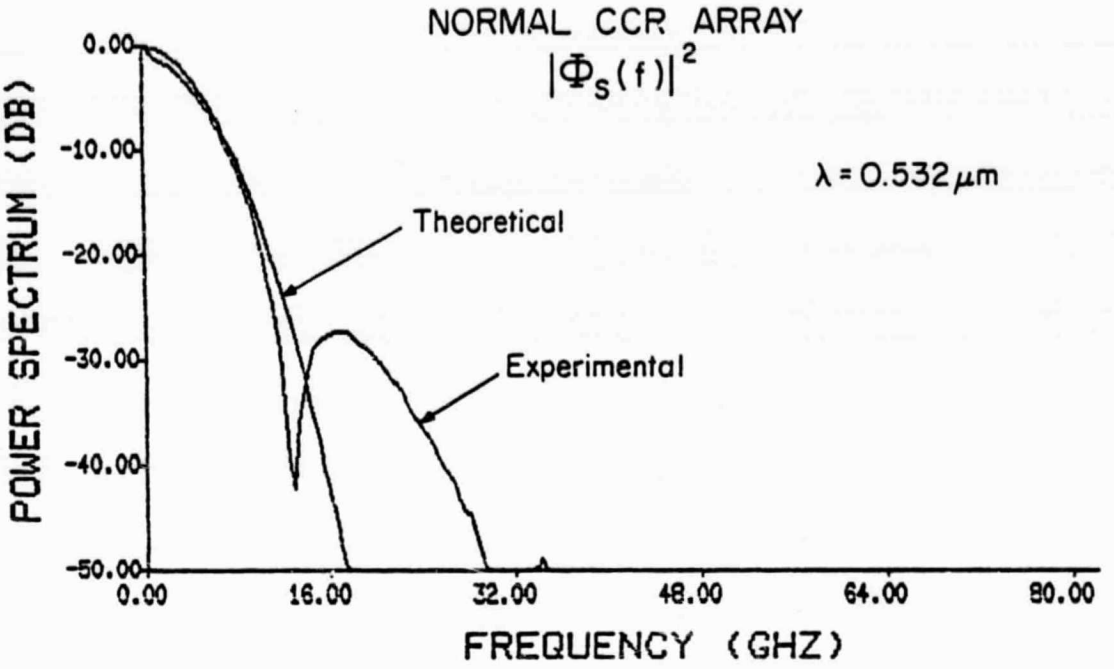

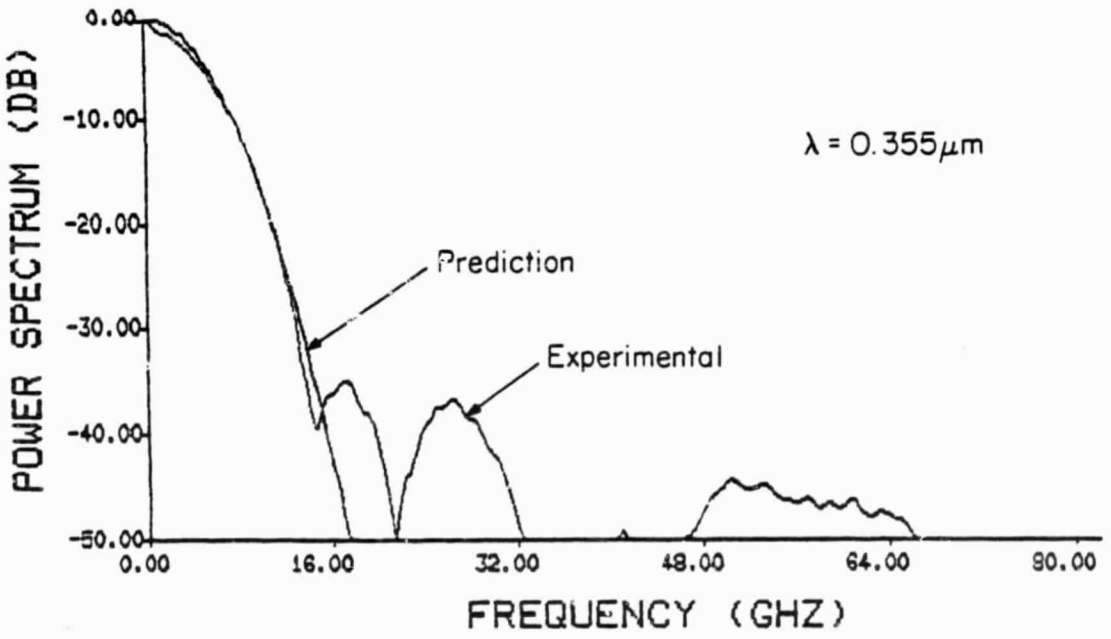

Fig. 7.9. Comparison of the predicted and measured power spectra of the mean signals ($|\Phi_S(\omega)|^2$) for the pulse reflections from the normal CCR array.

Eq. (7.17) is also plotted using the system parameters for comparison. At low frequencies the measured spectra are very similar to the predicted spectra. At higher frequencies the noise components, which arise from slight misalignments in computing the mean signals, distort the spectra slightly. However, the noise levels are at least 30 dB lower than the signal spectra and can be neglected. Notice from Eq. (7.17) that the power spectrum is directly proportional to the magnitude of the system transfer function ($|H(\omega)|$) when the system response width (σ_h) is much larger than the transmitted pulse width (σ_f). Consequently, we can estimate $|H(\omega)|$ using the power spectrum of the mean signal when σ_f is small and when the target range spread is negligible.

The power spectrum of the mean signals reflected from the tilted array is

$$|\Phi_S(\omega)|^2 = \langle N \rangle^2 \, e^{-\omega^2(\sigma_h^2 + \sigma_f^2)} \left[\frac{1}{4} + \frac{1}{8} \sum_{m=1}^{4} (4 - m) \cos\left(\frac{2\omega}{c} mr\right) \right] \tag{7.18}$$

where r is the range spacing between adjacent CCR's. Both Eq. (7.18) and the spectrum of the mean signals shown in Fig. 7.8 are plotted in Fig. 7.10 for comparison. From this figure, we can see that the measured results agree in general with the theoretical prediction at low frequency. Because of the large speckle fluctuations in the returned pulses from this array, the measured signals were not perfectly aligned, which results in the high frequency noise components in the spectra.

The RMS bandwidths of the mean signals can be computed using Eq. (7.9) and the system and target parameters. The predicted values are 3.87 GHz

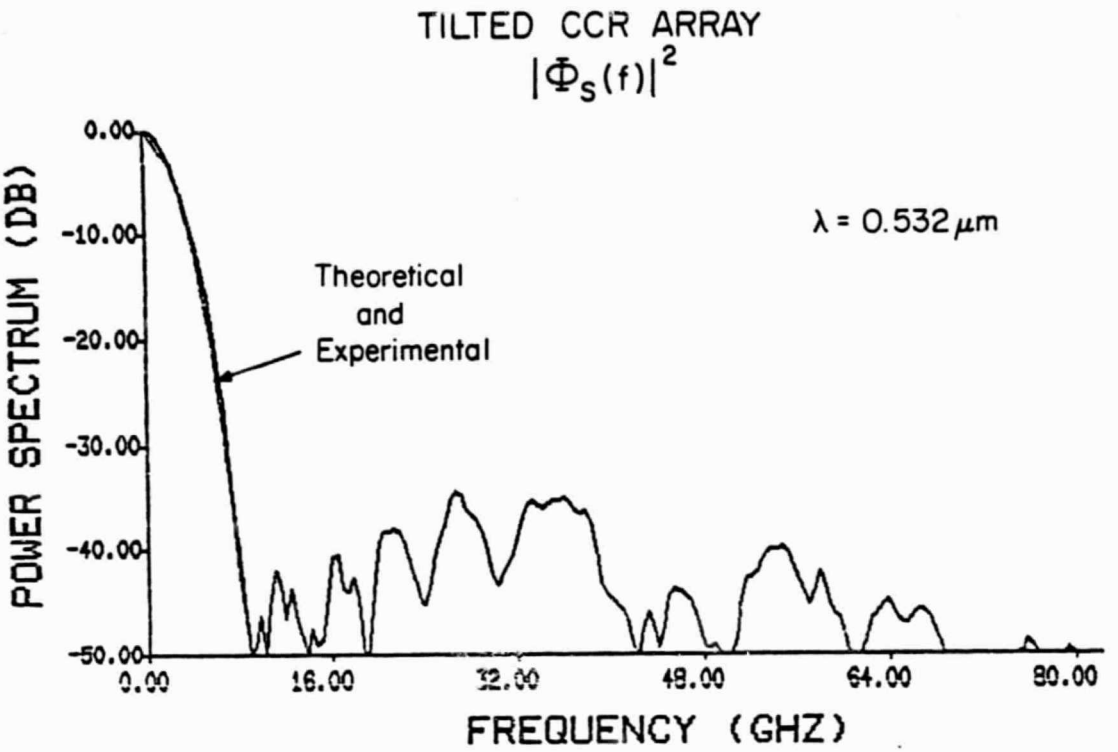

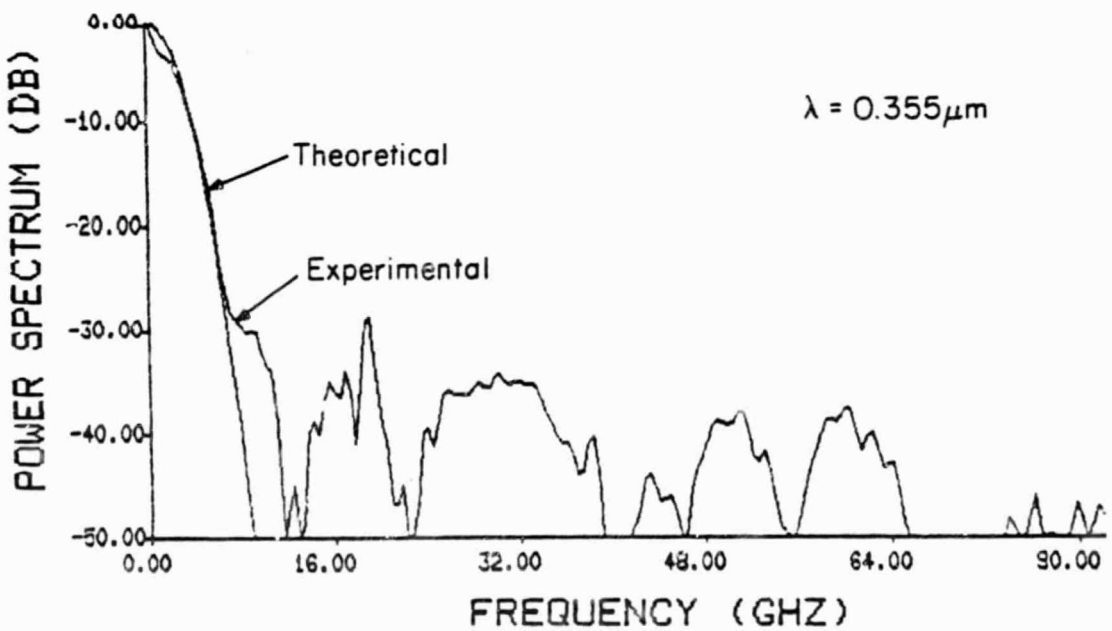

Fig. 7.10. Comparison of the predicted and measured power spectra of the mean signals ($|\Phi_S(\omega)|^2$) for the pulse reflections from the tilted CCR array.

for the normal array and 2.74 GHz for the tilted array. The measured results at both wavelengths are shown in the last two columns of Table 7.2. For the normal array, the 0.532-μm mean signal bandwidth ranges from 2.4 to 4.2 GHz with an average value of 3.38 GHz, and the 0.355-μm mean signal bandwidth ranges from 3.4 to 4.2 GHz with an average value of 3.87 GHz. For the tilted array, the 0.532-μm mean signal bandwidth ranges from 1.7 to 2.8 GHz with an average of 2.19 GHz, the 0.355-μm mean signal bandwidth ranges from 1.8 to 2.8 GHz with an average of 2.28 GHz.

The mean power spectra ($\langle|S(\omega)|^2\rangle$) in each data set were computed by averaging the power spectra of the measured signal waveforms. The typical results are plotted in Fig. 7.11 and 7.12 for the returns from the normal and tilted CCR array, respectively. The power spectra of the mean signals are also plotted for comparison. The flat region in the high frequency band corresponds to the speckle and shot noise levels. As expected, $\langle|S|^2\rangle$ and $|\Phi_S|^2$ are very similar at low frequency. Consequently, $\langle|S|^2\rangle$ can be used to estimate $|\Phi_S|^2$ when the mean signals are not available. At high frequency, however, the shot noise and speckle dominate the mean spectra so that they are very different from $|\Phi_S|^2$.

The atmospheric delay was predicted using the spherical model for the atmospheric refraction and the system parameters. The detailed calculation is shown in Appendix C. For the round-trip horizontal path of 778 m and for the operating wavelengths used in the experiment, the predicted differential propagation time is 59.7 psec. The differential propagation time was estimated by cross-correlating the measured pulse pairs and searching for the time occurrence of the correlation peak. In Fig. 7.13 the estimated results are compared with the prediction for the two-color returns from the normal CCR array. The error bar corresponds to ±1 standard deviation. During the

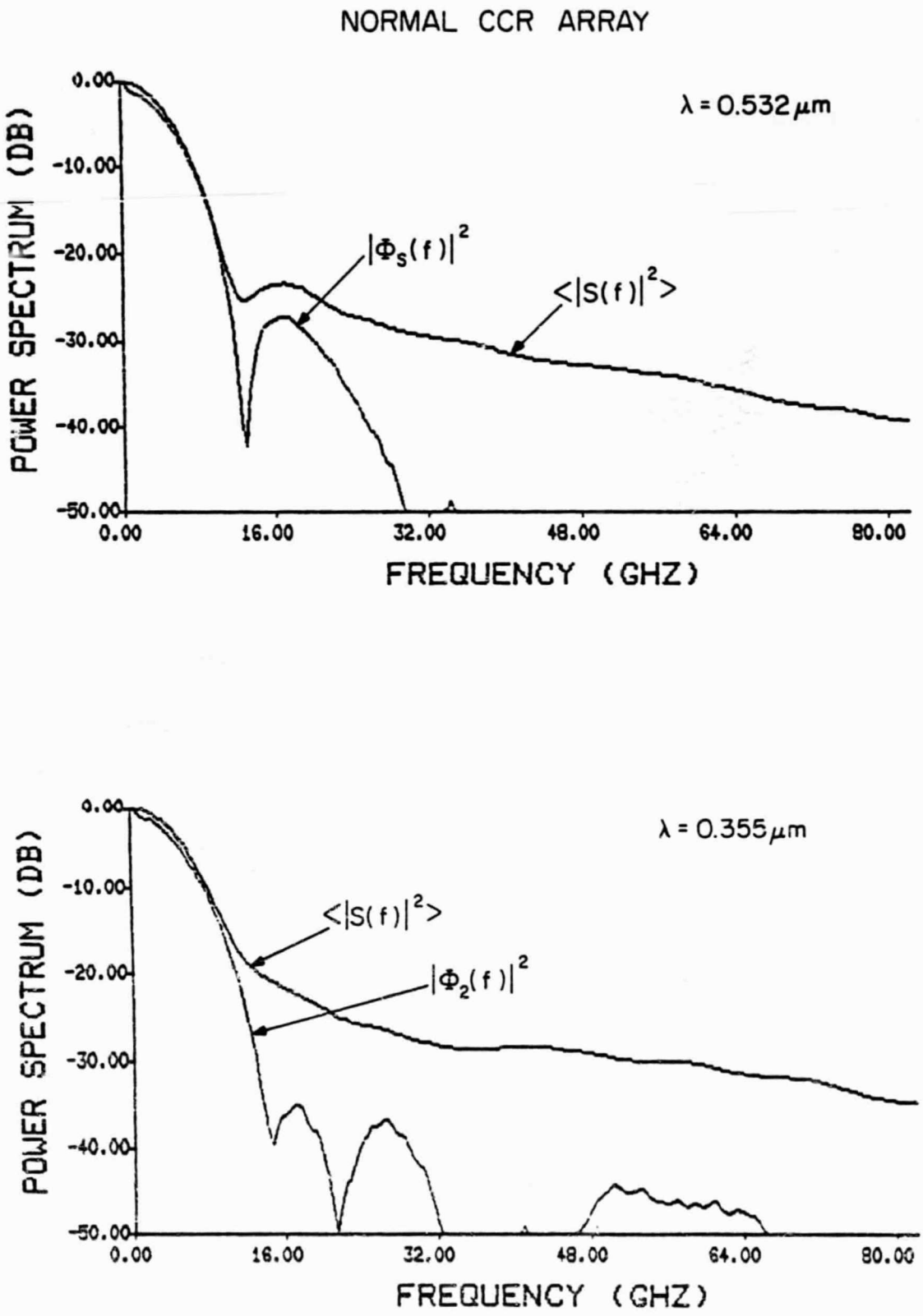

Fig. 7.11. Comparison of the measured results on the power spectra of the mean signals ($|\Phi_S(\omega)|^2$) and the average power spectra of the measured signals ($\langle|S(\omega)|^2\rangle$) for the pulse reflections from the normal CCR array.

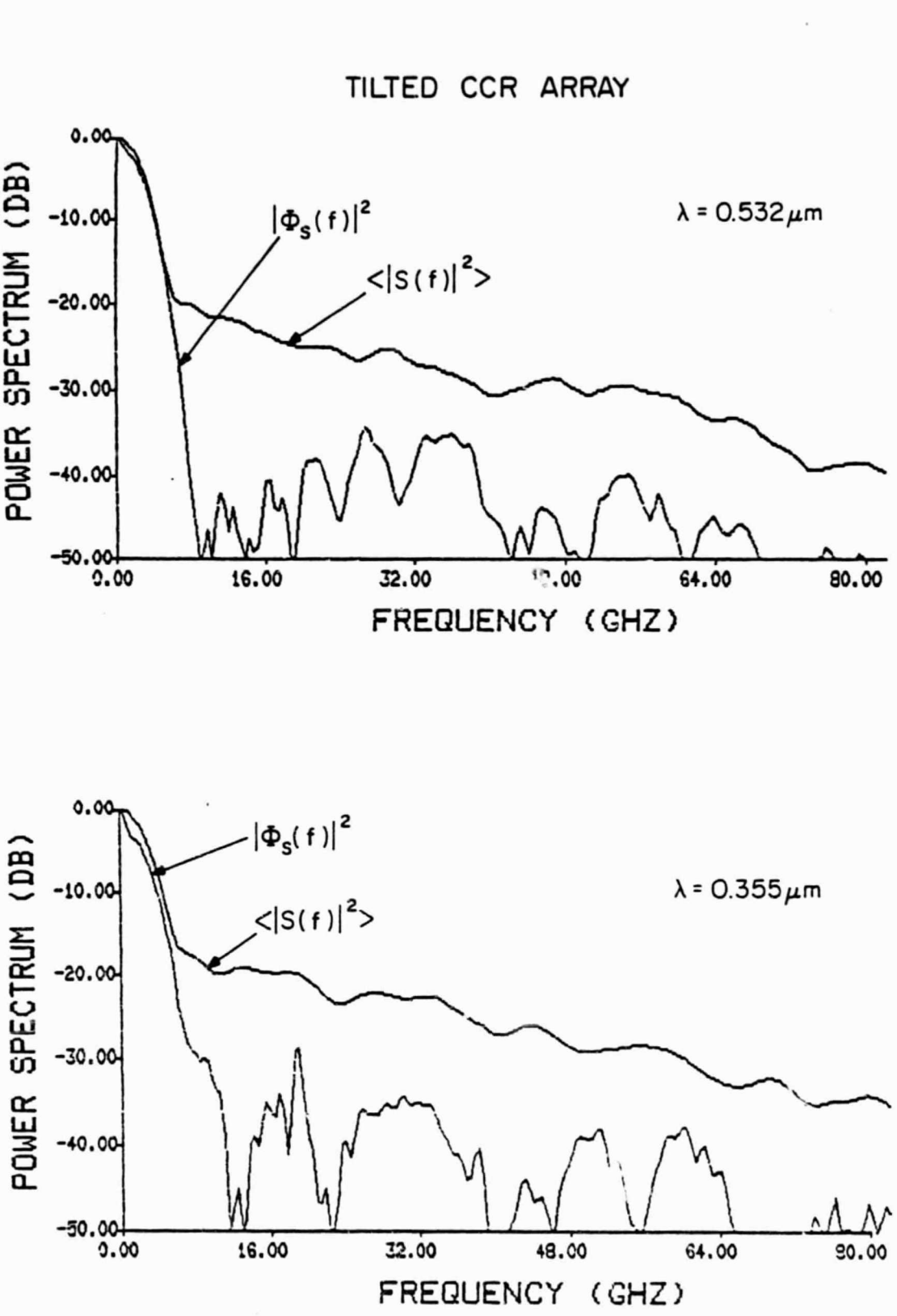

Fig. 7.12. Comparison of the measured results on the power spectra of the mean signals ($|\Phi_S(\omega)|^2$) and the average power spectra of the measured signals ($\langle|S(\omega)|^2\rangle$) for the pulse reflections from the tilted CCR array.

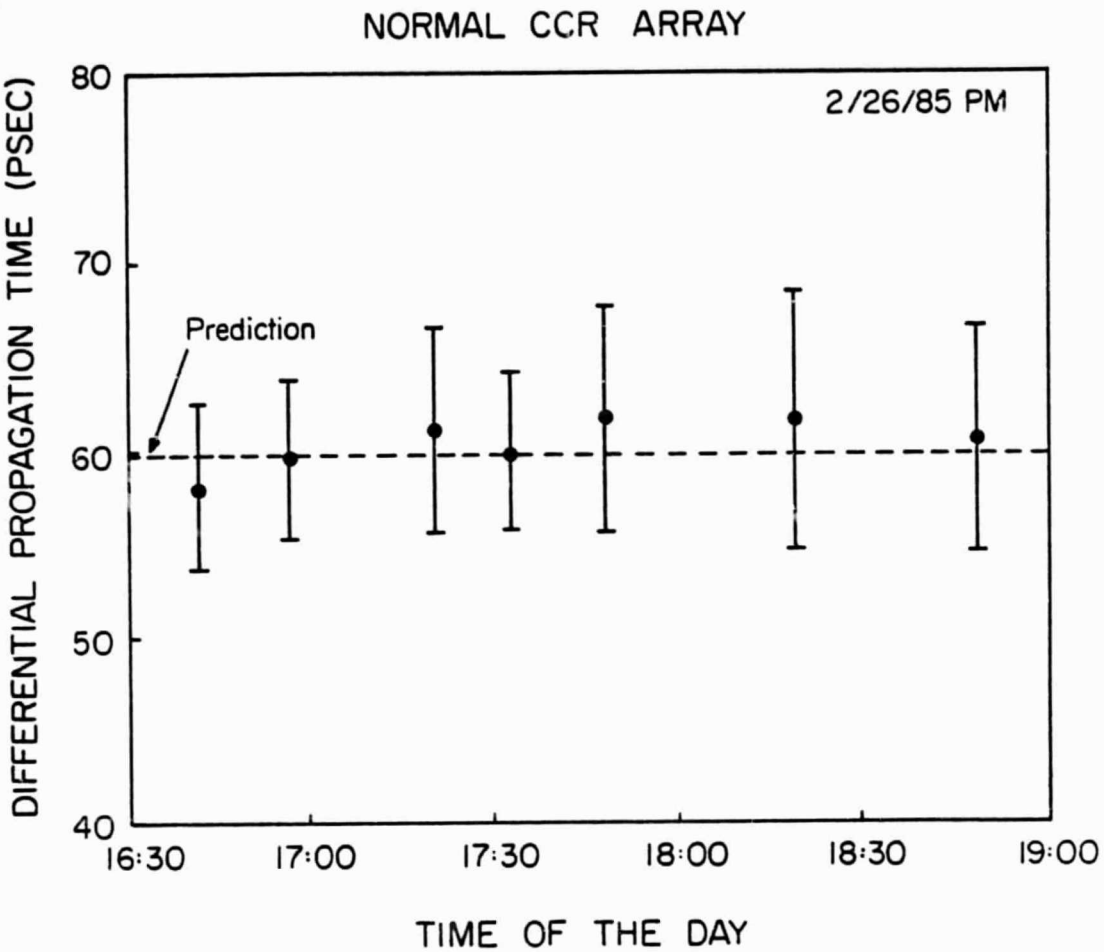

Fig. 7.13. The measured differential propagation time between signals at 0.532 and 0.355 μm using cross-correlation estimator for the pulse reflections from the normal CCR array.

experiment different receiver aperture sizes were used which gave rise to different timing accuracies. The estimated results agree consistently with the predicted dispersive delay. The average bias among seven measurment sets is 0.48 psec, which corresponds to an average bias of 0.072 mm on the one-way differential pathlength.

The estimated round-trip differential propagation times for the tilted CCR array is shown in Fig. 7.14. Because of the broader pulse and time-resolved speckle fluctuations, the accuracies of these measurements are worse than those of the normal target. The average bias among eight measurement sets is 6.1 psec, which corresponds to an average bias of 0.9 mm on the one-way differential pathlength.

Fig. 7.15 compares the timing performance of the correlation receiver to some commonly used estimating schemes. At the time of the experiment there were problems with the gain sensitivity of the streak camera, and it was not possible to measure the signal photocounts ($\langle N_i \rangle$) accurately. Therefore, three different receiver aperture sizes were used in order to determine the dependence of the timing error on the received signal strength. $\hat{\tau}_{ML}$ corresponds to the Maximum-Likelihood estimator of the form

$$\hat{\tau}_{ML} = \max_{\tau} \arg \left[\int_{-\infty}^{\infty} S_1(t) \ \ell n \ \langle S_1(t + \tau) \rangle \ dt \right] - \max_{\tau} \arg \left[\int_{-\infty}^{\infty} S_2(t) \ \ell n \ \langle S_2(t + \tau) \rangle \ dt \right] . \tag{7.19}$$

This estimator was first derived by Bar-David [1969], and it has been shown to be optimal when the speckle is negligible [Tsai and Gardner, 1985]. $\hat{\tau}_{PK}$

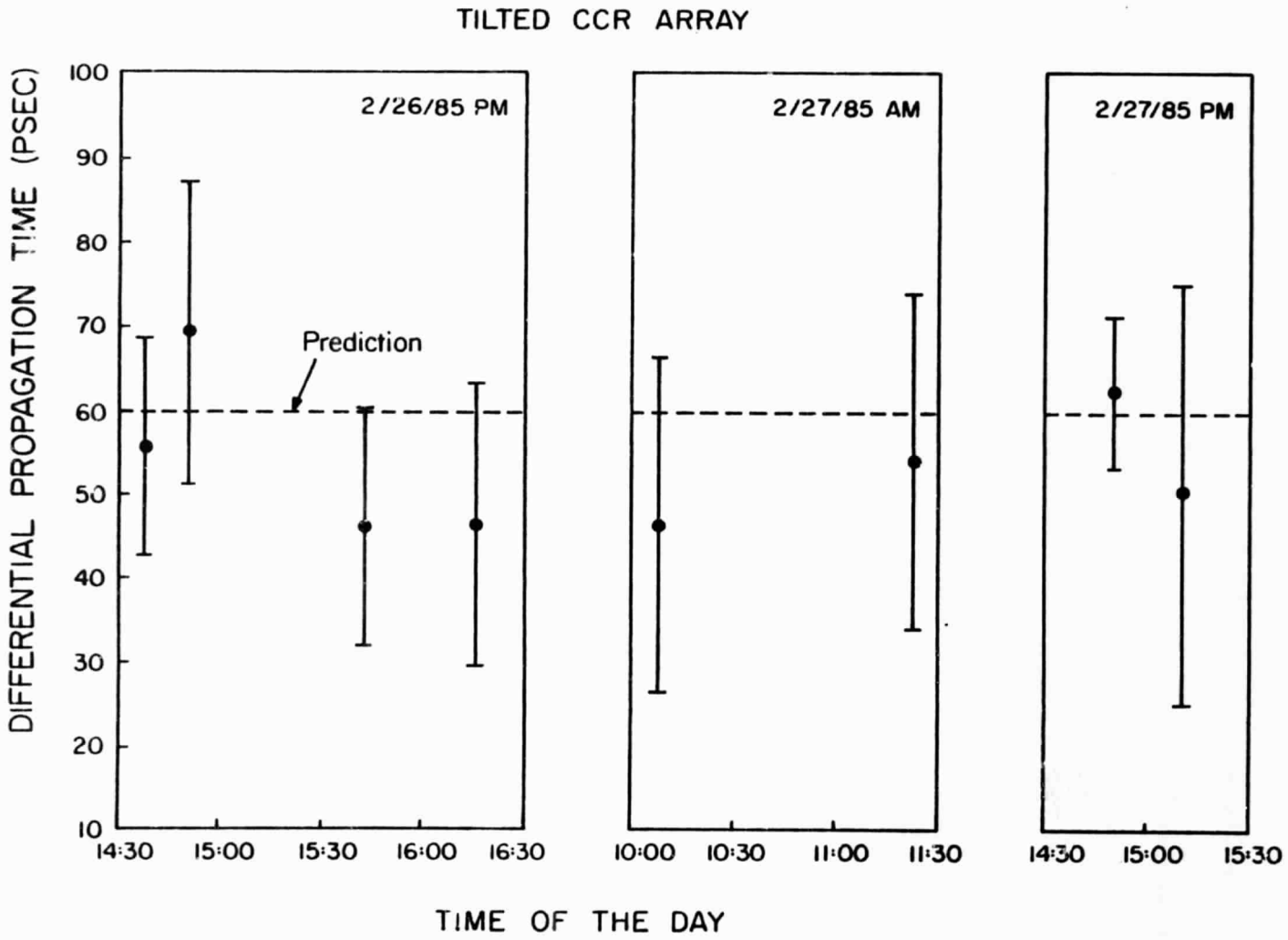

Fig. 7.14. The measured differential propagation time between signals at 0.532 and 0.355 m using cross-correlation estimator for the pulse reflections from the tilted CCR array.

corresponds to the peak detector of the form

$$\hat{\tau}_{PK} = \max_{t} \arg [S_1(t)] - \max_{t} \arg [S_2(t)] \quad . \tag{7.20}$$

Fig. 7.15(a) shows the timing errors when ranging to the normal CCR array. The results indicate that the timing errors are insensitive to the change in the received signal strength. This suggests that the system was operated under the speckle limited condition where the speckle SNR (K_i) at both wavelengths are much less than $\langle N_i \rangle$. This observation is predicted theoretically in Chapter 5. Under these ranging conditions, the performance of $\hat{\tau}_{COR}$ is comparable to that of $\hat{\tau}_{ML}$, and it is much better than that of $\hat{\tau}_{PK}$. Since the implemenation of $\hat{\tau}_{ML}$ requires a priori knowledge on the mean received pulse shape (refer to Eq. (7.19)), it can only be applied to the stationary targets. On the other hand, $\hat{\tau}_{COR}$ is applicable to dynamic targets, and its performance is only slightly inferior to that using $\hat{\tau}_{ML}$ when the speckle effect is dominant.

Fig. 7.15(b) compares the RMS timing errors for the returns from the tilted CCR array. The reference curve (solid line) demonstrates the $\langle N_i \rangle^{-1/2}$ dependence in the shot noise limited ranging condition. It should be pointed out that this reference curve does not give the actual error, it merely indicate the magnitude between the signal strength and the speckle SNR. The measured results show that the signal strength in this case is almost equal to speckle SNR. Within this region, $\hat{\tau}_{ML}$ is close to optimal and so its performance is much better than $\hat{\tau}_{COR}$ and $\hat{\tau}_{PK}$. It was pointed out

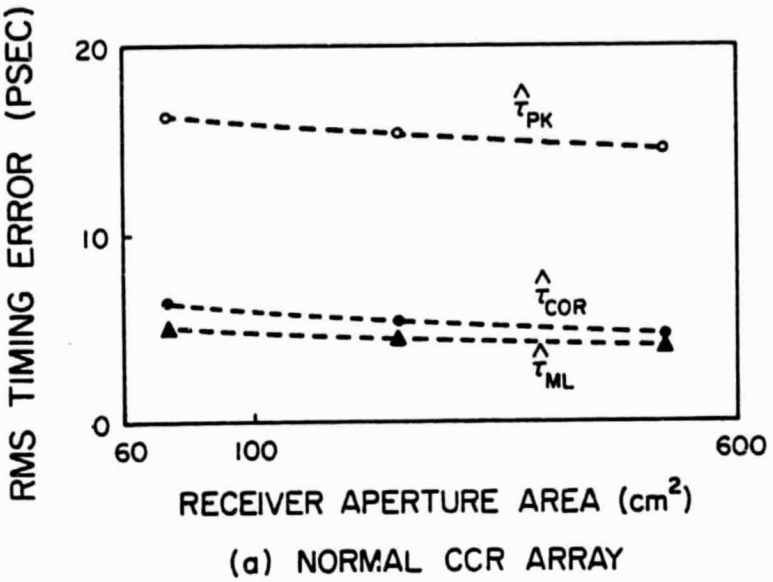

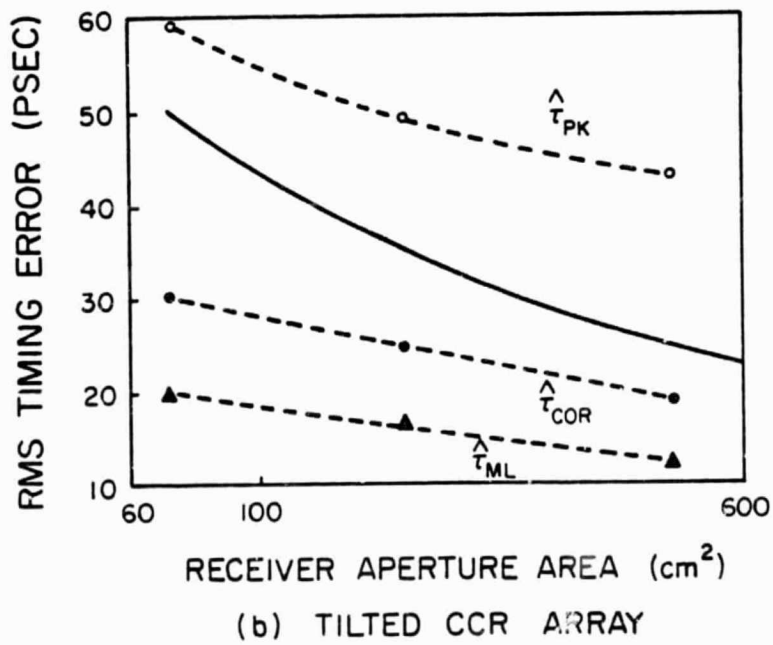

Fig. 7.15. Comparison of the measured RMS differential timing accuracies of the cross-correlation ($\hat{\tau}_{COR}$), Maximum-Likelihood ($\hat{\tau}_{ML}$), and peak detection ($\hat{\tau}_{PK}$) estimators for the pulse reflections from the normal CCR array and the tilted CCR array.

in Chapter 5, however, that the performance of τ_{COR} can be improved by choosing the receiver impulse response time properly.

7.5 Experimental Results for the Diffuse Target

The diffuse target experiment was performed at NASA/Goddard-Wallops Flight Facility during April, 1985. The target was a flat diffuse board tilted 10° with respect to the incident beam. The target geometry is given in Fig. 7.4(c). The target dimensions are accurate to within ±5 mm on the width and the length, and ±1° on the incidence angle. During this experiment a more sensitive streak camera was used. The receiving system had an RMS impulse response time of 36 psec. The transmitted pulse width at each operating wavelength was 30 psec FWHM. The laser beam divergence was 2 mrad FW at the 10% point (0.466 mrad RMS). The one-way target range was 362 meters.

The speckle SNR for the signal reflected from extended diffuse targets is given by (Eq. (5.26))

$$K_i = A_R \left(2 \tan \theta_{T_i} / \lambda_i\right)^2 \tag{7.21}$$

where A_R is the area of the receiver aperture, λ_i is the laser wavelength and θ_{T_i} is the RMS beam divergence angle. For the system parameters used during the experiment, the speckle SNR's at both wavelengths are on the order of 10^5. With these large speckle SNR's, speckle noise is negligible, and the system performance is expected to be dominated by shot noise.

The typical measured waveforms at both wavelengths are shown in Fig. 7.16. Notice that the signal intensities are relatively low compared to

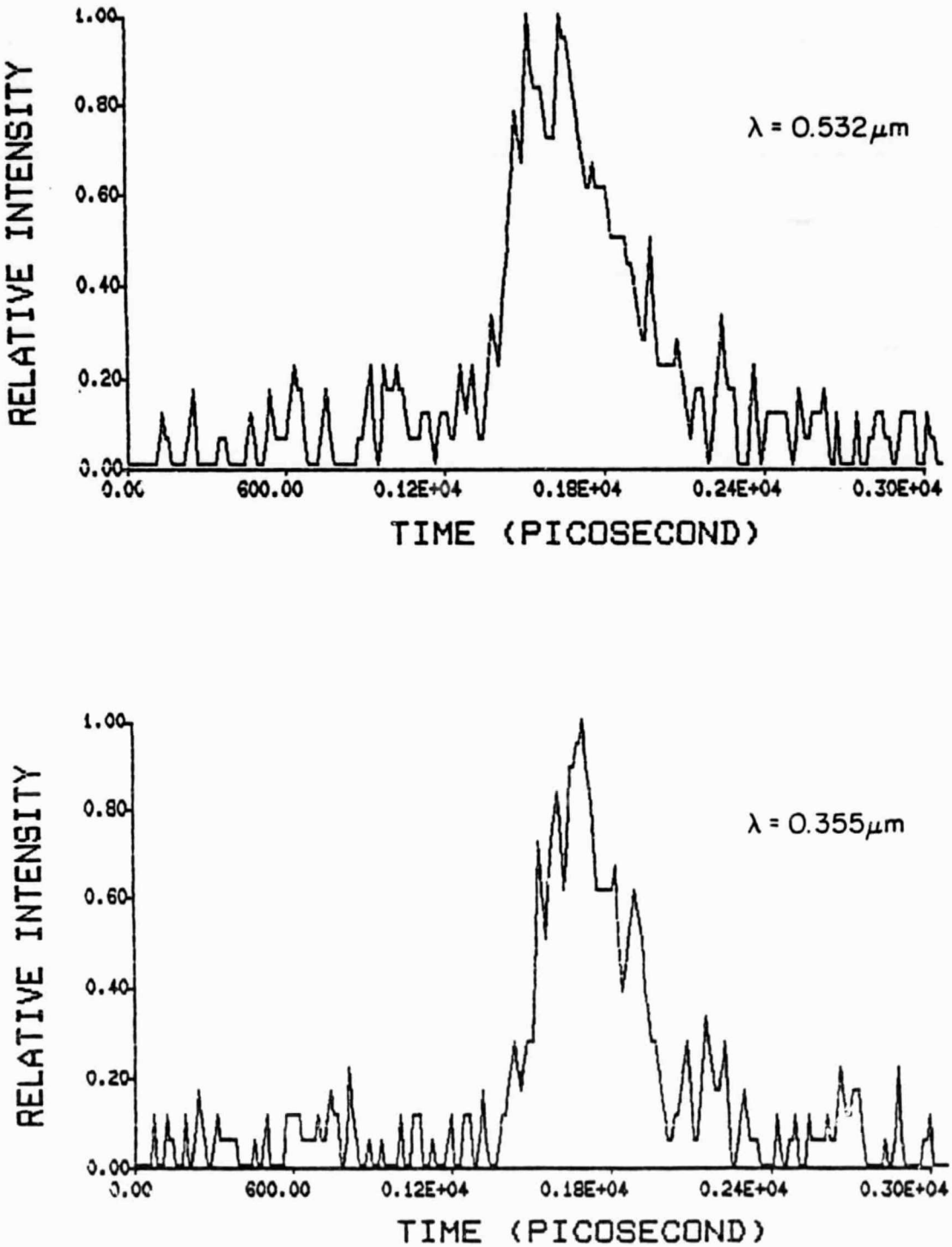

Fig. 7.16. Waveforms of the typical pulsed signals at 0.532 and 0.355 μm reflected from the diffuse flat board.

those returns from the CCR arrays. This is a consequence of the relatively small lidar cross-section of the Lambertian target. Since the relative magnitude of the background noise increases, background radiation may introduce additional ranging error. The fluctuations within the pulse returns were most likely due to the receiver noise. Due to the nonlinear frequency mixing of the 1.064 μm and 0.532 μm pulses at the KD^*P (potassium dihydrogen phosphate) tripling crystal in producing the 0.355-μm pulses, the angular beamwidths of the 0.355-μm pulses are narrower than the 0.532 μm beamwidths [Hansch, 1977]. This difference in divergence became evident in Fig. 7.16 because the pulse broadening is directly related to the range spread of the target, which in turn is related to the divergence angle.

The typical mean return signals are shown in Fig. 7.17. The 0.355-μm return is approximately Gaussian shaped as predicted by Eq. (7.2). However, the 0.532-μm return is non-Gaussian due to the nonlinear process of the crystal.

It was mentioned in Chapter 7.2 that the mean spectrum ($\langle|S(\omega)|^2\rangle$) of the reflected signals from diffuse targets can be used to estimate the spectra of the mean signals ($|\Phi_S(\omega)|^2$), provided both the signal strength ($\langle N_i\rangle$) and the speckle SNR (K_i) are large. When $\langle N_i\rangle$ is small, which is the case for the target board returns, we would expect some differences between the two spectra. One way to quantify the difference is to compare the bandwidths of the two spectra. The MS bandwidth of the mean signal is given in Eq. (7.9). The MS width of $\langle|S(\omega)|^2\rangle$ can be defined as

$$\hat{B}^2 = \frac{\int_{-\infty}^{\infty} d\omega\ \omega^2 \langle|S(\omega)|^2\rangle}{\int_{-\infty}^{\infty} d\omega \langle|S(\omega)|^2\rangle} \quad . \qquad (7.22)$$

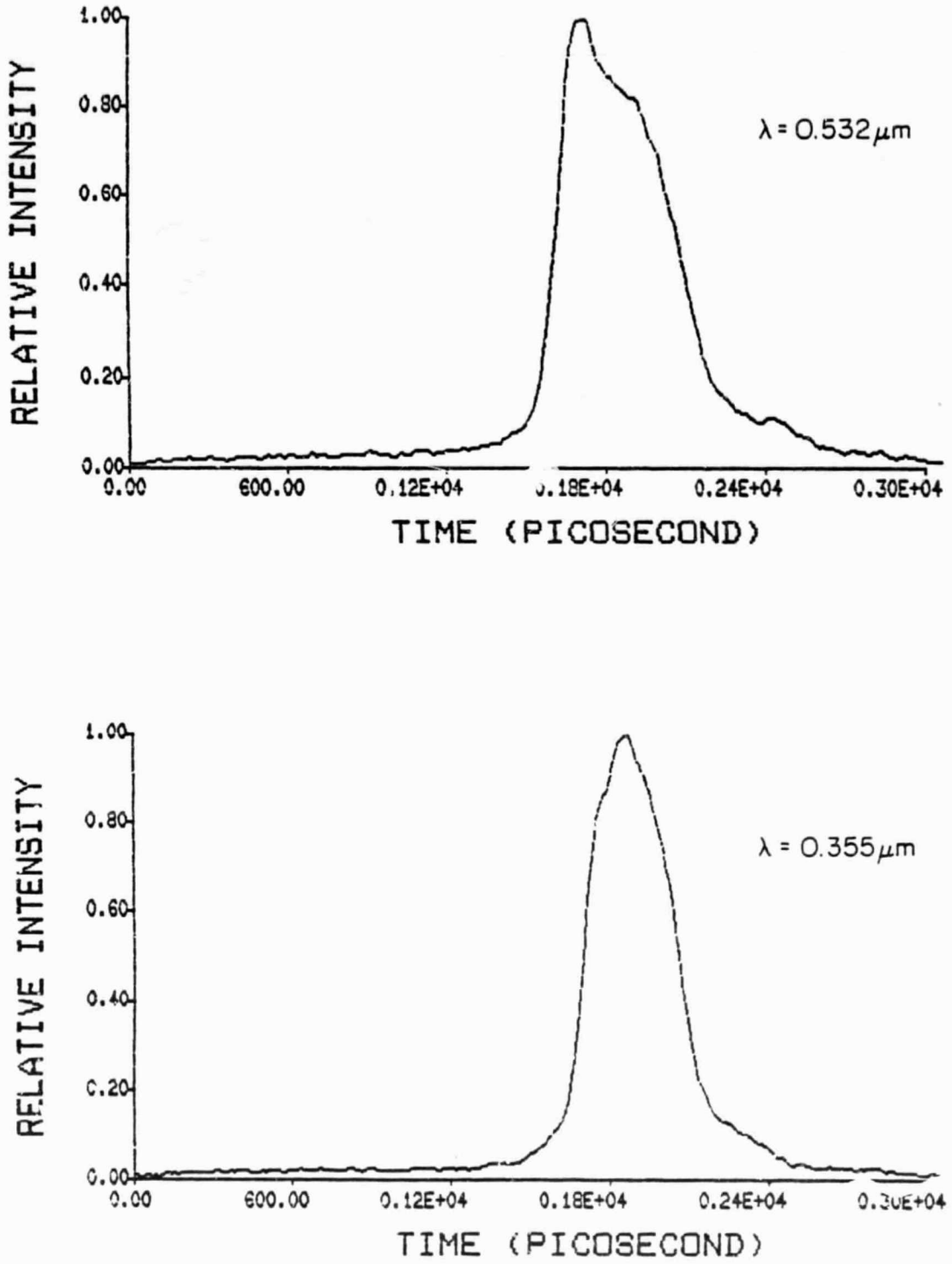

Fig. 7.17. Waveforms of the typical mean pulsed signals at 0.532 and 0.355 μm reflected from the diffuse flat board.

After substituting Eqs. (7.3) and (7.13) into Eq.(7.22) and using the fact that K_i is large, we have

$$\hat{B}^2 \cong \frac{1}{2\sigma_S^2} + \frac{\sigma_S}{2\langle N\rangle \sigma_h^3} \quad . \tag{7.23}$$

By comparing Eqs.(7.9) and (7.23), we can see that $\hat{B}^2$ is always larger than B_S^2, and it approaches B_S^2 only when $\langle N_i\rangle$ is large. In this experiment $\langle N_i\rangle$ is on the order of a few hundred. Consequently, we would expect the measured $\hat{B}^2$ to be larger than B_S^2.

Typical measured results on both $|\Phi_S|^2$ and $\langle|S|^2\rangle$ are shown in Fig. 7.18 for comparison. As expected the widths of $\langle|S|^2\rangle$ are larger than those of $|\Phi_S|^2$ at both wavelengths. The 0.355-μm pulse has a larger bandwidth because it is narrower.

The predicted differential propagation times between the two signals using spherical refraction model is 56 psec. In Fig. 7.19 the measured results using cross-correlation algorithm are compared with the prediction. In this figure each point corresponds to a set of 50 to 100 timing measurements. The error bars correspond to ±1 standard deviation from the mean. Since the received signal strength was varied by changing the MCP setting of the streak camera, the RMS timing accuracies vary considerably between different sets. The average bias among these six measurement sets is 4 psec, which corresponds to a average bias of 0.6 mm on the one-way differential pathlength measurements.

Because of the large speckle SNR's, speckle degradation of the timing accuracy is negligible. Therefore, we would expect the system performance

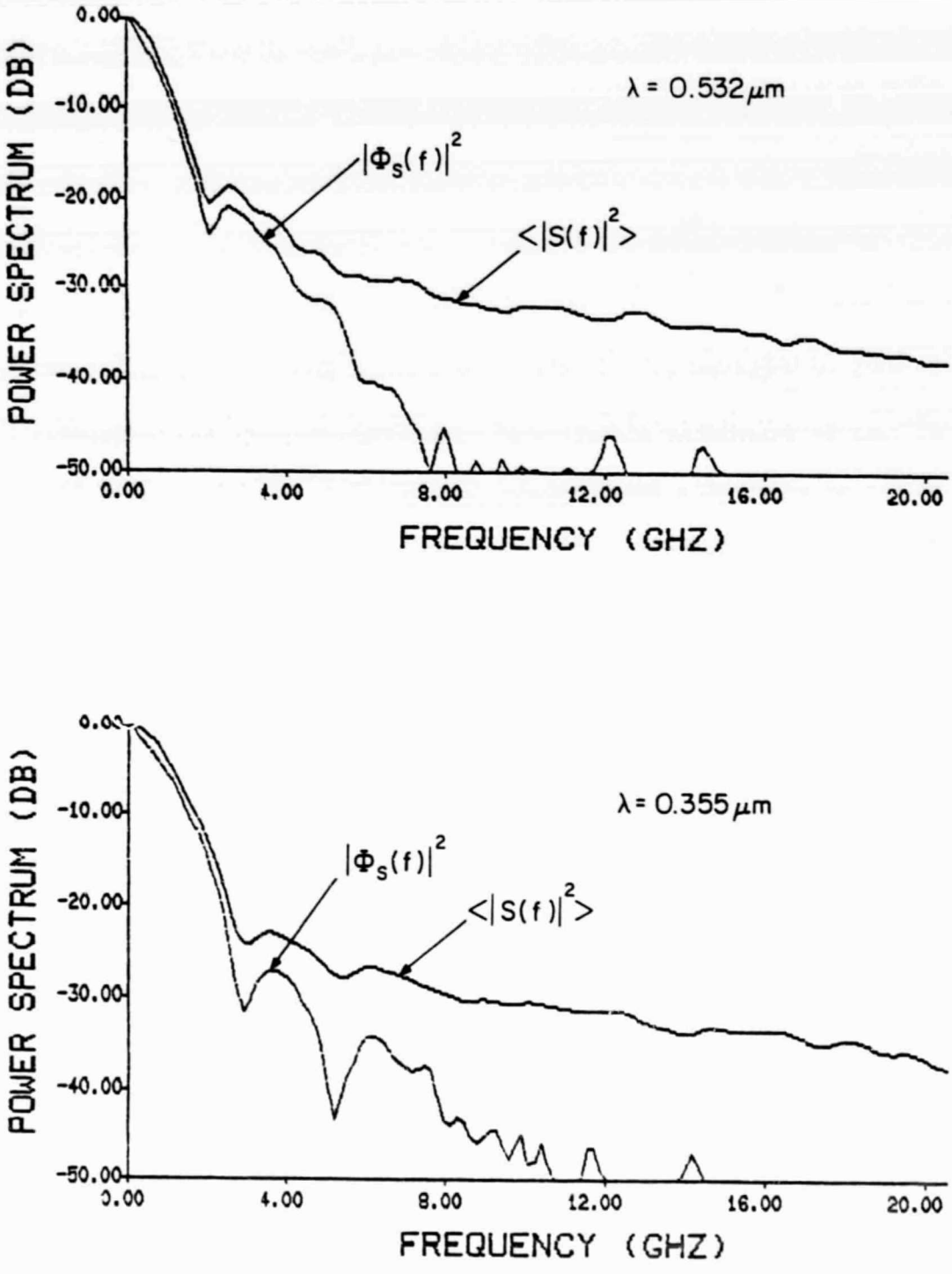

Fig. 7.18. Comparison of the measured results on the power spectra of the mean signals ($|\Phi_S(\omega)|^2$) and the average power spectra of the measured signals ($<|S(\omega)|^2>$) for the pulse reflections from the diffuse flat board.

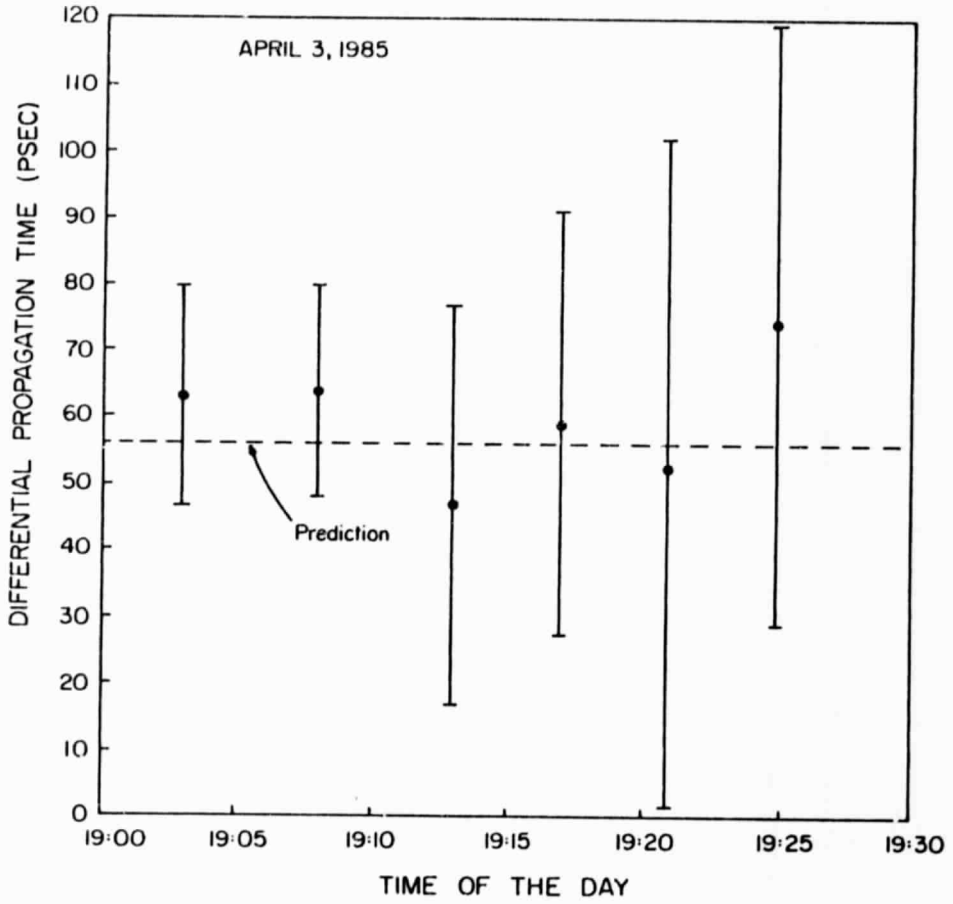

Fig. 7.19. The measured differential propagation time between signals at 0.532 and 0.355 μm using cross-correlation estimator for the pulse reflections from the diffuse flat board.

to be dominated by the shot noise. Within the shot-noise limited region, the MS timing accuracy of the correlation receiver (Eq. (5.27)) can be simplified to

$$\sigma^2_{\tau_{COR}} \cong \frac{8}{3\sqrt{3}} \left(\frac{1}{\langle N_1 \rangle} + \frac{1}{\langle N_2 \rangle} \right) \sigma_S^2 + \frac{\sigma_S^5 \, (1 - \sigma_h^2/2\sigma_S^2)}{\sqrt{2} \, \langle N_1 \rangle \langle N_2 \rangle \, \sigma_h^3} \qquad \langle N_i \rangle \ll K_i \; . \quad (7.24)$$

The first term in Eq. (7.24) is the MS error due to the first-order shot noise effects, and the second term is due to the second-order shot noise contributions. Equation (7.24) is evaluated using the system and target parameters and compare with the experimental results. The received signal strengths measured during the experiment were approximately equal at both wavelengths. The comparison between the theoretical and the experimental results is shown in Fig. 7.20. As expected, the experimental results show the signal dependence of the timing error. The difference between the prediction and the experimental results is between 4 to 15 psec. This discrepancy is primarily due to the difference in divergence angles, which causes the footprint intensities to be different and degrades the correlation between the two signals (refer to Chapter 6). The experimental results approach the predicted values as the signal strength increases. This is because the theoretical prediction is the lower bound of the differential timing error, and it was pointed out in Chapter 5 that the actual timing error will approach this bound when the SNR is large.

A typical error versus correlation coefficient plot is shown in Fig. 7.21. The vertical scale in this figure corresponds to the difference between the estimated differential propagation time and the mean differential

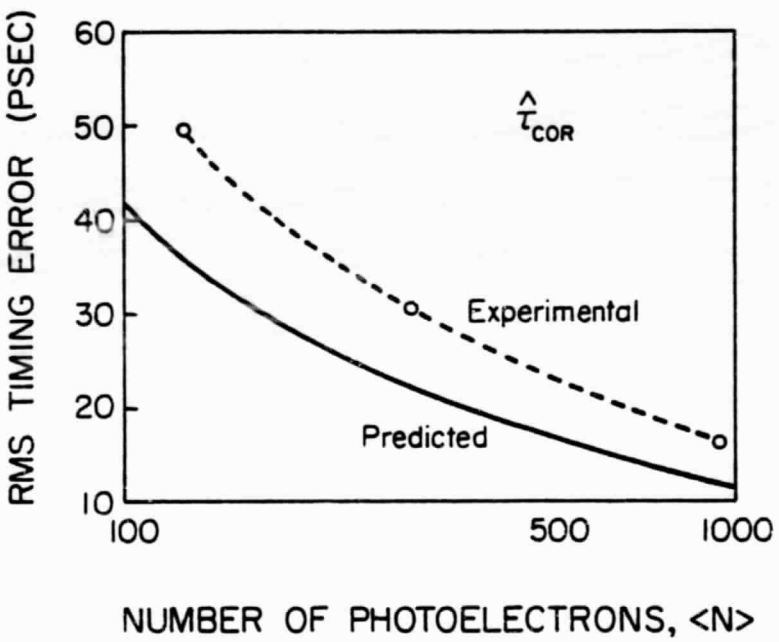

Fig. 7.20. Comparison of the predicted and measured RMS differential timing accuracies of the cross-correlation estimator for the pulse reflections from the diffuse flat board.

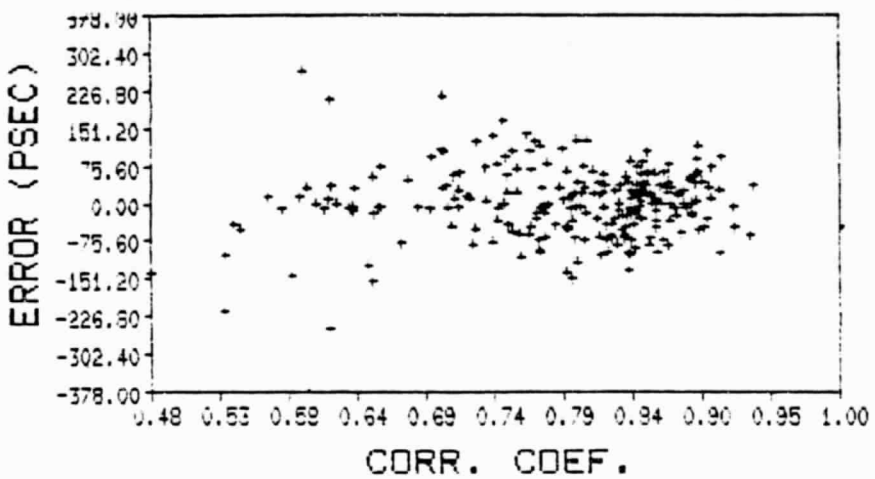

Fig. 7.21. Error of the measured differential propagation time versus correlation coefficient between 0.532 and 0.355 μm signals for the pulse reflections from the diffuse flat board. The error is the difference between the mean and the actual differential propagation time at each measurement using the cross-correlation estimator.

propagation time in each measurement by using the correlation algorithm, and the horizontal scale corresponds to the correlation coefficient of the measured pulse pair. We can see that the error appears to be smaller when the two signals are better correlated. Consequently, the timing accuracy may be improved by discarding the pulse pairs that have low correlation.

The comparison between the timing performances of different estimating schemes is shown in Fig. 7.22. The timing error of $\hat{\tau}_{COR}$ is larger than that of $\hat{\tau}_{ML}$. This is expected because there is an additional second-order error associated with $\hat{\tau}_{COR}$ due to the correlation of two noisy signals. The second-order error, however, can be reduced to negligible level by selecting the proper receiver bandwidth. The peak detector has the worst performance due to the presence of shot noise and speckle, which makes the peak intensity fluctuate randomly within the reflected pulse.

7.6 Conclusion

Pulsed two-color laser ranging is an effective technique in estimating the atmospheric delay. However, its success relies on proper design of the receiver timing algorithm, short laser pulses, and high resolution receivers. A cross-correlation timing algorithm has been developed and its performance has been analyzed. In parallel with the theoretical research, experimental work has been underway to verify the feasiblity of this algorithm under actual field conditions. In this chapter, we report on the recent experimental timing results when ranging to the cube corner arrays and a diffuse flat target. Streak camera-based optical receiver was used during the experiment which allowed us to observe the pulse fluctuations caused by the speckle. For the cube corner array test, the results show that the differential timing accuracy improves with the increase in signal strength when the speckle SNR is high, and it is insensitive to the change

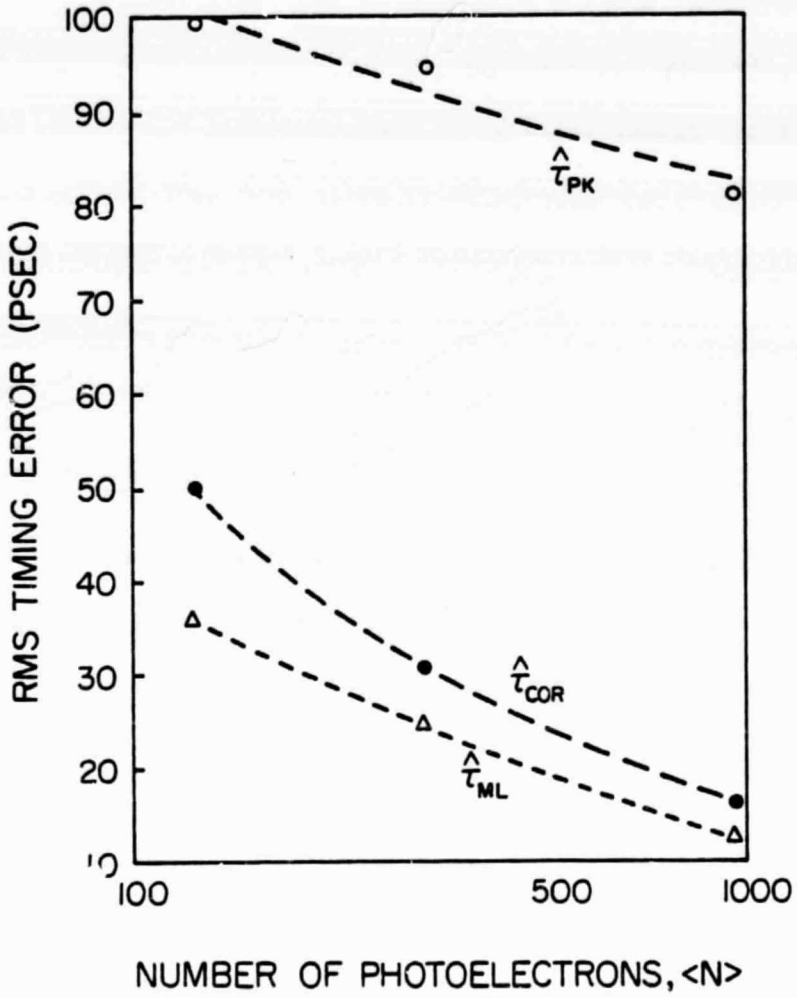

Fig. 7.22. Comparison of the measured RMS differential timing accuracies of the cross-correlation ($\hat{\tau}_{COR}$), Maximum-Likelihood ($\hat{\tau}_{ML}$), and peak detection ($\hat{\tau}_{PK}$) estimators for the pulse reflections from the diffuse flat board.

in signal strength when the speckle SNR is low. These results agree in general with the theoretical predictions. For the diffuse target test, the results show that the shot noise is the limiting factor, and the difference between the experimental results and the theoretical prediction is between 4 to 15 picosecond. This difference is primarily caused by the slight difference in the received signal intensity at the two wavelengths. By taking this into account, we feel that the theoretical and experimental results have very good agreement. In both tests, the performance of the correlation algorithm was compared with that of the Maximum-Likelihood estimator. The results indicate that both estimators perform almost as well in the speckle limited region, and the ML estimator performs better in the shot noise limited region. As point out in Chapter 5, however, the performance of the correlation algorithm can be improved in the shot noise limited region by choosing the receiver bandwidth properly. Based on the experimental results and those of Chapter 5, and by taking into account the versatility of the correlation algorithm, we do feel that it is an effective and practical algorithm in two-color differential timing estimation.

8. AIRBORNE MEASUREMENTS OF SEA STATE AND ATMOSPHERIC PRESSURE

8.1 Introduction

Atmospheric pressure over the ocean can be remotely measured by performing two-color ranging to the ocean surface [Gardner, 1979]. Recording the ocean reflected waveforms with high temporal resolution also permits sea state and wave height information to be obtained with this technique [Tsai and Gardner, 1982]. In order to verify the feasibility of this technique, initial airborne two-color pressure measurements were collected in 1983 with a photomultiplier-based system which had 500 psec time resolution [Abshire et al., 1984, Tsai and Gardner, 1984]. The airborne results indicated the change in atmospheric pressure between 1000 and 4000 ft flight altitudes, and the high correlation between the return waveforms at the two colors. Unfortunately, the pressure measurement accuracy was limited by the relatively low receiver bandwidth. In April 2 and 3 of 1985, another airborne experiment was conducted using a streak camera-based receiver with 80-picosecond resolution in each channel [Abshire et al., 1985]. In this chapter we shall present the sea-state observations and pressure measurements based on the experimental results. The pressure measurement results will also be compared with the theoretical prediction.

8.2 Theoretical Prediction

In Chapter 7 we calculated the average power sprectrum of the reflected signal

$$\langle |S(\omega)|^2 \rangle = |\Phi_S(\omega)|^2 + \langle N \rangle |H(\omega)|^2 + \frac{\langle N \rangle^2}{K} |G(\omega)|^2 \qquad (8.1)$$

where $H(\omega)$ is the transfer function of the receiver, $G(\omega)$ is the Fourier transform of the system point target response, $\Phi_S(\omega)$ is the Fourier transform of the mean received signal, $\langle N \rangle$ is the expected signal strength and K is the speckle SNR. If we take the expectation of Eq. (8.1) with respect to the target profile ξ we obtain

$$\langle |S(\omega)|^2 \rangle = \langle N \rangle |H(\omega)|^2 + \frac{\langle N \rangle^2}{K} |G(\omega)|^2 + \langle N \rangle^2 |G(\omega)|^2 D(\omega) \qquad (8.2)$$

where

$$D(\omega) = \int d^2\underline{\rho}_1 \int d^2\underline{\rho}_2 \; b_2(\underline{\rho}_1) \; b_2(\underline{\rho}_2) \iint d\xi_1 d\xi_2 \; p(\xi_1, \xi_2) \; e^{-j\omega(\xi_1 - \xi_2)/c} \; . \qquad (8.3)$$

b_2 was defined in Chapter 3 as the footprint intensity cross-section, and $p(\xi_1, \xi_2)$ is the joint probability density function of the ocean surface profile. We have neglected the beam curvature effects in Eq. (8.3). Since the wave height at any point of the ocean is due to the combined action of the wave motions from different directions which propagate to the observation point, it can be argued that the ocean wave height is approximately Gaussian distributed. If we further assume that the sea surface is isotropic, $D(\omega)$ can be express as

$$D(\omega) = \int d^2\underline{\rho}_1 \int d^2\underline{\rho}_2 \; b_2(\underline{\rho}_1) \; b_2(\underline{\rho}_2) \; e^{-\frac{4\omega^2}{c^2}[\sigma_\xi^2 - R_\xi(\underline{\rho}_1 - \underline{\rho}_2)]} \; . \qquad (8.4)$$

R_ξ is the correlation function of the ocean surface profile and σ_ξ^2 is the profile variance. If we model R_ξ as a Gaussian function

$$R_\xi(\underline{\rho}) = \sigma_\xi^2 \, e^{-\rho^2/2L^2} \tag{8.5}$$

where L is the profile correlation length and assume that the laser footprint is small compared to L, Eq. (8.4) can be approximated by

$$D(\omega) \cong \frac{1}{1 + (\omega/\omega_o)^2} \tag{8.6}$$

where

$$\omega_o = \frac{cL}{2\sigma_\xi \, z \, \tan\theta_T} \quad . \tag{8.7}$$

Notice that

$$S = \frac{\sqrt{2}\,\sigma_\xi}{L} \tag{8.8}$$

is the RMS slope of the ocean surface profile. The average signal spectrum now becomes

$$\langle |S(\omega)|^2 \rangle = \langle N \rangle \ |H(\omega)|^2 + \langle N \rangle^2 \ |G(\omega)|^2 \left[\frac{1}{1 + (\omega/\omega_o)^2} + \frac{1}{K} \right] . \quad (8.9)$$

If the system parameters are known a priori, Eq. (8.9) can be used to estimate the RMS slope of the ocean by choosing ω_o so that Eq. (8.9) fits the experimental data.

In order to minimize the pressure error dependence on temperature and elevation angle uncertainties, the two-color ranging system was reconfigured as an altimeter at a nadir viewing angle [Gardner, 1979]. By assuming a spherically symmetric model for the atmospheric refraction, the atmospheric correction (AC) can be approximated as

$$AC \cong 2 \int_o^{h_a} \frac{10^{-6} N_g}{\sin E} \, dh \quad (8.10)$$

where N_g is the group reflectivity, E is the elevation angle and h_a is the aircraft altitude. In Eq. (8.10), we have neglected the term due to the difference between the geometric length of the ray and the straight-line path. This term is negligible for a nadir viewing altimeter operating at airborne altitudes. From [Marini and Murray, 1973], the group refractivity is approximately given by

$$N_g \cong 80.343 \ f(\lambda) \frac{P}{T} \quad (8.11)$$

where P and T are the pressure and temperature, respectively, and $f(\lambda)$ was given previously by Eq. (2.10). In an isothermal atmosphere [Wallace and Hobbs, 1977], the pressure will vary exponentially with altitude:

$$P = P_s \exp\left[- \frac{h}{h_s} \right] \quad , \tag{8.12}$$

where

$$h_s = \frac{RT_s}{MG} \tag{8.13}$$

is the atmospheric scale height, P_s is the surface pressure, M is the molecular weight of air, R is the universal gas constant, T_s is the surface temperature in degrees of Kelvin, and G is the acceleration due to gravity. By substituting Eqs. (8.12) and (8.13) into Eq. (8.10), we have

$$AC \cong \frac{2 \times 10^{-6}}{\sin E} N_s h_s \left[1 - \exp\left(- \frac{h_a}{h_s} \right) \right] \quad , \tag{8.14}$$

where N_s is the surface refractivity

$$N_s = 80.343 \, f(\lambda) \frac{P_s}{T_s} \quad . \tag{8.15}$$

For E = 90°, P_s = 1010 mb, and T_s = 300°K, the scale height equals 8787 m. With these parameters, the difference between the roundtrip optical pathlengths measured at the two wavelengths (ΔR) is

$$\Delta R = AC_1 - AC_2 = 4.76 \text{ (m)} \left[1 - \exp\left(-\frac{h_a}{h_s}\right)\right] [f(\lambda_1) - f(\lambda_2)] \quad . \quad (8.16)$$

During the April airborne experiment, the 0.532- and 0.355-μm laser wavelengths were used. The corresponding value of ΔR is

$$\begin{aligned} \Delta R &= 0.3878 \text{ (m)} \left[1 - \exp\left(-\frac{h_a}{h_s}\right)\right] \\ &= 1326 \text{ (psec)} \left[1 - \exp\left(-\frac{h_a}{h_s}\right)\right] \quad . \end{aligned} \quad (8.17)$$

From Eq. (2.20), the pressure sensitivity to ΔR is

$$\frac{\partial P}{\partial \Delta R} \cong \frac{0.212 \sin E}{f(\lambda_1) - f(\lambda_2)} \text{ (mbar/mm)} \quad . \quad (8.18)$$

Consequently, pressure change of 1 mbar caused a differential atmospheric delay change of 1.34 psec.

8.3 System Configuration

The block diagram of the two-color laser altimeter used during the experiment is shown in Fig. 8.1 with the system parameters given in Table 8.1. The system was developed by J. B. Abshire and his colleagues at

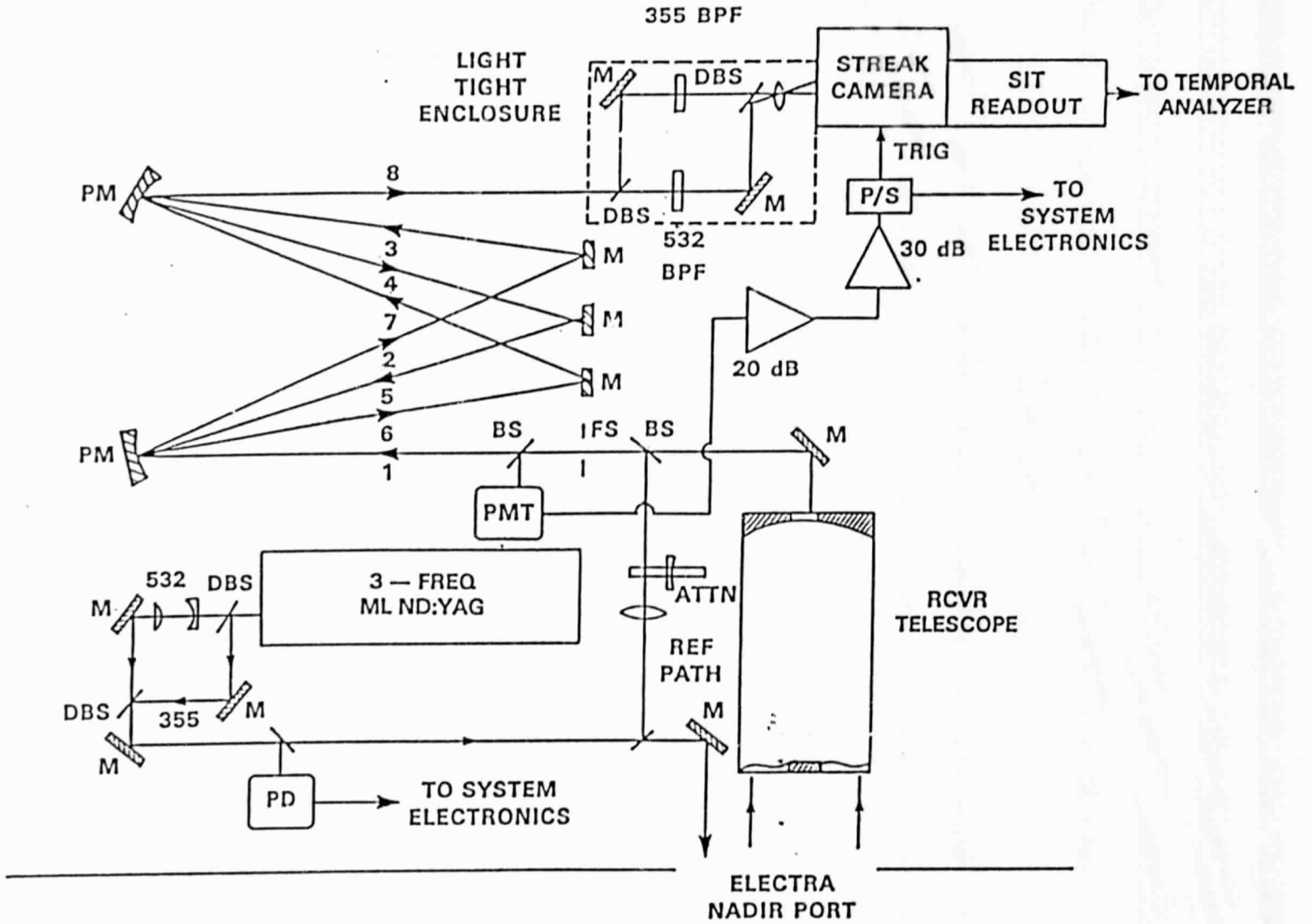

Fig. 8.1. The pulsed, two-color laser altimeter used during the airborne experiment in April, 1985.

TABLE 8.1.

SYSTEM PARAMETERS FOR THE TWO-COLOR LASER ALTIMETER USED DURING THE AIRBORNE EXPERIMENT OF APRIL, 1985

System Parameters
4/85 Flight Experiment

Laser	:	Quantel YG40 - Mode Locked ND:YAG nominal 30 psec pulses at 1.064, 0.532, and 0.355 μm 0.3 mJ at 0.532 μm, 0.5 mJ at 0.355 μm
Telescope	:	Celestron 14 - 36 cm dia. Schmidt Cassegrain 891 cm^2 effective collecting area
Mirror	:	CVI Laser double stack dielectric maximum reflection at both 0.532 and 0.355 μm
Photomultiplier	:	Hamamatsu R1294U, Dual MCP QE = 4% at 0.532 μm, gain = 1.3 x 106
Optical Delay	:	White Cell, 8 passes, 40 nsec
Streak Camera	:	Hamamatsu C1370, 5 psec resolution at sweep spreed = 2 85 psec impulse response in system
Readout	:	Hamamatsu C1098, Dual channel, DMA interface
TIU	:	HP 5370A, 100 psec accuracy
Computer	:	DEC LSI 11/23, Dual floppy disks

NASA-Goddard Space Flight Center. The operation of this system is essentially the same as that of the system used during the horizontal path experiments (refer to Chapter 7.3). The major difference is that the transmitter and the receiver assembly in this flight experiment was operated in a noncoaxial nadir viewing configuration. The transmitter and receiver axes were approximately parallel to ensure detectable signal returns at higher altitudes.

The system was installed on board the NASA Electra aircraft. A picture of this aircraft is shown in Fig. 8.2. The Celestron 14 receiving telescope used during the experiment is shown in Fig. 8.3. To the left of the telescope was the transmitting mirror which directed the laser beams down to the ocean surface. Both the telescope and the transmitting mirror were directly above the nadir viewing port. Fig. 8.4 shows the receiving optics assembly and the streak camera. Fig. 8.5 shows the waveform recording and timing units.

Two nighttime missions were flown with this system on April 2 and 3, 1985. The missions extended from the Chesapeake Bay just west of Wallops Island, Virginia, over the Bay-Bridge Tunnel, and out over the Atlantic Ocean. In the first mission more time was devoted to system adjustments. Receiver triggering problems were encountered during the course of this flight, and as a consequence only a few usable waveforms were recorded at 1000 ft altitude. The triggering problem was solved prior to the second mission, and the waveform collection process went smoothly thereafter. More than 1800 waveform pairs were collected at flight altitudes of 1000, 1500, and 2000 ft. The flight route that we followed during the April 3 mission is shown in Fig. 8.6.

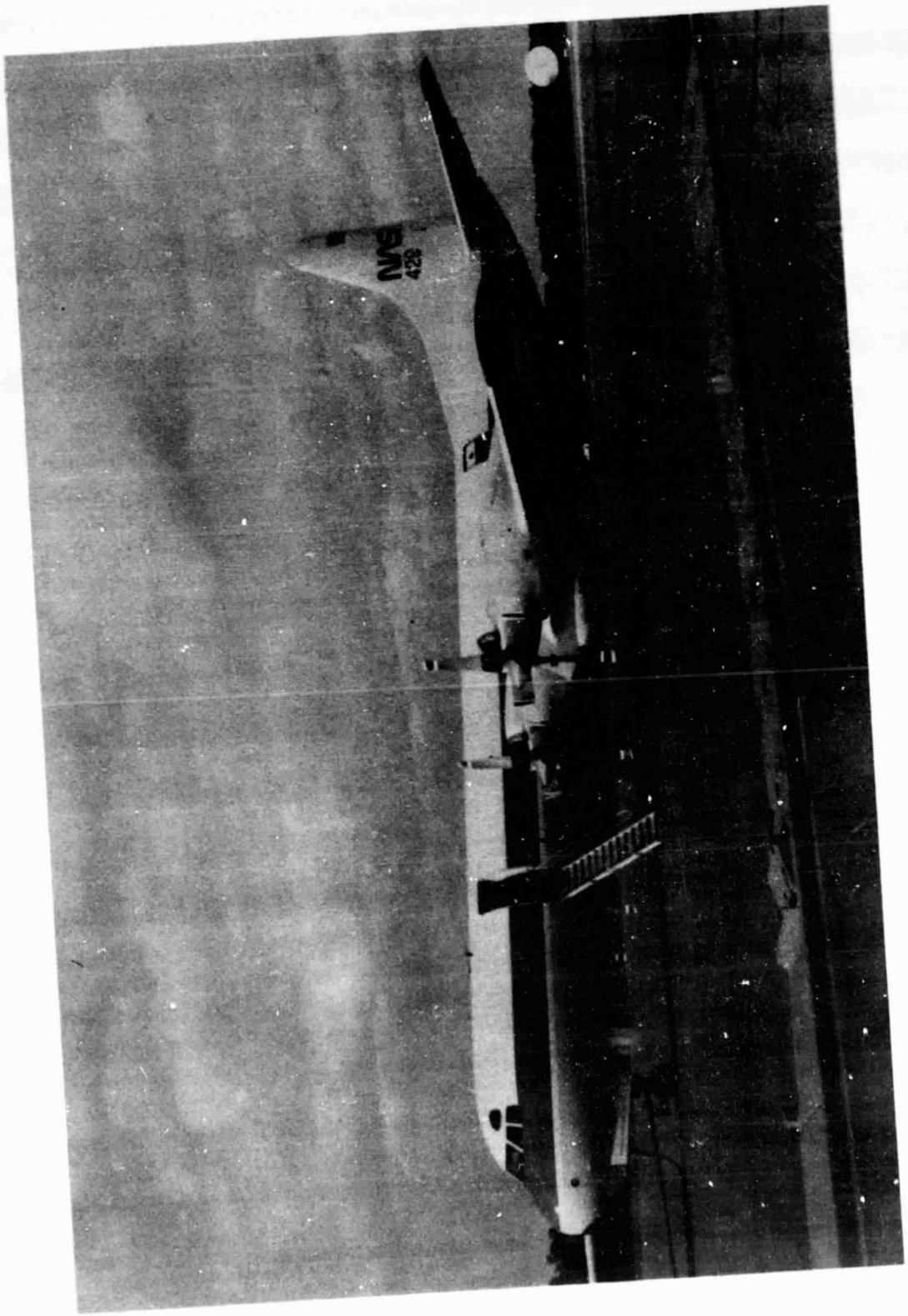

Fig. 8.2. A picture of the NASA Electra aircraft used during the airborne two-color laser altimeter experiment.

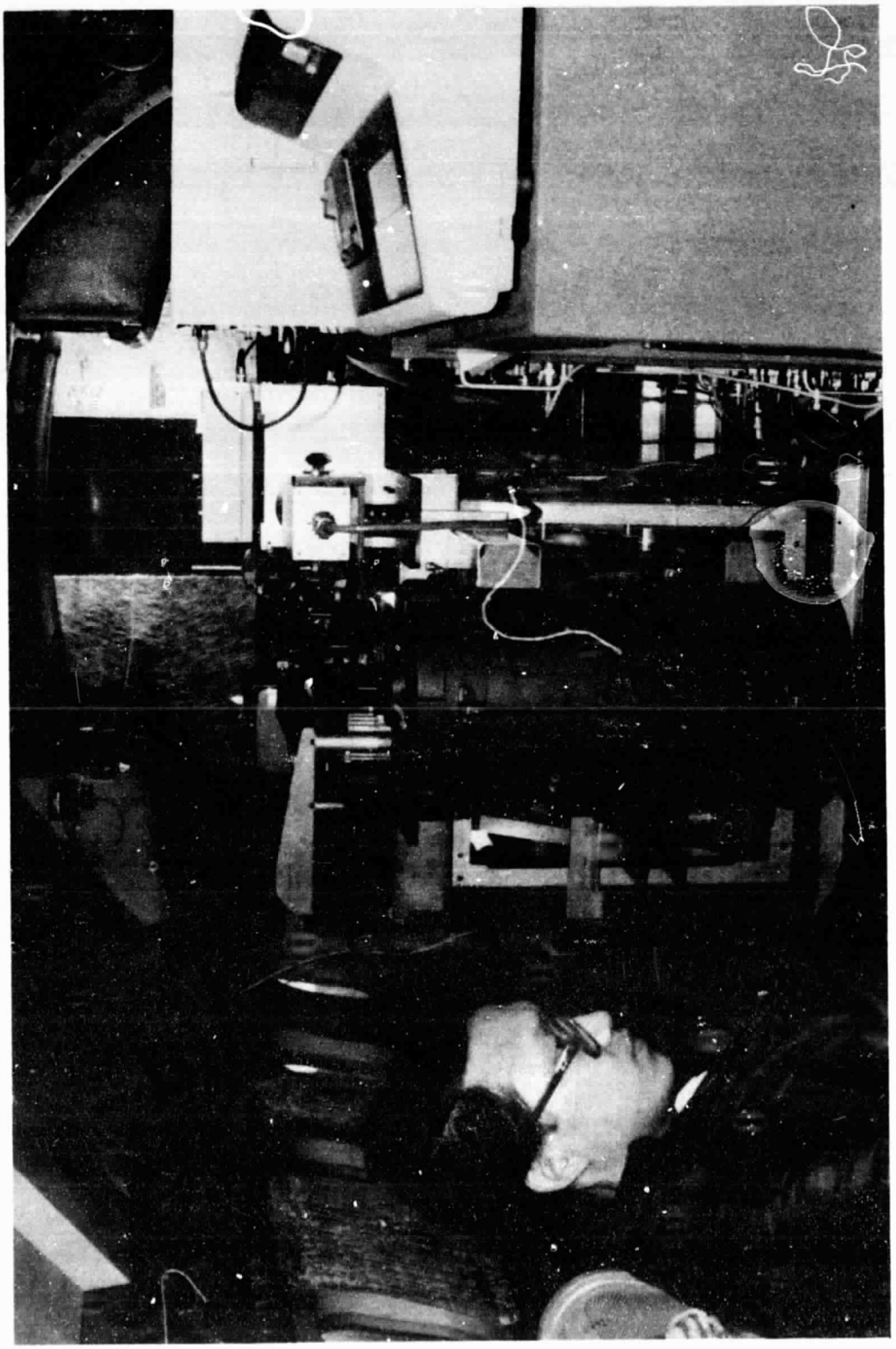

Fig. 8.3. A picture of the Celestron 14 receiving telescope on board the aircraft.

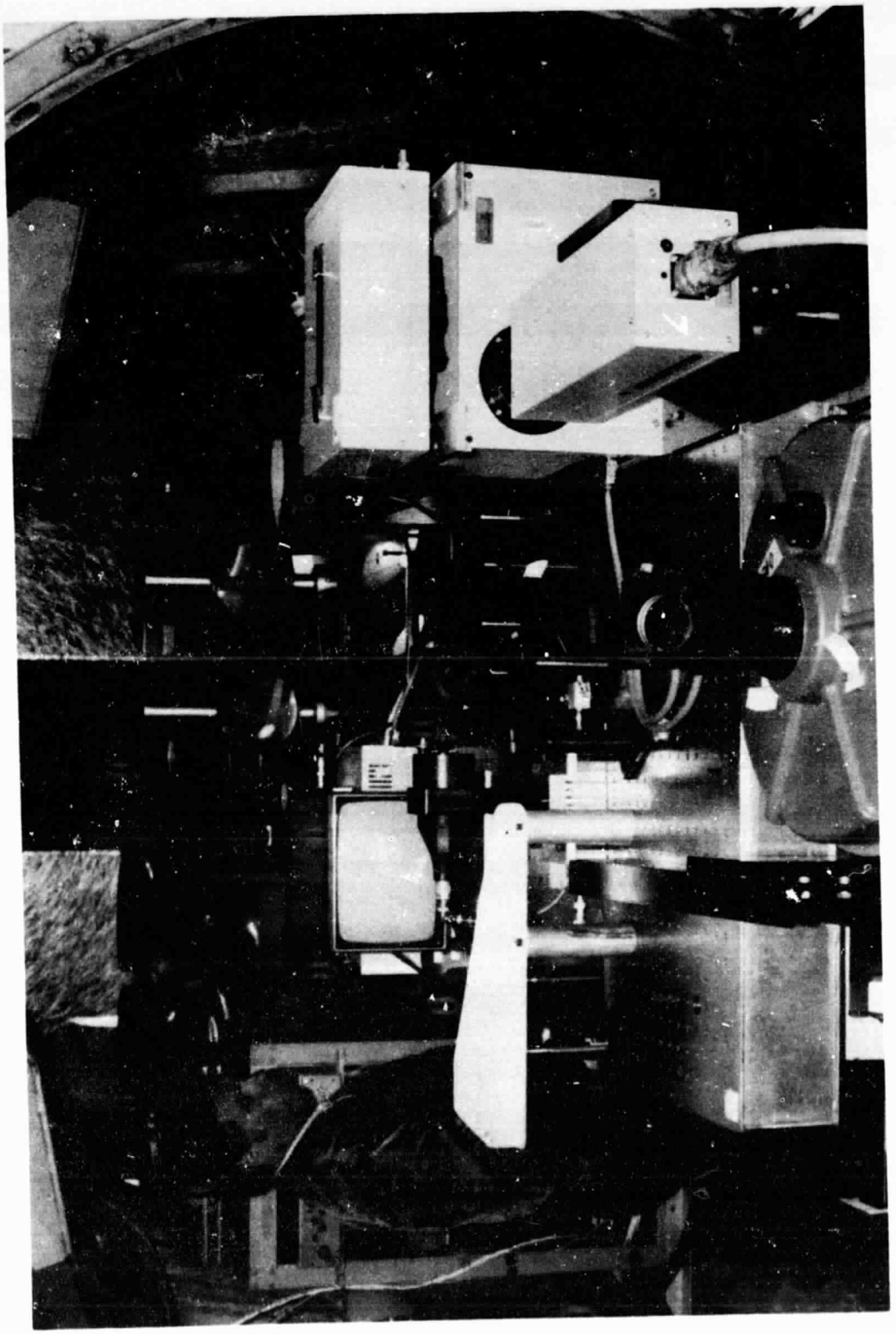

Fig. 8.4. A picture of the receiving optics assembly and the Hamamatsu streak camera.

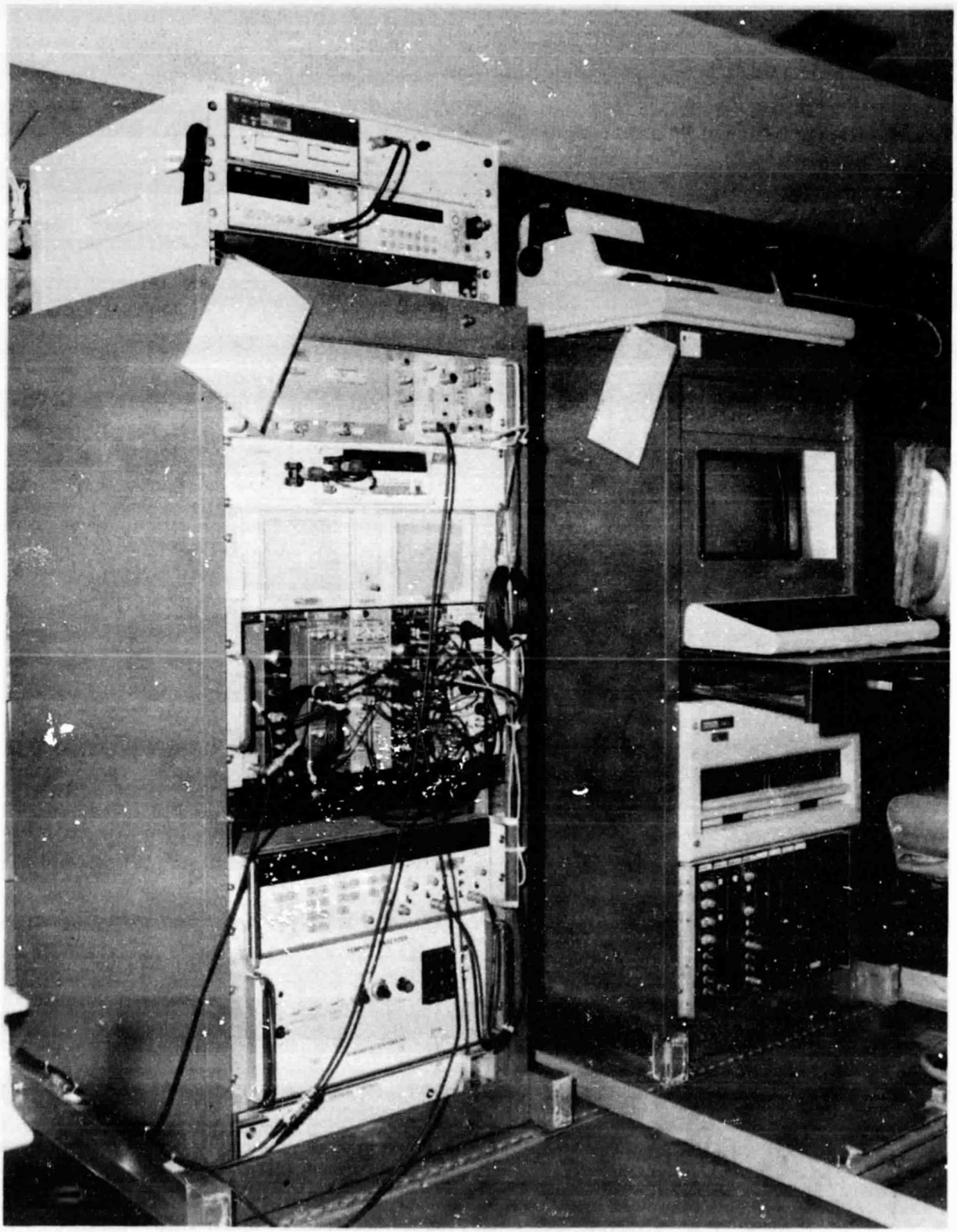

Fig. 8.5. A picture of the waveform recording and timing units.

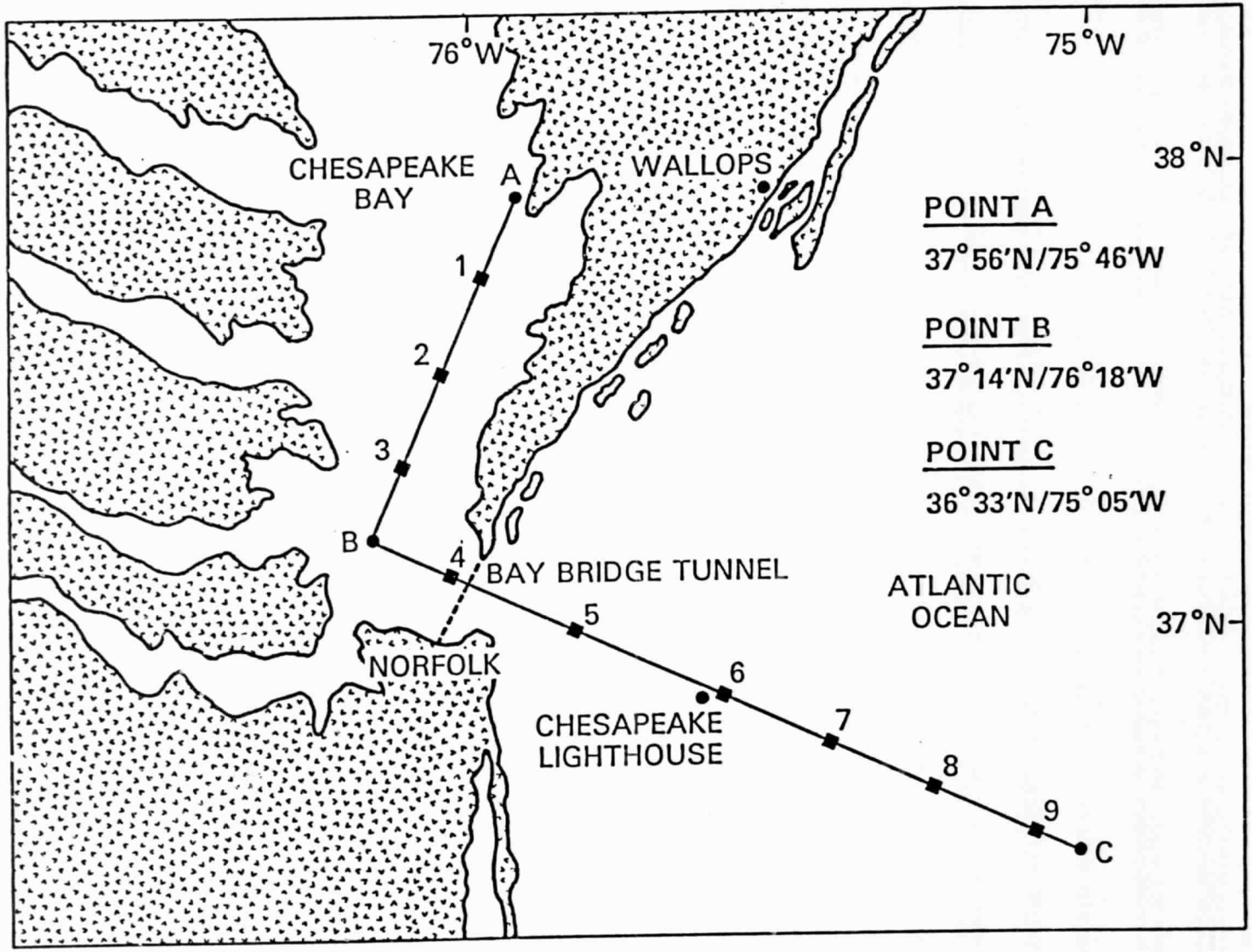

Fig. 8.6. The flight route of the April 3 airborne experiment.

8.4 Data Analysis - Sea State

The measured waveform pairs in all three altitudes exhibit pulse shapes that are related to the various local surface profiles of the ocean waves within the laser footprint.

Fig. 8.7 shows a typical return pulse pair that exhibits very sharp single glints. The widths of these glints are comparable to the point target response width. This seems to indicate that some part of the local ocean surface was relatively flat within the laser footprint so that return signals are dominated by the specular components. These sharp returns were obtained more frequently at lower altitudes (1000 to 1500) where the RMS laser footprint diameters were on the order of 30 to 43 cm, and near the bay where the ocean was relatively smooth.

Fig. 8.8 shows another type of measured waveform pairs that exhibit double peaks. This pulse type also occurred more frequently at lower altitudes. We believe that these returns were due to the reflections from ocean waves that had trochoidal (or sinusoidal) local surface profiles within the laser footprint. The first peaks of the returns correspond to the reflections from the wave crests and the second peaks correspond to the reflections from the wave troughs. Since the wave heights of these local trochoidal waves varied slightly, there were slight phase delays between reflections from various crests (or troughs). Consequently, the widths of the glints are slightly broader than the point target response width, and there are some speckle-induced pulse fluctuations. The mean wave height within the laser footprint can be approximated by measuring the separation time of the two peaks. In this particular example the separation times at both wavelengths are ~ 142 psec, which corresponds to the mean wave heigth of ~ 2 cm. This wave height value is typical for small gravity waves

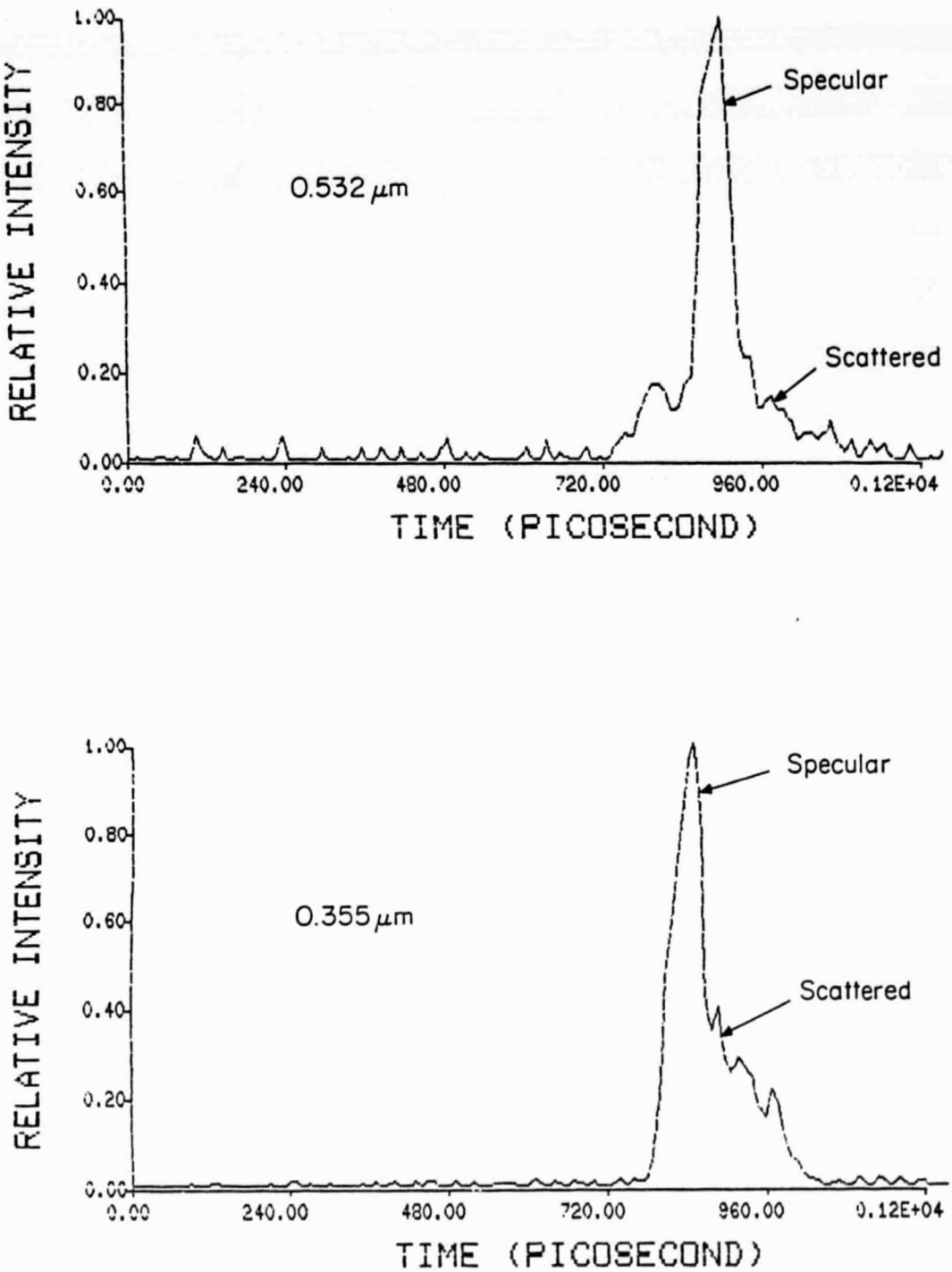

Fig. 8.7. A typical ocean-reflected pulse pair that exhibited single dominant glints.

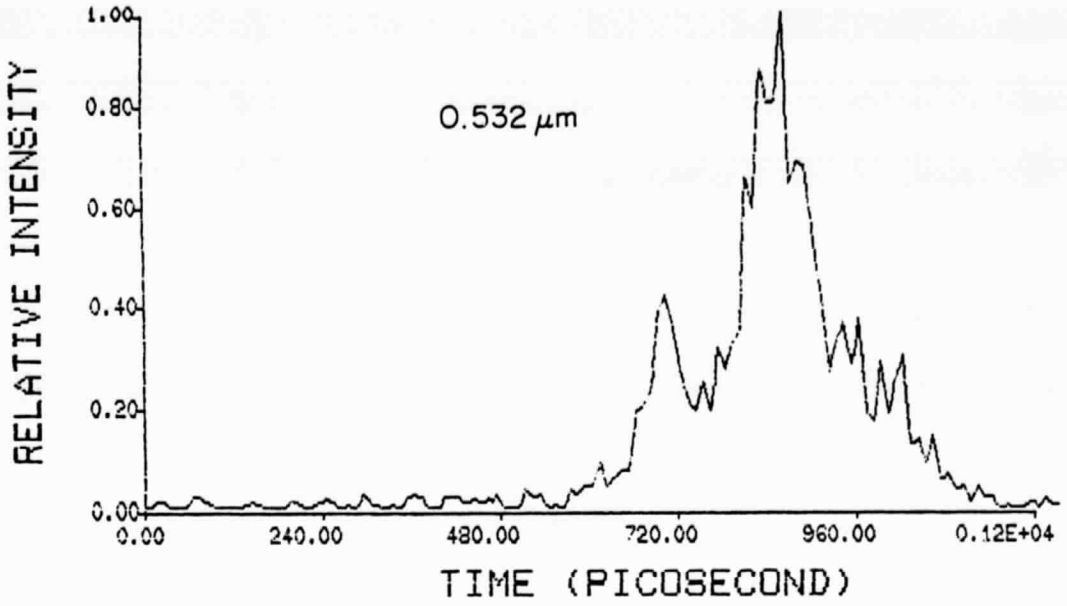

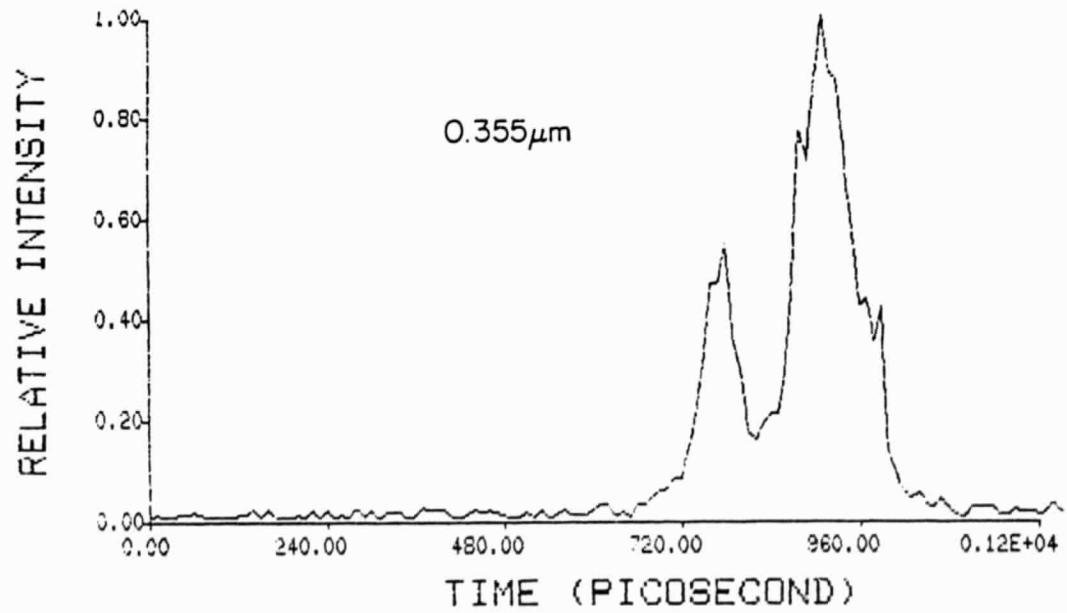

Fig. 8.8. A typical ocean-reflected pulse pair that exhibited double dominant glints.

generated by light wind as a disturbing force and gravity and surface tension as restoring forces. We thus believe that this pulse type corresponds to the reflections from a relatively calm local ocean surface that consists of a few small-amplitude trochoid gravity waves.

Fig. 8.9 shows yet another kind of measured pulse shape. This pulse type was observed more frequently at 2000 ft altitude where the laser footprint diameter was about 60 cm. The returns of this kind had widths that were in general much broader than those of the other two that we have just mentioned, and they also shaped more like a Gaussian. We believe that these pulse returns were probably the result when ocean waves from different regions propagated to the laser footprint and reflected the signals by the scattered specular points with slopes oriented normally to the optical path.

In order to illustrate the effects of ocean dynamics on the return pulse shapes, successive pulse measurements are shown at various flight line locations in the following two figures.

In Fig. 8.10 we show six pulse pairs collected successively near the bay and at 2000 ft altitude. These measurements were collected at the rate of about 1 per second. We can see that there were a lot of structural fluctuations between successive waveforms due to reflections from different parts of the ocean (aircraft speed was about 18 m/sec). This figure indicates a trend that the signal waveforms changed from double peaks to a broader Gaussian and so on. The same trend continued throughout the entire data set of 100 waveform pairs. This tended to support the argument that the sea around the bay area consisted mainly of the trochoid waves of long wave periods and the superimposed capillary wavelets of short correlation lengths. Trochoid waves have sharp crests and broad troughs so that the reflections from the crests are weaker than those from the crests. When the

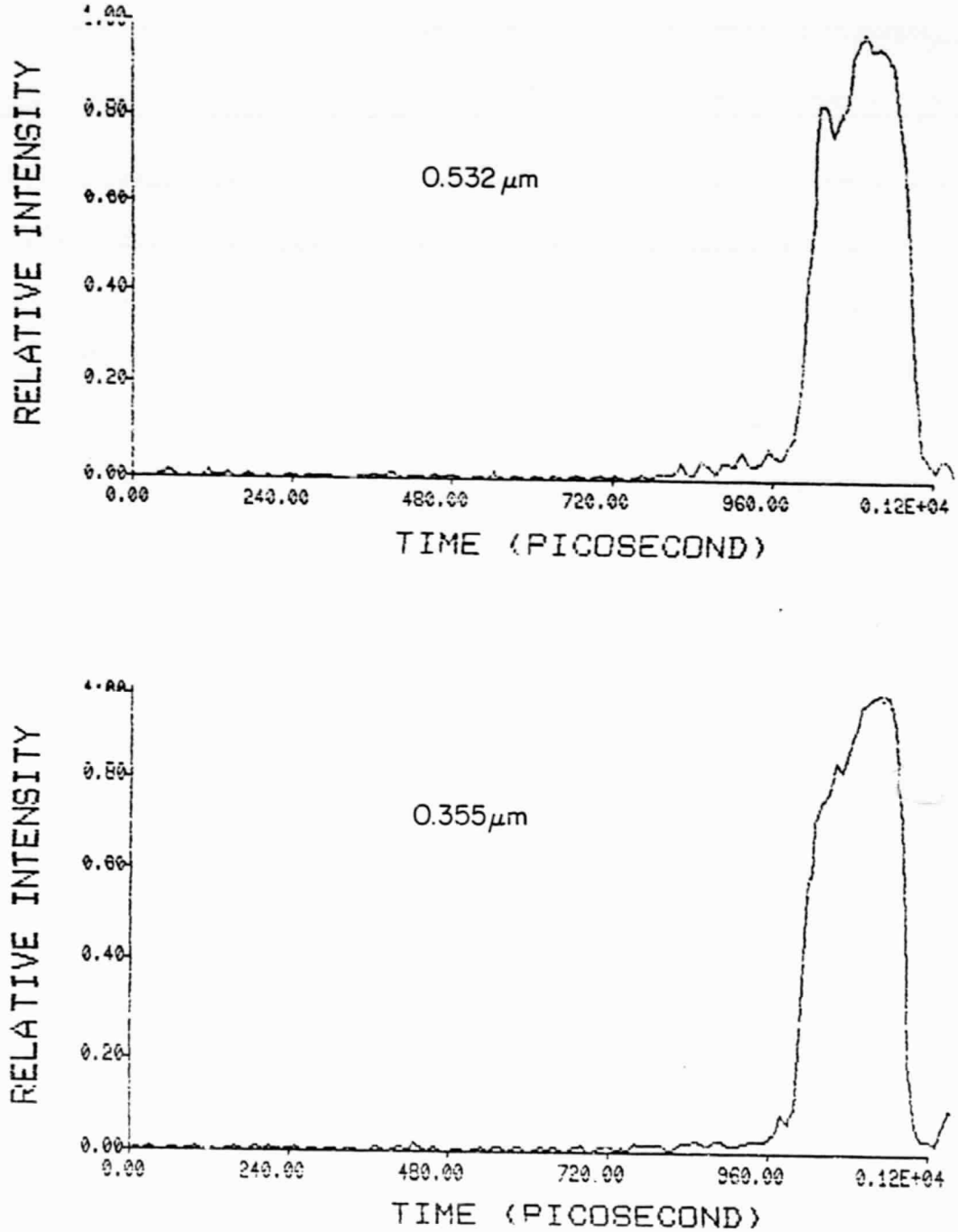

Fig. 8.9. A typical ocean-reflected pulse pair that exhibited Gaussian shaped pulse envelopes.

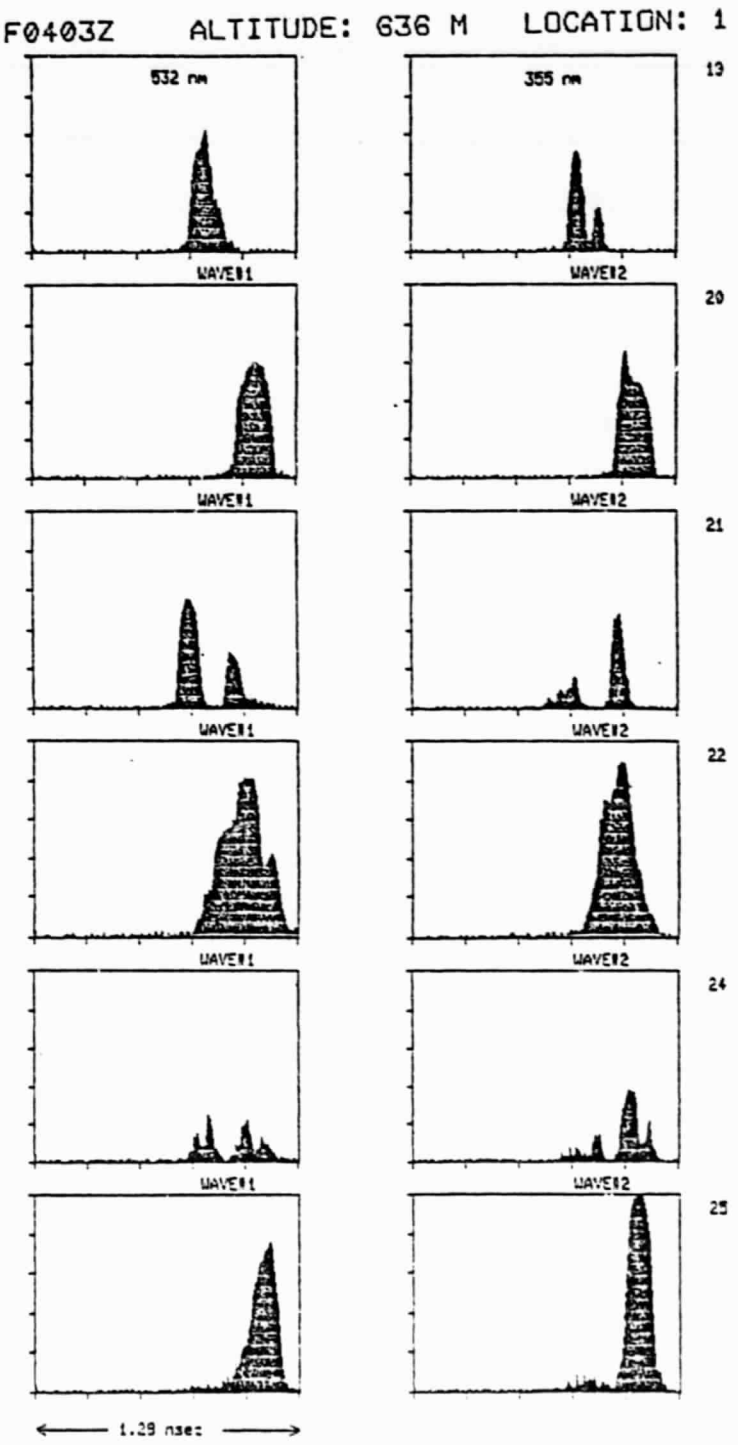

Fig. 8.10. Successive ocean-reflected pulse pairs measured at point 1 of the flight line and at 2000 ft flight altitude.

wave period was long, the laser footprint first illuminated the crest and the beginning portion of the trough which resulted in a double-glinted return signal. As the aircraft moved, the entire trough was illuminated next, which resulted in a Gaussian return. This Gaussian return was broader in time extent because of the range spread of the capillary wavelets and the possible slight tilt of the aircraft with respect to nadir. The pulse intensity fluctuations in successive waveform pairs were due to the combined effects of change in ocean dynamics, difference in laser footprint intensity, shot noise, and tilting of the aircraft. It should be noted that the aircraft instability (tilt) had a two-folded effect on the return signals. First, it attenuated the specular signal intensity; and second, it caused the delay (broadening) on the peak of the scattered component (refer to Chapter 5.3). The position shifts between successive waveforms were primarily due to the receiver time jitters.

In Fig. 8.11 we compare the pulse shapes between measurements collected around the bay and those collected over the open ocean. The first three points were measured near point 5 and the last two were measured near point 9 of the flight line (refer to Fig. 8.6). The altimeter was at 2000 ft flight altitude. The shapes of those pulse pairs collected near the bay followed the typical waveshapes given in Figs. 8.7 through 8.9. As the aircraft approached the open ocean, however, the received signal intensity dropped significantly and the pulse shapes changed randomly. The decrease in signal intensity was probably due to the increase of foams and white caps generated by the stronger sea wind. The white caps covered part of the local ocean surface, and so the number of specular points within the laser footprint became less. In this case, the ocean acted more like a diffuse

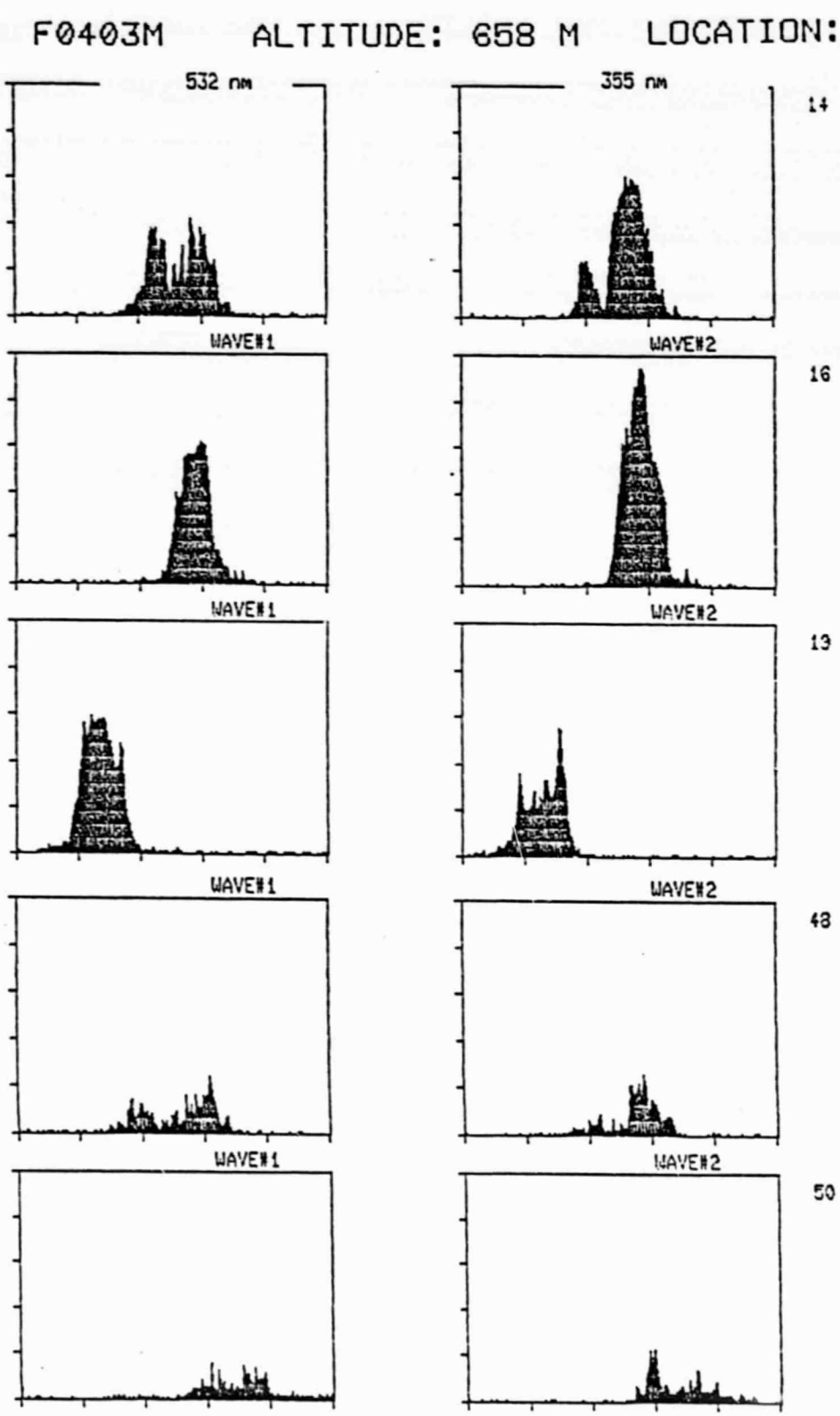

Fig. 8.11. Change in pulse shape between signals collected near the bay and over the open ocean.

target than a mirror-like reflector. The sea wind also perturbed the correlation of the ocean surface, which resulted in more fluctuations on the return signals. When ranging to an open sea, special attention must be given to the alignment of the two laser beams in order to assure good intensity correlation of the return signals.

The average power spectrum for the 0.355-μm returns in each data set was computed by averaging the power spectra of the measured waveforms. The results were used to estimate the RMS slope of the ocean surface profile (S). To do so Eq. (8.9) was used to curve fit the measured spectrum at the -8 dB point by using the system parameters and adjusting the RMS slope. The relationship between the -8 dB bandwidth (B_{-8}) and ω_o is given by

$$\omega_o = \frac{0.398\ B_{-8}}{\left(e^{-\sigma_g^2 B_{-8}^2} - 0.158\right)^{1/2}} \quad . \tag{8.19}$$

A typical result is shown in Fig. 8.12. The measured spectrum in this figure corresponds to the 0.355-μm returns collected at 1000 ft flight altitude and between point 7 and 8 of the flight line. The low intensity components of the measured spectrum was due to the various noise sources. The estimated RMS ocean slope for this particular example is 0.192. The measured ocean slope can be used to estimate the average ocean wind speed by applying the empirical relationship derived by Cox and Munk [1954]

$$S^2 = 0.003 + 0.00512W. \tag{8.20}$$

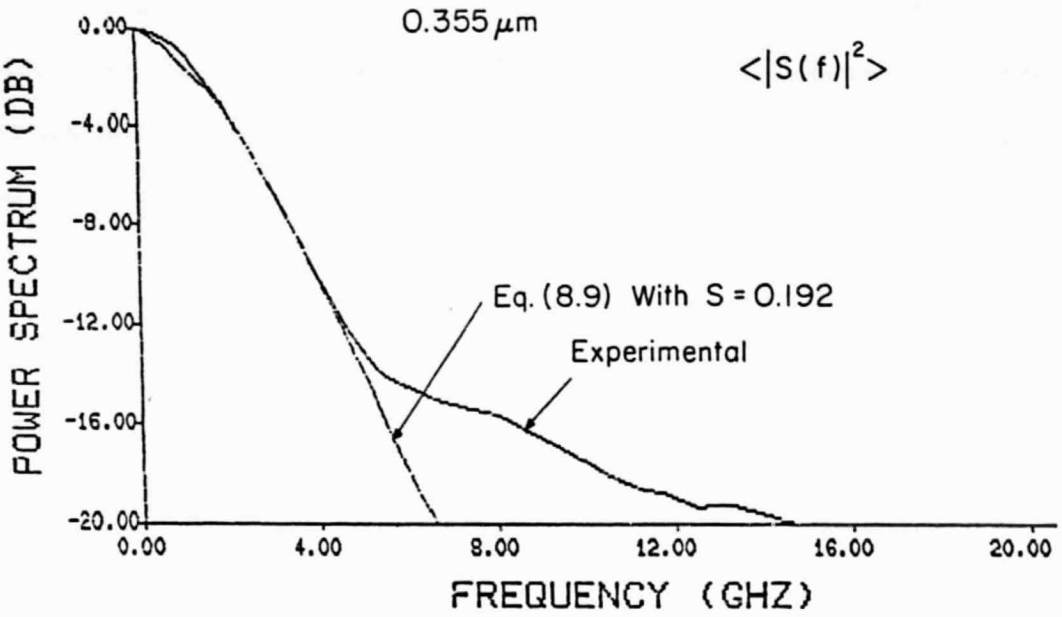

Fig. 8.12. Curve fit the measured average power spectrum ($\langle|S(\omega)|^2\rangle$) by using Eq. (8.9) and the system parameters.

W is the average wind speed in m/sec measured at 12.5 m above the mean sea level. By using the estimated value for S, W is ~ 6.6 m/sec (~ 13.2 knots).

The estimated RMS ocean slopes and wind speeds at different parts of the ocean are plotted in Fig. 8.13. The results were obtained at different flight altitudes. The results show that the ocean profile had a fairly constant slope of ~ 0.12 near the bay (point 1 to point 4), and got larger toward the open sea. This is reasonable because the wind over the open sea is usually stronger. From these values, the estimated wind speed was about 4.5 knots around the bay area, and it gradually increased to about 14 knots at point 9. As expected, the measured ocean slopes do not appear to be sensitive to the change in altitude.

Although we did not evaluate the sensitivities of the inferred ocean slope with respect to the various system parameters, the initial result, however, indicates that the spectral technique may be a possible way of estimating the sea state and cross-wind profile over the ocean.

8.5 Data Analysis - Pressure Sensing

The cross-correlation algorithm was used to estimate the differential propagation time of the laser pulses at 0.355 and 0.532 μm. The measured results were compared with the predicted two-color atmospheric delay and the pressure at different altitudes.

Fig. 8.14 shows the pressure measurement results at the mean altitude of 1064 ft. The length of the arrow indicates the duration of each set, while the arrow head indicates the forward direction. The error bar corresponds to ±1 normalized standard deviation (σ_n) of the form

$$\sigma_n = \sigma/\sqrt{n} \tag{8.21}$$

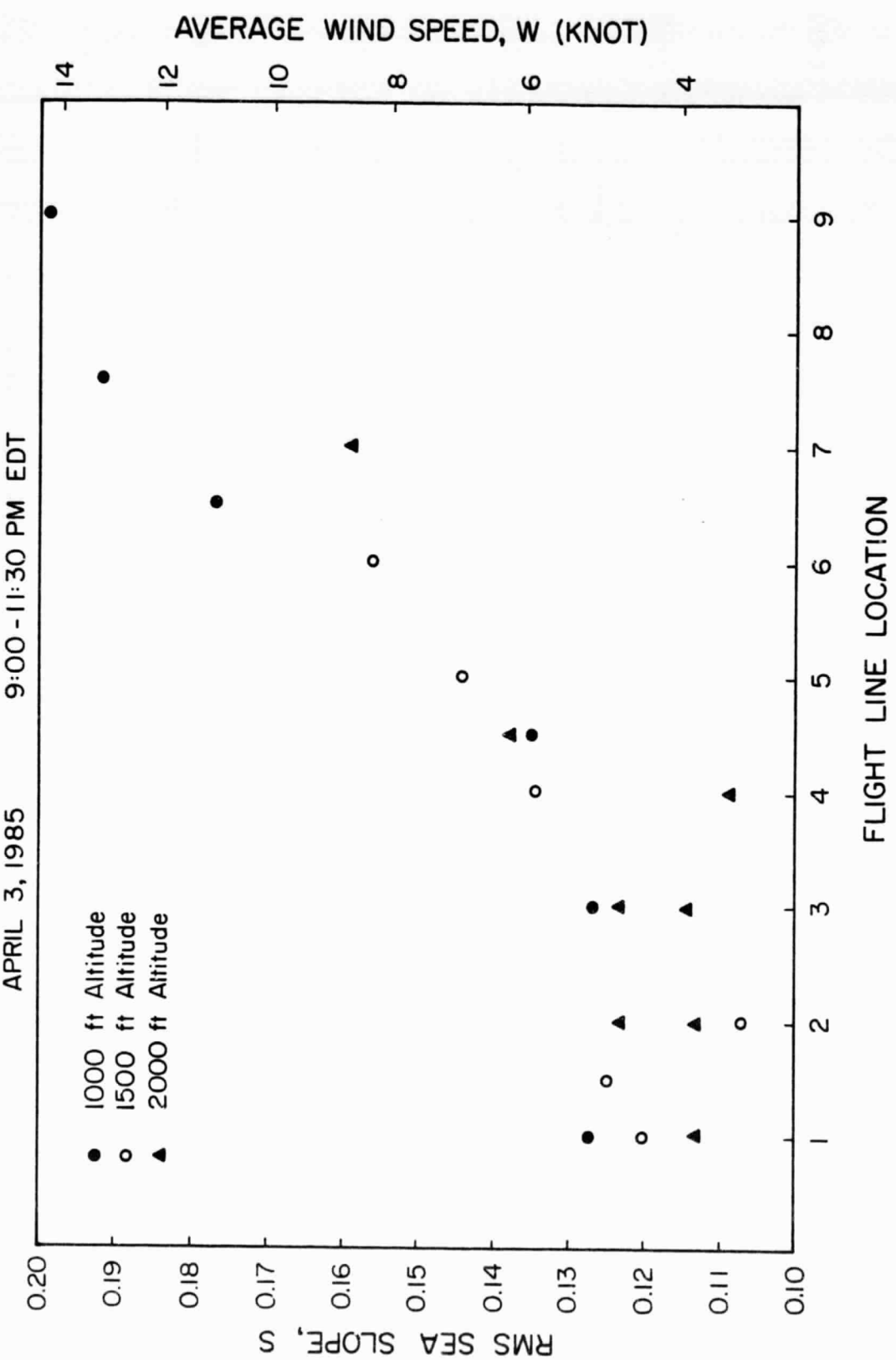

Fig. 8.13. The estimated RMS sea slope (S) and the ocean wind speed (W) using the spectral curve fitting technique.

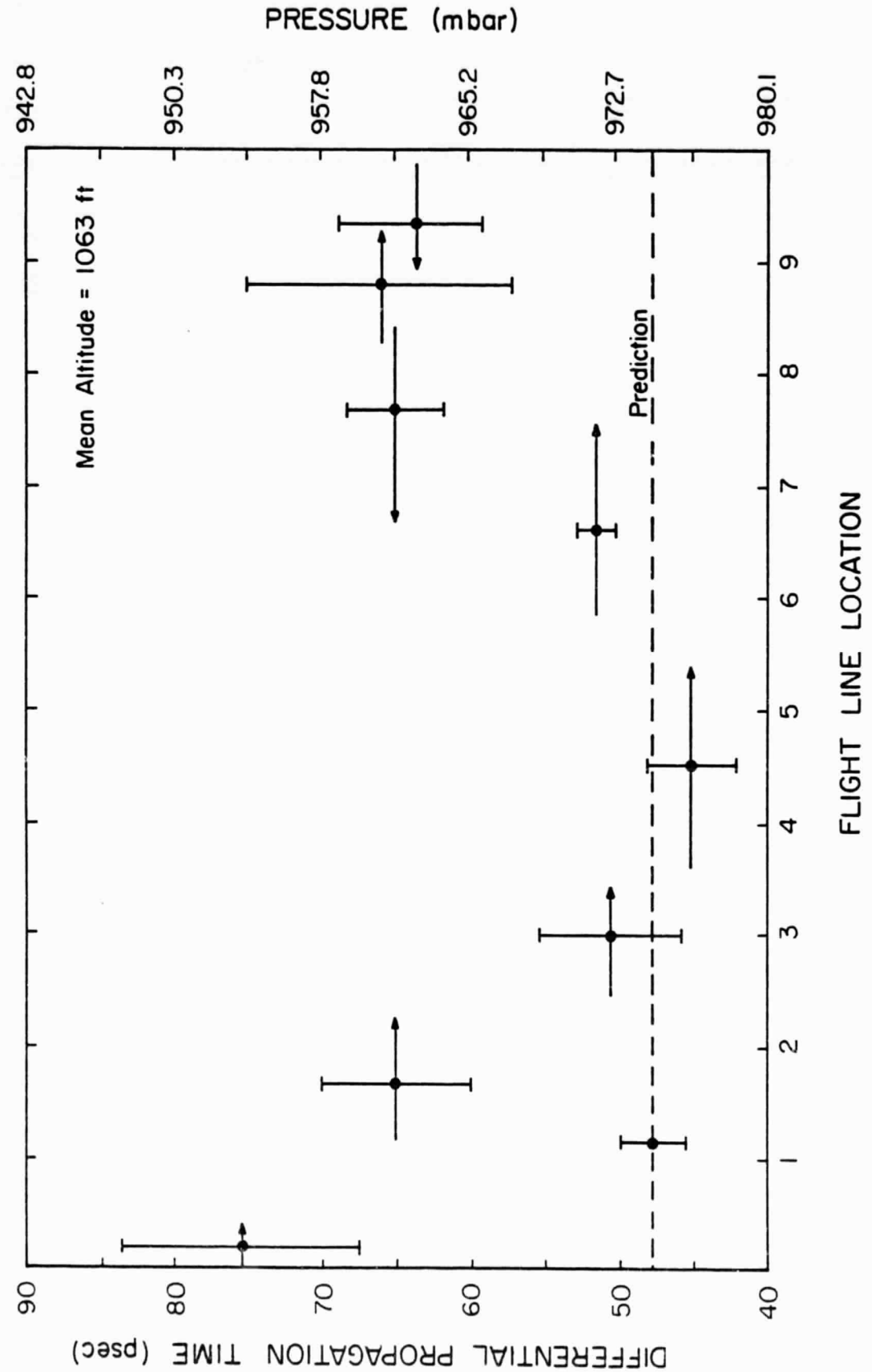

Fig. 8.14. Measured two-color differential propagation time using cross-correlation estimator and the inferred atmospheric pressure at 1063 ft. mean altitude.

where n is the total number of measurements and σ is the single-shot standard deviation in each data set. The result shows that three of the measurement sets at this altitude had errors less than 3.5 psec (2.6 mbar), four sets had errors between 16 and 18 psec (12 and 13.5 mbar). The set that had the largest error of 27.5 psec (20.5 mbar) was collected during the time that the aircraft encountered very strong turbulence. The average bias with respect to the predicted differential atmospheric delay among these eight measurement sets was 12.4 psec (9.25 mbar).

Fig. 8.15 shows the pressure measurement results at the mean altitude of 1535 ft. In these results, two of the measurement sets had errors less than 2 psec (1.49 mbar), two sets had errors of 4 to 5 psec (3 to 3.73 mbar), and two sets had errors between 7 and 9.5 psec (5.2 and 7.1 mbar). The average bias among these six measurement sets was 3.58 psec (2.67 mbar).

Fig. 8.16 shows the pressure measurement results at the mean altitude of 2103 ft. In these results, four sets had errors less than 2.5 psec (1.87 mbar), and the remaining sets had errors between 4 and 6 psec (3 and 4.48 mbar). The average bias among these nine sets was 1.72 psec (1.28 mbar).

For the pressure measurement results at all three altitudes, 10 of 23 sets showed errors less than 4 psec, 17 of 23 sets showed errors less than 7 psec. The large biases in some of the measurement sets were most likely due to the different intensity footprints of the 0.355- and 0.532-μm laser beams.

The RMS differential timing accuracies (single-shot) of the cross-correlation estimator are compared with those of the centroid estimator and peak detector in Table 8.2. We can see that the performance of the

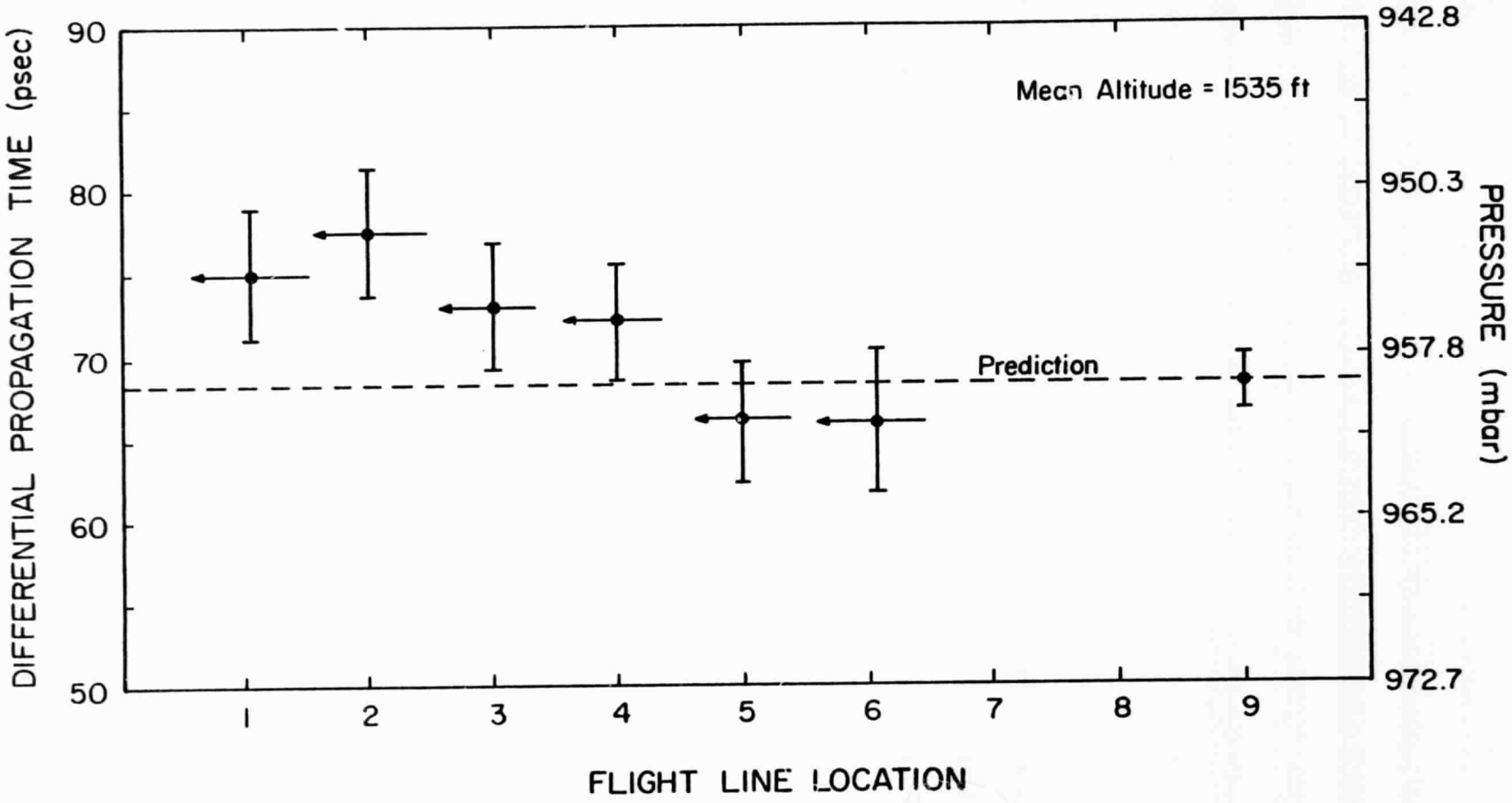

Fig. 8.15. Measured two-color differential propagation time using cross-correlation estimator and the inferred atmospheric pressure at 1535 ft mean altitude.

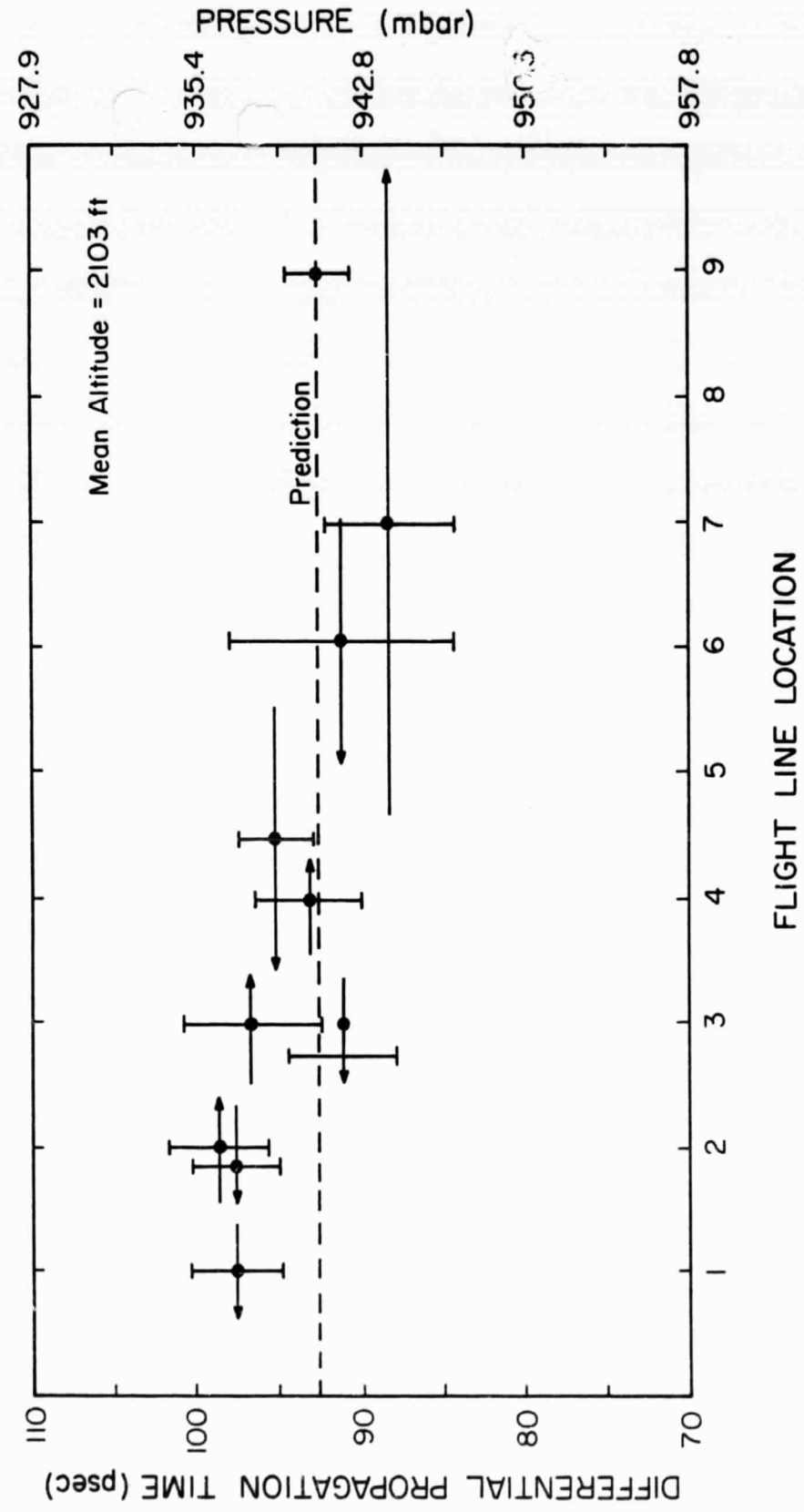

Fig. 8.16. Measured two-color differential propagation time using cross-correlation estimator and the inferred atmospheric pressure at 2103 ft. mean altitude.

TABLE 8.2.

COMPARISON OF THE SINGLE-SHOT DIFFERENTIAL TIMING ACCURACY FOR DIFFERENT ESTIMATORS

Estimator	RMS Differential Timing Accuracy (psec) 1000 ft	1500 ft	2000 ft
Cross-correlation	25.42	24.37	20.48
Centroid	62.81	59.47	53.51
Peak Detection	121.39	112.64	99.38

cross-correlation estimator is better than the other two suboptimal estimators. The peak detector is the one which is most sensitive to the shot noise, speckle, and ocean profile fluctuations. Consequently, its performance is the worst among the three estimators.

The timing accuracies of all three estimators increase with altitude. This was probably due to the effects of the non-coaxial arrangement mentioned in Chapter 6. For the non-coaxial systems, the received signal energy is directly proportional to the overlap area between the laser footprint and the receiver's field-of-view instead of following the usual z^{-2} dependence. During this experiment the laser footprint and receiver FOV from the 2000 ft altitude had the largest overlap area, while those from the 1000 ft altitude had the smallest. As a result, the 2000 ft measurements had the strongest signal returns while those measured at 1000 ft altitude had the weakest (refer to Fig. 6.11). Furthermore, it was shown in Chapter 5 that the RMS differential timing error is inversely related to the received signal strength. This was why the differential timing measurement error decreased from 1000 ft to 2000 ft for all three estimators.

The single shot measurement accuracy of the correlation estimator is between 20 and 26 psec. By averaging over 100 shots, we can improve the accuracy to 2 to 3 psec, which corresponds to the pressure measurement accuracy of less than 1.5 mbar.

8.6 Conclusions

In this chapter we analyzed the data obtained during the airborne two-color altimeter experiment. From these measurements, information on both the sea state and the atmospheric pressure was inferred.

At all three altitudes, the return signal waveforms exhibited either single glint, double glints, or Gaussian shape corresponds to different local ocean surface profiles within the laser footprint. Pulse spreading occurred more frequently at the higher altitudes and over the open ocean as expected. The RMS slope at different parts of the ocean was estimated using a spectral curve fitting technique. The result indicated that the sea slope is smaller near the bay than over the open ocean.

The atmospheric delay and pressure were estimated using a cross-correlation algorithm. In all, 10 out of 23 measurement sets showed pressure measurement errors less than 4 mbar, and 17 out of 23 sets showed errors less than 7 mbar. The large bias in some measurement sets were likely due to the different footprint intensities at the two wavelengths. However, the accuracies of these initial high resolution airborne two-color measurements demonstrated that this approach to pressure measurements is both promising and viable.

9. CONCLUSIONS

In satellite laser ranging, atmospheric refraction is the most dominant error source because it increases the optical pathlengths from the ground to the orbiting satellite by over 2.4 m when the satellite is at zenith. Pulsed two-color laser ranging systems can be used to correct the refraction error by directly measuring the difference in propagation times between two optical pulses that are transmitted simultaneously at two frequencies. However, proper design of the receiver timing algorithm is necessary in order to obtain picosecond differential timing accuracies which are required for most applications. The requirement is further complicated by the various random noises associated with laser ranging such as shot noise and speckle. The study showed that speckle noise is particularly severe when ranging to retro-reflector equipped satellites due to the coherence interference in signal reflections from retro-reflectors of different ranges on the array.

By taking advantage of the pulse correlation at the two wavelengths, a cross-correlation technique is used to estimate the differential propagation times. The performance of the cross-correlation technique is analyzed by considering both shot noise and speckle. The accuracy of this estimator is in general a function of the detected signal strength, speckle signal-to-noise ratio, receiver bandwidth and the detected signal bandwidth.

Pulse reflections from the diffuse targets, the satellite-based retro-reflector arrays, and the ocean were analyzed in order to evaluate quantitatively the performance of this estimator. For the flat diffuse targets, the timing accuracy is highly dependent on the receiver bandwidth and the characteristics of the time-resolved speckle. At low signal levels, it was shown that the timing performance of the correlation estimator is comparable to

that of the optimal Maximum-Likelihood (ML) estimator when the receiver bandwidth is chosen to match the bandwidth of the target reflected pulses. At high signal levels, however, time-resolved speckle places a fundamental limit on the performance of the correlation estimator. For the retro-reflector arrays, the timing performance is dominated by partially developed speckle so that the differential propagation time cannot be resolved to better than the pulse width of the detected signals. For the ocean, the timing accuracy is highly dependent on the local ocean surface profile and the surface correlation length. It was shown that picosecond timing accuracy is only feasible over regions where the surface correlation length is larger than the laser footprint radius. Based upon the analytical results, it appears that the overall performance of the two-color satellite laser ranging systems is dominated by the receiver bandwidth, transmitted laser pulse width and the pulse repetition rate and not the detected signal strength.

The results for the retro-reflector arrays are of particular interest in this dissertation because both flat and spherical retro-reflector arrays have been deployed on satellites and the moon and are routinely used as targets for geodetic measurements. Chapter 5 serves as the first analytical treatment on this target configuration by considering coherent fading.

Experimental data analysis is also an integral part of this dissertation. In Chapter 7 the two-color ranging measurement made over the horizontal paths were analyzed in order to verify the theoretical results of Chapter 5. The theoretical and experimental results appeared to agree with each other in general. In Chapter 8 the ocean-reflected pulse measurements were analyzed in order to infer the sea state and to verify the pressure measurement technique.

The reflected pulse shapes were in general related to the local sea state within the laser footprint. A spectral curve fitting technique was used to estimate the sea slope and wind speed. The results showed an increase in both the sea slope and wind speed as the aircraft approached the open ocean. This spectral technique is a new approach to the wind speed estimation, and the initial inferred results appeared to be reasonable. However, the wind speed sensitivities to various parameters must be investigated in order to determine the accuracy of this technique, and more experimental studies are needed in order to verify its feasibility under a broader range of wind conditions. The measured results in atmospheric pressure were in close agreement with the theoretical predictions at all three flight altitudes. Thus, it demonstrated that the two-color ranging technique in atmospheric pressure measurement is both promising and viable.

APPENDIX A. MEAN AND AUTOCOVARIANCE OF THE REFLECTED SIGNALS FROM A CUBE CORNER REFLECTOR (CCR) ARRAY

The complex amplitude of the pulsed laser beam at the transmitting telescope is

$$U_T(\underline{r},t) = f(t)\, A_T(r) \exp(j\omega t) \tag{A.1}$$

where $f(t)$ = laser pulse amplitude,

$a_T(\underline{r})$ = complex amplitude cross-section of the laser beam, and

ω = laser frequency.

If the CCR array is at a large range, the field incident on the array can be calculated using the Fresnel diffraction formula

$$U_1(\underline{\rho},z,t) = T_a^{1/2}\, f(t - \frac{2z}{c} - \frac{\rho^2}{2cz})\, a(\underline{\rho},z) \exp[j(\omega t - kz - \frac{k}{2z}\rho^2)], \tag{A.2}$$

$$a(\underline{\rho},z) = \frac{1}{\lambda z} \int d^2\underline{r}\; a_T(\underline{r}) \exp[-j\frac{k}{z}(\frac{r^2}{2} - \underline{\rho}\cdot\underline{r})] \quad . \tag{A.3}$$

T_a is the one-way intensity transmittance of the atmosphere, k is the wave number, and λ is the laser wavelength. In deriving Eq. (A.2) we have assumed that the RMS laser pulse width (σ_f) and the area of the transmitting telescope (A_T) satisfy the condition

$$c\sigma_f >> A_T / z \; . \tag{A.4}$$

If there are M CCR's illuminated by the incident beam, the reflected field at the reference plane immediately in front of the array can be approximated by the formula [Wang, 1984]

$$U_2(\underline{\rho},z,t) \cong \sum_{m=1}^{M} \beta_{r_m}^{1/2} A_m U_1\left(\underline{\rho},z,t - \frac{2\xi(\underline{\rho})}{c}\right) \delta(\underline{\rho} - \underline{\rho}_m) e^{j\phi_m} \tag{A.5}$$

where ϕ_m is the random phase angle associated with reflection from the m-th CCR. The ϕ_m's are assumed to be mutually independent and uniformly distributed over $(0,2\pi)$. $\xi(\underline{\rho})$ is the range displacement of the reflecting surface with respect to the reference plane, and the remaining quantities in Eq. (A.5) are defined in Chapter 3. The field in the plane of the receiving telescope is

$$U_R(\underline{r},z,t) = a_R(\underline{r},z,t) \exp(j\omega t) \quad , \tag{A.6}$$

$$a_R(\underline{r},z,t) = \frac{T_a}{\lambda z} \exp\left[-j\left(2kz + \frac{k}{2z} r^2\right)\right] \sum_{m=1}^{M} \beta_{r_m}^{1/2} A_m f(t - \psi(\underline{\rho}_m)) \cdot a(\underline{\rho}_m,z)\, e^{j\phi_m} \exp\left[-jk\left(\frac{\rho_m^2}{2z} - 2\xi(\underline{\rho}_m) - \frac{\underline{\rho}_m \cdot \underline{r}}{z}\right)\right] . \tag{A.7}$$

We assume the receiver field-of-view is adjusted so that all the signal energy which is incident on the telescope objective is focused onto the photodetector. Therefore, the total received signal power is given by

$$P(t) = \int d^2\underline{r}\; w(\underline{r}) \left|A_R(\underline{r},z,t)\right|^2 \tag{A.8}$$

where $w(\underline{r})$ is an appropriate aperture weighting function. $w(\underline{r})$ is equal to one for $\underline{r}$ inside the aperture and zero otherwise. The mean received power can be found by averaging the power over the random phase:

$$\langle P(t)\rangle = T_a^2 A_R z^{-2} \sum_{m=1}^{M} \sigma_m \left|a(\underline{\rho}_m, z)\right|^2 \left|f(t - \psi(\underline{\rho}_m))\right|^2 \quad , \tag{A.9}$$

$$\sigma_m = \beta_{r_m} A_m^2 / \lambda^2 \quad . \tag{A.10}$$

σ_m is the lidar cross-section of the m-th CCR on the array, A_m is its effective area, β_{r_m} is its reflectivity and A_R is the area of the receiver aperture.

The covariance of P(t) can be written as

$$C_P(t_1,t_2) = \langle P(t_1)P(t_2)\rangle - \langle P(t_1)\rangle\langle P(t_2)\rangle \tag{A.11}$$

and can be evaluated by using Eqs. (A.7) and (A.8). By using the statistical property of the uniform random variable

$$\langle \exp\left[j(\phi_k - \phi_\ell + \phi_m - \phi_\ell)\right]\rangle = \delta_{k,\ell}\,\delta_{m,n} + \delta_{k,n}\delta_{\ell,m} + \delta_{k,\ell,m,n} \tag{A.12}$$

where

$$\delta_{ij} = \begin{cases} 1 & i=j \\ 0 & i\neq j \end{cases} \quad ,$$

$$\delta_{i,j,k,\ell} = \begin{cases} 1 & i=j=k=\ell \\ 0 & \text{otherwise} \end{cases} \quad .$$

Eq. (A.11) can be expressed as

$$C_p(t_1,t_2) = T_a^4 A_R^2 z^{-4} \sum_{\substack{m=1 \\ m\neq n}}^{M} \sum_{n=1}^{M} \sigma_m \sigma_n |a(\underline{\rho}_m,z)|^2 |a(\underline{\rho}_n,z)|^2 W(\underline{\rho}_m,\underline{\rho}_n,z,\lambda)$$

$$\cdot f(t_1 - \psi(\underline{\rho}_m)) f^*(t_1 - \psi(\underline{\rho}_n)) f^*(t_2 - \psi(\underline{\rho}_m)) f(t_2 - \psi(\underline{\rho}_n))$$

where W was given by Eq. (3.18). However, when the following condition

$$|\underline{\rho}_m - \underline{\rho}_n| \ll \lambda z / 4(\pi A_R)^{1/2} \qquad \forall\ m,n \tag{A.14}$$

is satisfied, Eq. (A.13) can be simplified to

$$C_p(t_1,t_2) = T_a^4 A_R^2 z^{-4} \sum_{\substack{m=1 \\ m\neq n}}^{M} \sum_{n=1}^{M} \sigma_m \sigma_n |a(\underline{\rho}_m,z)|^2 |a(\underline{\rho}_n,z)|^2$$

$$\cdot f(t_1 - \psi(\underline{\rho}_m)) f^*(t_1 - \psi(\underline{\rho}_n)) f^*(t_2 - \psi(\underline{\rho}_m)) f(t_2 - \psi(\underline{\rho}_n)). \tag{A.15}$$

Inequality (A.14) is generally satisfied in satellite laser ranging where the one-way range distance is of the order of 10^3-10^4 kilometers.

The signal-to-noise ratio of the speckle (K) is defined as the quotient between the square of the mean received energy and the energy variance [Gardner, Dec. 1977]. That is,

$$K = \left[\int_{-\infty}^{\infty} dt \langle P(t) \rangle \right]^2 / \int_{-\infty}^{\infty} dt_1 \int_{-\infty}^{\infty} dt_2\, C_p(t_1,t_2) \quad . \tag{A.16}$$

Eq. (A.16) can be evaluated directly using Eqs. (A.9) and (A.13) and the result is given by Eq. (3.13).

For direct detection the mean and autocovariance of the signal at the receiver output can be calculated using Campbell's theorem [Papoulis, 1974]

$$\langle S(t)\rangle = \frac{\eta}{hf} \langle P(t)\rangle * h(t) \quad , \tag{A.17}$$

$$C_S(t_1,t_2) = \frac{\eta}{hf} \int_{-\infty}^{\infty} d\tau \langle P(\tau)\rangle\, h(t_1 - \tau)\, h(t_2 - \tau) + \left(\frac{\eta}{hf}\right)^2 \int_{-\infty}^{\infty} d\tau_1 \int_{-\infty}^{\infty} d\tau_2\, C_P(t_1 - \tau_1)\, h(t_1 - \tau_1)\, h(t_2 - \tau_2) \tag{A.18}$$

where η is the quantum efficiency of the photodetector, and hf is the energy of one signal photon.

The expected number of detected photons can be calculated using link equation:

$$\langle N\rangle = \frac{\eta}{hf} Q\, G\, T_a^{\,2}\, A_R\, z^{-2} \tag{A.19}$$

with

$$Q = \int d^2\underline{\rho}\, |a(\underline{\rho},z)|^2 \int_{-\infty}^{\infty} dt\, |f(t)|^2 \tag{A.20}$$

and

$$G = \sum_{m=1}^{M} \sigma_m \,|\, a(\underline{\rho}_m,z)\,|^2 \,/\, \int d^2\underline{\rho} \,|\, a(\underline{\rho},z)\,|^2 \quad . \tag{A.21}$$

Q is the transmitted signal energy, G is the gain of the CCR array. If the laser footprint has a Gaussian cross-section (Eq. (4.38)), Eqs. (A.19) and (A.21) can be expressed as

$$\langle N \rangle = (2\pi)^{-1} \frac{\eta}{hf} Q T_a^2 A_R z^{-4} \tan^{-2} \theta_T \sum_{m=1}^{M} \sigma_m \qquad (A.22)$$

and

$$G = \sum_{m=1}^{M} \sigma_m / (2\pi z^2 \tan^2 \theta_T) \quad , \qquad (A.23)$$

respectively. $\langle S(t) \rangle$ and $C_S(t_1,t_2)$ can now be calculated readily by using Eqs. (A.9) through (A.21), and the final results are given by Eqs. (3.9) and (3.10), respectively.

APPENDIX B. EVALUATION OF THE BANDWIDTH OF THE OCEAN REFLECTED SIGNAL

The bandwidth of the received signal defined previously in Chapter 5 is given by

$$B_S^2 = \frac{\int d\omega\ \omega^2 |\phi_S(\omega)|^2}{\int d\omega |\phi_S(\omega)|^2} \quad . \tag{B.1}$$

From Eqs. (3.1) and (5.19), the power spectrum of the expected signal is

$$|\phi_S(\omega)|^2 = \int d^2\underline{\rho}_1 \int d^2\underline{\rho}_2\ b_2(\underline{\rho}_1,z)\ b_2(\underline{\rho}_2,z)\ e^{-\omega^2\sigma_g^2} < e^{j\omega(\psi_1 - \psi_2)} >$$

$$= \frac{e^{-\omega^2\sigma_g^2}}{4\pi z^4 \tan^4\theta_T} \int d^2\underline{\rho}_1 \int d^2\underline{\rho}_2\ e^{-\frac{(\rho_1^2 + \rho_2^2)}{2 z^2 \tan^2\theta_T} + j\omega\frac{(\rho_1^2 - \rho_2^2)}{cz}} \tag{B.2}$$

$$\cdot < \exp\left[-j\frac{2\omega}{c}\left[\xi(\underline{\rho}_1) - \xi(\underline{\rho}_2)\right]\right] > \quad ,$$

where we have assumed a Gaussian laser footprint with a radius of $z \tan\theta_T$ at the exp(-1/2) point. The expectation is with respect to the surface profile. For a Gaussian surface profile with RMS surface height σ_ξ, we have

$$< \exp\left[-j\frac{2\omega}{c}\left[\xi(\underline{\rho}_1) - \xi(\underline{\rho}_2)\right]\right] > = \exp\left\{-\frac{4\omega^2\sigma_\xi^2}{c^2}\left[1 - R_\xi(\underline{\rho}_1,\underline{\rho}_2)\right]\right\} \tag{B.3}$$

where $R_\xi(\underline{\rho}_1, \underline{\rho}_2)$ is the normalized autocorrelation function of the surface profile ξ.

We first assume $L \geq z \tan \theta_T$ and a quadratic autocorrelation function with $R_\xi(\underline{\rho}_1, \underline{\rho}_2)$ given by

$$R_\xi(\underline{\rho}_1, \underline{\rho}_2) = 1 - \frac{|\underline{\rho}_1 - \underline{\rho}_2|^2}{2L^2} \quad , \tag{B.4}$$

where L is the correlation length of the surface profile. The case of $L \ll z \tan \theta_T$ is treated later.

By substituting Eqs. (B.3) and (B.4) into (B.2) and making the following changes of variables

$$\underline{\rho}_d = \underline{\rho}_1 - \underline{\rho}_2 \quad ,$$

and

$$\underline{\rho}_s = (\underline{\rho}_1 + \underline{\rho}_2)/2 \quad ,$$

we have

$$|\phi_S(\omega)|^2 = \frac{e^{-\omega^2 \sigma_g^2}}{4\pi z^4 \tan^4 \theta_T} \int d^2\underline{\rho}_s \int d^2\underline{\rho}_d \, e^{-\frac{2\rho_s^2 + \frac{1}{2}\rho_d^2}{2 z^2 \tan^2 \theta_T}} \quad .$$

$$\cdot\, e^{-\frac{2\,\omega^2\sigma_g^2}{c^2L^2}\,\rho_d^2 \,+\, j\,\frac{2\omega}{cz}\,\underline{\rho}_s\,\cdot\,\underline{\rho}_d} \qquad \text{(B.5)}$$

$$= \frac{\gamma_1\, e^{-\omega^2\sigma_g^2}}{\gamma_1^2 + \sigma_g^2\omega^2} \qquad L \geq z \tan\theta_T$$

where

$$\gamma_1 = \frac{c\sigma_g}{2\,z\tan\theta_T\left[\frac{2\sigma_g^2}{L^2} + \tan^2\theta_T\right]^{1/2}}\,, \qquad L \geq z\tan\theta_T. \quad \text{(B.6)}$$

By substituting Eq. (B.5) into Eq. (B.1), we obtain

$$B_S^2 = \frac{\gamma_1\, e^{-\gamma_1^2}}{\sqrt{\pi}\,(\sigma_g^2)\,\operatorname{erfc}(\gamma)} - \frac{\gamma_1^2}{\sigma_g^2} \qquad L \geq z\tan\theta_T\,. \quad \text{(B.7)}$$

For the case when $L \ll z \tan\theta_T$, the autocorrelation function can be approximated by a delta function. Therefore,

$$|\phi_S(\omega)|^2 = \frac{e^{-\omega^2(\sigma_g^2 + \frac{4}{c^2}\sigma_\xi^2)}}{4\pi z^4 \tan^4\theta_T} \int d^2\underline{\rho}_s \int d^2\underline{\rho}_d \; e^{-\frac{2\rho_s^2 + \frac{1}{2}\rho_d^2}{2z^2\tan^2\theta_T} + j\frac{2\omega}{cz}\underline{\rho}_s\cdot\underline{\rho}_d}$$

$$= \frac{\gamma_1^2 \, e^{-\omega^2(\sigma_g^2 + \frac{4}{c^2}\sigma_\xi^2)}}{\gamma_1^2 + (\sigma_g^2 + \frac{4}{c^2}\sigma_\xi^2)\omega^2}, \qquad L < z \tan\theta_T \tag{B.8}$$

where

$$\gamma_1 = \frac{c(\sigma_g^2 + \frac{4}{c^2}\sigma_\xi^2)^{1/2}}{2z\tan\theta_T} \qquad L \ll z\tan\theta_T \; . \tag{B.9}$$

In this case, the expected bandwidth is

$$B_S^2 = \frac{\gamma_1 \, e^{-\gamma_1^2}}{\sqrt{\pi}\,(\sigma_g^2 + \frac{4}{c^2}\sigma_\xi^2)\,\mathrm{erfc}(\gamma)} - \frac{\gamma_1^2}{(\sigma_g^2 + \frac{4}{c^2}\sigma_\xi^2)} \qquad L \ll z\tan\theta_T \; . \tag{B.10}$$

The combined results under these two conditions were given in Eqs. (5.46) to (5.48).

APPENDIX C. DIFFERENTIAL PROPAGATION TIME OVER A HORIZONTAL PATH

In the spherically symmetric refraction model, the roundtrip optical pathlength (R_o) measured by a pulsed laser ranging system is given by

$$R_o = 2 \int_{r_o}^{r_1} dr \frac{1 + 10^{-6} N_g}{\sin \theta} \tag{C.1}$$

where N_g is the group refractivity, and θ is given by Snell's law for a spherically stratified medium. It follows from Eq. (C.1) that the roundtrip differential pathlength at the two optical frequencies is

$$\Delta R = R_{o_1} - R_{o_2} = 2 \int_{r_o}^{r_1} \frac{dr}{\sin \theta} \; 10^{-6} \; (N_{g_1} - N_{g_2}) \quad . \tag{C.2}$$

When ranging over a horizontal path and by neglecting the fluctuations in the horizontal refractive gradient, N_{g_i} will be constant with r. Consequently, we have

$$\Delta R \cong 2 \times 10^{-6} \; (N_{g_1} - N_{g_2}) \int_{r_o}^{r_1} \frac{dr}{\sin \theta} \quad . \tag{C.3}$$

After combining Eqs. (C.1) and (C.3), the differential optical path-length can be expressed as

$$\Delta R = \frac{10^{-6} (N_{g_1} - N_{g_2}) R_{o_i}}{1 + 10^{-6} N_{g_i}} \cong 10^{-6} (N_{g_1} - N_{g_2}) R_{o_i} [1 - 10^{-6} N_{g_i}] . \quad (C.4)$$

The corresponding roundtrip differential propagation time is

$$\tau = 10^{-6} (N_{g_1} - N_{g_2}) T_i [1 - 10^{-6} N_{g_i}] , \quad (C.5)$$

where T_i is the roundtrip propagation time of the optical pulse at wavelength λ_i. For the wavelengths used during the experiment, $N_{g_{0.355}}$ and $N_{g_{0.532}}$ are 313 and 290 PPM, respectively [Abshire, et al., 1983].

REFERENCES

Abshire, J. B., "Pulse Multiwavelength Laser Ranging System," NASA Memorandum 83917 (Mar. 1982).

Abshire, J. B. and J. E. Kalshoven, Jr., Appl. Opt. 22, 2578 (Sept. 1983).

Abshire, J. B., C. S. Gardner and B. M. Tsai, "Airborne Laser Altimeter Measurement of Atmospheric Pressure," Proc. 12th International Laser Radar Conference, Aix en Provence, France, 403 (Aug. 1984).

Abshire, J. B. and C. S. Gardner, "Atmospheric Refractivity Corrections in Satellite Laser Ranging," to be published, IEEE Trans. Geo. and Remote Sensing, (Sept. 1985).

Abshire, J. B., J. F. McGarry, R. S. Chabot and H. E. Rowe, "Airborne Measurements of Atmospheric Pressure with a Two-Color Streak Camera-Based Laser Altimeter," Proc. CLEO'85 (May 1985).

Bar-David, I., IEEE Trans. Inform. Theory IT-15, 31 (Jan. 1969).

Bar-David, I., IEEE Trans. Inform. Theory, 326, (May 1975).

Bender, P. L. and J. C. Owens, J. Geophys. Res. 70, 2461 (May 1965).

Bufton, J. L., R. S. Iyer and L. S. Taylor, Appl. Opt. 16, 2408 (Sept. 1977).

Cox C. and W. Munk, JOSA, 44, 838 (1954).

Davis, J. L., A. E. E. Rodgers, A. Herring and I. I. Shapiro, "Geodesy by Radio Interferometry : Calibration of the Wet and Dry Troposphere," Trans. Amer. Geophys. Union (EOS), 65, 853 (1984).

Fitzmaurice, M. W., P. O. Minot, and W. D. Kahn, "Development and Testing of a Spaceborne Laser Ranging System Engineering Model," NASA Tech. Rept. X-723-75-307 (Nov. 1975).

Fitzmaurice, M. W., P. O. Minott, J. B. Abshire and H. E. Rowe, "Prelaunch Testing of the Laser Geodynamic Satellite (LAGEOS)," NASA Tech. Paper No. 1062 (Oct. 1977).

Gardner, C. S., Appl. Opt. 16, 2427 (Sept. 1977).

Gardner, C. S., "Speckle Noise in Satellite Based Lidar Systems," Radio Res. Lab. Tech. Rep. No. 488, University of Illinois (Dec. 1977).

Gardner, C. S., J. R. Rowlett and B. E. Hendrickson, Appl. Opt. 17, 3143 (Oct. 1978).

Gardner, C. S., Appl. Opt. 18, 3184 (Sept. 1979).

Gardner, C. S. and R. A. Axford, Jr., "Regression Models for Multicolor Satellite Laser Ranging," Radio Res. Lab. Tech. Rep. No. 505, University of Illinois (Mar. 1980).

Gardner, C. S., Appl. Opt. 21, 448 (Feb. 1982).

Gardner, C. S., B. M. Tsai and K. E. Im, Appl. Opt. 22, 2571 (Sept. 1983).

Goodman, J. W., Proc. IEEE 53, 1688 (Nov. 1965).

Goodman, J. W., In Remote Techniques for Capillary Wave Measurements, Ed. K. S. Krishnan and N. A. Peppers (Stanford Research Inst. Rep., Stanford, Calif., 1973).

Goodman, J. W., "Statistical Properties of Laser Speckle Pattern," in Laser Speckle and Related Phenomena, J. C. Dainty, Ed., 9 (Springer, New York, 1975).

Hansch, T. W., "Application of Dye Lasers," in Dye Laser, F. P. Schafer, Ed., 1 (Springer, New York, 1977).

Harms, J., W. Lahmann and C. Weitkamp, Appl. Opt. 17, 1131 (Apr. 1978).

Harms, App. Opt. 18, 1559 (May 1979).

Helstrom, C. W., Statistical Theory of Signal Detection (Pergamon Press, London, 1960).

Im, K. E., B. M. Tsai and C. S. Gardner, "Analysis of Short Pulse Laser Altimetry Data obtained over Horizontal Path," Radio Res. Lab. Tech. Rep. No. 526, University of Illinois (Sept. 1983).

Im, K. E. and C. S. Gardner, "Estimation of the Differential Pulse Propagation Times in Two-Color Laser Ranging Systems," accepted for publication in JOSA A (1985).

Iyer, R. S., IEEE Trans. Aerosp. Electron. Syst. AES-12, 577 (Sept. 1976).

Kinsman, B., Wind Waves (Prentice Hall, Englewood Cliffs, 1965).

Mandel L., "Fluctuations of Photon Beams : The Distribution of Photoelectrons," Proc. Phy. Soc. (London), 74, No. 475, 233, 1959.

Marini J. W. and C. W. Murray, Jr., "Correction of Laser Ranging Tracking Data for Atmospheric Refraction at Elevations Above 10 Degrees," NASA Tech. Rep. X-591-73-531 (Nov. 1973).

Papoulis, A., IEEE Trans. Commun. COM-22, 162 (Feb. 1974).

Plotkin, H. H., T. S. Johnson, P. L. Spadin, and M. Moye, Proc. IEEE 53, 301 (Mar. 1965).

Prabhakara, C., H. D. Chang and A. T. C. Chang, J. Appl. Meteorol. 21, 59 (1982).

Prilepin, M. T., "Light Modulating Method for Determining Average Index of Refraction of Air along a line," Tr. Tsentr. Nauchne., Issled, Inst. Geod., Aero. i Kartog., 114, 127 (1957).

Saastamoinen, J., "Introduction to Practical Computation of Astronomical Refraction," Bull. Geod., 107, 383 (1972).

Smith, D. E., R. Kolenkiewicz P. J. Dunn and T. S. Johnson, Science 178, 405 (Oct. 1972).

Smith, D. E., R. Kolenkiewicz, and P. J. Dunn, Nature 244, 498 (Aug. 1973).

Smith, D. E., R. Kolenkiewicz, R. W. Agreen, and P. J. Dunn, "Dynamic Techniques for Studies of Secular Variations in Position from Ranging to Satellites," Proceedings of Symposium on the Earth's Gravitational Field and Secular Variations in Position, Sydney, Australia (Nov. 1973).

Treuhaft, R. N., G. E. Lanyi, and O. J. Sovers, Trans. Amer. Geophys. Union (EOS), 65, 191 (1984).

Tsai, B. M. and C. S. Gardner, Appl. Opt. 21, 3932 (Nov. 1982).

Tsai, B. M. and C. S. Gardner, "Theoretical and Experimental Analysis of Laser Altimeters for Barometric Measurements over the Ocean," Radio Res. Lab. Tech. Rept. No. 527, University of Illinois (Mar. 1984).

Tsai, B. M. and C. S. Gardner, JOSA A 2, 649 (May 1985).

Wallace, J. M. and P. V. Hobbs, "Atmospheric Science : An Introductory Survey," Academic Press, New York (1977).

Wang, J. Y. Appl. Opt. 23, 2950 (Sept. 1984).

CUMULATIVE LIST OF RADIO RESEARCH LABORATORY

AND ELECTRO-OPTIC SYSTEMS LABORATORY REPORTS

PREPARED UNDER NASA GRANT NSG-5049

RRL Rep. No. 469 - Gardner, C. S. and N. N. Rao (December 1975), The Effects of Random Path Fluctuations on the Accuracy of Laser Ranging Systems.

RRL Rep. No. 471 - Zanter, D. L., C. S. Gardner and N. N. Rao (January 1976), The Effects of Atmospheric Refraction on The Accuracy of Laser Ranging Systems.

RRL Rep. No. 477 - Gardner, C. S. and J. R. Rowlett (November 1976), Atmospheric Refraction Errors in Laser Ranging Data.

RRL Rep. No. 478 - Hendrickson, B. E. and C. S. Gardner (December 1976), Correction of Laser Ranging Data for the Effects of Horizontal Refractivity Gradients.

RRL Rep. No. 481 - Gardner, C. S. (February 1977), Statistics of the Residual Refraction Errors in Laser Ranging Data.

RRL Rep. No. 486 - Gardner, C. S. (July 1977), Comparison Between the Refraction Error Covariance Model and Ray Tracing.

RRL Rep. No. 488 - Gardner, C. S. (September 1977), Speckle Noise in Satellite Based Lidar Systems.

RRL Rep. No. 495 - Gardner, C. S. and G. S. Mecherle (April 1978), Speckle Noise in Direct-Detection Lidar Systems.

RRL Rep. No. 496 - Gardner, C. S. and A. M. Saleh (October 1978), Speckle Noise in Differential Absorption Lidar Systems.

RRL Rep. No. 499 - Gardner, C. S. (January 1979), A Technique for Remotely Measuring Surface Pressure from a Satellite Using a Multicolor Laser Ranging System.

RRL Rep. No. 502 - Palluch, E., J. D. Shelton and C. S. Gardner (May 1979), Operating Manual for the RRL 8 Channel Data Logger.

RRL Rep. No. 505 - Gardner, C. S. and R. Axford, Jr. (March 1980), Regression Models for Multicolor Satellite Laser Ranging.

RRL Rep. No. 510 - Gardner, C. S. (April 1981), Analysis of Target Signatures for Laser Altimeters.

RRL Rep. No. 511 - Gardner, C. S. (June 1981), Atmospheric Refraction Effects in Air Borne Laser Ranging.

RRL Rep. No. 514 - Tsai, B. and C. S. Gardner (December 1981), Remote Sensing of Sea State by Laser Altimeters

RRL Rep. No. 518 - Gardner, C. S. (August 1982), Optical Communications.

RRL Rep. No. 519 - Im, K. E. and C. S. Gardner (September 1982), Atmospheric Refraction Effects on Baseline Error in Satellite Laser Ranging Systems.

RRL Rep. No. 526 - Im, K. E., B. M. Tsai and C. S. Gardner (September 1983), Analysis of Short Pulse Laser Altimetry Data Obtained Over Horizontal Path.

RRL Rep. No. 527 - Tsai, B. M. and C. S. Gardner (March 1984), Theoretical and Experimental Analysis of Laser Altimeters for Barometric Measurements Over the Ocean.

EOSL Rep. No. 84-001 - Lafaw, D. A. and C. S. Gardner (August 1984), Timing Performance of Phase-Locked Loops in Optical Pulse Position Modulation Communication Systems.

EOSL Rep. No. 85-002 - Im, K. E. and C. S. Gardner (April 1985), Estimation of the Differential Pulse Propagation Times in Two-Color Laser Ranging Systems.

EOSL Rep. No. 85-003 - Chen, C. C. and C. S. Gardner (May 1985), Phase-Locked Loop Synchronization for Direct Detection Optical PPM Communication Systems.

EOSL Rep. No. 85-006 - Im, K. E. and C. S. Gardner (August 1985), Theoretical and Experimental Analysis of the Performance of Two-Color Laser Ranging Systems.

PAPERS PUBLISHED

C. S. Gardner, "Effects of Random Path Fluctuations on the Accuracy of Laser Ranging Data," Applied Optics, 15, 2539-2545, October 1976.

C. S. Gardner, "Effects of Horizontal Refractivity Gradients on the Accuracy of Laser Ranging to Satellites," Radio

C. S. Gardner, "Correction of Laser Tracking Data for the Effects of Horizontal Refractivity Gradients," Applied Optics, 16, 2427-2432, September 1977.

C. S. Gardner, R. Rowlett and B. E. Hendrickson, "Ray Tracing Evaluation of a Technique for Correcting the Refraction Errors in Satellite Tracking Data," Applied Optics, 17, 3143-3145, October 1978.

C. S. Gardner, "Technique for Remotely Measuring Surface Pressure from a Satellite Using a Multicolor Laser Ranging System," Applied Optics, 18, 3184-3189, September 1979.

C. S. Gardner, "Target Signatures for Laser Altimeters: An Analysis," Applied Optics, 21, 448-453, February 1982.

B. M. Tsai and C. S. Gardner, "Remote Sensing of Sea State Using Laser Altimeters," Applied Optics, 21, 3932-3940, November 1982.

C. S. Gardner, B. M. Tsai and J. B. Abshire, "Remote Sensing of Atmospheric Pressure and Sea State from Satellites Using Short-Pulse Multicolor Laser Altimeters," Proceedings of NATO-AGARD Symposium on Propagation Factors Affecting Remote Sensing by Radio Waves, Oberammergau, FRG, May 24-28, 1983.

C. S. Gardner, B. M. Tsai and K. E. Im, "Multicolor Laser Altimeters for Barometric Measurements over the Ocean: Theoretical," Applied Optics, 22, September, 1983.

C. S. Gardner and J. B. Abshire, "Atmospheric refraction and target speckle effects on the accuracy of laser ranging systems," Proc. Int. Assoc. Geodesy Conf. on Laser Ranging Instrumentation, Royal Greenwich Observatory, Hearstmonceux, UK, September 24-28, 1984 (invited paper).

B. M. Tsai and C. S. Gardner, "Time-resolved speckle effects on the estimation of laser pulse arrival times," J. Opt. Soc. Amer. A., vol. 2, May 1985.

J. B. Abshire and C. S. Gardner, "Atmospheric refractivity corrections in satellite laser ranging," IEEE Trans. Geosci. Remote Sensing, vol. GE-2, September 1985.